



Development of 3D printed and injectable scaffolds for the treatment of bone lesions induced by cancer metastases

Habib Belaid

► To cite this version:

Habib Belaid. Development of 3D printed and injectable scaffolds for the treatment of bone lesions induced by cancer metastases. Material chemistry. Université Montpellier, 2019. English. NNT : 2019MONT080 . tel-04416239

HAL Id: tel-04416239

<https://theses.hal.science/tel-04416239>

Submitted on 25 Jan 2024

HAL is a multi-disciplinary open access archive for the deposit and dissemination of scientific research documents, whether they are published or not. The documents may come from teaching and research institutions in France or abroad, or from public or private research centers.

L'archive ouverte pluridisciplinaire **HAL**, est destinée au dépôt et à la diffusion de documents scientifiques de niveau recherche, publiés ou non, émanant des établissements d'enseignement et de recherche français ou étrangers, des laboratoires publics ou privés.

THÈSE POUR OBTENIR LE GRADE DE DOCTEUR DE L'UNIVERSITÉ DE MONTPELLIER

En Chimie et Physico Chimie des matériaux

École doctorale Sciences Chimiques Balard (ED459)

Institut Européen des Membranes (IEM)

Institut de Recherche en Cancérologie de Montpellier (IRCM)

Development of 3D printed and injectable scaffolds for the treatment of bone lesions induced by cancer metastases

Présentée par Habib BELAID

Le 28 octobre 2019

Sous la direction de David CORNU et Vincent CAVAILLES
et le co-encadrement de Catherine TEYSSIER et Mikhael BECHELANY

Devant le jury composé de

Joëlle AMEDEC-VILAMITJANA, Directrice de recherche INSERM, Université de Bordeaux

Rapportrice

Christele COMBES, Professeur, INP-ENSIACET

Rapportrice

Gilles SUBRA, Professeur, Université de Montpellier

Examineur

Olivier PEYRUCHAUD, Directeur de recherche INSERM, Université de Lyon

Examineur

David CORNU, Professeur, ENSCM

Directeur de thèse

Vincent CAVAILLES, Directeur de recherche INSERM, Université de Montpellier

Directeur de thèse

Catherine TEYSSIER, Chargée de recherche INSERM, Université de Montpellier

Invitée

Mikhael BECHELANY, Chargé de recherche CNRS, Université de Montpellier

Invité



UNIVERSITÉ
DE MONTPELLIER

A ma famille,

A tous ceux qui ont toujours cru en moi

« Vis comme si tu devais mourir demain.

Apprends comme si tu devais vivre toujours."

Gandhi

Acknowledgments

Au vue de l'importance pour moi de remercier toutes les personnes qui m'ont accompagné pendant ces trois années de thèse et bien plus, pour que je puisse exprimer ma gratitude au mieux, cette partie sera rédigée en français.

Je voudrais tout d'abord adresser mes remerciements aux membres du jury, Dr. Joëlle Amedee-Vilamitjana, Pr. Christele Combes, Pr. Gilles Subra et Dr. Olivier Peyruchaud d'avoir accepté d'examiner ce manuscrit.

Mes prochains remerciements s'adressent au Pr. David Cornu qui a dirigé cette thèse et qui m'a soutenu tout au long de cette période. Je souhaite remercier Dr. Vincent Cavaillès de m'avoir accueilli au sein de son équipe à l'IRCM et d'avoir su diriger cette thèse du côté biologie, les discussions qu'on a pu avoir ont permis de faire avancer ce travail dans le bon chemin. Je voudrais aussi remercier Dr. Catherine Teyssier de m'avoir formé à la culture cellulaire ainsi que tous ses conseils pour les manips et je sais que ce n'était pas gagné de former un chimiste à la biologie ! Enfin, un spécial merci pour le Dr. Mikhael Bechelany sans qui cette thèse n'aurait jamais eu lieu, merci de m'avoir aidé à évoluer depuis ce stage de M2 réalisé avec toi.

Je souhaite chaleureusement remercier les collaborateurs extérieurs qui ont participé à ce projet de thèse. Dr. Raphael Tetreau pour son expertise côté clinique. Dr. Vincent Huon et Jonathan Barés de m'avoir donné la possibilité de faire la partie méca au LMGC. Dr. Sébastien Blanquer pour ton temps et tes conseils sur la partie stéréolithographie. Pr. Frédéric Cuisinier, Dr. Pierre-Yves Collart-Dutilleul et Alban Desoutter du LBN pour les études *in vivo*. Je souhaite aussi remercier les collaborateurs de l'IEM, Dr Sébastien Balme, Dr. Céline Pochat et Dr. Mona Semsarilar pour votre aide sur différents aspects de mes expériences.

Ces 3 années de thèse ont été une période plutôt fructueuse en termes de rencontres de personnes formidables. Avec cette thèse en co-direction j'ai passé un peu de temps à l'IRCM où j'ai eu la chance de partager de très bons moments avec pas mal de personnes et notamment avec ceux de l'équipe Cavaillès, je pense à Valentin, Antoine, Nour, Romain et Sandrine avec qui j'ai partagé mon bureau. Mais aussi Sam, Madi et Manda avec qui ce fut un plaisir de faire ces parties de fléchettes pendant l'happy hour ou le barbacue de l'after JET.

La plupart de mon temps, je l'ai quand même passé à l'IEM où je suis arrivé il y a plus de trois et demi maintenant. Je voudrais commencer par remercier Pr. Philippe Miele en tant que directeur de l'Institut de m'avoir soutenu notamment pendant mon mandat à la tête de

« YOCHIN » ainsi que le personnel de l'IEM, les membres du département DM3 et plus particulièrement ceux du cluster PNM qui m'ont beaucoup aidé durant cette thèse.

Il y a beaucoup de gens à citer et je vais commencer par les « anciens », Maryline qui m'a fait découvrir son incroyable pays qui est le Liban, Antoine (avec qui j'ai pu partager sa passion pour les verts dans le chaudron), Ana (on se voit bientôt en Australie), Socrates (c'était un véritable plaisir de travailler avec toi, faut qu'on finisse toutes ces publi !). Un spécial mot pour Sakthivel, un des piliers des anciens du labo, ces trois années à tes côtés ont été incroyables, merci pour toutes ces idées qui ont fait avancer nos recherches mais aussi pour tous ces fous rires ensemble !

Il reste encore quelques personnes à mentionner avec qui je partage mon quotidien dans le laboratoire, Octavio, Matthieu, Carole et toute l'équipe des libanaises Sara, Maya, Syreina et Marleine (merci pour tous les kg que j'ai pris avec vos gâteaux!).

Il y a aussi les thésards avec qui je partage cette joie de la rédaction de dernière année Lucie et Quike (courage mon pote). Mais aussi les jeunes avec qui j'ai pu faire un certain nombre de sorties et apéros, Cyril, Marine, Marianne, Alice, Julien, Carlos, Quentin, Gabi et tous ceux que j'aurais pu oublier par mégarde...

Comment ne pas faire un mot à part pour mon binôme Thomas de l'équipe « tu tires ou tu pintes », ces tournois de beer-pong gagnés, cette coloc au top jusqu'à que tu deviennes docteur.

Bien évidemment, je te dois à mon tour un paragraphe spécial, Danae. J'ai eu la chance de rencontrer une personne formidable. Tu es la personne avec qui j'ai passé le plus de temps pendant cette thèse que ce soit au labo, au bureau ou en voyage. Je savais que je te manquais trop et t'as préféré revenir travailler à l'IEM après ta thèse pour me soutenir pour la fin de la mienne. J'espère que cette relation avec toi et ton Pierrot perdurera encore longtemps et qu'on continuera à se voir.

Finalement, je vais remercier ceux sans qui je ne serais pas arrivé jusque-là, mes parents, mes frères et ma sœur qui m'ont toujours soutenu dans mes choix et qui m'ont aidé à devenir la personne que je suis aujourd'hui. Un dernier remerciement pour la personne qui a dû le plus supporter ma mauvaise humeur de ces derniers mois et qui m'a encouragé et soutenu pour que je donne toujours le meilleur de moi-même, Hana t'es la meilleure.

Table of contents

Abstract	11
Résumé	13
List of abbreviations	15
General introduction	19
 Part 1: Introduction	 21
A- Bone physiopathology and breast cancer metastases	23
1. Bone tissue	23
2. Breast cancer and bone metastases	30
3. Breast cancer-induced bone metastasis treatments	39
B- Bone tissue engineering	48
1. Injectable scaffolds: From poly(methyl methacrylate) to calcium phosphate cement	49
2. Generation of 3D scaffolds: From conventional methods to 3D printing	58
C- 3D scaffold improvement	72
1. 2D nanosheets materials	73
2. Microspheres	77
D- Conclusions and objectives	85
 Part 2: Results and discussion	 101
A- 3D Printed Graphene Oxide-based Scaffolds for Bone Tissue Engineering	103
Abstract	104
1. Introduction	105
2. Experimental section	107
2.1. Materials	107
2.2. Preparation of the PLA/GO scaffolds.	108
2.3. Morphological properties.	108
2.4. Chemical and structural properties	109
2.5. Thermal properties.	109
2.6. Mechanical properties.	110
2.7. Cell viability and adhesion assays	110
2.8. Mineralization assay	111
3. Results and discussion	112
3.1. Generation and morphological analysis of PLA/GO scaffolds.	112
3.2. Structural characterization of PLA/GO scaffolds.	114
3.3. Chemical characterization of the scaffolds	116
3.4. Thermal analysis of the PLA/GO scaffolds.	117
3.5. Mechanical properties of the 3D printed nanocomposites.	120
3.6. Biological studies.	122
4. Conclusions	124
REFERENCES	125
Supporting Information	129

B- Boron nitride-based nano-biocomposites: Design by 3D printing for bone tissue engineering	133
Abstract	134
1. Introduction	135
2. Experimental section	137
2.1. Materials.....	137
2.2. Preparation of PLA/EBN scaffolds.	138
2.3. Chemical and structural properties.....	138
2.4. Thermal properties.	139
2.5. Mechanical properties.	139
2.6. Morphological properties.	140
2.7. Cell viability and adhesion assays.....	140
2.8. Mineralization assay.....	141
3. Results and discussion.....	142
3.1. Structural and chemical characterization of the scaffolds.....	142
3.2. Thermal analysis of the PLA/EBN scaffolds.	143
3.3. Mechanical properties of the 3D printed nanocomposites.	146
3.4. Morphological analysis of PLA/EBN scaffolds.....	147
3.5. Biological studies.	148
4. Conclusions	150
REFERENCES.....	151
Supporting Information	154
C- Stereolithographic 3D printing of a PPF scaffold containing drug-loaded PLGA microspheres.....	157
Abstract	158
2. Experimental section	163
2.1. Materials.....	163
2.2. Synthesis of the poly(propylene fumarate) polymer	163
2.3. Scaffold printing by stereolithography.....	164
2.4. Morphological and size distributions of scaffolds.	164
2.5. Mechanical properties	165
2.6. Thermal properties.	165
2.7. Preparation of AL-loaded PLGA microspheres.	165
2.8. Preparation of RH-loaded PLGA microspheres.....	166
2.9. Determination of drugs encapsulation efficiency.....	166
2.10. Determination of drug release.	167
2.11. Biocompatibility and bioefficacy of microspheres.	168
3. Results and discussion.....	168
3.1. Generation and characterization of a 3D printed PPF scaffold.....	168
3.2. Thermal analysis of the PPF scaffolds.	170

3.3. Generation and morphological analysis of PLGA microspheres.	171
3.4. Drug release studies.	173
3.5. Biocompatibility and bioefficacy of drug-loaded microspheres.	174
3.6. Generation and morphological analysis of the PPF/PLGA scaffold.	176
4. Conclusions	176
REFERENCES	177
Supporting information	180
D- Fabrication of injectable calcium phosphate cement containing PLGA microspheres....	183
Abstract	184
1. Introduction	185
2. Experimental section	188
2.1. Materials.	188
2.2. Preparation of PLGA microspheres.	189
2.3. Fabrication of CPC/PLGA samples.	190
2.4. Opacity measurements.	190
2.5. Morphology analysis.	190
2.6. Mechanical properties.	191
2.7. Structural and chemical properties.	191
2.8. Degradation study.	191
2.9. Setting time and injectability.	192
2.10. Cell viability assays.	193
2.11. Implantation in rat vertebrae.	193
2.12. X-ray micro-CT analysis.	194
3. Results and discussion	194
3.1. Obtention of a radio-opaque CPC.	194
3.2. Introduction of PLGA microspheres in the CPC.	196
3.3. Biological studies.	202
4. Conclusions	204
REFERENCES	205
Supporting information	207
Part 3: General discussion and perspectives	211
A- 3D printed scaffold.....	213
1. Mechanical properties	214
2. Biocompatibility	214
3. Bioefficacy	215
4. Drug delivery	217
B- Injectable Calcium Phosphate Cement.....	221
1. Opacity	222
2. Mechanical properties and porosity	222

3. Bioefficacy	224
C- In vivo study	225
D- Conclusions and perspectives	227
REFERENCES	228
 Part 4: Materials and methods	 233
A- Materials	235
B- Two-dimensional nanosheets	236
1. Graphene oxide	236
2. Boron nitride	237
C- PLGA microspheres	239
1. Single and double emulsion solvent evaporation method	239
2. Characterization techniques	241
D- 3D printing	245
1. Fused Deposition Modeling	245
2. Stereolithography	246
3. Synthesis of polypropylene fumarate	247
4. Characterization techniques	248
E- Calcium Phosphate Cement	255
1. Materials and synthesis	255
2. Characterization techniques	256
F- Biological studies	260
1. In vitro	260
2. In vivo	261
Scientific contributions	263

Abstract

Despite its inert appearance, bone is alive and constantly renewing itself. This bone remodeling is essential to maintain its mechanical and metabolic functions. In many cases, bone fractures caused by trauma or resulting from diseases cannot self-repair and require the use of bone grafts. The use of synthetic bioactive or bioresorbable biomaterials has a great interest for bone tissue engineering. The aim of this thesis was to develop new scaffolds able to treat bone fractures arising from breast cancer metastasis, *i.e.* scaffolds which could support bone formation but also eradicate cancer cell proliferation.

Firstly, 2D nanomaterials including graphene oxide (GO) and boron nitride (BN) were used to reinforce poly(lactic acid) (PLA) in order to improve its mechanical properties and bioactivity. Composite PLA/GO and PLA/BN scaffold were fabricated by fused deposition modeling. With the addition of 0.2%wt of GO, the Young's modulus was increased while with the addition of 0.1%wt of BN, the proliferation and mineralization of MG63 osteosarcoma cells were higher. Then, to improve the bioefficacy of the scaffolds, two drugs were used. Alendronate (AL) and raloxifene (RH) were encapsulated in Poly (lactic-co-glycolic acid) (PLGA) microspheres of 1 μm by emulsion method. The AL-loaded microspheres showed much higher encapsulation efficiency and release than the PLGA/RH microspheres. Both PLGA microspheres were biocompatible and bioactive on MCF7 breast cancer cells. To use those drugs efficiently in bone substitute, AL and RH-loaded PLGA-microsphere were embedded in poly (propylene fumarate) (PPF). PPF scaffold was created by stereolithography (SLA) and showed mechanical properties similar to those of trabecular bones. Finally, in the case of non-invasive surgery such as vertebroplasty, we developed an injectable macroporous calcium phosphate cement (CPC) brushite cement phase which contained 20% ZrO_2 as radio-opacifier to monitor cement leakage. This CPC exhibited good handling properties (injectability, initial and final setting time, cohesive properties) and a good radio-opacity. Upon addition of PLGA microspheres of 100 μm , the CPC/PLGA scaffold showed a good macroporosity but exhibited a decreased compression strength and lower handling properties, though still workable. The *in vivo* study in caudal vertebrae of rat showed good retention of the CPC up to a month. Moreover, CPC/PLGA30 was partially resorbed and replaced by the formation of new bone.

In conclusion, these two types of scaffolds (3D printed or injectable cement) are very promising to treat pathologic fractures of bone metastasis of breast cancer.

Résumé

Malgré son aspect inerte, l'os est vivant et se renouvelle continuellement. Ce remodelage osseux est essentiel pour maintenir ses fonctions mécaniques et métaboliques. Avec l'augmentation globale de l'âge de la population, les fractures osseuses ont augmenté ces dernières années. Elles sont habituellement causées par un traumatisme, mais certaines fractures peuvent être le résultat de maladies. Dans de nombreux cas, lors de fractures osseuses, l'os ne peut pas se réparer seul et l'utilisation de greffes osseuses est nécessaire. L'utilisation de biomatériaux synthétiques a suscité un grand intérêt pour la réparation osseuse.

L'objectif de cette thèse était de développer un nouveau type de scaffold capable de traiter les fractures liées aux métastases osseuses du cancer du sein. Ces scaffolds pourraient favoriser la formation osseuse mais aussi bloquer la prolifération des cellules cancéreuses.

Tout d'abord, des nanomatériaux 2D tels que l'oxyde de graphène (GO) et le nitrure de bore (BN) ont été utilisés pour renforcer l'acide polylactique (PLA) afin d'améliorer ses propriétés mécaniques et sa bioactivité. Des scaffolds composites PLA/GO et PLA/BN ont été fabriqués à l'aide de la technique de dépôts par filament (FDM). Avec l'ajout de 0,2 % de GO, le module de Young du scaffold de PLA a augmenté, tandis qu'avec l'ajout de 0,1 % de BN, la prolifération et la minéralisation des cellules d'ostéosarcome MG63 étaient plus élevées. Ensuite, pour améliorer la bioefficacité des scaffolds, deux médicaments ont été utilisés. L'alendronate (AL) et le raloxifène (RH) ont été encapsulés dans des microsphères d'acide polylactique-co-glycolique (PLGA) de 1 μm par émulsion. Les microsphères chargées en AL ont montré une efficacité d'encapsulation et de libération beaucoup plus élevée que les microsphères de PLGA/RH. Les deux microsphères de PLGA chargées en médicaments étaient biocompatibles et aussi bioactives sur les cellules cancéreuses du sein (MCF7). Pour utiliser efficacement ces médicaments dans des substituts osseux, ces microsphères de PLGA chargées en AL et RH ont été incorporées dans du poly(fumarate de propylène) (PPF). Le scaffold à base de PPF a été créé par stéréolithographie (SLA) et des propriétés mécaniques similaires à celles des os trabéculaires ont été observées. Enfin, dans le cas de la chirurgie mini invasive comme la vertébroplastie, nous avons développé un ciment injectable macroporeux à base de phosphate de calcium (CPC). Des microsphères de PLGA de 100 μm ont été ajoutées au ciment (CPC/PLGA). Le ciment contenait 20% de ZrO_2 comme radioopacifiant pour prévenir les fuites de ciment. Le CPC s'est avéré avoir une bonne manipulation (injectabilité, temps de prise initiale et finale, propriétés cohésives) mais aussi

une bonne radioopacité. Le scaffold CPC/PLGA a montré une bonne macroporosité mais une moins bonne maniabilité, bien qu'il soit correctement manipulable et une diminution de la résistance à la compression a été observée. L'étude *in vivo* sur des vertèbres caudales de rats a montré une bonne rétention du CPC à un mois. De plus, le CPC/PLGA30 a été partiellement résorbé et remplacé par la formation de nouvel os.

En conclusion, ces deux types de scaffolds (imprimés en 3D ou ciment injectable) sont très prometteurs en vue de traiter les fractures provenant de métastases osseuses de cancer du sein.

List of abbreviations

μSL	Micro-stereolithography
3DP	Powder-based 3D printing
AL	Alendronate
BAPO	Bis-acylphosphine oxide
BMD	Bone mineral density
BMP2	Bone morphogenetic protein 2
BN	Boron nitride
BPs	Bisphosphonates
BSA	Bovine Serum Albumin
BTE	Bone tissue engineering
CaP	Calcium phosphate
CDHA	Calcium-deficient hydroxyapatite
CH ₂ Cl ₂	Dichloromethane
CPC	Calcium phosphate cement
DCPA	Anhydrous dicalcium phosphate
DCPD	Dicalcium phosphate dehydrate
DEF	Diethyl fumarate
DLP	Dynamic light processing
DLS	Digital light scattering
DMA	Dynamic mechanical analysis
DMSO	Dimethyl sulfoxide
DNA	Deoxyribonucleic acid
DSC	Differential scanning calorimetry
E2	Estradiol
EBN	Exfoliated boron nitride
EDX	Energy-dispersive X-ray
EE	Encapsulation efficiency
ER	Estrogen receptor
FDA	U.S. Food and Drug Administration
FDM	Fused deposition modeling
FTIR	Fourier Transform Infrared
GO	Graphene oxide

H ₂ O ₂	Hydrogen peroxide
H ₂ SO ₄	Sulfuric acid
H ₃ PO ₄	Phosphoric acid
HA	Hydroxyapatite
HER2	Human epidermal growth factor receptor-2
KMnO ₄	Potassium permanganate
L-TPO	Monoacylphosphine oxide
MCF-7	Michigan Cancer Foundation-7
MCPM	Monocalcium phosphate monohydrate
MeOH	Methanol
MG-63	Human bone cells
MTT	Dimethylthiazol-2-yl)-2,5-diphenyl tetrazolium bromide
OCP	Octacalcium phosphate
PBS	Phosphate buffered saline
PCL	Polycaprolactone
PDI	Polydispersity index
PEG	Polyethylene glycol
PGA	Poly (glycolic acid)
PHA	Precipitated HA
PLA	Poly (lactic acid)
PLGA	Poly (lactic-co-glycolic acid)
PMMA	Poly (methyl methacrylate)
PPF	Poly (propylene fumarate)
PR	Progesterone
PTHrP	Parathyroid hormone-related protein
RANK	Receptor activator of nuclear factor
RANKL	Receptor activator of nuclear factor kappa-B ligand
RH	Raloxifene hydrochloride
ROI	Region of interest
SEM	Scanning electron microscopy
SERMs	Selective estrogen receptor modulators
SL or SLA	Stereolithography
SLS	Selective Laser Sintering
SREs	Skeletal-related events

Tcc	Cold temperature crystallization
TCP	Tricalcium phosphate
Tg	Glass transition temperature
TGA	Thermogravimetric analysis
TGF- β	Transforming growth factor- β
TiO ₂	Titanium oxide
Tm	Melting temperature
TTCP	Tetra-calcium phosphate
TV	Tissue Volume
UV	Ultraviolet
χ_c	Crystallinity
XRD	X-ray diffraction
ZrO ₂	Zirconium Oxyde

General introduction

The repair of bone defects caused by diseases, such as breast cancer bone metastases, has become a major health issue over the years. These fractures cannot be repaired by natural curing processes and they require the involvement of new technologies such as bone tissue engineering. The aim of this thesis is the development and characterization of novel biomimetic biodegradable implants allowing both bone regeneration and breast cancer cell eradication. Our goal is to develop new original processes for the development of 3D printed polymer and injectable calcium phosphate cement scaffolds. The objective is to incorporate in the scaffolds two molecules stimulating bone formation (Alendronate) and inhibiting the proliferation of estrogen dependent breast cancer cells (Raloxifene). Firstly, a review of the literature on bone metastases of breast cancer which are responsible of pathologic fractures is provided. The solutions existing to treat these pathologic fractures are also summarized. Then results obtained during the thesis are presented and divided in four different articles (2 are submitted and in revision). The two first sections are focusing on scaffold based poly (lactic acid) (PLA) obtained by fused deposition modeling. In a first study, PLA was modified with graphene oxide nanosheets to reinforce mechanical properties of this one. Then, in a second article, PLA was modified by the incorporation of boron nitride nanosheets to improve biocompatibility and bioactivity of the scaffold. In the third result section, Alendronate and Raloxifene were encapsulated in Poly (lactic-co-glycolic acid) (PLGA) microspheres. These microspheres were embedded in Poly (propylene fumarate) (PPF) scaffolds obtained by stereolithography. Finally, in the last section, in the case of non-invasive surgery, we fabricated injectable macroporous calcium phosphate cement (CPC) to be used for instance in vertebroplasty. To conclude this thesis, a general discussion is given with additional data which complete the different studies. In this last part, some perspectives of this thesis will also be presented.

Part 1

Introduction

For decades, bone fracture treatment has been a big challenge. Fractures are usually caused by traumas (fall or shock, for example); however, some fractures can be the result of a pathologic condition. In the last years, the frequency of such pathologic fractures has been increasing due to population ageing¹. In many cases of pathologic fracture, bone cannot self-repair, and bone grafts are required to restore the damaged bone. Due to the limited availability of donor tissue and other issues linked to bone grafting, the use of synthetic biomaterials are of great interest for bone repair, and are now being used as bone graft substitutes. Bone tissue engineering is very interesting for complete bone recovery. Indeed, initially, biomaterials were selected for structural restoration based on their biomechanical properties. Now, it is possible to engineer biomaterials, also called scaffolds, that are bioactive or bioresorbable to enhance tissue growth. The last steps in scaffold improvement are to induce bone formation and vascularization. Different scaffold types, made of biodegradable materials that support different growth factors, drugs, genes, or stem cells, are available.

The aim of the Introduction chapter is to give some background information on pathologic fractures in patients with bone metastases from breast cancer and on the different scaffold types used for bone repair. The chapter is divided in four sections: i) bone physiopathology and breast cancer; ii) bone tissue engineering and 3D printing; iii) scaffold improvement strategies; and iv) thesis objectives.

A- Bone physiopathology and breast cancer metastases

1. Bone tissue

Bone is a major component that provides structural support for the body of higher vertebrates. Bone is a dynamic tissue that can heal and remodel itself. Indeed, this tissue undergoes continuous remodeling throughout the lifetime. Injury or disease can lead to major alterations in the bone structure and can dramatically alter the body equilibrium and quality of life. In the

case of diseases or fractures, the bone tissue cannot self-repair. Therefore, a bone graft or “scaffold”, which is a biomaterial to support bone regeneration, is necessary².

1.1. Bone functions

Bones have many functions. They structurally support the body, keep safe our vital organs, and allow moving. Bones also act as a storage area for minerals and provide an environment for bone marrow (Figure 1).

The main bone functions are:

- Mechanical: Bones provide a structure to support the body. Muscles, tendons, and ligaments are attached to the bones.
- Protection: Some bones protect internal organs. For instance, the ribs protect the heart and lungs, while the skull protects the brain.
- Metabolic: Bones act as a reserve for minerals, mostly calcium and phosphorous.
- Hematopoietic: Cancellous bone produces red blood cells, platelets, and white blood cells.

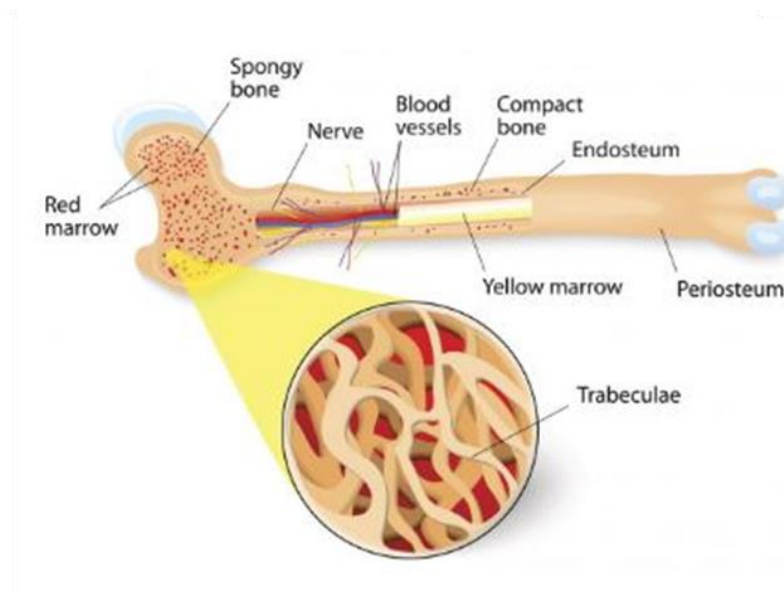


Figure 1. Bone anatomy (adapted from REF 3)

1.2. Bone structure

The human body possesses about 200 bones that can be divided in different types:

- Long bones (femur and shinbone): These are mostly compact bones with little marrow and include most of the limb bones. These bones tend to support weight and help movement.
- Short bones (wrist and ankle): Only a thin layer of compact bone.
- Flat bones (skull, and sternum or breastbone): These bones are usually thin and curved. They consist of two outer layers of compact bone and an inner layer of spongy bone. They tend to have a protective role.
- Sesamoid bones (patella or kneecap): They protect tendons from wear and stress.
- Irregular bones (spine and pelvis): These have an unusual shape and often protect organs or tissues.

Each bone is composed of two tissue types:

- Compact or cortical bone:

Compact bone forms the outer layer of all bones and most of the "long bone" structure. Cortical bone forms a dense cylinder that is strong and durable. It accounts for about 80% of the adult bone mass with a low surface area and a low porosity. It provides protection and support to the bone while helping long bones to withstand the stress of the body weight and limb use.

- Cancellous or trabecular bone:

Cancellous bone has an open honeycomb structure. It is located at the ends of long bones. It accounts for around 20% of the bone mass in the human body. This tissue consists of a network of trabeculae. It is lighter, less dense, and more flexible than compact bone. It is also composed of a non-mineral matrix (collagen fibers and non-collagenous proteins or osteoid)

and inorganic mineral salts (small crystals) deposited within the matrix. Osteoid is made of type I collagen (~94%) and non-collagenous proteins. The synthesis of organic matrix is the first phase during bone formation. The organic matrix is mainly constituted of type I collagen that is the main fibrous protein in the body. It has a triple helical structure, and specific points along the collagen fibers serve as nucleation sites for the bone mineral crystals. Collagen gives bone its tensile strength, namely the resistance to being pulled apart. Bone hardness and rigidity are due to the presence of mineral salts in the osteoid matrix, which is a crystalline compound of calcium and phosphate (hydroxyapatite). Calcified bone contains about 25% of organic matrix (2-5% of which are cells), 5% of water, and 70% of inorganic mineral (hydroxyapatite) in varying proportions, depending on the bone. The mineral component can be described as hydroxyapatite (HA), with the chemical formula $\text{Ca}_{10}(\text{PO}_4)_6(\text{OH})_2$. However, whereas HA has a Ca:P ratio of 1.67, bone mineral itself has a Ca:P ratio between 1.37 and 1.87. This is because the bone mineral composition is much more complex and contains additional ions, such as silicon, carbonate, and zinc. HA gives the bones compressive strength (i.e., resistance to being compressed).

1.3. Bone modeling and remodeling

Bones are not a static tissue, but are constantly maintained and remodeled. Bone formation is an essential process during the human body growth. It starts during the fetal period and continues throughout childhood and adolescence as the skeleton grows. Bone remodeling is a life-long process, consisting of resorption (the breaking down of old bone) and ossification (formation of new bone), and is crucial for shaping the skeleton and for repairing bone fractures. A fine equilibrium between the two types of bone cells, bone-forming cells (osteoblasts and osteocytes) and bone-resorbing cells (osteoclasts), is required for bone remodeling. These cells are responsible for bone production, maintenance, and resorption.

- Osteoblasts

These “bone-forming” cells, found near the bone surface, are derived from mesenchymal stem cells. They are responsible for bone matrix synthesis by making a protein mixture called osteoid. Osteoblasts secrete alkaline phosphatase to create sites for calcium and phosphate deposition, which allows the growth of bone mineral crystals at these sites. The osteoid becomes mineralized, thus forming bone. They also produce hormones, including prostaglandins.

- Osteocytes

These cells are osteoblasts that are no longer on the bone surface and are incorporated within the newly formed osteoid, which eventually becomes calcified bone. Osteocytes are situated in lacunae between the lamellae in the deep bone matrix. Their main role is homeostasis. They are important for the cross-talk within the bone tissue via their connections with other osteocytes in the osteoid and with osteoblasts and bone-lining cells at the bone surfaces, through an extensive network of cell processes (canaliculi). They are thought to be ideally situated to respond to changes in physical forces and to transduce messages to cells at the bone surface, directing them to initiate bone resorption or formation.

- Osteoclasts

They are large multinucleated cells responsible for bone resorption, and derived from the hematopoietic lineage. Osteoclasts are attached to the bone surface and travel to specific sites where they resorb mineralized tissue. Their main feature is the secretion of bone-resorbing enzymes and acids that digest the mineralized bone and remove calcium. Osteoclasts help to remodel injured bones and create pathways for nerves and blood vessels to travel through.

Bone modeling defines the occurrence of bone resorption and bone formation at separate surfaces (i.e., bone formation and resorption are not coupled). An example of this process is during long bone growth in length and diameter. Bone modeling occurs from birth to adulthood and is responsible for the gain in skeletal mass and changes in skeletal form.

Bone remodeling is the replacement of old by new bone tissue. This mainly occurs in the adult skeleton to maintain bone mass. In this process bone formation and bone resorption are coupled. It includes five phases:

1. Activation: pre-osteoclasts are stimulated and differentiate into mature active osteoclasts under the influence of cytokines and growth factors
2. Resorption: osteoclasts digest mineral matrix (old bone)
3. Reversal: end of resorption
4. Formation: osteoblasts synthesize new bone matrix
5. Quiescence: osteoblasts become resting bone-lining cells in the newly formed bone surface.

When the modeling and remodeling cycle is disrupted and bone cannot self-repair, different natural or synthetic biomaterials can be used for bone healing.

1.4. Bone graft

Natural bone substitutes were the first to be developed. Nowadays, bone graft remains the most widely used bone substitute. There are three graft types: autografts, allografts, and xenografts.

- Autograft is the use of bone from the same individual for implantation into another site. Autologous bone grafting is currently considered as the gold standard in the field of bone substitutes. It allows correcting any loss of bone substance, while avoiding the risk of rejection. Moreover, it has all the characteristics required for bone growth (osteoconduction, osteogenesis, and osteoinduction) and optimal mechanical properties. However, the quantity and quality of available bone stock may be limited. In addition, access to the donor site may require a surgical intervention, and may be followed by major complications, such as inflammation, infection and pain⁴⁻⁶.
- Allograft is an alternative to autologous bone in which bone is taken from another human being (living or deceased donors^{7,8}). Despite the good osteoconductive and osteoinductive properties of allografts and the higher proportion of available bone compared with autografts⁹, the risk of disease transmission from the donor is high¹⁰.
- Xenograft is a bone substitute taken from an organism of a different species, such as beef or pork. Recolonization occurs as for an allograft, but in a more limited and slower way and requires a well-vascularized recipient bone. Due to its low osteogenic potential, xenografts are not suitable for large volumes¹¹. Moreover, the theoretical risk of transmission of bovine- or porcine-specific pathogens has considerably limited its development¹². Besides the complications associated with these grafts, social, ethical or religious reasons may also limit their use.

The limitations of the different bone graft types have motivated the development of alternative strategies. Various synthetic biomaterials based on polymers, ceramics or

composites have been developed and many have been commercialized. Scaffolds come in different forms, and they can be injectable or 3D printed. They will be discussed in part B.

In diseases, such as cancer metastases, bone can be disrupted. In the next section, we will describe the consequences of bone metastases on the quality of life of patients with breast cancer and their management.

2. Breast cancer and bone metastases

2.1. Breast cancer

In women, breast cancer is the most common invasive cancer and the second cause of cancer death. According to the estimates by the International Agency for Research on Cancer around 2.1 million people had breast cancer in 2018, and this accounted for approximately 11.6% of the total cancer incidence burden¹³. Around 350 000 new patients with breast cancer are detected in Europe every year, and 60 000 cases were estimated in France in 2017¹⁴. About one in eight women will have breast cancer during their lifetime¹⁵. Although 87% of patients are still alive 5 years after diagnosis, unfortunately, nearly 12.000 deaths occur in France each year.

Breast cancer is classified in different types. Ductal carcinoma in situ represents 80% of all breast cancer cases. In this breast cancer type, cancer cells are located within the breast ducts or lobules. When cancer cells spread and infiltrate the tissue surrounding the ducts and lobules, it is called invasive carcinoma. The breast cancer classification is based on the immunohistochemical detection of estrogen (ER) and progesterone (PR) receptors, and the overexpression of the oncoprotein human epidermal growth factor receptor-2 (HER2) and of cytokeratin 5 and 6. Different groups of breast cancers can be defined in function of their expression profile¹⁶ (Table 1).

Table 1. Classification of breast cancer in different subcategories.

Form	Subtype	Molecular characteristics
Luminal	A	ER+,PR+,HER2-
	B	ER+,PR+,HER2+
HER2+		ER-, PR-, HER2+
Triple negative		ER-, PR-, HER2-

The patient treatment will be dictated by the cancer classification. Treatment may be considered before resection or after resection to reduce the metastasis risk. As luminal breast cancers are ER+ and PR+, their treatment is based on hormone therapy that either modifies hormone secretion or blocks their action in order to stop tumor cell proliferation. HER2+ cancers are associated with a low survival rate (50% at 5 years). However, the use of targeted therapies in combination with chemotherapy has increased patient survival. As breast cancer treatments have greatly improved the patients' survival, nowadays mortality is increasingly linked to the occurrence of distant metastases.

2.2. Breast cancer metastases

Cancer is a disease characterized by the uncontrolled proliferation of malignant cells within a tissue. By multiplying in an uncontrolled way, cancer cells give rise to increasingly large tumors that invade and destroy the surrounding organs. During primary tumor development, malignant cells undergo a series of genetic and epigenetic changes that enable them to overcome cellular and host tumor suppressor mechanisms. They provide the cells with the ability to escape the confines of the primary tumor site, enter the systemic circulation, and eventually find a distant site in which cancer cell survival and growth are facilitated¹⁷. The growth of disseminated tumor cells at metastatic locations is the primary cause of death in patients with cancer¹⁸. Some organs are preferred sites for metastasis development. Bone is

the third most common site of metastases after lung and liver. Breast cancer will metastasize in up to 70% of cases. Breast cancer bone metastases develop as the result of a series of complex interactions between tumor cells, bone marrow cells, and resident bone cells. They alter the functions of bone-resorbing (osteoclasts) and bone-forming cells (osteoblasts). The clinical course of patients with breast cancer metastases in bones is relatively long, with sequential skeletal-related events¹⁹ that can profoundly impair their quality of life.

2.3. Bone metastases

2.3.1. Generalities

Bone is a common site of metastatic cancer. Stephen Paget first described a non-random pattern of metastases to organs in 1889, while analyzing autopsy specimens from women who died of breast cancer²⁰. Bone metastases cause serious skeletal complications, including spinal cord or nerve compression, hypercalcemia, pain, and pathologic fractures²¹ (Figure 2). The median survival after the diagnosis of overt skeletal metastases is approximately 2–3 years. These facts illustrate the clinical importance of preventing or curing bone metastases. Bone invasion by tumor cells is associated with osteoclast and osteoblast recruitment, resulting in the liberation of growth factors from the bone matrix, which in turn can enhance tumor cell growth, leading to a ‘vicious cycle’ of bone metastases. Besides the effects on osteoclasts and osteoblasts, metastatic tumor cells in the bone microenvironment recruit and modulate the function of platelets, myeloid cells, immune cells and nerve cells, and induce the formation of new blood vessels.

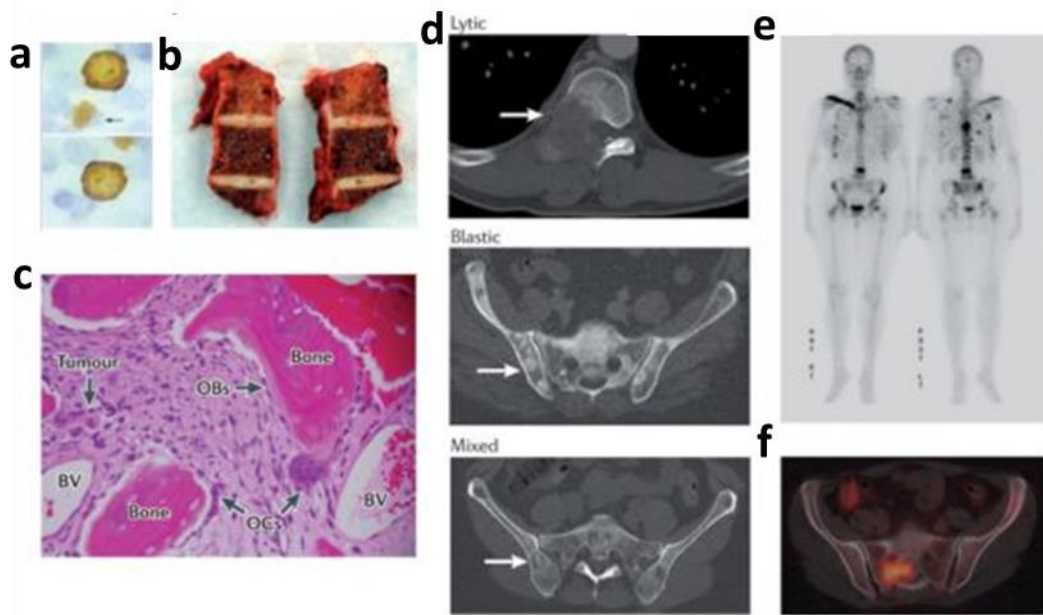


Figure 2. Clinical presentation of bone metastases (adapted from REF 21). a) Immunohistochemical staining for cytokeratin shows the presence of disseminated tumor cells in a bone marrow smear taken from a patient with breast cancer; b) Post-mortem examination showing osteoblastic lesions of vertebral bodies; c) Bone biopsy sample stained with hematoxylin and eosin from a patient with metastatic breast cancer shows the bone invasion by tumor cells with the presence of osteoclasts (OCs) and osteoblasts (OBs); d) Computerized tomography images showing the different types of bone lesions; e) Full body bone scans of a patient with metastatic breast cancer; f) Positron emission tomography combined with computed tomography shows active bone metastases in the sacrum.

2.3.2. Mechanisms of bone metastasis formation

Once metastatic breast cancer cells are in the bone marrow microenvironment, they can activate local bone and bone marrow cells, thereby facilitating the release of factors from the bone that support tumor cell survival and proliferation²². Indeed, a ‘vicious cycle’ is established whereby metastatic cells in the bone marrow secrete factors that stimulate osteoclast-mediated bone resorption, while growth factors released from resorbed bone stimulate tumor growth²³ (Figure 3). Breast cancer cells may also interact with pre-osteoclasts, resulting in indirect stimulation of osteoclast differentiation and maturation²⁴. Furthermore, breast cancer cells secrete factors that inhibit osteoblast differentiation and activity²⁵. Their interaction with osteoblasts also induces the release of cytokines that promote tumor growth²⁴. All these effects lead to an imbalance between bone resorption and bone

formation, resulting in enhanced bone destruction and pathological fractures, as a consequence of osteolysis²⁶.

The predominant bone lesion due to breast cancer metastases is lytic and destructive. Often, there is a local bone formation response, which represents an attempt at local bone repair²⁷. Of note, tumor osteolysis and bone destruction, as well as tumor-induced bone formation, are entirely the results of tumor-mediated activation of resident bone cells and are not related to any direct action of the tumor cells on the skeleton.

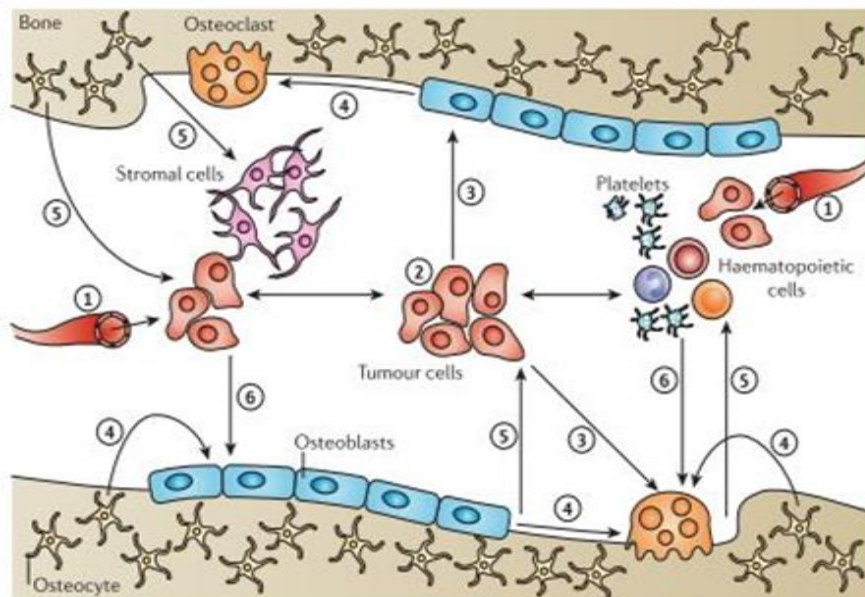


Figure 3. Cells in the bone marrow environment (adapted from REF 22). 1) Circulating tumor cells, as well as normal circulating platelets and other normal hematopoietic progenitor cells arrive from blood vessels in the highly vascularized bone marrow compartment; 2) Tumor cells that arrive in the bone marrow can interact with the resident normal host cells to establish, maintain and survive in a bone marrow niche; 3) Resident tumor cells also can drive the activity of resident bone-residing cells; 4). Activation of resident bone cells before, during or after the dissemination of metastatic tumor cells enhances osteolysis induction, osteoblast proliferation, and even bone formation; 5) These effects provide additional growth factors and nutrients that promote the survival and progression of tumor cells and of supporting resident bone and bone marrow cells; 6) Activation of bone remodeling and normal marrow cells also results in the release of molecules that regulate the bone cell activity and function.

Several molecules that are produced by breast cancer cells, for example parathyroid hormone-related protein, interleukins (IL-6, IL-8, and IL-11), cytokines (macrophage colony stimulating factor; M-CSF) and prostaglandins, stimulate osteoclast activity through

activation of the receptor activator of nuclear factor- κ B ligand (RANKL)/RANK pathway. The RANKL-induced increase in osteoblast production indirectly stimulates osteoclast formation²⁸, leading to osteoclast-mediated bone resorption²⁹.

Breast cancer cells may also directly stimulate osteoclast-mediated bone resorption by interacting with pre-osteoclasts through the Jagged1-Notch pathway²⁴. In addition, breast cancer cells secrete activin A (a member of the transforming growth factor (TGF)- β super family of growth factors), noggin (a bone morphogenetic protein (BMP) antagonist), and dickkopf-1 (DKK-1; a Wntless protein antagonist). All these factors inhibit osteoblast differentiation³⁰, leading to bone lesions (Figure 4).

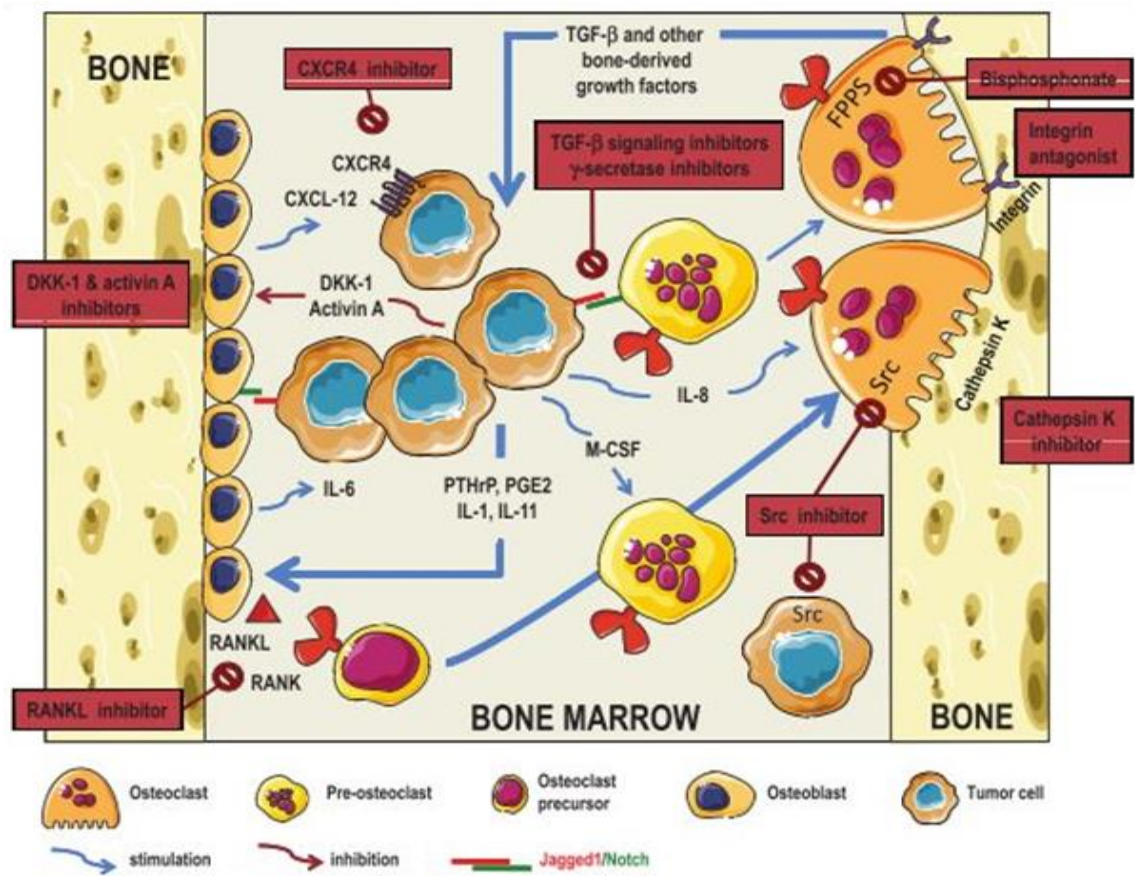


Figure 4. In bone, breast cancer cells secrete different factors that stimulate osteoclast differentiation and maturation through the activation of the RANKL/RANK and the Jagged1/Notch signaling pathways (adapted from REF 26). Integrin, Src and cathepsin K play an essential role in the bone-resorbing activity of mature osteoclasts. Moreover, breast cancer cells secrete factors (DKK-1, activin A) that inhibit osteoblast differentiation. This leads to enhanced bone destruction and as a consequence, to the release of bone derived-factors (TGF-β) that stimulate tumor growth. Moreover, CXCL-12 produced by osteoblasts promotes the recruitment and survival of CXCR4-expressing breast cancer cells. Therefore, a ‘vicious cycle’ (depicted by the large blue arrows) is established whereby metastatic cancer cells stimulate osteoclast-mediated bone resorption, and growth factors released from resorbed bone stimulate tumor growth. Red boxes highlight components that are attractive therapeutic targets, some of which are in clinical development. Abbreviations: CXCL-12, C-X-C motif chemokine 12; CXCR4, C-X-C chemokine receptor type 4; DKK-1, dickkopf-1; FPPS, farnesyl pyrophosphate synthase; IL, interleukin; M-CSF, macrophage-colony stimulating factor; PGE2, prostaglandin E2; PTHrP, parathyroid hormone-related peptide; RANK, receptor activator of nuclear factor κB; RANKL, RANK ligand; Src, proto-oncogene tyrosine-protein kinase; TGF-β, transforming growth factor-β.

2.3.3. Bone metastatic lesions

Bone metastatic lesions can be osteolytic or osteoblastic³¹ (Figure 5):

- Osteoblastic lesions

Osteoblastic lesions are characterized by increased bone formation. They can be identified on radiographs as increased areas of sclerosis within the skeleton³². Metastatic lesions from prostate carcinomas are the most well-known producer of osteoblastic lesions^{33,34}.

Interestingly, pathology reports indicate that osteoblastic lesions often form in an area of prior osteolysis in the pre-metastatic niche³⁵. Although areas of increased bone formation could seem beneficial, the resulting inconsistent structure leads to unequal distribution of mechanical loads through the bone, producing bone fractures.

- Osteolytic lesions

Osteolytic lesions are caused by bone resorption over-activation, and can be identified on radiographs as areas with decreased bone mineral density³⁶. Disseminated tumor cells initiating metastatic lesions enter the bone surface by stimulating osteolysis via enhanced osteoclast differentiation³⁷. Continued stimulation and loss of bone resorption regulation by osteoclast activation form the basis of an osteolytic lesion³³. In bone, TGF- β is the growth factor that most contributes to osteolytic lesions³⁸. It has been hypothesized that TGF- β released by osteoclasts induces pro-osteolytic gene expression, leading to production of parathyroid hormone-related protein (PTHrP) by cancer cells^{39,40}. In many patients, mixed osteolytic and osteoblastic lesions increase the risk of fractures, and the bone structure becomes even more patch-worked.

How each type of lesion is initiated and develops remains a mystery that will eventually be solved through new bone metastasis models. Nevertheless, continuous bone resorption causes the release of more bone matrix proteins and growth factors that stimulate further tumor cell proliferation, leading to a cycle of osteolysis³⁸. Furthermore, TGF- β increases cyclooxygenase-2 expression that correlates with an increase in IL-8. IL-8 induces osteoclast formation and activity, independently of the RANK ligand pathway⁴¹. This continued breakdown of the bone structure contributes to the bone pain and to pathological fractures experienced by patients with osteolytic bone metastases.

Finally, there is another type breast cancer cells: dormant tumor cells that can be found in the bone marrow. The concept of dormancy is one of the least understood in metastatic disease⁴².

Dormancy describes the persistence of disseminated tumor cells in a long-term state of quiescence. When such cells are eventually reactivated, they induce metastatic relapse⁴³.

Reactivation can occur months to years after resolution of the primary tumor⁴⁴. Once cancer cells are reactivated, metastatic bone lesions can be osteolytic, osteoblastic, or mixed.

Breast cancer commonly results in osteolytic metastases (73%)^{37,45,46}. The current treatment options for bone metastases are seldom curative, and are mostly palliative. Moreover, metastatic bone disease represents a significant burden for healthcare systems.

In the next section, we will describe the available treatments to manage bone metastases from breast cancer.

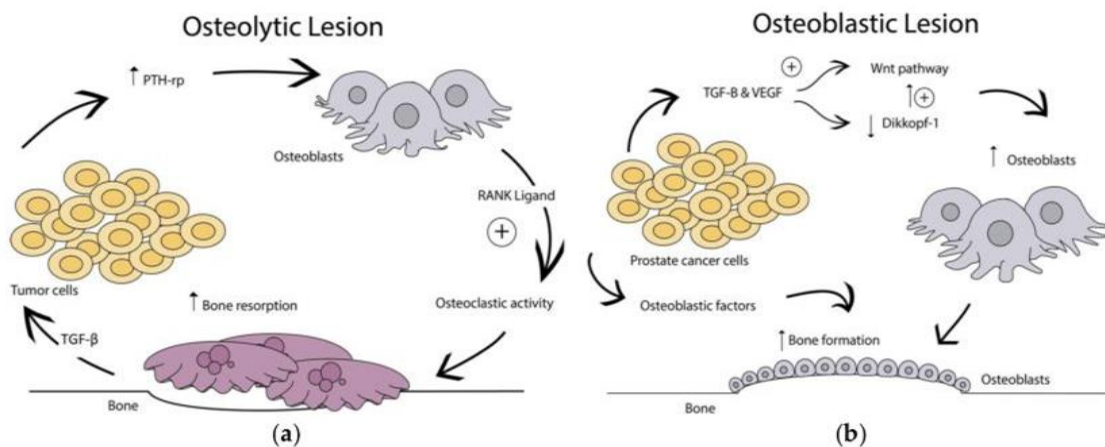


Figure 5. Osteolytic and osteoblastic lesions (adapted from REF 31). a) Osteolytic lesions are caused by over-activation of osteoclast bone resorption; b) Osteoblastic lesions result from direct tumor stimulation of osteoblasts.

3. Breast cancer-induced bone metastasis treatments

3.1. Treatments

Currently, bone metastasis treatment is mainly palliative. It is intended to allow the patient to maintain mobility and a certain quality of life by relieving pain, and may also target complications, such as fractures or hypercalcemia. Treatment may also limit tumor growth in the bone. Treatment can be local or systemic.

3.1.1. Local treatments

Advances in cancer treatment are prolonging the survival of patients, including those with bone metastases. When bone metastases are painful or pose the risk of fracture, instability or spinal cord damage, local treatment by radiotherapy or interventional radiology⁴⁷ is often necessary in addition to systemic treatment. Interventional radiology procedures include bone and analgesic consolidation techniques (cementoplasty, percutaneous placement of screws, metal reinforcements or intrabody implants). Other treatments, such as thermal (radiofrequency, cryotherapy), chemical (alcohol) or pharmaceutical (chemo-embolization) tumor destruction techniques, are less frequently proposed.

- External radiation therapy

External radiotherapy provides pain relief in about 70 to 80% of cases. Ionizing radiation leads to the formation of hydroxyl radicals and to DNA damage that are toxic for the cells. External irradiation can be performed once or in different sessions^{48,49}.

- Radiofrequency

Radiofrequency has an analgesic effect because this treatment destroys the tumor mass. Thermal destruction is achieved by inserting electrodes into the tumor^{50,51}. This technique is painful and cannot be performed if metastases are close to the spinal cord, brain, bladder, and colon.

- Surgery

Surgery is indicated for patients with bone metastases and high risk of fractures or with bone fractures. The used method depends on the bone. Weight-bearing bones can be consolidated with screws and plates. In knee and hip bones, damaged bone can be removed and replaced by a prosthetic implant. In the case of spinal cord compression, surgery can be completed by laminectomy to remove one or more posterior and lateral parts of a vertebra⁵². Cementoplasty is indicated for vertebral lesions, and consists in the injection of surgical cement (e.g., the synthetic resin polymethyl methacrylate) into the bone lesion. When surgery is contraindicated, external stabilization can be performed with orthopedic devices or plaster, for example.

To improve the patients' quality of life, the implant stability must be increased by limiting local cancer progression and decreasing the possible failure of reconstructive devices. The treatment of pathological fractures with bone cement loaded with antineoplastic drugs to fill in defects and strengthen the fixation of orthopedic implants is an emerging promising approach⁵³. Much research is now focused on the development of local drug delivery devices that couple the precise controlled release of the therapeutic agent(s) with the device degradation and replacement by bone.

3.1.2. Systemic treatments

- External radiation therapy

Systemic external radiotherapy is based on the use of radioisotopes (strontium-89⁵⁴ and samarium-153⁵⁵) that might lead to myelosuppression⁵⁶. More recently, a Phase III clinical trial showed that radium-223 improves the survival of patients with prostate cancer and bone metastases⁵⁷ and is better tolerated.

- Chemotherapy and/or hormonotherapy

Chemotherapy and hormonotherapy are used for the treatment of primary breast tumors and also of bone metastases.

- Bone resorption inhibitors

The understanding the mechanisms involved in bone metastasis development led to the use of bone resorption inhibitors, including bisphosphonates (BPs)^{58,59}. Different drugs have been tested for bone metastasis treatment, especially when patients also have osteoporosis. Such drugs are classified in two groups: anti-resorptive and anabolic agents^{60–62} (Table 2).

Table 2. Classification of drugs to treat osteoporosis and bone metastases

Anti-resorptive drugs	Estrogens
	Bisphosphonates
	SERMs
	Strontium
	Denosumab
Anabolic drugs	Parathyroid hormone
	Teriparatide

Here, we will focus on two families of anti-resorptive drugs: BPs and Specific Estrogen-receptor Modulators (SERMs).

3.2. Bisphosphonates

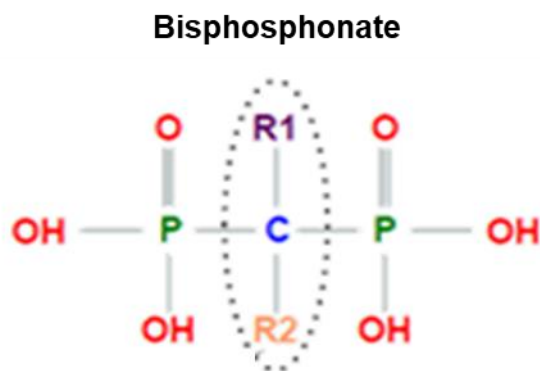
BPs are the most prescribed medications for osteoporosis^{63,64} due to their high affinity for bone (Table 3). Such drugs reduce skeleton morbidity by decreasing the risk of fractures⁶⁵. BPs have four different effects on osteoclasts: (1) inhibition of osteoclast recruitment, (2) inhibition of osteoclast adhesion to the mineral matrix, (3) shortening of osteoclast lifespan, and (4) direct inhibition of osteoclast activity⁶⁶.

BPs have a P–C–P structure and the P–C bond is resistant to most chemical reagents and inert to enzymatic degradation (Figure 6).

Table 3. Relative potency of bisphosphonates for bone resorption inhibition

Bisphosphonate	Generation	Relative potency
Etidronate	First	1
Clodronate		10
Pamidronate	Second	100-1000
Alendronate		100-1000
Ibandronate	Third	1000-10000
Risedronate		1000-10000
Zoledronate		10000+

In general, BPs are divided in two categories: N-BPs (molecules with nitrogen-containing functional groups at the R2 position) and non-N-BPs (without nitrogen) ⁶⁷. For example, alendronate belongs to the N-BP group.

**Figure 6. Molecular structure of bisphosphonate.**

In patients with bone metastases, BPs are used as inhibitors of osteoclast-mediated bone resorption²³. N-BPs specifically inhibit the activity of osteoclast farnesyl pyrophosphate synthase, a key enzyme in the mevalonate pathway. This leads to inhibition of small GTPase prenylation and the subsequent inactivation of osteoclasts. Besides inhibition of osteoclast activation and function, several preclinical findings indicate that N-BPs exert direct and/or

indirect antitumor effects. BP anti-resorptive and antitumor effects have been already reviewed⁶⁸ (Figure 7).

However, BPs may have adverse effects on other tissues, including the gastrointestinal tract and kidney⁶⁹, based on their pharmacokinetics^{70,71}. Moreover, alendronate may have negative effects on the bone structure by increasing bone volume⁷². Also, only 1% of BPs are absorbed after oral administration, and only 20% of the absorbed drug is incorporated in bones⁷³.

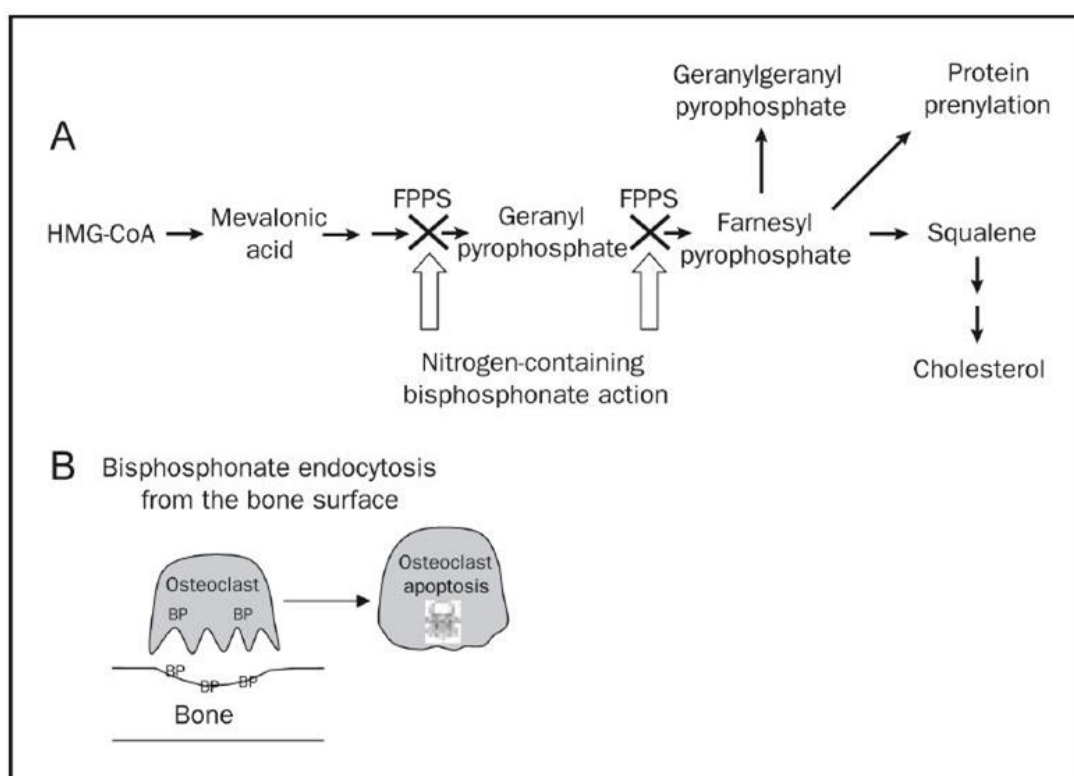
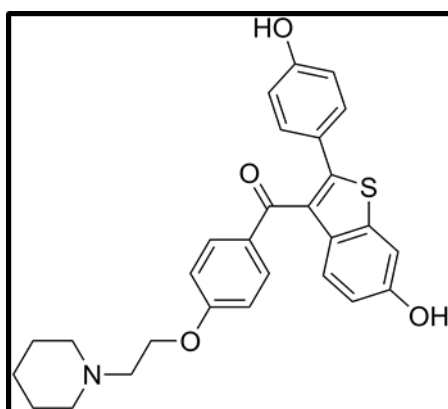


Figure 7. Mechanisms of action of bisphosphonates (adapted from REF 65); a) Nitrogen-containing bisphosphonates inhibit farnesyl pyrophosphate synthase (FPPs); **b)** Osteoclast endocytosis of bisphosphonate from the bone surface leads to FPPs inhibition and osteoclast apoptosis.

Currently, there are three major SERM groups. First-generation SERMs are triphenylethylene derivatives. This group includes tamoxifen that has been widely used in the clinic, and is effective for the prevention⁷⁶ and treatment of breast cancer⁷⁷. Second-generation SERMs includes raloxifene hydrochloride (RH), a benzothiophene derivative used in the clinic for osteoporosis treatment and prevention⁷⁸. Finally, to improve SERM efficacy, third-generation compounds have been produced, such as bazedoxifene⁴⁸ and arzoxifene⁷⁹ that are in Phase III clinical trials. In bone, SERMs generally act as estrogen agonists⁸⁰.



RH, a nonsteroidal benzothiophene derivative (Figure 8), is a second-generation SERM. In breast cells, RH binds to ERs to prevent estrogen-induced DNA transcription^{81,82}, and

therefore acts as an ER antagonist⁸³ (Figure 9). It has been shown that RH decreases breast cancer incidence in high-risk postmenopausal women⁸⁴. In 1998, RH was approved by the Food and Drug Administration (FDA) for the treatment and prevention of osteoporosis, and in 2007 for reducing breast cancer risks⁸⁵. Moreover, it has been shown that RH has fewer serious adverse effects than tamoxifen and that both agents are equally efficient for breast cancer prevention. Although about 60% of RH administered orally is absorbed, its absolute bioavailability is only 2%. Systemic administration of higher RH doses would increase the risk of side effects in different organs (e.g., venous thromboembolism, pulmonary embolism, hot flushes, and leg cramps)^{85,86}.

Moreover, RH is as efficient as alendronate in preventing osteoporosis-related fractures, but with fewer adverse effects⁸⁷.

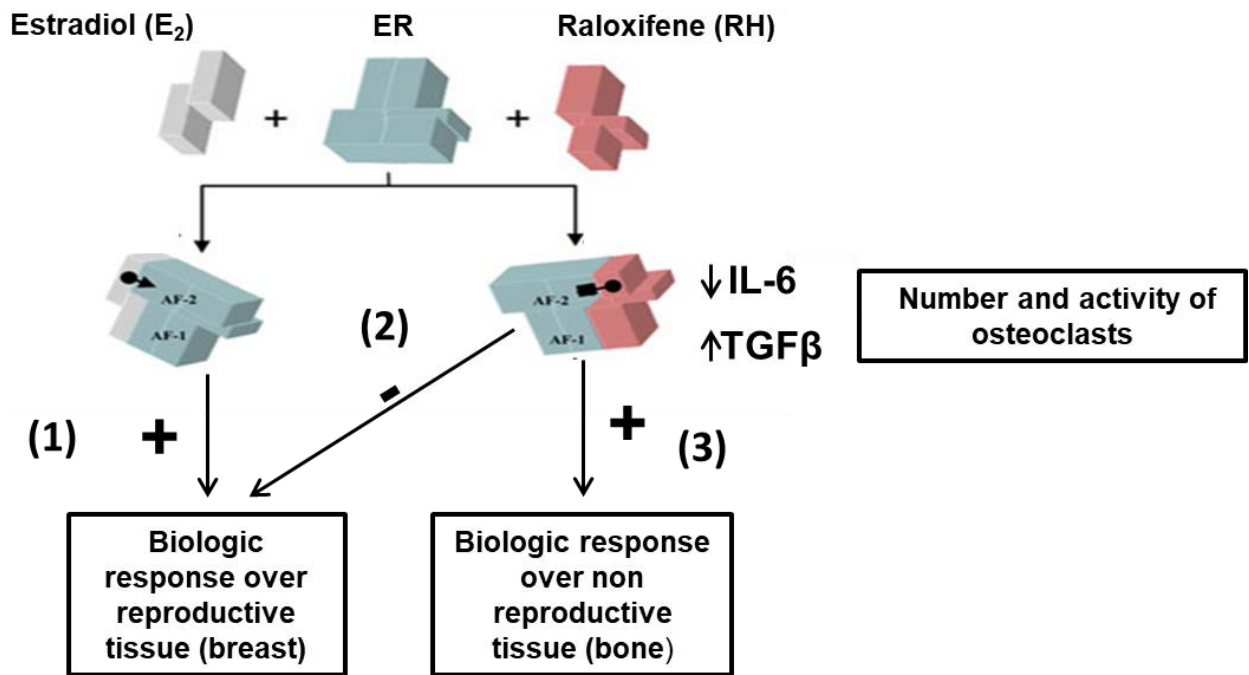


Figure 9. Raloxifene mechanisms of action (Adapted from REF 83). 1) Estradiol (E₂) enters in the nucleus of the target organ cells where it binds to ER with agonist effects on the target reproductive tissues, such as breast; 2) ER has a binding site for estrogen-type ligands and another one for SERMs. Depending on the ligand binding site, the ligand had a pure estrogen agonist action, or a pure estrogen antagonist action; 3) Raloxifene exerts two other direct actions on bone tissue: i) reducing osteoclastic resorptive activity by up to 50% and interleukin-6 (IL-6) production; and ii) increasing the production of TGF-β, thereby decreasing the number of osteoclasts and their resorptive activity.

Combining two anti-resorptive agents with different mechanisms of action, such as alendronate (osteoclast metabolism suppression) and RH (RANKL access to osteoclasts decrease) could be an interesting option for the treatment of pathologic fractures due to bone metastases of breast cancer.

3.4. Combination treatment with alendronate and raloxifene hydrochloride

RH and alendronate reduce the risk of new vertebral fractures by 30% to 65%, increase bone mineral density (BMD), and decrease biochemical markers of bone turnover in postmenopausal women with osteoporosis⁸⁸.

Different studies have found that greater skeletal benefits are obtained when two anti-resorptive drugs are administered in combination, compared with each single agent^{89,90}. Indeed, each anti-resorptive molecule achieves its therapeutic effects on bone through different modes of action. For instance it has been shown that due to their different mechanisms of action, addition of alendronate to RH has an independent, additive effect on the changes in BMD and bone turnover markers^{91,92}. Moreover, the effects of combining RH and alendronate on the structural and material biomechanical properties of vertebral bone have been investigated using in Sprague-Dawley rats with bilateral ovariectomy to simulate osteoporosis⁷². This study showed that the drug combination has greater beneficial effects on bone volume and the biomechanical properties of vertebral bone compared with each single agent. After prosthesis implantation, patients often receive drugs (orally or systemically) for the treatment of damaged bone⁹³. A new approach to treat pathologic fractures in patients with osteoporosis exposed to immune suppressive drugs or energetic irradiation to fight cancer is to deliver the appropriate drugs at the time of prosthetic implantation. This method could avoid systemic side effects by using lower and safer quantities of drug, with more localized effects. For instance, a study demonstrated that coating implants with alendronate or RH-loaded titanium oxide (TiO₂) improves the bone–implant integration in rats⁹⁴.

B- Bone tissue engineering

In patients with bone metastases from breast cancer, large bone defects (e.g., fractures) can be observed. The management of such pathological fractures requires new technologies, such as bone tissue engineering. The concept of Tissue Engineering was defined by Langer and Vacanti⁹⁵ as an interdisciplinary field for the development of biological substitutes for many applications. For instance, Tissue engineering methods can be used to fabricate artificial 3D scaffolds to replace damaged tissues in regenerative medicine⁹⁶.

In bone repair, a scaffold will provide a suitable 3D architecture and mechanical properties to support bone formation. Such scaffolds must meet several requirements.

1) Biocompatibility:

This is an important prerequisite of any biomaterial designed for tissue regeneration. A biocompatible material does not induce any cytotoxicity⁹⁷, and must allow cell adhesion, proliferation and differentiation.

2) Bioactivity:

Scaffold bioactivity is an important requirement for bone tissue engineering. Specifically, osteoconduction is a passive process that allows bone formation on the biomaterial surface and can be defined as “bone growth on a surface or into pores, channels or pipes” without blocking new bone progression⁹⁸.

3) Structure:

The external shape and internal structure are very important properties of bone scaffolds. The external shape influences the interaction between scaffold and receiving site. The contact surface between damaged bone and implanted biomaterial should be as large as possible to enable the efficient adsorption of proteins and other elements from the surrounding tissue. A suitable internal architecture for bone tissue engineering scaffolds is represented by interconnected pores of specific size to allow cell proliferation and migration. Ideally, bone scaffolds should have

interconnected pores of 100-300 μm to promote cell seeding and attachment, colonization and migration⁹⁹.

4) Biodegradation:

Bone scaffolds must be also biodegradable and ideally, they should be degraded during formation of the new tissue¹⁰⁰. The scaffold biodegradation time can be controlled by modulating the biomaterial composition.

5) Mechanical properties:

Scaffolds must support mechanical forces at the implantation site. The biomaterial composition has an important effect on mechanical properties of the final scaffold.

Depending on the size and morphology of the damaged bone, different types of biomaterials and procedures are required for patient management. For example, for filling small bone defects, the injection of biomaterials through minimally invasive surgery seems the most appropriate strategy. On the other hand, for the management of large bone defects with complex morphology, the insertion of a 3D printed scaffold by traditional surgery is a good option to recreate the bone shape.

These two types of materials (injectable scaffolds and 3D printed scaffolds) and their respective characteristics are presented in this section.

1. Injectable scaffolds: From poly(methyl methacrylate) to calcium phosphate cement

The repair of bone defects caused by diseases, such as breast cancer bone metastases, has become a major health issue over the years. The use of bone substitutes is in constant development in orthopedic surgery and remains a major challenge for bone reconstruction. A vertebral fracture occurs every 22 seconds in the world¹⁰¹. In France, it is estimated that 50,000 to 75,000 vertebral fractures occur each year¹⁰². Vertebral fractures are caused by different pathologies, such as osteoporosis and metastases. They are disabling and involve a significant economic cost. This problem makes bone tissue engineering a rapidly expanding

field. Several types of materials are currently available, but they must display specific properties and very strict specifications for the use in the management of vertebral fractures in order to relieve pain and restore the spinal support function.

In this section, the most common techniques and the materials used for vertebra repair will be described as well as alternative materials, such as calcium phosphate.

1.1. Vertebroplasty (cementoplasty)

Percutaneous vertebroplasty is a minimally invasive technique to stabilize the fracture by controlled injection (under radiography or computerized tomography guidance) of bone cement in the center of the vertebra¹⁰³ (Figure 10). Most of the time, this procedure is performed by radiologists. It is used for fractures caused by tumor lesions¹⁰⁴, aggressive angioma¹⁰⁵, and also osteoporosis¹⁰⁶. Vertebroplasty is an effective short-term treatment to reduce pain, and is performed between three weeks and four months after the fracture occurrence.

In vertebroplasty, a bone puncture needle is inserted in the vertebral body transcutaneously under radioscopy control using a large diameter trocar, and then cement (i.e., a low viscosity paste) is injected. After injection, the cement will harden and rebuild a hard core that will consolidate around this mass in the vertebral body.

In most cases, a methyl methacrylate resin is used as cement due to its good mechanical properties and ease of use¹⁰⁷.

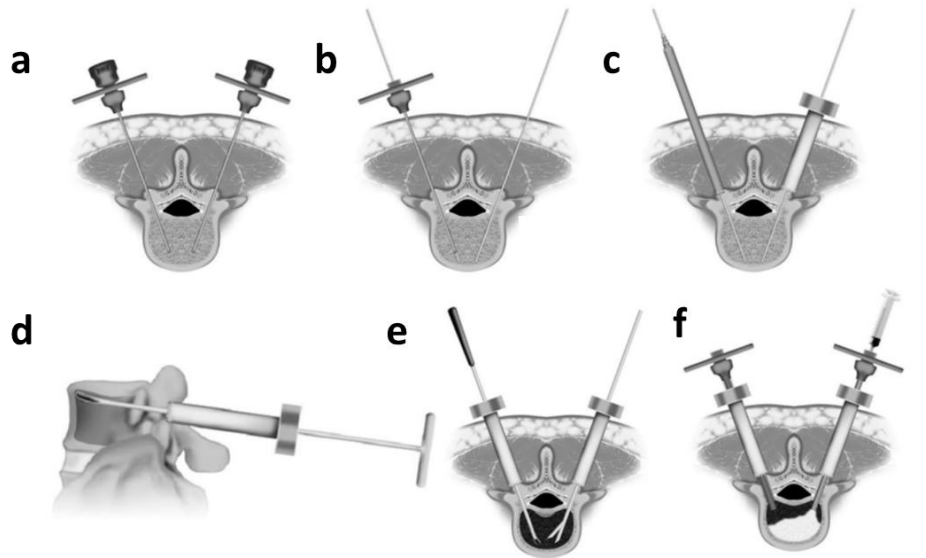


Figure 10. Diagrams showing the vertebroplasty procedure (adapted from REF 103). a) Two Jamshidi needles are inserted percutaneously and transpedicularly under fluoroscopic guidance; b) Guide pins (1.5-mm diameter) are inserted through the needles; c) Two portals are set on the bilateral laminae after dilating using dilators; d, e) Debridement of the pathologic tissues in the vertebral body and reduction are performed using rongeurs, curettes, probes, and a urinary balloon; f) Finally, injection and filling are performed after injection of the contrast medium and washing with saline.

1.2. Poly(methyl methacrylate) (PMMA)

Poly(methyl methacrylate) (PMMA) acrylic cement was used for the first time in dentistry in 1932. PMMA use in orthopedics was initiated by Charnley in 1960¹⁰⁸, particularly for prosthesis sealing and resealing¹⁰⁹. The polymerization reaction is produced by mixing a liquid (monomer) and a solid phase (MMA homopolymer + initiator) to obtain a paste of variable viscosity. The injected cement is amalgamated with a contrast agent to allow the visualization of the cement path through the vertebra. The injection is carried out under general or local anesthesia, in one or more vertebrae. The paste hardens in a few minutes to permanently anchor the prosthesis on an irregular bone surface (sealing). As there is no chemical bond between bone and PMMA and the cement is retained only mechanically by inter-digitation in bone crevices, it is very important to prepare the recipient site whose porous relief must be dry¹¹⁰. The polymerization is exothermic and causes temperature peaks up to

75°C in the center of the vertebral body. It is accompanied by volume retraction that can alter the bone/cement contact. The analgesic role of vertebroplasty is explained by the fracture consolidation, stabilization, and the thermal reaction.

PMMA is present in all orthopedic surgical blocks because it is easy to use, inexpensive, bio-inert, biocompatible and has excellent mechanical properties. However, its hydrophobic nature and bio-inertia do not allow good integration into the surrounding bone tissue. Moreover, its hardness may cause fractures of adjacent vertebrae due to poor load distribution. Its high setting temperature causes necrosis, and residual monomers are associated with the risk of cytotoxicity and emboli¹¹¹. In addition, the injectable material should lead to immediate strength recovery and induce secondary bone reconstruction. This is not the case with PMMA, which remains a foreign body in the recipient bone. Therefore, new injectable polyphosphate cements have been developed and marketed, such as Norian Skeletal Repair System® (SRS) and chronOS inject®. However, vertebroplasty is not sufficient because the pathology that led to the fracture is not treated. Moreover, there is no bone regeneration, which in many cases leads to the risk of new fractures. Therefore, new injectable cements that can treat the disease by delivering drugs and support new bone tissue formation are needed.

1.3. Calcium phosphate ceramics and cement

1.3.1. Generalities

As the bone mineral phase is made of a polysubstituted non-stoichiometric apatite. Phosphocalcic biomaterials, with a composition similar to that of calcified tissues, have been developed in recent years. Ceramics and phosphocalcic cements are not only perfectly biocompatible materials, but are also bioactive and can be bioresorbable depending on the phase type (i.e., they facilitate bone reconstruction and the complete recolonization of lesions through their progressive resorption)^{112,113}. Ceramics are an interesting alternative due to their

richness of compositions and formulations. Among the ceramics employed for bone reconstruction, bioinert ceramics, such as alumina and zirconia, are used in the heads of total hip prostheses, as well as in dentistry for dental implants. Bioactive ceramics, particularly those based on calcium phosphates, are used for bone filling and can be found in various forms (granules, dense or porous solid parts, etc.).

1.3.2. Calcium phosphate ceramics

Calcium phosphate (CaP) ceramics are synthetic biomaterials used in dentistry since the 1970s and in orthopedics since the 1980s^{114,115}. They have been widely used to fill bone loss^{116,117}. Among the different CaP ceramics, the most studied and used are based on HA [$\text{Ca}_{10}(\text{PO}_4)_6(\text{OH})_2$] and/or tricalcium phosphate (TCP) [$\text{Ca}_3(\text{PO}_4)_2$]¹¹⁸. TCP exists in two crystalline forms: α -TCP and β -TCP. CaP ceramics are obtained by high-temperature sintering of these powders. HA and TCP have different Ca/P ratios (1.5 for TCP and 1.67 for HA), crystal systems (hexagonal R3C for TCP and hexagonal P63/m for HA), and resorption capacities. The resorbability of ceramics depends on their chemical composition, their specific surface area and the solubility of their phases. HA ceramics are considered to be poorly absorbable, while TCP-based ceramics are highly absorbable because of their faster biodegradation compared with HA^{119,120}. TCP remains fragile upon mechanical stresses due to its rapid resorption¹²¹. These ceramics are used pure or as a mixture of HA and β -TCP or calcium-deficient hydroxyapatite (CDHA) to form a two-phase CaP ceramic after sintering [biphasic calcium phosphate (BCP) ceramics]^{122,123}. BCP ceramics are the most widespread bioceramics because they allow controlling the substitute bioactivity^{124,125}. Although macroporous, these ceramics do not have sufficient mechanical properties to be used as prostheses (e.g., for long bone diaphysis), but they are suitable for bone and alveolar cavity filling¹²⁶.

There are different CaP types also obtained by precipitation in aqueous medium at low temperature. The majority of these calcium orthophosphates are monobasic salts (monocalcium phosphate monohydrate, MCPM) or dibasic salts (anhydrous dicalcium phosphate, DCPA, and dicalcium phosphate dihydrate, DCPD). They are not used directly as bone substitutes, but as components of the solid phase of CaP cement (CPCs). The final product of the CPC setting reaction is always a low-temperature CaP. The low-temperature CaPs most commonly used to prepare cement are: MCPM, DCPA, DCPD, octacalcium phosphate (OCP) and precipitated HA (PHA). Some of these CaPs are present in the calcified tissues of our body.

1.3.3. Injectable calcium phosphate cements

The main advantage of biomedical cement over bioceramics is the possibility to fill the bone defect in the correct shape due to their malleable or injectable paste form. The first CPC was developed by Brown and Chow in 1982¹²⁷. Since this discovery, many formulations have been described and some have been patented. The principle is to obtain injectable cements that can be molded to the walls of the bone defect to be filled. Hydraulic cement can be obtained either by acid-base reaction in aqueous phase (water, acid solution or different buffer) between acidic and more basic CaPs¹²⁸ or by dissolution-(re) crystallization of a metastable amorphous or crystallized phase. After mixing, the dissolution of these species in the aqueous phase results in the precipitation of CaP of less soluble intermediate basicity, usually stoichiometric (HA) or CDHA or DCPD. The precipitation conditions often determine the final mechanical and rheological characteristics of the cement. This setting reaction is generally isothermic, thus eliminating the risk of bone necrosis encountered with PMMA cements¹²⁹. During mixing, a paste is obtained that can be worked and molded and that hardens more or less rapidly at room temperature. These cements have osteogenic properties and are absorbable (more or less rapidly) with satisfactory mechanical properties. CPC

advantage is mainly explained by their biological properties (biocompatibility and bioactivity), their ability to adapt to the shape of the bone defect to be filled, and their ease preparation and implantation using minimally invasive surgical techniques. The first commercial CPC products were introduced in the 1990s for the treatment of maxillofacial defects¹³⁰ and of fractures¹³¹. Their biocompatibility and resorbability have been determined in animals¹³² and confirmed in humans¹³³.

1.3.4. CPC types

Despite the large number of formulations, CPCs can be classified according to the nature of the product resulting from the setting reaction: apatite and brushite. Brushite is the most thermodynamically stable CaP at low pH and will then turn into apatite after *in vivo* implantation^{132,134,135} (Figure 11).

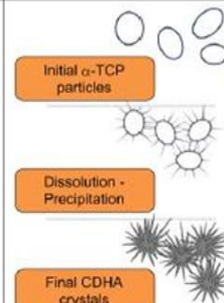
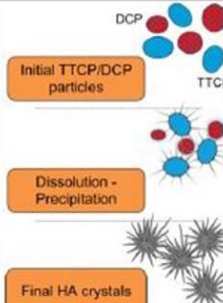
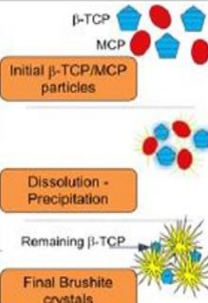
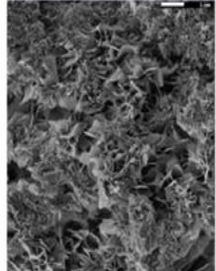
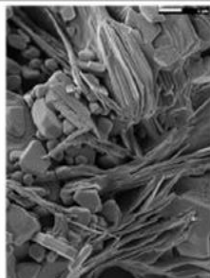
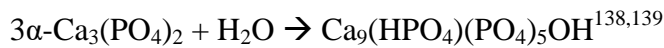
	Apatitic Cement		Brushitic Cement
	Single Component	Multiple Components	
Reactives	α -TCP	TTCP + DCPA/DCPD	β -TCP + MCPM/MCPA
Reaction	$3\alpha\text{-Ca}_3(\text{PO}_4)_2 + \text{H}_2\text{O} \rightarrow \text{Ca}_9(\text{HPO}_4)(\text{PO}_4)_5(\text{OH})$	$2\text{Ca}_4(\text{PO}_4)_2\text{O} + 2\text{CaHPO}_4 \rightarrow \text{Ca}_{10}(\text{PO}_4)_6(\text{OH})_2$	$\beta\text{-Ca}_3(\text{PO}_4)_2 + \text{Ca}(\text{H}_2\text{PO}_4)_2 \cdot \text{H}_2\text{O} + 7\text{H}_2\text{O} \rightarrow 4\text{CaHPO}_4 \cdot 2\text{H}_2\text{O}$
Type of Reaction	Hydrolysis	Acid-Base	Acid-Base
Setting mechanism and crystal morphology	 <p>Initial α-TCP particles</p> <p>Dissolution - Precipitation</p> <p>Final CDHA crystals</p>	 <p>Initial TTCP/DCP particles</p> <p>Dissolution - Precipitation</p> <p>Final HA crystals</p>	 <p>Initial β-TCP/MCP particles</p> <p>Dissolution - Precipitation</p> <p>Remaining β-TCP</p> <p>Final Brushite crystals</p>
SEM		<div style="display: flex; align-items: center; justify-content: center;"> <div style="writing-mode: vertical-rl; transform: rotate(180deg);">APATITE</div> <div style="margin: 0 10px;">←</div> <div style="writing-mode: vertical-rl; transform: rotate(180deg);">BRUSHITE</div> </div>	

Figure 11. CPC classification in apatitic and brushitic cements (adapted from REF 128)

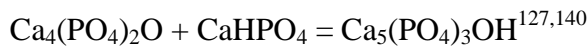
- Apatite

The bone mineral phase is made of a non-stoichiometric carbonate apatite that is poorly crystallized. Therefore, HA is a relevant bone substitute. When set, CPCs consist of a network of CaP crystals, with chemical composition and crystal size that can be tailored to closely resemble the biological HA present in living bone^{136,137}. CPCs leading to the formation of HA or CDHA can be classified in two main categories:

1) Mono-component CPCs, in which CDHA can be obtained via the hydrolysis of a metastable CaP (α - TCP):

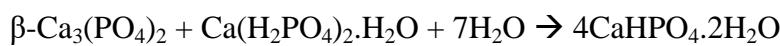


2) Multi-component CPCs, in which HA can be formed via an acid-base reaction of tetra-calcium phosphate (TTCP; basic) with a slightly acidic component (DCPA or DCPD). The Ca/P ratio of the final HA depends on the ratio between TTCP and acidic component:



- Brushite

All brushitic CPCs are obtained through an acid-base reaction. For instance, brushite (slightly acidic) can be obtained by a reaction between β -TCP (almost neutral) and MCPM (acidic)¹⁴¹:



1.3.5. Properties

For use in vertebroplasty, injectable CPCs must satisfy a number of standards¹⁴² summarized in Table 4.

In addition to biocompatibility, compressive strength, setting time and *in situ* settability, which allows excellent adaptation to the most complex cavity shapes, CPCs must display good radio-opacity, good injectability and be easy to handle and available. Furthermore, CPCs have to be osteoconductive with a macroporous structure.

Table 4. Desirable properties of Calcium Phosphate Cements for Vertebroplasty.

Radiopacity higher than bone
Ease of preparation and handling
Easy injectability
Low curing temperature
Working time of 6-10 minutes
Setting time of 15 minutes
Mechanical properties similar to those of vertebral bone
Appropriate cohesion
Viscosity not influenced by the setting time
No toxicity
Micro- and macro-porosity (<10 μm and >100 μm)
Appropriate resorption rate
Excellent osteoconductivity
Excellent osteoinductivity
Excellent biocompatibility
Excellent bioactivity
Low cost

In conclusion, injectable scaffolds, such as CPCs, can be used as an alternative to PMMA for bone repair by vertebroplasty. In the case of larger bone defect, graft of new 3D material is needed. In the next section, the method and the type of materials used to obtain 3D scaffolds will be described.

2. Generation of 3D scaffolds: From conventional methods to 3D printing

2.1. Materials used for tissue engineering

Different natural and synthetic biomaterials can be used for scaffold fabrication. They can be made of CaP, as described in the previous chapter, or of natural and synthetic polymers.

- Natural polymers:

These are polymers that occur naturally or are produced by living organisms; they can be obtained from raw materials found in nature.

Collagen, for example, can form hydrogels that contain about 90% of water and that are degraded by enzymes or by hydrolysis. Their internal architecture is similar to that of extracellular matrices of most tissues, and they are easy to produce¹⁴³. In tissue engineering, they are often used as carriers for stem cells. The main disadvantage of hydrogels for bone tissue engineering is their low mechanical properties and low availability¹⁴⁴.

- Synthetic polymers:

Synthetic polymers are human-made polymers developed to overcome the limits of natural polymers, such as collagen or chitosan. They can be produced in a reproducible manner without limits in quantity, and are suitable for different fabrication methods. However, they may induce immunogenic reactions. Polyacrylates and polyphosphoesters are mostly used in bone tissue engineering applications¹⁴⁵. There are several advantages in using synthetic scaffolds, such as the possibility to control their internal and external shape and architecture, and the absence of viral transmission¹⁴⁶. A wide range of thermoplastic polymers and copolymers have been approved by the U.S. Food and Drug Administration (FDA), and custom materials can be produced by combining different raw materials for scaffold fabrication. They show good biocompatibility and tunable biodegradation rate¹⁴⁷. Synthetic polymers are suitable for different fabrication methods. Poly (glycolic acid) (PGA), poly (lactic acid) (PLA), poly (lactic-co-glycolic acid) PLGA, and polycaprolactone (PCL) are frequently used for tissue engineering.

2.2. Traditional methods to produce scaffolds

Several traditional methods exist to fabricate bone scaffolds with polymers and their composites.

2.2.1. Solvent-casting and particle leaching

In these techniques, the polymer is dissolved in a solution with uniformly distributed specific size salt particles. After solvent evaporation, salt particles remain in the matrix, immersed in water where salt leaches produce a porous structure. The main limit of this method is that it allows the production of scaffolds only in the shape of flat sheets and tubes. Moreover, some residues of cytotoxic solvents can be observed¹⁴⁸.

2.2.2. Freeze drying

In this process, the polymer is dissolved and the solution is cooled below its freezing temperature. It leads to solvent solidification and evaporation by sublimation, leaving a dry porous scaffold. However, this technique is time-consuming, and requires high energy and cytotoxic solvents. Moreover, scaffolds display irregular and small pore size¹⁴⁹.

2.2.3. Thermally induced phase separation

The polymer solution is quenched and undergoes liquid-liquid phase separation, forming polymer-rich and polymer-poor phases. The polymer-rich phase solidifies and the polymer-poor phase is removed, leaving a porous nanofibrous network. Low temperatures favor the incorporation of bioactive molecules¹⁵⁰.

2.2.4. Gas foaming

In this process, inert gas-foaming agents, such as carbon dioxide or nitrogen, are used to pressurize molded biodegradable polymers with water, producing sponge-like structures. The disadvantage of this technique is that it relies on the use of excessive heat during compression molding, leading to the appearance of not interconnected pores and of a nanoporous skin layer at the scaffold surface¹⁵¹.

2.2.5. Electrospinning

Electrospinning is a versatile process that involves the use of an electrical polarization to create non-woven scaffolds from a polymer solution. The polymer is dissolved in a suitable solvent, and then is loaded into a reservoir to initiate fiber formation. Then, high voltage is applied to overcome the surface tension and form a fine-charged liquid jet. The polymer solution is ejected, dried, and solidified onto the collector plates with the opposite potential. The disadvantages of this technique are the use of organic solvents, which could be cytotoxic, and the limited possibility to produce complex 3D scaffolds with good mechanical properties¹⁵².

As scaffold should have numerous properties, their fabrication using conventional methods is difficult and often it is impossible to obtain all these properties. Overall, the main issues of these methods are the limited control of the scaffold architecture (shape and porosity) and the use of organic solvents that can have a negative effect on cell viability and/or biological functions¹⁵³. All the advantages and drawbacks of traditional methods to fabricate scaffolds are summarized in Table 5.

Table 5. Advantages and drawbacks of traditional methods to produce scaffolds.

Method	Advantages	Drawbacks
Solvent-casting and particle leaching	Simple method Highly porous structure with control over porosity and pore size Crystallinity can be tailored	Poor control over orientation and degree of pore connectivity Limited to fabrication of thin membranes Limited mechanical properties Residual solvents and porogens
Freeze-drying	No high temperature or leaching Good porosity	Long processing time Small pore size Low mechanical properties
Phase separation	Simple method Ease to combine with other techniques Retains the biomolecule activity Highly porous structure with control over porosity and pore size	Difficulty to control scaffold morphology Time-consuming Residual solvents Shrinkage issues Small-scale production
Gas foaming	No organic solvents Ability to keep the activity of biomolecules Highly porous structure with control over porosity and pore size	Inadequate pore interconnectivity Limited pore size Formation of non-porous surface Insufficient mechanical integrity
Electrospinning	Simple methods Controllable porosity, pore size and fiber diameter High surface area to volume ratio	Limited mechanical properties Residual solvents Limitation of thickness

Alternatively, 3D printing is a recent technology that can be used to overcome some of the limitations of conventional methods for scaffold production.

2.3. Different 3D printing techniques

Additive manufacturing or 3D printing is emerging as a powerful technology to overcome the limits of conventional production methods. Indeed, this technique has a great potential to produce final scaffolds with complex shape and the desired microarchitecture (pore geometry and size). Interest in rapid prototyping is growing in the field of bone tissue scaffold fabrication because it allows the fast fabrication of 3D models with high resolution as well as

the production of patient-specific scaffold shapes using medical images made by Computed Tomography.

In the last few decades, many different 3D printing techniques have been created and many different 3D printers are now available on the market¹⁵⁴ (Figure 13). In the next section, the most common additive manufacturing techniques will be described. The advantages and disadvantages of 3D printing techniques are summarized in Table 6.

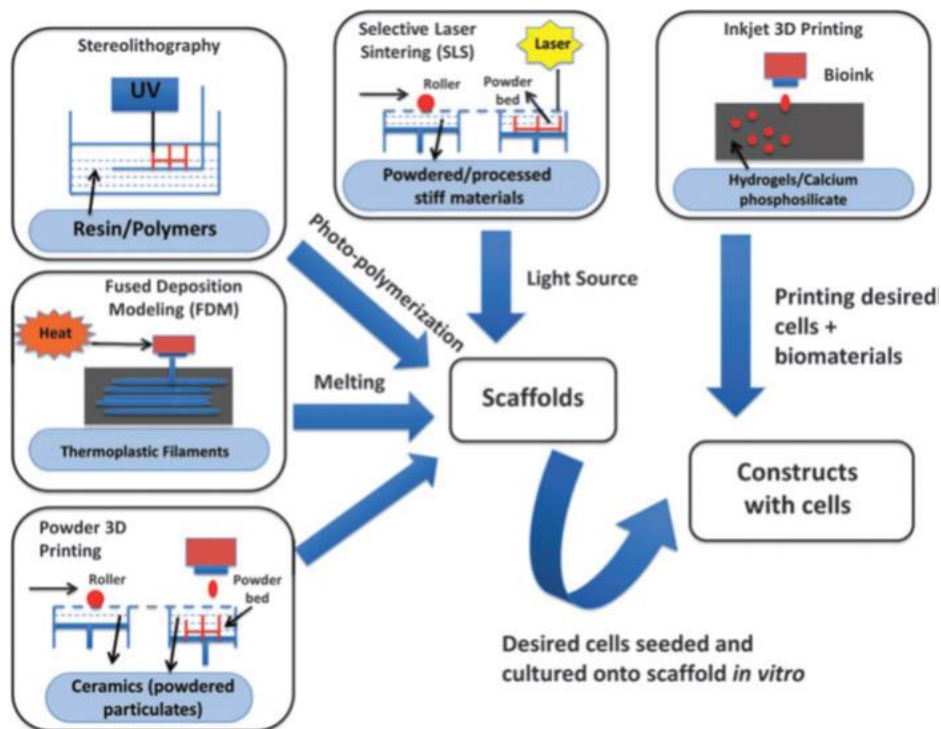


Figure 13. Different 3D printing techniques for scaffold production (adapted from REF 154).

2.3.1. Powder-based 3D printing (3DP)

The 3DP technique was invented at the Massachusetts Institute of Technology, and can fabricate an object by using liquid binders sprayed onto powders at room temperature conditions¹⁵⁵. A wide range of materials has been used in printing because most biomaterials exist in either a solid or liquid state. The process begins by spreading a layer of fine powder material evenly across the piston. The X-Y positioning system and the print head are synchronized to print the desired 2D pattern by selective deposition of binder droplets onto

the powder layer through inkjet print heads, thus bonding the particles together.¹⁵⁶ The piston, powder bed, and layer are lowered, and the next layer of powder is spread. By repeating the process of laying out powder and bonding, the different layers are built in the powder bed. Removal of the unbound powder reveals the fabricated scaffold (Figure 14).

The drawbacks of these techniques are: the use of organic solvents as binders, the difficulty to remove unbound powder from complex shapes, and the limited pore size of the final constructs¹⁵⁷.

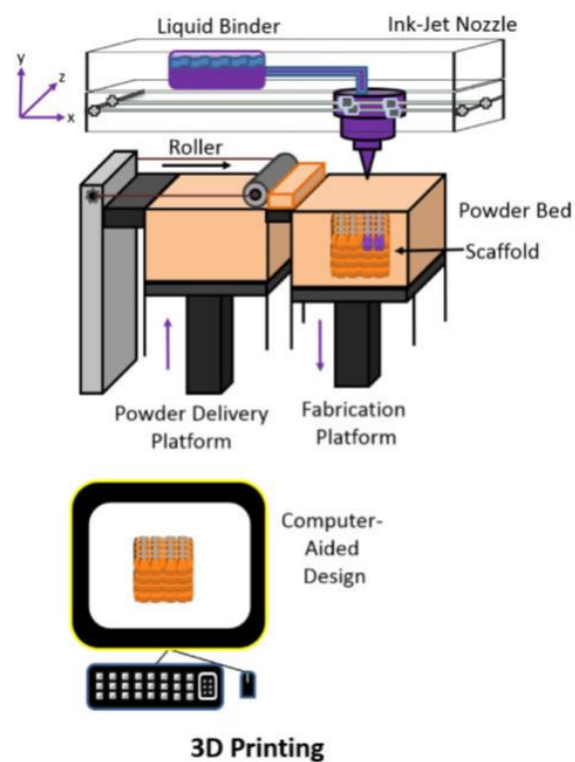


Figure 14. Powder-based 3D printing technique (adapted from REF 96)

2.3.2. Selective Laser Sintering (SLS)

SLS was developed at the University of Texas in Austin. SLS is similar to 3DP because powder particles are bound together in thin layers with a high-power CO₂ laser beam¹⁵⁸. A layer is created by heating the powdered polymer above the glass transition temperature. Then, the piston containing the layer is lowered, and a fresh layer of powder material is rolled across the top surface. The subsequently formed layers are then bound to the previous ones. Unbound, loose powder is removed after the part is completed and is heat-treated to achieve full density (Figure 15). As the powders are maintained with low compaction forces after the sintering process to form new layers, structures have an internally porous structure suitable for bone scaffolds. SLS key advantage is its ability to directly produce implants with high mechanical resistance and to fabricate the hierarchical structure. Its disadvantages include the post-processing phase necessary to remove the trapped powder, and the high operating temperature that limits the number of suitable biomaterials.

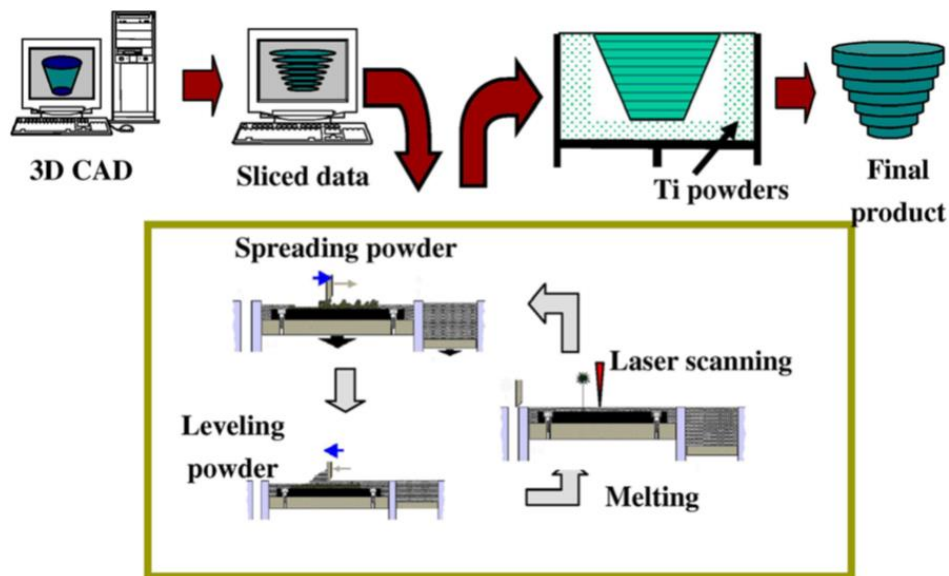


Figure 15. Selective Laser Sintering Technique (adapted from REF 159).

2.3.3. Bioprinting

Bioprinting is a 3D printing–like technique that has gained much attention due to its ability to address some of the challenges encountered using traditional bone tissue engineering approaches¹⁶⁰. Currently, this approach is particularly suitable for natural biomaterials to create hydrogels¹⁶¹. The most used bioprinting technologies are jetting-, extrusion- and laser-based printing^{162–165} (Figure 16). This technique allows combining cells, growth factors, and biomaterials to create tissue-like structures that can imitate natural tissues. Generally, 3D bioprinting uses the layer-by-layer method to deposit materials known as bioinks to create tissue-like structures that are later used for medical and tissue engineering applications. The key advantages are the material flexibility and room temperature processing with direct incorporation of cells. The main disadvantages are the limited mechanical stiffness and low resolution.

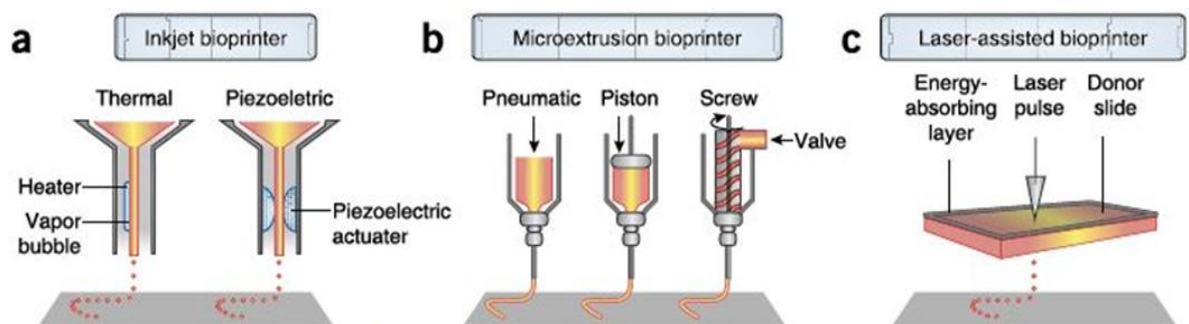


Figure 16. Bioprinting techniques (adapted from REF 166). a) Inkjet, b) Micro-extrusion and c) Laser-assisted bioprinting.

2.3.4. Fused deposition modeling (FDM)

Fused deposition modeling (FDM) is a common technique for scaffold fabrication¹⁶⁷ whereby molten thermoplastic materials are deposited on a platform through a heated extrusion head, called nozzle¹⁶⁸. The structure is built in a layer-by-layer fashion where the layers are fused together. After a layer in the XY plane is finished, the platform (z-axis) is lowered and the procedure is repeated (Figure 17). This results in scaffolds with controlled pore size,

morphology, and interconnectivity. FDM main advantages are the production of material with high porosity and good mechanical strength, no toxic solvent requirement, and flexibility in material handling and processing. The main issues are the limited number of available thermoplastic materials and the requirement for preformed fibers with a consistent size and material properties to feed through the rollers and nozzle. Another disadvantage of FDM is the inability to incorporate living cells or temperature-sensitive biological agents during extrusion due to the high processing temperature.

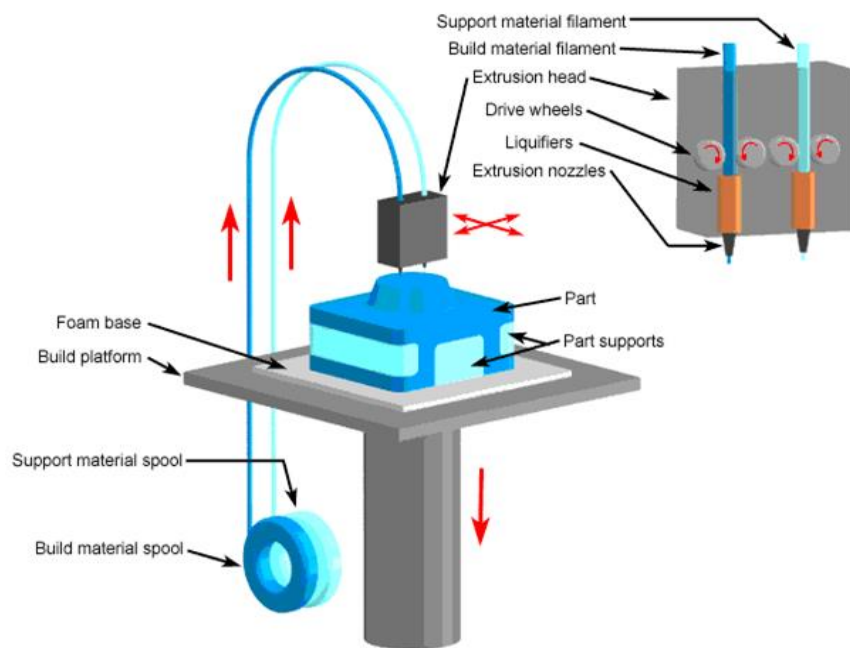


Figure 17. Fused Deposition Modeling technique (adapted from REF 167).

2.3.5. Stereolithography (SL or SLA)

SL is considered the first rapid prototyping process and was created by Charles Hull who invented the technique described in his U.S. Patent issued in 1986¹⁵⁹. He defined a method and apparatus for making solid objects by successively printing thin layers of ultraviolet (UV) curable material one on top of the other¹⁴⁷. Schematically, an SL system consists of a tank of photo-sensitive liquid resin, a moveable built platform, a UV laser to irradiate the resin and a dynamic mirror system. The process starts with the deposition by the UV laser of a layer of

photo-sensitive liquid resin onto the platform. Once the layer is completely solidified, the platform is vertically lowered. Then, another layer is deposited onto the first one. These steps are repeated until a complete 3D scaffold is formed. Finally, the UV-uncured resin is washed off and the scaffold is post-cured under UV light, yielding a fully cured support. The reduction in the laser power and the improvement of both lateral and vertical resolutions have led to the development of new SL techniques, such as micro-stereolithography (μ SL), two-photon polymerization, and digital light processing (DLP)¹⁴⁶ (Figure 18). As an example, in DLP, dynamic masks are used to cure a whole layer at a time¹⁶⁹. SL advantages are the ability to create complex shapes with internal architecture and extremely high feature resolution¹⁷⁰. The main disadvantage is that few biodegradable and biocompatible biomaterials are dimensionally stable during photo-polymerization for tissue engineering applications¹⁷¹. Additional challenges are skin irritation and cytotoxicity caused by photo-sensitive resins¹⁷². Moreover, photo-polymerized resins display poor mechanical properties that are needed for hard tissue engineering.

The number of commercially available resins for SL is limited. The first resins developed for SL were based on low molecular weight polyacrylate or epoxy macromers. Over the past two decades, several resins have been developed, and the mechanical properties of the networks obtained after curing have improved¹⁷³. The biodegradable macromers used for SL are based on functionalized oligomers with hydrolysable ester or carbonate linkages in the main chain.

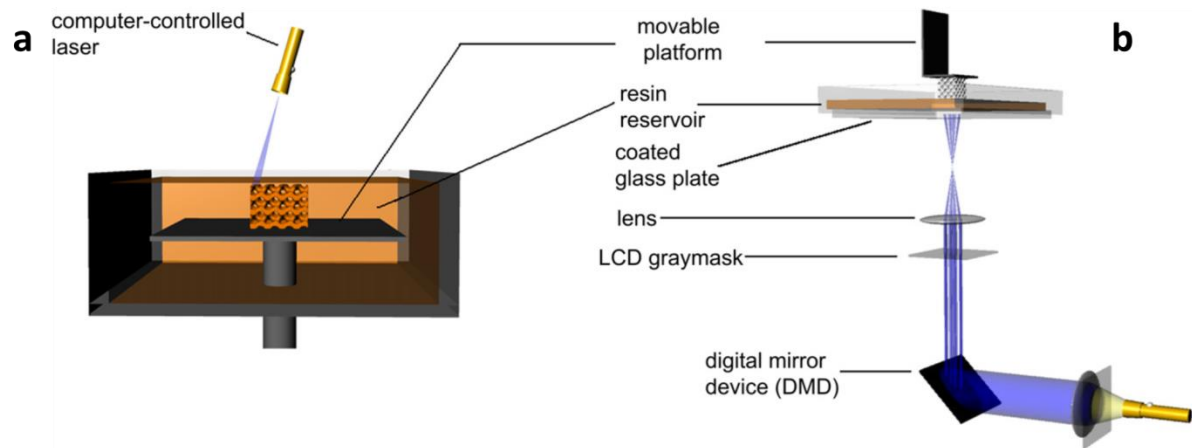


Figure 18. Stereolithography technique (adapted from REF 173). a) Laser and b) Digital Light Processing.

3D printing is a suitable method to obtain scaffolds with good properties for bone tissue engineering; however, the different 3D printing technologies do not work with every material. In the next section, the most common polymers used with 3D printers will be described.

Table 6. Advantages and drawbacks of various 3D printing techniques.

Method	Advantages	Drawbacks
Powder-based	Ability to create complex shapes No heat source No need for build plate	Post-processing needed Considerable porosity Low surface quality Not available for part reparation
Selective Laser Sintering	No need for support No post-processing needed	High cost Need heat treatment Porous part and rough surface Thermal distortion No available for part reparation
Bioprinting	No post-processing needed Low material waste Cell-compatible	Low accuracy Poor mechanical strength Slow
Fused Deposition Modeling	Fast Low cost Simple Acceptable strength Multi material No solvent	Nozzle clogging Limitation in usable material High temperature
Stereolithography	Fast High-dimensional accuracy Material flexibility Acceptable mechanical strength Good surface	High cost Cytotoxicity Material limitation Need support

2.4. Materials for 3D printing

Different types of materials can be used in bone tissue engineering. In this section, we will focus on some examples of synthetic polymers generally used in 3D printing, such as PLA and poly (propylene fumarate) (PPF).

2.4.1. Polylactic acid (PLA)

PLA and its copolymers and composites are commonly utilized for scaffold fabrication in bone tissue engineering¹⁷⁴. PLA is one of the most popular materials because of its low crystallization rate, high dimensional stability and tunable properties that allow many

applications, such as wound care materials, tissue regeneration, bone defect management, and controlled drug delivery^{175–177}. PLA is a thermoplastic polyester derived from renewable bio-resources such as corn starch and sugar beets^{178,179}. PLA can be synthesized by different methods, including direct condensation polymerization, azeotropic dehydration polymerization, or ring-opening polymerization. Depending on the choice of pre-polymers and route of synthesis, many different PLAs can be fabricated with a wide range of physicochemical properties. For instance, PLA optical composition significantly affects the polymer crystallinity. Due to the presence of a chiral carbon atom, lactic acid exists in two stereoisomers: L (+) and D (–) enantiomers. Depending on their ratios, the polymer mechanical properties can vary as well as its biodegradation time¹⁸⁰. PLA thermal properties also depend on the L/D ratios as well as on the molecular weight¹⁸¹. PLA glass transition temperature and melting temperature are approximately 55°C and 180°C, respectively. Molecular weight also influences the polymer degradation time into water and carbon dioxide. PLA physicochemical properties enable the fabrication of scaffolds using different technologies and in different forms (hydrogels, microspheres, blocks, fibers, and membranes). PLA has already found its place in numerous biomedical applications¹⁸² and has been widely used to produce scaffolds to aid tissue regeneration (e.g., bone¹⁸³, breast¹⁸⁴), or as drug carrier¹⁸⁵.

Most PLA-based scaffolds have been fabricated using conventional techniques and also by 3D printing with high resolution¹⁸⁶ and variety of geometries^{186,187}. FDM is the most frequently used technique to create PLA-based scaffolds for bone tissue engineering. The scaffold geometry, including pore size, shape, struts size, and orientation, significantly affects its mechanical performance and bioactivity¹⁸⁸. For example, mesenchymal stem cell differentiation and proliferation of pre-osteoblastic cells are strongly influenced by the geometry of individual pores within the scaffold¹⁸⁹. 3D-printed PLA scaffolds with different

architectures are investigated for biomedical applications because of their good biocompatibility and biodegradation¹⁹⁰. Only one study demonstrated the use of PLA scaffolds for cartilage and nucleus pulposus tissue regeneration¹⁹¹.

2.4.2. Poly(propylene fumarate) (PPF)

PPF is a linear unsaturated co-polyester based on fumaric acid, a component of the Krebs cycle¹⁹² (Figure 19). PPF is an amorphous polymer with a glass transition temperature that varies from -30°C up to 32°C, in function of the molecular weight.

The main advantages of PPF are the unsaturated carbon-carbon double bonds of the fumaric acid unit that allow crosslinking of the polymer into a covalent polymer network via free radical polymerization or photoinitiation using photoinitiators, such as bisacylphosphine oxide. The other advantage is the formation of biocompatible and extractable degradation products, primarily fumaric acid and propylene glycol, upon hydrolysis of the ester linkages¹⁹³. Due to its tailorable mechanical performance¹⁹⁴, biocompatibility¹⁹⁵, and biodegradability¹⁹⁶, PPF-based polymers have been widely investigated for a number of biomedical applications, such as the fabrication of orthopedic implants¹⁹⁷, scaffolds for tissue engineering¹⁹⁸, controlled bioactive factor delivery systems¹⁹⁹, and cell transplantation vehicles^{200,201}.

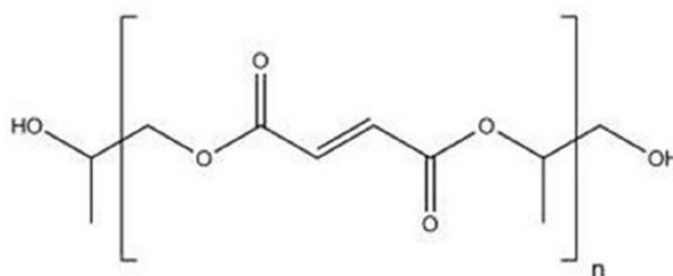


Figure 19. Poly(propylene fumarate) molecular structure.

Photo-crosslinkable PPF²⁰² is commonly used in SL for the fabrication of 3D scaffold complexes with controlled microstructures that were evaluated for the reconstruction of rabbit cranial defects²⁰³. PPF requires a reactive diluent, such as diethyl fumarate or N-vinyl-2-pyrrolidone, to reduce the resin viscosity for proper processing conditions. Typically, the highest resin viscosities that can be employed in SL are approximately 5Pas²⁰⁴. However, these diluents introduce significant amounts of a non-degradable component, and the obtained scaffolds display hydrophobic surface properties that limit cell adhesion²⁰⁵.

C- 3D scaffold improvement

To improve the previously described 3D scaffolds, particularly their mechanical properties, resorption rate and controlled release of drugs, different types of materials (e.g., 2D materials and microspheres) can be used.

1. 2D nanosheets materials

For bone tissue engineering in regenerative medicine scaffold morphology, chemical composition and physico-chemical properties should mimic the multi-scale structure of bone extracellular matrix to facilitate cell adhesion and proliferation^{206,207}. Unfortunately, the mechanical properties and hydrophobic surface of the biodegradable synthetic materials frequently used for scaffold production are incompatible with biological tissues¹⁷⁵. To overcome this issue, the scaffold properties could be improved by incorporating 2D nanosheets, such as graphene oxide (GO)²⁰⁸ or boron nitride (BN) in its graphene form²⁰⁹.

1.1. Generalities on scaffold improvement

3D polymer scaffolds used in bone tissue engineering have some limitations, such as low mechanical properties, bioinertia, and inadequate degradation time. To overcome these limitations, different fillers have been used, such as ceramics, metals and nanomaterials in different forms (2D nanosheets, microspheres, etc...).

For instance, PLA has promising osteoconductive properties¹⁸⁷, but requires often a surface treatment to improve cell attachment. Moreover, PLA mechanical properties and degradation time can be improved by co-polymerization²¹⁰. To limit the inflammatory response caused by PLA degradation, this polymer is often combined with bioglass or CaP²¹¹. Moreover, HA and titanium (Ti) have been used to improve PLA tensile strength and stability¹⁸². Addition of 15% of HA in 3D-printed PLA scaffolds with shape recovery of 98% was used for small bone defect management²¹². However, the successful incorporation of bioactive components into scaffolds and the inclusion of bioactive growth factors might be limited by the PLA type and scaffold fabrication technique (e.g., FDM that requires high printing temperature)²¹³. In this case, a surface modification treatment can be performed to improve the biocompatibility and functionality of 3D printed PLA scaffolds, and to broaden their potential for biomedical application. For instance, polydopamine coating of 3D printed PLA scaffolds enhanced the adhesion and proliferation of human adipose-derived stem cells²¹⁴. To overcome the drawbacks of FDM techniques, SL can be used to fabricate PLA scaffolds. Melchels *et al*, found that pre-osteoblasts can efficiently adhere on PLA porous scaffolds fabricated by SL²¹⁵. Moreover, Ronca *et al*, showed that PLA can be tuned with nanosized HA to obtain poly(D,L-lactide)/nanosized HA scaffolds²¹⁶. However, these materials present reduced mechanical properties and bioactivity²¹⁷.

For its use in orthopedics as scaffold, PPF is often combined with particles of ceramic materials, such as HA, calcium carbonate, or CaP²¹⁸, to improve its bioactivity. By mixing

PPF and HA particles in diethyl fumarate as a reactive diluent, a photopolymerizable composite resin was obtained²¹⁹. Furthermore, specific protein binding molecules can be included in the resins²²⁰, and proteins have been grafted on to the surface of the scaffold network²²¹. Copolymerization with hydrophilic polymers, such as PEG, and modification with peptides are useful methods for increasing PPF hydrophilicity and broadening its medical applications²²². PPF scaffold bioactivity can be improved also by the integration of proteins, such as BMP-2, to promote bone formation *in vivo*²²³.

To further improve PPF and PLA mechanical properties and extend their application range, new approaches have been developed, such as the addition of nanofillers^{224,225}. For instance, for surface modification, PLA can be tuned directly by addition of fillers, such as the 2D nanomaterials GO²²⁶ and BN²²⁷.

1.2. 2D materials

Two-dimensional (2D) materials have attracted tremendous research interest since the breakthrough identification and production of graphene in 2004²²⁸. Their atomic thickness and huge exposed surface make them highly designable and easy to handle, leading to extensive application potentials.

In 2D materials the atomic organization and bond strength along two dimensions are similar and much stronger than along the third dimension. They have attracted scientists attention due to their extraordinary physical and outstanding electrical properties²²⁹. They possess strong in-plane chemical bonds, but weak coupling van der Waals interactions between layers, thus offering the opportunity for cleavage into individual freestanding atomic layers. The process that changes the pristine bulky materials into nano-scale thin films is known as exfoliation. After exfoliation, the newly obtained material will not possess all the original properties of the bulk crystal. In addition, some new and interesting properties will appear, making the

nanosheets unique for their potential applications in various fields. Nowadays, a large range of 2D nanomaterials exists, such as GO, hexagonal BN, metal chalcogenides, and metal oxides. These nanostructures present interesting features, such as large surface area, ultralow weight, and high strength.

In this section, we will focus particularly on GO and hexagonal BN.

1.3. Graphene oxide

Graphene (the elementary structure of graphite) is a single-layer sheet composed of sp²-bonded carbon atoms arranged in a flat honeycomb structure (Figure 20a). Its remarkable properties, such as chemical purity, high mechanical strength, extremely large surface area, aqueous processability, and surface functionalizability^{230,231}, make of graphene a potential material for bio-applications. GO has a similar structure, but with additional polar functional groups (epoxides, hydroxyl or carboxylic groups) that are crucial for promoting interaction with the polymer matrix^{232,233}. GO has been used in different biomedical applications (e.g., biosensors, cancer therapy, and drug delivery²³⁴).

Different studies have investigated PLA reinforcement with GO^{226,235}. For example, Pinto *et al.* showed that GO addition increases PLA Young's modulus by 115% and the yield strength by 95%²²⁶. Other studies demonstrated that biopolymer reinforcement with GO is biocompatible, promotes cell adhesion and proliferation, and improves composite wetting^{236–238}. Similarly, PPF can be improved by incorporating GO to increase the polymer thermal stability and also the matrix hydrophilicity and mechanical properties²³⁹.

1.4. Boron Nitride

BN is an isoelectric analogue of graphite (Figure 20b), non-toxic to cells. BN-functionalized polymers are highly dispersed in aqueous and organic solvents²⁴⁰. Among the different nanofillers used to reinforce polymer matrices, BN is electrically insulating and displays good chemical, mechanical and thermal stability²⁴¹. Moreover, the production of BN nanosheets does not involve the use of acids or organic solvents²⁴². Several biomedical applications of BN have already been investigated, mostly as nanotubes rather than hexagonal BN²⁴¹.

BN (mainly as nanotubes) has been used as filler to reinforce different materials and for various biomedical applications^{243,244}. Boron-containing compounds are of great interest also for anticancer therapy²⁴⁵, including hexagonal BN in material composites for anticancer drug loading and releasing²⁴⁶. Moreover, BN nanotubes can improve osteogenic differentiation of mesenchymal stem cells *in vitro*²⁴⁷ and *in vivo*²⁴⁸. FDM has been used to print different BN-based polymers, such as thermoplastic polyurethane or acrylonitrile butadiene styrene, that showed better thermal conductivity^{249,250}. Photosensitive polymer-based BN nanoplatelets printed using SL displayed enhanced damping behavior²⁵¹. A nanomaterial for bioelectronic applications printed using a bio-ink containing PLGA-based hexagonal BN showed controllable mechanical and thermal properties, using the right amount of fillers, without any cytotoxicity²²⁷.

In this thesis, GO and BN as 2D materials fillers for scaffold reinforcement will be studied.

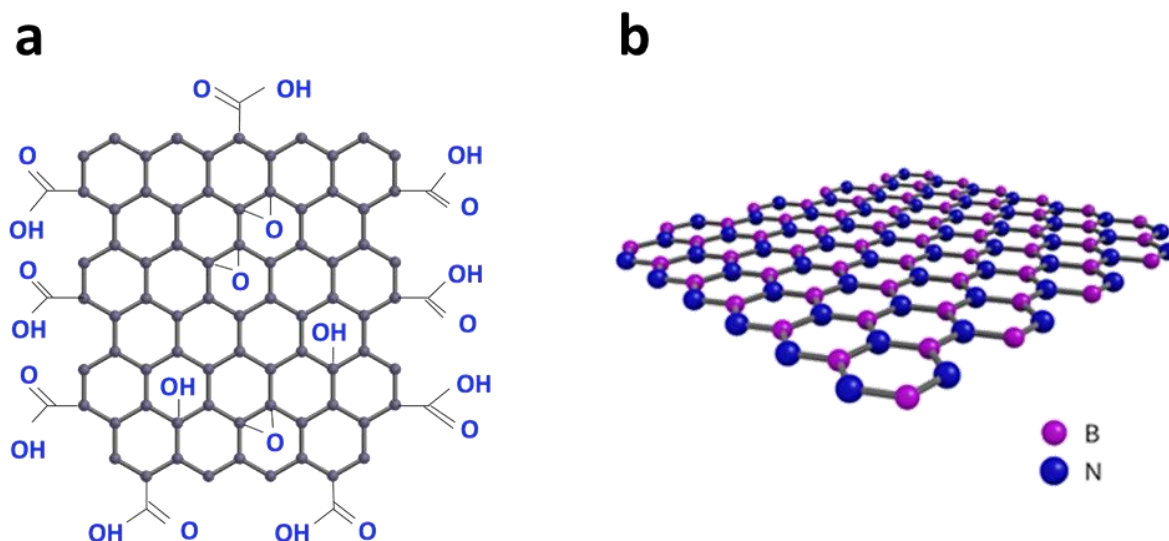


Figure 20. Molecular structure of a) graphene oxide and b) boron nitride.

2. Microspheres

The 2D nanomaterials presented in the previous section have been used to improve the mechanical properties or bioactivity of scaffolds. When anticancer drugs need to be used, microspheres can be used as fillers. In some cases, microspheres can have a double effect. Indeed, they can act as vehicle for local drug delivery, and they can also increase the scaffold porosity and by consequence accelerate its resorption rate.

2.1. Macroporosity

As mentioned above, CPCs are used as bone substitutes because of their similarity in composition to the bone mineral phase^{114,252}. This gives them good biocompatibility and excellent bioactivity, but low osteoconductivity. Osteoconduction indicates that a surface allows bone growth, and is directly related to the scaffold internal architecture. Indeed, an interconnected macroporous structure is required to allow vascular and cell penetration within the biomaterial before its resorption. This kind of structure often tends to resemble that of the trabecular bone. The macropore size must be at least $50\text{ }\mu\text{m}$ ¹²⁶, or higher than $100\text{ }\mu\text{m}$ ²⁵³ and up to $300\text{ }\mu\text{m}$ ²⁵⁴. CPCs are naturally microporous due to the presence of water from the liquid

phase and the acid-base setting reaction. These micropores are generally less than 5 μm in size and represent 35 to 50% of the cement volume, depending on the liquid/powder ratio used for its preparation²⁵⁵. This pore size allows only the penetration of biological fluids, but not of cellular or vascular elements. The absence of natural macroporosities explains CPC low osteoconductivity. Moreover, cements are generally resorbed slowly, and *in vivo* biodegradation is slower than the growth of neoformed bone¹²⁶. This limits their clinical applications. Several strategies have been evaluated to improve their resorbability, particularly by adding a porous agent to improve the macroporosity architecture²⁵⁶, or by using a phase with a better resorbability, such as calcium sulfate or a metastable calcium carbonate²⁵⁷. In recent years, the creation of new composite materials has led to interesting results. The term composite refers to a broad range of solid materials that contain at least two distinct phases at the macroscopic, micrometric, or even nanometric scale²⁵⁸. In the case of CPCs, composite refers mostly to the introduction during the mixing of the cement paste of a rapidly absorbable organic phase that initially stabilizes the CPC and then is gradually dissolved by revealing free gaps for bone regrowth (i.e., secondary macroporosity). The polymer can be introduced in the liquid phase, as a solution, or in the solid phase, mainly in the form of powders, fibers or microspheres. Different polymers have been developed using for instance, gelatin^{259,260} or poly(trimethylene carbonate)^{261,262}. However, the most commonly used is poly(glycolide-co-lactide)^{263–268}. The composite nature of CPCs has been developed to improve some of their properties, mainly porosity, by introducing microspheres into the intrinsically microporous matrix, and mechanical properties. Moreover, many study have evaluated CPCs as candidates for the release of active agents, such as growth factors²⁶⁶, antibiotics²⁶⁹, anti-osteoporosis drugs²⁷⁰ and anti-cancer drugs²⁷¹.

2.2. Drug delivery: state of the art

2.2.1. Drug delivery systems

Drugs can be administered through numerous conventional routes (e.g., intravenous, intramuscular or oral). Oral administration is the most popular route because is less invasive, can be done by the patient (thus providing higher compliance) and is associated with a lower cost of manufacture. Nevertheless, these drug administration routes are not always optimal. For example, inside the body, drug bioavailability may be very weak due to its low solubility and dissolution and/or high systemic clearance. Therefore, the drug amount has to be increased to reach the therapeutic dose. The use of high drug doses increases the risk of side effects. Moreover, when a drug is administered through a systemic route, many parts of the body will be exposed to the effects. Hence, alternative systems are required to safely deliver the drug at the required concentration to reach the therapeutic dose, at the right time, and to the specific target.

In the next section, the possibility of using microspheres to administer the right drug dose will be described.

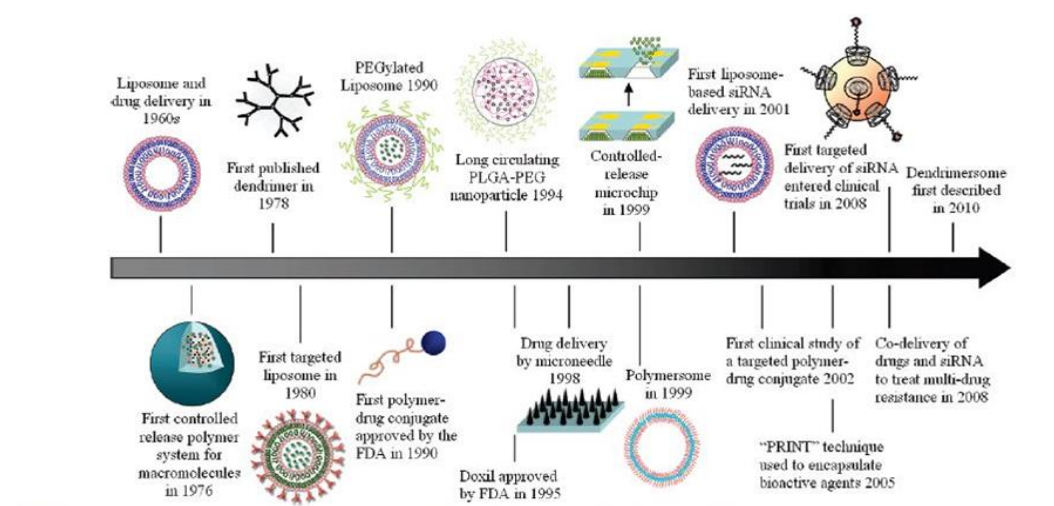


Figure 21. Timeline of nanotechnology-based drug delivery (adapted from REF 272).

To develop effective drug delivery systems²⁷², various organic/inorganic nanomaterials and devices have been tested as delivery vehicles (Figure 21). Several nanotechnology-based therapeutic products have been approved by the FDA for clinical use^{273–275}. Most of these devices include a non-targeted delivery system (e.g., liposomes, hydrogels, polymer-based disks, rods, pellets or microparticles) and a drug²⁷⁶. Such systems offer numerous advantages over the traditional drug delivery methods. They can enhance the therapeutic activity by extending the drug half-life, by improving the solubility of hydrophobic drugs, by reducing the potential immunogenicity, and/or by releasing the drug in a controlled way. Consequently, the toxic side effects and the administration frequency might be reduced.

For instance, polymeric micro-/nanoparticles pre-loaded with growth factors have been incorporated in porous scaffolds and hydrogels²⁷⁷. Furthermore, the release of each individual biological factor can be tailored by tuning the particle formulation and composition in order to promote tissue growth.

2.2.2. Materials used for drug delivery

Among the many drug delivery systems, biodegradable polymers have been widely used as drug delivery systems because of their biocompatibility and biodegradability²⁷⁸.

These properties can be obtained by using natural polymers, such as polysaccharides²⁷⁹ (cellulose²⁸⁰ and chitosan²⁸¹, for example), or synthetic polymers made of repeated structural units called monomers, such as polyanhydrides²⁸², poly(ortho esters)²⁸³, polyphosphazenes²⁸⁴, and polyesters²⁸⁵. Biodegradable (synthetic or natural) polymers can be cleaved into biocompatible byproducts by chemical or enzyme-catalyzed hydrolysis. Their biodegradability allows their implantation in the body without the need of subsequent removal by surgery. The drug release rate from biodegradable polymers can be controlled via a number of factors, such as the polymer biodegradation kinetics²⁸⁶, the drug and/or polymer

physicochemical properties²⁸⁷, the thermodynamic compatibility between polymer and drug²⁸⁸, and the device shape²⁸⁹.

Polymeric microspheres composed of a biodegradable polymer matrix in which the drug is encapsulated are the most commonly used system and are advantageous for several reasons²⁹⁰. Indeed, microspheres can encapsulate many drug types, including small molecules, proteins, and nucleic acids, and can easily deliver medication in a rate-controlled manner²⁹¹ without a surgical procedure. Drugs are released from the microsphere by leaching from the polymer, or by degradation of the polymer matrix. Many different drug types, regardless of their molecular weight and water solubility, can be loaded into biodegradable microspheres using different manufacturing techniques^{292,293}.

2.3. Poly(lactic-co-glycolide) microspheres

2.3.1 Poly(lactic-co-glycolide)

The most commonly used biodegradable synthetic polymers in biomedical applications are saturated poly(α -hydroxy esters), including PLA and poly(glycolic acid) (PGA), and as PLGA copolymers^{294,295}. PLGA is among the most attractive polymeric candidates for drug delivery and tissue engineering applications for many reasons: 1) its chemical biocompatibility, biodegradability and non-toxic degradation products; 2) it has been approved by the U.S. FDA, and 3) is a tunable surface with mechanical properties. PLGA has shown immense potential as a drug delivery carrier and as scaffold for tissue engineering. PLGA has been extensively studied for the development of devices for controlled delivery of small-molecule drugs, proteins, and other macromolecules²⁸⁵. Polyester PLGA is a copolymer of PLA and PGA (Figure 22). Depending on the lactide to glycolide ratio used for the polymerization, different PLGA forms can be obtained that are usually identified on the basis of this ratio. PGA is a hydrophilic and highly crystalline polymer with a relatively fast degradation rate. PLA exhibits different chemical, physical, and mechanical properties because of the presence

of a pendant methyl group on the alpha carbon. Generally, the copolymer PLGA is preferred compared with its constituent homopolymers for the fabrication of bone substitute constructs. It is possible to tune PLGA physical properties by controlling the polymer molecular weight, the lactide to glycolide ratio and the drug concentration to achieve the desired dosage and release interval, depending on the drug type²⁹⁶.

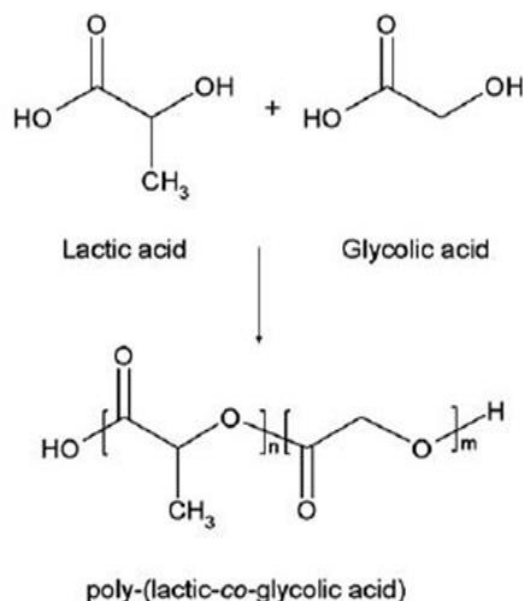


Figure 22. Molecular structure of poly-(lactic-co-glycolic acid).

2.3.2. Poly(lactic-co-glycolide) microsphere preparation

For biomedical applications, PLGA can be easily processed and fabricated in a wide variety of forms, such as films, porous scaffolds, hydrogels, or microspheres. The microsphere shape is preferred for drug delivery²⁹⁷. Compared with films, microspheres offer many advantages, including controlled release and protection of the drug from degradative enzymes and chemicals within the body. Microspheres can be used to microencapsulate various drug types (small molecules, proteins, and nucleic acid) and increase the patient compliance due to the reduced frequency of drug intake²⁹⁸. Microencapsulation is a common method for the production of drug-loaded PLGA microspheres²⁹⁹. The packaging of liquids and solids in spherical particles of micron size was developed in the mid-1950s and since then has been

used for many applications. Several methods have been described for the preparation of drug-containing microspheres using biodegradable polymers, including spray drying³⁰⁰ and hot-melt techniques³⁰¹. However, these methods are limited to specific substances. The oil-in-water emulsion and solvent evaporation technique, where the drug is evenly distributed throughout a soluble PLGA matrix and then emulsified, is commonly used³⁰². After the organic solvent evaporation, a suspension of solid microparticles is obtained. The bioactive compound can be co-dissolved in the PLGA matrix if hydrophobic³⁰³, or produced as a double emulsion or suspension if not³⁰⁴. For clinical applications, the microsphere shape and size, release pattern within the body, and degradation behavior are strictly regulated to avoid any risk of critical complications after their administration³⁰⁵. When emulsion techniques are used for microsphere preparation, a number of processing factors influences the final structure of the microspheres: choice of solvents and surfactants, phase viscosity, ratio of the dispersed to the continuous phase, mixing speed, processing temperature, and time³⁰⁶. Microsphere size can be varied from ten to several hundred microns, by careful modification of the processing conditions³⁰⁷. For clinical applications, the most effective size range is 10–200 μm . Microspheres smaller than 10 μm can diffuse and also be phagocytosed by immune cells. Microspheres larger than 200 μm may have a deleterious effect on the tissue structure at the implantation site, they can potentially activate the immune response, and lead to inflammation³⁰⁸.

2.3.3. Poly(lactic-co-glycolide) degradation

PLGA copolymers are degraded by hydrolysis or through cleavage of its backbone ester linkages into oligomers and, finally monomers³⁰⁹. The degradation of PLGA copolymer is a collective process of bulk diffusion, surface diffusion, bulk erosion, and surface erosion.³¹⁰ The effect of physicochemical properties on the drug release rate from biodegradable PLGA, such as the glass transition temperature, molecular weight³¹¹, size and shape^{312–314} and the polymer composition, have to be considered. The biodegradation and properties of PLGA microparticles can be tuned from a few weeks to several months by varying the PLA to PGA ratio that influences the release and degradation rates of the incorporated drug molecules³¹⁵. Other parameters, such as drug type and loading^{316,317}, pH³¹⁸ or enzymes³¹⁹, can also influence the device biodegradation and drug release.

D- Conclusions and objectives

In this chapter, first bone tissue and breast cancer were rapidly described. The mechanisms of bone metastasis formation and its consequence on bone were discussed, followed by the different (local or systemic) treatments and the two drug families (BPs and SERMs) mainly used for breast cancer bone metastases. Then, the generalities of bone tissue engineering and the properties necessary for scaffolds were presented. Particularly, two different biomaterials and the techniques currently used to obtain scaffolds, based on the size and shape of the damaged bone to be repaired, were discussed. For instance, CPC can be injected in the case of small bone defect (vertebroplasty). For larger and complex bone defects that need bigger biomaterial, 3D printed biopolymer scaffolds can be introduced as bone substitute. Finally, different strategies to improve scaffolds for bone repair, in the case of bone metastases, were presented. Different materials, such as 2D nanomaterials (GO and BN), to reinforce the scaffold mechanical properties and bioactivity were described. Another way to improve

scaffold capability is to incorporate PLGA microspheres. PLGA microspheres can encapsulate different drugs for local delivery with controlled liberation kinetics. The scaffold resorption rate can be accelerated by creating micro- or macro-porosities. Hence, it would be interesting to fabricate different scaffolds, such as CPC and 3D printed polymers, and to reinforce them with 2D nanomaterials or drug-loaded PLGA for the treatment of pathologic fractures in patients with breast cancer bone metastases.

The aim of the present work is to develop new 3D scaffolds for the treatment of bone pathologies caused, for instance, by breast cancer metastatic spread. Our research will focus first on the development and characterization of 3D printed PLA scaffolds reinforced with exfoliated GO or BN produced by FDM. Then, the encapsulation of two drugs (alendronate and RH) in PLGA microspheres will be studied. Specifically, microspheres of 1 to 10 μ m will be incorporated in 3D PPF scaffolds for the treatment of long bones, and microspheres of about 100 μ m will be incorporated in injectable CPC for vertebroplasty. Finally, *in vitro* and preliminary *in vivo* experiments will be performed to test these materials.

REFERENCES

1. Amin, S., Achenbach, S. J., Atkinson, E. J., Khosla, S. & Melton, L. J. Trends in fracture incidence: A population-based study over 20 years. *J. Bone Miner. Res.* **29**, 581–589 (2014).
2. Petite, H. *et al.* Tissue-engineered bone regeneration. *Nat. Biotechnol.* **18**, 959–963 (2000).
3. Newman, T. Bones: All you need to know. *Medical News Today* (2018). Available at: <https://www.medicalnewstoday.com/articles/320444.php>. (Accessed: 30th July 2019)
4. Summers, B. N. & Eisenstein, S. M. Donor site pain from the ilium. A complication of lumbar spine fusion. *J. Bone Joint Surg. Br.* **71**, 677–80 (1989).
5. Younger, E. M. & Chapman, M. W. Morbidity at bone graft donor sites. *J. Orthop. Trauma* **3**, 192–5 (1989).
6. Ross, L. Tacconi, J. B. Miles, N. Heterotopic bone formation causing recurrent donor site pain following iliac crest bone harvesting. *Br. J. Neurosurg.* **14**, 476–479 (2000).
7. Dennis, D. A. & Little, L. R. The structural allograft composite in revision total knee arthroplasty. *Orthopedics* **28**, 1005–7 (2005).
8. Graham, N. M. & Stockley, I. The use of structural proximal femoral allografts in complex revision hip arthroplasty. *J. Bone Joint Surg. Br.* **86**, 337–43 (2004).
9. Poitout, D. & Novakovitch, G. [Use of allografts in oncology and traumatology]. *Int. Orthop.* **11**, 169–78 (1987).
10. Zimmermann, G. & Moghaddam, A. Allograft bone matrix versus synthetic bone graft substitutes. *Injury* **42**, S16–S21 (2011).

11. Salama, R. Xenogeneic bone grafting in humans. *Clin. Orthop. Relat. Res.* 113–21 (1983).
12. Melo, H., Brandao, C., Rego, G. & Nunes, R. Ethical and legal issues in xenotransplantation. *Bioethics* **15**, 427–42 (2001).
13. Iarc. *Dernières données mondiales sur le cancer : le fardeau du cancer atteint 18,1 millions de nouveaux cas et 9,6 millions de décès par cancer en 2018*. (2018).
14. FRM. Les cancers du sein en chiffres. Available at: <https://www.frm.org/recherches-cancers/cancer-du-sein/les-cancers-du-sein-en-chiffres>. (Accessed: 30th July 2019)
15. Breastcancer.org. U.S Breast Cancer Statistics. Available at: https://www.breastcancer.org/symptoms/understand_bc/statistics. (Accessed: 30th July 2019)
16. Rivenbark, A. G., O'Connor, S. M. & Coleman, W. B. Molecular and cellular heterogeneity in breast cancer: Challenges for personalized medicine. *Am. J. Pathol.* **183**, 1113–1124 (2013).
17. Hanahan, D. & Weinberg, R. A. Hallmarks of cancer: the next generation. *Cell* **144**, 646–74 (2011).
18. Coleman, R. E., Gregory, W., Marshall, H., Wilson, C. & Holen, I. The metastatic microenvironment of breast cancer: Clinical implications. *Breast* **22**, S50–S56 (2013).
19. Oster, G. *et al.* Natural history of skeletal-related events in patients with breast, lung, or prostate cancer and metastases to bone: A 15-year study in two large US health systems. *Support. Care Cancer* **21**, 3279–3286 (2013).
20. Stephen, P. The distribution of secondary growths in cancer of the breast. *Lancet* **133**, 571–573 (1889).
21. Weilbaecher, Katherine N. Guise, T. A. & McCauley, L. K. Cancer To Bone: a Fatal Attraction. *Nat. Rev.* **11**, 411–425 (2013).
22. Makhoul, I., Montgomery, C. O., Gaddy, D. & Suva, L. J. The best of both worlds-managing the cancer, saving the bone. *Nat. Rev. Endocrinol.* **12**, 29–42 (2016).
23. Mundy, G. R. Metastasis to bone: causes, consequences and therapeutic opportunities. *Nat. Rev. Cancer* **2**, 584–593 (2002).
24. Sethi, N., Dai, X., Winter, C. G. & Kang, Y. Tumor-Derived Jagged1 Promotes Osteolytic Bone Metastasis of Breast Cancer by Engaging Notch Signaling in Bone Cells. *Cancer Cell* **19**, 192–205 (2011).
25. Clezardin, P. & Teti, A. Bone metastasis: Pathogenesis and therapeutic implications. *Clin. Exp. Metastasis* **24**, 599–608 (2007).
26. Clézardin, P. Therapeutic targets for bone metastases in breast cancer. *Breast Cancer Res.* **13**, (2011).
27. STEWART, A. F. *et al.* Quantitative Bone Histomorphometry in Humoral Hypercalcemia of Malignancy: Uncoupling of Bone Cell Activity*. *J. Clin. Endocrinol. Metab.* **55**, 219–227 (1982).
28. Kitazawa, S. & Kitazawa, R. RANK ligand is a prerequisite for cancer-associated osteolytic lesions. *J. Pathol.* **198**, 228–236 (2002).
29. Leibbrandt, A. & Penninger, J. M. RANK/RANKL: Regulators of Immune Responses and Bone Physiology. *Ann. N. Y. Acad. Sci.* **1143**, 123–150 (2008).
30. Leto, G. Activin A and bone metastasis. *J. Cell. Physiol.* **225**, 302–309 (2010).
31. Jinnah, A. H., Zacks, B. C., Gwam, C. U. & Kerr, B. A. Emerging and established models of bone metastasis. *Cancers (Basel)*. **10**, 1–15 (2018).
32. Gunalp, B. *et al.* Evaluation of radiographic and metabolic changes in bone metastases in response to systemic therapy with ¹⁸FDG-PET/CT. *Radiol. Oncol.* **49**, 115–120 (2015).
33. Fradet, A. *et al.* A New Murine Model of Osteoblastic/Osteolytic Lesions from Human Androgen-Resistant Prostate Cancer. *PLoS One* **8**, 1–11 (2013).
34. Dai, J., Hensel, J., Wang, N., Kruithof-de Julio, M. & Shiozawa, Y. Mouse models for studying prostate cancer bone metastasis. *Bonekey Rep.* **5**, 1–10 (2016).
35. SINGH, A. S. & FIGG, W. D. IN VIVO MODELS OF PROSTATE CANCER METASTASIS TO BONE. *J. Urol.* **174**, 820–826 (2005).
36. Lu, Y. *et al.* Monocyte chemotactic protein-1 mediates prostate cancer-induced bone resorption. *Cancer*

- Res.* **67**, 3646–3653 (2007).
37. Suva, L. J., Washam, C., Nicholas, R. W. & Griffin, R. J. Bone metastasis: Mechanisms and therapeutic opportunities. *Nat. Rev. Endocrinol.* **7**, 208–218 (2011).
 38. Kingsley, L. A., Fournier, P. G. J., Chirgwin, J. M. & Guise, T. A. Molecular Biology of Bone Metastasis. *AACR Educ. B.* **2008**, 443–457 (2008).
 39. Käkönen, S. M. *et al.* Transforming growth factor- β stimulates parathyroid hormone-related protein and osteolytic metastases via Smad and mitogen-activated protein kinase signaling pathways. *J. Biol. Chem.* **277**, 24571–24578 (2002).
 40. Yin, J. J. *et al.* TGF- β signaling blockade inhibits PTHrP secretion by breast cancer cells and bone metastases development. **103**, 197–206 (1999).
 41. Bendre, M. S. *et al.* Tumor-derived interleukin-8 stimulates osteolysis independent of the receptor activator of nuclear factor- κ B ligand pathway. *Cancer Res.* **65**, 11001–11009 (2005).
 42. Ghajar, C. M. *et al.* The perivascular niche regulates breast tumor dormancy HHS Public Access. *Nat Cell Biol* **15**, 807–817 (2013).
 43. Lingala, S. M. & Ghany, M. G. M. Mhs. 可乐定和右美托咪啶产生抗伤害协同作用 HHS Public Access. **25**, 289–313 (2016).
 44. Linde, N., Fluegen, G. & Aguirre-Ghiso, J. A. The Relationship Between Dormant Cancer Cells and Their Microenvironment. *Adv. Cancer Res.* **132**, 45–71 (2016).
 45. Brunetti, G., Colaianni, G., Faienza, M. F., Colucci, S. & Grano, M. Osteotropic cancers: From primary tumor to bone. *Clin. Rev. Bone Miner. Metab.* **11**, 94–102 (2013).
 46. Thibaudau, L. *et al.* A tissue-engineered humanized xenograft model of human breast cancer metastasis to bone. *Dis. Model. Mech.* **7**, 299–309 (2014).
 47. Laredo, J. D. & Chiras, J. Radiologie interventionnelle dans les metastases osseuses. *Bull. Acad. Natl. Med.* **202**, 737–753 (2018).
 48. Lutz, S. *et al.* Palliative radiotherapy for bone metastases: An ASTRO evidence-based guideline. *Int. J. Radiat. Oncol. Biol. Phys.* **79**, 965–976 (2011).
 49. MA Gillentine, LN Berry, RP Goin-Kochel, MA Ali, J Ge, D Guffey, JA Rosenfeld, V Hannig, P Bader, M Proud, M Shinawi, BH Graham1, A Lin, SR Lalani, J Reynolds, M Chen, T Grebe, CG Minard, P Stankiewicz, AL Beaudet, and C. & Schaaf. 氢气和蛛网膜下腔出血HHS Public Access. *J Autism Dev Disord* **47**, 549–562 (2017).
 50. Santiago, F. R., Del Mar Castellano García, M., Montes, J. L. M., García, M. R. & Fernández, J. M. T. Treatment of bone tumours by radiofrequency thermal ablation. *Curr. Rev. Musculoskelet. Med.* **2**, 43–50 (2009).
 51. Palussière, J., Pellerin-Guignard, A., Descat, E., Cornélis, F. & Dixmérias, F. Radiofrequency ablation of bone tumours. *Diagn. Interv. Imaging* **93**, 680–684 (2012).
 52. Aboulafia, A. J., Levine, A. M., Schmidt, D. & Aboulafia, D. Surgical Therapy of Bone Metastases. *Semin. Oncol.* **34**, 206–214 (2007).
 53. Pountos, I. & Giannoudis, P. V. Drug-eluting implants for the suppression of metastatic bone disease: current insights. *Expert Rev. Med. Devices* **15**, 301–311 (2018).
 54. Reddy, E. K., Robinson, R. G. & Mansfield, C. M. Strontium 89 for Palliation of Bone Metastases. **78**,

- 27–32 (1986).
55. Sartor, O. Overview of samarium sm 153 lexidronam in the treatment of painful metastatic bone disease. *Rev. Urol.* **6 Suppl 10**, S3–S12 (2004).
 56. Gartrell, B. A. & Saad, F. Managing bone metastases and reducing skeletal related events in prostate cancer. *Nat. Rev. Clin. Oncol.* **11**, 335–345 (2014).
 57. Jeanny, J. E.-A. & Aragon-Ching, B. OTT-44291-radium-223-for-the-treatment-of-castration-resistant-prostat. *Onco. Targets. Ther.* **8**, 1103–1109 (2015).
 58. Dunford, J. E. *et al.* Structure-activity relationships for inhibition of farnesyl diphosphate synthase in vitro and inhibition of bone resorption in vivo by nitrogen-containing bisphosphonates. *J. Pharmacol. Exp. Ther.* **296**, 235–42 (2001).
 59. Rogers, M. J. *et al.* Cellular and molecular mechanisms of action of bisphosphonates. *Cancer* **88**, 2961–2978 (2000).
 60. Sambrook, P. & Cooper, C. Osteoporosis. *Lancet* **367**, 2010–2018 (2006).
 61. Gennari, L., Merlotti, D., De Paola, V. & Nuti, R. Lasofoxifene: Evidence of its therapeutic value in osteoporosis. *Core Evid.* **4**, 113–29 (2010).
 62. Rachner, T. D., Khosla, S. & Hofbauer, L. C. Osteoporosis: now and the future. *Lancet* **377**, 1276–1287 (2011).
 63. Shaw, N. J. & Bishop, N. J. Bisphosphonate treatment of bone disease. *Arch. Dis. Child.* **90**, 494–499 (2005).
 64. Bhuvanewari Ramaswamy, M. C. L. S. M. Bisphosphonates in the Prevention and Treatment of Bone Metastases. (2003).
 65. Manley, G. Bisphosphonates: Mechanism of Action and Role in Clinical Practice. **71**, 233–236 (2013).
 66. Rodan, G. A. & Reszka, A. A. Bisphosphonate mechanism of action. *Curr. Mol. Med.* **2**, 571–7 (2002).
 67. WANG, D., MILLER, S., KOPECKOVA, P. & KOPECEK, J. Bone-targeting macromolecular therapeutics. *Adv. Drug Deliv. Rev.* **57**, 1049–1076 (2005).
 68. Clézardin, P. Bisphosphonates’ antitumor activity: An unravelled side of a multifaceted drug class. *Bone* **48**, 71–79 (2011).
 69. Lu, P. Y., Hsieh, C. F., Tsai, Y. W. & Huang, W. F. Alendronate and raloxifene use related to cardiovascular diseases: Differentiation by different dosing regimens of alendronate. *Clin. Ther.* **33**, 1173–1179 (2011).
 70. Sato, M. *et al.* Advantages of raloxifene over alendronate or estrogen on nonreproductive and reproductive tissues in the long-term dosing of ovariectomized rats. *J. Pharmacol. Exp. Ther.* **279**, 298–305 (1996).
 71. Komatsu, K. *et al.* Alendronate promotes bone formation by inhibiting protein prenylation in osteoblasts in rat tooth replantation model. *J. Endocrinol.* **219**, 145–158 (2013).
 72. Diab, T., Wang, J., Reinwald, S., Guldberg, R. E. & Burr, D. B. Effects of the combination treatment of raloxifene and alendronate on the biomechanical properties of vertebral bone. *J. Bone Miner. Res.* **26**, 270–276 (2011).
 73. Ezra, A. & Golomb, G. Administration routes and delivery systems of bisphosphonates for the treatment of bone resorption. *Adv. Drug Deliv. Rev.* **42**, 175–195 (2000).

74. Cho, C. H. & Nuttall, M. E. Therapeutic potential of oestrogen receptor ligands in development for osteoporosis. *Expert Opin. Emerg. Drugs* **6**, 137–54 (2001).
75. Nilsson, S. & Koehler, K. F. Oestrogen Receptors and Selective Oestrogen Receptor Modulators: Molecular and Cellular Pharmacology. *Basic & Clin. Pharmacol. & Toxicol.* **96**, 15–25 (2005).
76. Early Breast Cancer Trialists' Collaborative Group (EBCTCG) *et al.* Relevance of breast cancer hormone receptors and other factors to the efficacy of adjuvant tamoxifen: patient-level meta-analysis of randomised trials. *Lancet* **378**, 771–784 (2011).
77. Fisher, B. *et al.* Tamoxifen for Prevention of Breast Cancer: Report of the National Surgical Adjuvant Breast and Bowel Project P-1 Study. *JNCI J. Natl. Cancer Inst.* **90**, 1371–1388 (1998).
78. Ettinger, B. *et al.* Reduction of vertebral fracture risk in postmenopausal women with osteoporosis treated with raloxifene: results from a 3-year randomized clinical trial. Multiple Outcomes of Raloxifene Evaluation (MORE) Investigators. *JAMA* **282**, 637–45 (1999).
79. Deshmane, V., Krishnamurthy, S., Melemed, A. S., Peterson, P. & Buzdar, A. U. Phase III Double-Blind Trial of Arzoxifene Compared With Tamoxifen for Locally Advanced or Metastatic Breast Cancer. *J. Clin. Oncol.* **25**, 4967–4973 (2007).
80. American Association for Cancer Research., C. K., Shou, J., Massarweh, S. & Schiff, R. *Clinical cancer research: an official journal of the American Association for Cancer Research. Clinical Cancer Research* **11**, (Association for Cancer Research, 1995).
81. Grese, T. A. *et al.* Molecular determinants of tissue selectivity in estrogen receptor modulators. *Proc. Natl. Acad. Sci.* **94**, 14105–14110 (1997).
82. Brzozowski, A. M. *et al.* Molecular basis of agonism and antagonism in the oestrogen receptor. *Nature* **389**, 753–758 (1997).
83. Rey, J. R. C. *et al.* Raloxifene: Mechanism of Action, Effects on Bone Tissue, and Applicability in Clinical Traumatology Practice. *Open Orthop. J.* **3**, 14–21 (2009).
84. Vogel, V. G. *et al.* Effects of Tamoxifen vs Raloxifene on the Risk of Developing Invasive Breast Cancer and Other Disease Outcomes<SUBTITLE>The NSABP Study of Tamoxifen and Raloxifene (STAR) P-2 Trial</SUBTITLE> *JAMA* **295**, 2727 (2006).
85. Maximov, P. Y., Lee, T. M. & Jordan, V. C. The discovery and development of selective estrogen receptor modulators (SERMs) for clinical practice. *Curr. Clin. Pharmacol.* **8**, 135–55 (2013).
86. Ellison, N. Goodman & Gilman's The Pharmacological Basis of Therapeutics, 10th Edition. *Anesth. Analg.* **94**, 1377 (2002).
87. Lee, W.-L., Chao, H.-T., Cheng, M.-H. & Wang, P.-H. Rationale for using raloxifene to prevent both osteoporosis and breast cancer in postmenopausal women. *Maturitas* **60**, 92–107 (2008).
88. Rossouw, J. E. *et al.* Risks and benefits of estrogen plus progestin in healthy postmenopausal women: principal results From the Women's Health Initiative randomized controlled trial. *JAMA* **288**, 321–33 (2002).
89. Bone, H. G. *et al.* Alendronate and Estrogen Effects in Postmenopausal Women with Low Bone Mineral Density. *J. Clin. Endocrinol. Metab.* **85**, 720–726 (2000).
90. Lindsay, R. *et al.* Addition of Alendronate to Ongoing Hormone Replacement Therapy in the Treatment of Osteoporosis: A Randomized, Controlled Clinical Trial. *J. Clin. Endocrinol. Metab.* **84**, 3076–3081 (1999).
91. O., J. *et al.* Additive effects of raloxifene and alendronate on bone density and biochemical markers of bone remodeling in postmenopausal women with osteoporosis. *J. Clin. Endocrinol. Metab.* **87**, 985–992 (2002).
92. Article, O. Combination Therapy of Raloxifene and Alendronate for Treatment of Osteoporosis in Elderly Women. 56–62 (2017).

93. Vallet-Regí, M., Balas, F. & Arcos, D. Mesoporous Materials for Drug Delivery. *Angew. Chemie Int. Ed.* **46**, 7548–7558 (2007).
94. Harmankaya, N. *et al.* Raloxifene and alendronate containing thin mesoporous titanium oxide films improve implant fixation to bone. *Acta Biomater.* **9**, 7064–7073 (2013).
95. Langer, R. & Vacanti, J. Advances in tissue engineering. *J. Pediatr. Surg.* **51**, 8–12 (2016).
96. Do, A.-V., Khorsand, B., Geary, S. M. & Salem, A. K. 3D Printing of Scaffolds for Tissue Regeneration Applications. *Adv. Healthc. Mater.* **4**, 1742–62 (2015).
97. Wang, W. & Yeung, K. W. K. Bone grafts and biomaterials substitutes for bone defect repair: A review. *Bioact. Mater.* **2**, 224–247 (2017).
98. T., A. & C., J. Osteoinduction, osteoconduction and osseointegration. *Eur. Spine J.* **10**, S96–S101 (2001).
99. Perez, R. A. & Mestres, G. Role of pore size and morphology in musculo-skeletal tissue regeneration. *Mater. Sci. Eng. C* **61**, 922–939 (2016).
100. Fleischer, S. & Dvir, T. Tissue engineering on the nanoscale: lessons from the heart. *Curr. Opin. Biotechnol.* **24**, 664–671 (2013).
101. IOF. Osteoporosis. Available at: <http://www.osteofound.org/>. (Accessed: 30th July 2019)
102. Inserm. Ostéoporose. Available at: <https://www.inserm.fr/information-en-sante/dossiers-information/osteoporose>. (Accessed: 30th July 2019)
103. Nakano, M. *et al.* Vertebroplasty Using Calcium Phosphate Cement for Osteoporotic Vertebral Fractures: Study of Outcomes at a Minimum Follow-up of Two Years. *Asian Spine J.* **6**, 34 (2012).
104. Kaemmerlen, P. *et al.* [Percutaneous vertebroplasty in the treatment of metastases. Technic and results]. *J. Radiol.* **70**, 557–62 (1989).
105. Galibert, P., Deramond, H., Rosat, P. & Le Gars, D. [Preliminary note on the treatment of vertebral angioma by percutaneous acrylic vertebroplasty]. *Neurochirurgie.* **33**, 166–8 (1987).
106. Cortet, B. *et al.* Percutaneous vertebroplasty in the treatment of osteoporotic vertebral compression fractures: an open prospective study. *J. Rheumatol.* **26**, 2222–8 (1999).
107. McGraw, J. K. *et al.* Society of Interventional Radiology quality improvement guidelines for percutaneous vertebroplasty. *J. Vasc. Interv. Radiol.* **14**, 827–31 (2003).
108. A. Hardinger, S. & Wijaya, N. A mild method for rapid tert-butylphenylsilylation of primary and secondary alcohols. *Tetrahedron Lett.* **34**, 3821–3824 (1993).
109. CHARNLEY, J. THE BONDING OF PROSTHESES TO BONE BY CEMENT. *J. Bone Joint Surg. Br.* **46**, 518–29 (1964).
110. Pasquier, G., Hardouin, P., Fontaine, C., Migaud, H. & Duquennoy, A. [Different methods of bone filling in orthopedic surgery]. *Rev. Rhum. Mal. Osteoartic.* **59**, 821–8 (1992).
111. Lieberman, I. H., Togawa, D. & Kayanja, M. M. Vertebroplasty and kyphoplasty: filler materials. *Spine J.* **5**, S305–S316 (2005).
112. Nguyen, L. H. *et al.* Vascularized bone tissue engineering: approaches for potential improvement. *Tissue Eng. Part B. Rev.* **18**, 363–82 (2012).
113. Saijo, H. *et al.* Maxillofacial reconstruction using custom-made artificial bones fabricated by inkjet printing technology. *J. Artif. Organs* **12**, 200–205 (2009).
114. Bohner, M. Calcium orthophosphates in medicine: from ceramics to calcium phosphate cements. *Injury* **31 Suppl 4**, 37–47 (2000).
115. Hak, D. J. The use of osteoconductive bone graft substitutes in orthopaedic trauma. *J. Am. Acad. Orthop.*

- Surg.* **15**, 525–36 (2007).
116. Oonishi, H. *et al.* Hydroxyapatite in revision of total hip replacements with massive acetabular defects: 4- to 10-year clinical results. *J. Bone Joint Surg. Br.* **79**, 87–92 (1997).
 117. Yamamoto, T., Onga, T., Marui, T. & Mizuno, K. Use of hydroxyapatite to fill cavities after excision of benign bone tumours. Clinical results. *J. Bone Joint Surg. Br.* **82**, 1117–20 (2000).
 118. Zijderfeld, S. A., Zerbo, I. R., van den Bergh, J. P. A., Schulten, E. A. J. M. & ten Bruggenkate, C. M. Maxillary sinus floor augmentation using a beta-tricalcium phosphate (Cerasorb) alone compared to autogenous bone grafts. *Int. J. Oral Maxillofac. Implants* **20**, 432–40
 119. Daculsi, G., LeGeros, R. Z., Heughebaert, M. & Barbieux, I. Formation of carbonate-apatite crystals after implantation of calcium phosphate ceramics. *Calcif. Tissue Int.* **46**, 20–7 (1990).
 120. Nandi, S. K., Kundu, B., Ghosh, S. K., De, D. K. & Basu, D. Efficacy of nano-hydroxyapatite prepared by an aqueous solution combustion technique in healing bone defects of goat. *J. Vet. Sci.* **9**, 183 (2008).
 121. Cesarano, J. *et al.* Customization of Load-Bearing Hydroxyapatite Lattice Scaffolds. *Int. J. Appl. Ceram. Technol.* **2**, 212–220 (2005).
 122. Kohri, M., Miki, K., Waite, D. E., Nakajima, H. & Okabe, T. In vitro stability of biphasic calcium phosphate ceramics. *Biomaterials* **14**, 299–304 (1993).
 123. Gauthier, O., Bouler, J. M., Aguado, E., Pilet, P. & Daculsi, G. Macroporous biphasic calcium phosphate ceramics: influence of macropore diameter and macroporosity percentage on bone ingrowth. *Biomaterials* **19**, 133–9
 124. Ransford, A. O. *et al.* Synthetic porous ceramic compared with autograft in scoliosis surgery. A prospective, randomized study of 341 patients. *J. Bone Joint Surg. Br.* **80**, 13–8 (1998).
 125. Delécrin, J., Takahashi, S., Gouin, F. & Passuti, N. A synthetic porous ceramic as a bone graft substitute in the surgical management of scoliosis: a prospective, randomized study. *Spine (Phila. Pa. 1976)*. **25**, 563–9 (2000).
 126. Bohner, M. Design of ceramic-based cements and putties for bone graft substitution. *Eur. Cell. Mater.* **20**, 1–12 (2010).
 127. Brown, W. E. & Chow, L. C. Dental restorative cement pastes. (1985).
 128. Ginebra, M., Canal, C., Pastorino, D. & Montufar, E. B. Calcium phosphate cements as drug delivery materials ☆. *Adv. Drug Deliv. Rev.* **64**, 1090–1110 (2012).
 129. Passuti, N. & Gouin, F. Antibiotic-loaded bone cement in orthopedic surgery. *Joint. Bone. Spine* **70**, 169–74 (2003).
 130. Friedman, C. D., Costantino, P. D., Takagi, S. & Chow, L. C. BoneSource hydroxyapatite cement: a novel biomaterial for craniofacial skeletal tissue engineering and reconstruction. *J. Biomed. Mater. Res.* **43**, 428–32 (1998).
 131. Constantz, B. *et al.* Skeletal repair by in situ formation of the mineral phase of bone. *Science (80-.)*. **267**, 1796–1799 (1995).
 132. Apelt, D. *et al.* In vivo behavior of three different injectable hydraulic calcium phosphate cements. *Biomaterials* **25**, 1439–51
 133. Sarkar, M. R., Wachter, N., Patka, P. & Kinzl, L. First histological observations on the incorporation of a novel calcium phosphate bone substitute material in human cancellous bone. *J. Biomed. Mater. Res.* **58**,

- 329–334 (2001).
134. Brown, P. W. & Fulmer, M. Kinetics of Hydroxyapatite Formation at Low Temperature. *J. Am. Ceram. Soc.* **74**, 934–940 (1991).
135. Constantz, B. R. *et al.* Histological, chemical, and crystallographic analysis of four calcium phosphate cements in different rabbit osseous sites. *J. Biomed. Mater. Res.* **43**, 451–61 (1998).
136. Montufar, E. B. *et al.* Self-hardening calcium deficient hydroxyapatite/gelatine foams for bone regeneration. *J. Mater. Sci. Mater. Med.* **21**, 863–869 (2010).
137. MORGAN, E. F., YETKINLER, D. N., CONSTANTZ, B. R. & DAUSKARDT, R. H. Mechanical properties of carbonated apatite bone mineral substitute: strength, fracture and fatigue behaviour. *J. Mater. Sci. Mater. Med.* **8**, 559–570 (1997).
138. Ginebra, M.-P., Fernández, E., Driessens, F. C. M. & Planell, J. A. Modeling of the Hydrolysis of α -Tricalcium Phosphate. *J. Am. Ceram. Soc.* **82**, 2808–2812 (2004).
139. Ginebra, M. P. *et al.* Setting Reaction and Hardening of an Apatitic Calcium Phosphate Cement. *J. Dent. Res.* **76**, 905–912 (1997).
140. Brown. Dental resporative cement pastes. (1983).
141. Dorozhkin, S. V. Self-setting calcium orthophosphate formulations. *J. Funct. Biomater.* **4**, 209–311 (2013).
142. Lewis, G. Injectable bone cements for use in vertebroplasty and kyphoplasty: State-of-the-art review. *J. Biomed. Mater. Res. Part B Appl. Biomater.* **76B**, 456–468 (2006).
143. Drury, J. L. & Mooney, D. J. Hydrogels for tissue engineering: scaffold design variables and applications. *Biomaterials* **24**, 4337–51 (2003).
144. Van Vlierberghe, S., Dubrue, P. & Schacht, E. Biopolymer-Based Hydrogels As Scaffolds for Tissue Engineering Applications: A Review. *Biomacromolecules* **12**, 1387–1408 (2011).
145. Liu, X. & Ma, P. X. Polymeric Scaffolds for Bone Tissue Engineering. *Ann. Biomed. Eng.* **32**, 477–486 (2004).
146. Roseti, L. *et al.* Scaffolds for Bone Tissue Engineering: State of the art and new perspectives. *Mater. Sci. Eng. C* **78**, 1246–1262 (2017).
147. Cordonnier, T., Sohier, J., Rosset, P. & Layrolle, P. Biomimetic Materials for Bone Tissue Engineering - State of the Art and Future Trends. *Adv. Eng. Mater.* **13**, B135–B150 (2011).
148. Agrawal, C. M. & Ray, R. B. Biodegradable polymeric scaffolds for musculoskeletal tissue engineering. *J. Biomed. Mater. Res.* **55**, 141–150 (2001).
149. Zhu, N. & Che, X. Biofabrication of Tissue Scaffolds. in *Advances in Biomaterials Science and Biomedical Applications* (InTech, 2013). doi:10.5772/54125
150. Nam, Y. S. & Park, T. G. Porous biodegradable polymeric scaffolds prepared by thermally induced phase separation. *J. Biomed. Mater. Res.* **47**, 8–17 (1999).
151. Harris, L. D., Kim, B.-S. & Mooney, D. J. Open pore biodegradable matrices formed with gas foaming. *J. Biomed. Mater. Res.* **42**, 396–402 (1998).
152. Sill, T. J. & von Recum, H. A. Electrospinning: Applications in drug delivery and tissue engineering. *Biomaterials* (2008). doi:10.1016/j.biomaterials.2008.01.011
153. Bajaj, P., Schweller, R. M., Khademhosseini, A., West, J. L. & Bashir, R. 3D Biofabrication Strategies

- for Tissue Engineering and Regenerative Medicine. *Annu. Rev. Biomed. Eng.* **16**, 247–276 (2014).
154. Jariwala, S. H., Lewis, G. S., Bushman, Z. J., Adair, J. H. & Donahue, H. J. 3D Printing of Personalized Artificial Bone Scaffolds. *3D Print. Addit. Manuf.* **2**, 56–64 (2015).
 155. Cima, S. M. *et al.* *Three Dimensional Printing: Rapid Tooling and Prototypes Directly from CAD Representation.*
 156. Lee, J. W., Kim, J. Y. & Cho, D.-W. Solid Free-form Fabrication Technology and Its Application to Bone Tissue Engineering. *Int. J. stem cells* **3**, 85–95 (2010).
 157. Abou Neel, E. A., Chrzanowski, W., Salih, V. M., Kim, H.-W. & Knowles, J. C. Tissue engineering in dentistry. *J. Dent.* **42**, 915–928 (2014).
 158. Noorani, R. *Rapid prototyping : principles and applications.* (Wiley, 2006).
 159. Apparatus for production of three-dimensional objects by stereolithography. (1984).
 160. Murphy, S. V. & Atala, A. 3D bioprinting of tissues and organs. *Nat. Biotechnol.* **32**, 773–785 (2014).
 161. Sawkins, M. J. *et al.* Cell and protein compatible 3D bioprinting of mechanically strong constructs for bone repair. *Biofabrication* **7**, 35004 (2015).
 162. Seol, Y.-J., Kang, H.-W., Lee, S. J., Atala, A. & Yoo, J. J. Bioprinting technology and its applications. *Eur. J. Cardio-Thoracic Surg.* **46**, 342–348 (2014).
 163. Ozbolat, I. T. & Yin Yu, Y. Bioprinting Toward Organ Fabrication: Challenges and Future Trends. *IEEE Trans. Biomed. Eng.* **60**, 691–699 (2013).
 164. Obregon, F., Vaquette, C., Ivanovski, S., Hutmacher, D. W. & Bertassoni, L. E. Three-Dimensional Bioprinting for Regenerative Dentistry and Craniofacial Tissue Engineering. *J. Dent. Res.* **94**, 143S–152S (2015).
 165. Mandrycky, C., Wang, Z., Kim, K. & Kim, D.-H. 3D bioprinting for engineering complex tissues. *Biotechnol. Adv.* **34**, 422–434 (2016).
 166. Murphy, S. V & Atala, A. 3D bioprinting of tissues and organs. *Nat. Biotechnol.* **32**, 773 (2014).
 167. Reddy Bathula, I. S. 3D Printing for Foot. *MOJ Proteomics Bioinforma.* **5**, (2017).
 168. Zein, I., Hutmacher, D. W., Tan, K. C. & Teoh, S. H. Fused deposition modeling of novel scaffold architectures for tissue engineering applications. *Biomaterials* **23**, 1169–1185 (2002).
 169. Zeng, Y. *et al.* 3D printing of hydroxyapatite scaffolds with good mechanical and biocompatible properties by digital light processing. *J. Mater. Sci.* (2018). doi:10.1007/s10853-018-1992-2
 170. Zhang, X., Jiang, X. N. & Sun, C. *Micro-stereolithography of polymeric and ceramic microstructures. Sensors and Actuators* **77**,
 171. Chia, H. N. & Wu, B. M. Recent advances in 3D printing of biomaterials. *J. Biol. Eng.* **9**, 4 (2015).
 172. Heller, C. *et al.* Vinyl esters: Low cytotoxicity monomers for the fabrication of biocompatible 3D scaffolds by lithography based additive manufacturing. *J. Polym. Sci. Part A Polym. Chem.* **47**, 6941–6954 (2009).
 173. Melchels, F. P. W., Feijen, J. & Grijpma, D. W. A review on stereolithography and its applications in biomedical engineering. *Biomaterials* **31**, 6121–6130 (2010).
 174. Poh, P. S. P. *et al.* Polylactides in additive biomanufacturing. *Adv. Drug Deliv. Rev.* **107**, 228–246 (2016).
 175. Hamad, K., Kaseem, M., Yang, H. W., Deri, F. & Ko, Y. G. Properties and medical applications of

- polylactic acid: A review. *Express Polym. Lett.* **9**, (2015).
176. Mills, D. *et al.* Antibiotic and chemotherapeutic enhanced three-dimensional printer filaments and constructs for biomedical applications. *Int. J. Nanomedicine* **357** (2015). doi:10.2147/IJN.S74811
177. Narayanan, G., Vernekar, V. N., Kuyinu, E. L. & Laurencin, C. T. Poly (lactic acid)-based biomaterials for orthopaedic regenerative engineering. *Adv. Drug Deliv. Rev.* **107**, 247–276 (2016).
178. Lim, L.-T., Auras, R. & Rubino, M. Processing technologies for poly(lactic acid). *Prog. Polym. Sci.* **33**, 820–852 (2008).
179. Garlotta, D. A Literature Review of Poly(Lactic Acid). *J. Polym. Environ.* **9**, 63–84 (2001).
180. Masutani, K. & Kimura, Y. Chapter 1. PLA Synthesis. From the Monomer to the Polymer. in 1–36 (2014). doi:10.1039/9781782624806-00001
181. Lunt, J. Large-scale production, properties and commercial applications of polylactic acid polymers. *Polym. Degrad. Stab.* **59**, 145–152 (1998).
182. Tyler, B., Gullotti, D., Mangraviti, A., Utsuki, T. & Brem, H. Polylactic acid (PLA) controlled delivery carriers for biomedical applications. *Adv. Drug Deliv. Rev.* **107**, 163–175 (2016).
183. Messias, A. D., Lucchesi, C., Coraça-Huber, D. C., Pavani Filho, A. & Duek, E. A. R. Lithograph-moulded poly-L-co-D,L lactide porous membranes for osteoblastic culture. *Mater. Res.* **17**, 7–15 (2013).
184. Chhaya, M. P., Melchels, F. P. W., Holzapfel, B. M., Baldwin, J. G. & Huttmacher, D. W. Sustained regeneration of high-volume adipose tissue for breast reconstruction using computer aided design and biomanufacturing. *Biomaterials* **52**, 551–560 (2015).
185. Han, S. *et al.* Nanoparticle carriers based on copolymers of poly(l-aspartic acid co-l-lactide)-1,2-dipalmitoyl-sn-glycero-3-phosphoethanolamine for drug delivery. *J. Nanoparticle Res.* **13**, 4371–4385 (2011).
186. Serra, T., Planell, J. A. & Navarro, M. High-resolution PLA-based composite scaffolds via 3-D printing technology. *Acta Biomater.* **9**, 5521–5530 (2013).
187. Serra, T., Mateos-Timoneda, M. A., Planell, J. A. & Navarro, M. 3D printed PLA-based scaffolds: A versatile tool in regenerative medicine. *Organogenesis* **9**, 239–244 (2013).
188. Charles-Harris, M. *et al.* A PLA/calcium phosphate degradable composite material for bone tissue engineering: an in vitro study. *J. Mater. Sci. Mater. Med.* **19**, 1503–1513 (2008).
189. Kilian, K. A., Bugarija, B., Lahn, B. T. & Mrksich, M. Geometric cues for directing the differentiation of mesenchymal stem cells. *Proc. Natl. Acad. Sci.* **107**, 4872–4877 (2010).
190. Yang, E. *et al.* Bio-Based Polymers for 3D Printing of Bioscaffolds. *Polym. Rev.* **58**, 668–687 (2018).
191. Rosenzweig, D. H., Carelli, E., Steffen, T., Jarzem, P. & Haglund, L. 3D-printed ABS and PLA scaffolds for cartilage and nucleus pulposustissue regeneration. *Int. J. Mol. Sci.* **16**, 15118–15135 (2015).
192. Kasper, F. K., Tanahashi, K., Fisher, J. P. & Mikos, A. G. Synthesis of poly(propylene fumarate). *Nat. Protoc.* **4**, 518–525 (2009).
193. Fisher, J. P., Holland, T. A., Dean, D. & Mikos, A. G. Photoinitiated Cross-Linking of the Biodegradable Polyester Poly(propylene fumarate). Part II. In Vitro Degradation. *Biomacromolecules* **4**, 1335–1342 (2003).
194. Kharas, G. B. *et al.* Synthesis and characterization of fumarate-based polyesters for use in bioresorbable bone cement composites. *J. Appl. Polym. Sci.* **66**, 1123–1137 (1997).

195. Gunatillake, P. A. & Adhikari, R. Biodegradable synthetic polymers for tissue engineering. *Eur. Cell. Mater.* **5**, 1–16; discussion 16 (2003).
196. Shanfeng Wang, Lichun Lu, and & Yaszemski*, M. J. Bone-Tissue-Engineering Material Poly(propylene fumarate): Correlation between Molecular Weight, Chain Dimensions, and Physical Properties. (2006). doi:10.1021/BM060096A
197. Timmer, M. D., Carter, C., Ambrose, C. G. & Mikos, A. G. Fabrication of poly(propylene fumarate)-based orthopaedic implants by photo-crosslinking through transparent silicone molds. *Biomaterials* **24**, 4707–14 (2003).
198. Cooke, M. N., Fisher, J. P., Dean, D., Rimnac, C. & Mikos, A. G. Use of stereolithography to manufacture critical-sized 3D biodegradable scaffolds for bone ingrowth. *J. Biomed. Mater. Res.* **64B**, 65–69 (2003).
199. Hacker, M. C. *et al.* Biodegradable fumarate-based drug-delivery systems for ophthalmic applications. *J. Biomed. Mater. Res. Part A* **88A**, 976–989 (2009).
200. Payne, R. G., McGonigle, J. S., Yaszemski, M. J., Yasko, A. W. & Mikos, A. G. Development of an injectable, in situ crosslinkable, degradable polymeric carrier for osteogenic cell populations. Part 3. Proliferation and differentiation of encapsulated marrow stromal osteoblasts cultured on crosslinking poly(propylene fumarate). *Biomaterials* **23**, 4381–7 (2002).
201. Payne, R. G., McGonigle, J. S., Yaszemski, M. J., Yasko, A. W. & Mikos, A. G. Development of an injectable, in situ crosslinkable, degradable polymeric carrier for osteogenic cell populations. Part 2. Viability of encapsulated marrow stromal osteoblasts cultured on crosslinking poly(propylene fumarate). *Biomaterials* **23**, 4373–80 (2002).
202. Lee, K.-W. *et al.* Poly(propylene fumarate) Bone Tissue Engineering Scaffold Fabrication Using Stereolithography: Effects of Resin Formulations and Laser Parameters. *Biomacromolecules* **8**, 1077–1084 (2007).
203. Fisher, J. P., Dean, D. & Mikos, A. G. Photocrosslinking characteristics and mechanical properties of diethyl fumarate/poly(propylene fumarate) biomaterials. *Biomaterials* **23**, 4333–43 (2002).
204. Hinczewski, C., Corbel, S. & Chartier, T. Ceramic suspensions suitable for stereolithography. *J. Eur. Ceram. Soc.* **18**, 583–590 (1998).
205. Diez-Pascual, A. M. Tissue engineering bionanocomposites based on poly(propylene fumarate). *Polymers (Basel)* **9**, 1–19 (2017).
206. Rezwani, K., Chen, Q. Z., Blaker, J. J. & Boccaccini, A. R. Biodegradable and bioactive porous polymer/inorganic composite scaffolds for bone tissue engineering. *Biomaterials* **27**, 3413–3431 (2006).
207. Bose, S., Roy, M. & Bandyopadhyay, A. Recent advances in bone tissue engineering scaffolds. *Trends Biotechnol.* **30**, 546–554 (2012).
208. Kim, H., Abdala, A. A. & Macosko, C. W. Polymer Nanocomposites with Graphene. *Young* 1–13 (2010). doi:10.1021/ma100572e
209. Kumar, A., Rao, T. V., Chowdhury, S. R. & Reddy, S. V. S. R. Compatibility confirmation and refinement of thermal and mechanical properties of poly (lactic acid)/poly (ethylene-co-glycidyl methacrylate) blend reinforced by hexagonal boron nitride. *React. Funct. Polym.* **117**, 1–9 (2017).
210. Zhang, Q. *et al.* Fluorescent PLLA-nanodiamond composites for bone tissue engineering. *Biomaterials* **32**, 87–94 (2011).
211. Ceccarelli, G. *et al.* Emerging Perspectives in Scaffold for Tissue Engineering in Oral Surgery. *Stem Cells Int.* **2017**, 1–11 (2017).
212. Senatov, F. S. *et al.* Mechanical properties and shape memory effect of 3D-printed PLA-based porous scaffolds. *J. Mech. Behav. Biomed. Mater.* **57**, 139–148 (2016).
213. Cui, H., Zhu, W., Holmes, B. & Zhang, L. G. Biologically Inspired Smart Release System Based on 3D Bioprinted Perfused Scaffold for Vascularized Tissue Regeneration. *Adv. Sci.* **3**, 1600058 (2016).
214. Kao, C. T. *et al.* Poly(dopamine) coating of 3D printed poly(lactic acid) scaffolds for bone tissue engineering. *Mater. Sci. Eng. C* **56**, 165–173 (2015).

215. Melchels, F. P. W., Feijen, J. & Grijpma, D. W. A poly(d,l-lactide) resin for the preparation of tissue engineering scaffolds by stereolithography. *Biomaterials* **30**, 3801–3809 (2009).
216. Ronca, A., Ambrosio, L. & Grijpma, D. W. Preparation of designed poly(d,l-lactide)/nanosized hydroxyapatite composite structures by stereolithography. *Acta Biomaterialia* **9**, 5989–5996 (2013).
217. Shrivats, A. R., McDermott, M. C. & Hollinger, J. O. Bone tissue engineering: state of the union. *Drug Discov. Today* **19**, 781–786 (2014).
218. Cai, Z.-Y. *et al.* Poly(propylene fumarate)/(calcium sulphate/ β -tricalcium phosphate) composites: Preparation, characterization and in vitro degradation. *Acta Biomater.* **5**, 628–635 (2009).
219. Lan, P. X., Lee, J. W., Seol, Y.-J. & Cho, D.-W. Development of 3D PPF/DEF scaffolds using micro-stereolithography and surface modification. *J. Mater. Sci. Mater. Med.* **20**, 271–279 (2009).
220. Farsari, M. *et al.* Three-dimensional biomolecule patterning. *Appl. Surf. Sci.* **253**, 8115–8118 (2007).
221. Northen, T. R., Brune, D. C. & Woodbury, N. W. Synthesis and Characterization of Peptide Grafted Porous Polymer Microstructures. *Biomacromolecules* **7**, 750–754 (2006).
222. Shin, J. H., Lee, J. W., Jung, J. H., Cho, D.-W. & Lim, G. Evaluation of cell proliferation and differentiation on a poly(propylene fumarate) 3D scaffold treated with functional peptides. *J. Mater. Sci.* **46**, 5282–5287 (2011).
223. Lee, J. W. *et al.* Bone regeneration using a microstereolithography-produced customized poly(propylene fumarate)/diethyl fumarate photopolymer 3D scaffold incorporating BMP-2 loaded PLGA microspheres. *Biomaterials* **32**, 744–752 (2011).
224. Díez-Pascual, A. M. & Díez-Vicente, A. L. PEGylated boron nitride nanotube-reinforced poly(propylene fumarate) nanocomposite biomaterials. *RSC Adv.* **6**, 79507–79519 (2016).
225. Díez-Pascual, A. M. & Díez-Vicente, A. L. Poly(propylene fumarate)/Polyethylene Glycol-Modified Graphene Oxide Nanocomposites for Tissue Engineering. *ACS Appl. Mater. Interfaces* **8**, 17902–17914 (2016).
226. Pinto, A. M. *et al.* Biocompatibility of poly (lactic acid) with incorporated graphene-based materials. *Colloids Surfaces B Biointerfaces* **104**, 229–238 (2013).
227. Guiney, L. M. *et al.* Three-Dimensional Printing of Cytocompatible, Thermally Conductive Hexagonal Boron Nitride Nanocomposites. *Nano Lett.* **18**, 3488–3493 (2018).
228. Novoselov, K. S. *et al.* Electric Field Effect in Atomically Thin Carbon Films. *Phys. Rev. Lett* **404**, (Kluwer, 2000).
229. Lee, C., Wei, X., Kysar, J. W. & Hone, J. Measurement of the elastic properties and intrinsic strength of monolayer graphene. *Science* (80-.). **321**, 385–388 (2008).
230. Geim, A. K. Graphene : Status and Prospects. **1530**, 1530–1535 (2010).
231. Stankovich, S. *et al.* Graphene-based composite materials. *Nature* **442**, 282–286 (2006).
232. Zhu, Y. *et al.* Graphene and graphene oxide: Synthesis, properties, and applications. *Adv. Mater.* **22**, 3906–3924 (2010).
233. Gao, W. The chemistry of graphene oxide. *Graphene Oxide Reduct. Recipes, Spectrosc. Appl.* 61–95 (2015). doi:10.1007/978-3-319-15500-5_3
234. Maiti, D., Tong, X., Mou, X. & Yang, K. Carbon-Based Nanomaterials for Biomedical Applications: A Recent Study. *Front. Pharmacol.* **9**, 1–16 (2019).
235. Chen, Q. *et al.* 3D printing biocompatible polyurethane/poly(lactic acid)/graphene oxide nanocomposites: Anisotropic properties. *ACS Appl. Mater. Interfaces* **9**, 4015–4023 (2017).
236. Papageorgiou, D. G., Kinloch, I. A. & Young, R. J. Mechanical properties of graphene and graphene-based nanocomposites. *Prog. Mater. Sci.* **90**, 75–127 (2017).
237. Ryoo, S.-R. *et al.* Biomedical Applications of Graphene and Graphene Oxide. *Acc. Chem. Res.* **46**, 2211–2224 (2013).
238. Nanda, S. S., Papaefthymiou, G. C. & Yi, D. K. Functionalization of Graphene Oxide and its Biomedical Applications. *Crit. Rev. Solid State Mater. Sci.* **40**, 291–315 (2015).
239. Ana, M. D. & Angel, L. D. Poly (propylene fumarate)/ Polyethylene Glycol-Modified Graphene Oxide Nanocomposites for Tissue Engineering. (2016). doi:10.1021/acsami.6b05635
240. Ciofani, G., Raffa, V., Menciassi, A. & Cuschieri, A. Boron nitride nanotubes: An innovative tool for nanomedicine. *Nano Today* (2009). doi:10.1016/j.nantod.2008.09.001
241. Golberg, D. *et al.* Boron nitride nanotubes and nanosheets. *ACS Nano* (2010). doi:10.1021/nn1006495

242. Biscarat, J., Bechelany, M., Pochat-Bohatier, C. & Miele, P. Graphene-like BN/gelatin nanobiocomposites for gas barrier applications. *Nanoscale* **7**, 613–618 (2015).
243. Lahiri, D. *et al.* Boron nitride nanotube reinforced polylactide–polycaprolactone copolymer composite: mechanical properties and cytocompatibility with osteoblasts and macrophages in vitro. *Acta Biomater.* **6**, 3524–3533 (2010).
244. Ciofani, G., Raffa, V., Mencias, A. & Cuschieri, A. Cytocompatibility, interactions, and uptake of polyethyleneimine-coated boron nitride nanotubes by living cells: Confirmation of their potential for biomedical applications. *Biotechnol. Bioeng.* **101**, 850–858 (2008).
245. I. Scorei, R. & Popa, R. Boron-Containing Compounds as Preventive and Chemotherapeutic Agents for Cancer. *Anticancer. Agents Med. Chem.* **10**, 346–351 (2012).
246. Weng, Q. *et al.* Highly water-soluble, porous, and biocompatible boron nitrides for anticancer drug delivery. *ACS Nano* **8**, 6123–6130 (2014).
247. Li, X. *et al.* Boron nitride nanotube-enhanced osteogenic differentiation of mesenchymal stem cells. *J. Biomed. Mater. Res. - Part B Appl. Biomater.* (2016). doi:10.1002/jbm.b.33391
248. Salvetti, A. *et al.* In vivo biocompatibility of boron nitride nanotubes: Effects on stem cell biology and tissue regeneration in planarians. *Nanomedicine* (2015). doi:10.2217/nnm.15.46
249. Liu, J., Li, W., Guo, Y., Zhang, H. & Zhang, Z. Improved thermal conductivity of thermoplastic polyurethane via aligned boron nitride platelets assisted by 3D printing. *Compos. Part A Appl. Sci. Manuf.* **120**, 140–146 (2019).
250. Quill, T. J. *et al.* Thermal and mechanical properties of 3D printed boron nitride – ABS composites. *Appl. Compos. Mater.* **25**, 1205–1217 (2018).
251. Bustillos, J., Montero-Zambrano, D., Loganathan, A., Boesl, B. & Agarwal, A. Stereolithography-based 3D printed photosensitive polymer/boron nitride nanoplatelets composites. *Polym. Compos.* **40**, 379–388 (2019).
252. Dorozhkin, S. V. *Journal of materials science. Journal of Materials Science* **43**, (Chapman & Hall).
253. Takagi, S. & Chow, L. C. Formation of macropores in calcium phosphate cement implants. *J. Mater. Sci. Mater. Med.* **12**, 135–9 (2001).
254. Karageorgiou, V. & Kaplan, D. Porosity of 3D biomaterial scaffolds and osteogenesis. *Biomaterials* **26**, 5474–5491 (2005).
255. Espanol, M. *et al.* Intrinsic porosity of calcium phosphate cements and its significance for drug delivery and tissue engineering applications. *Acta Biomater.* **5**, 2752–2762 (2009).
256. Ginebra, M. P., Espanol, M., Montufar, E. B., Perez, R. A. & Mestres, G. New processing approaches in calcium phosphate cements and their applications in regenerative medicine. *Acta Biomater.* **6**, 2863–2873 (2010).
257. Combes, C., Bareille, R. & Rey, C. Calcium carbonate–calcium phosphate mixed cement compositions for bone reconstruction. *J. Biomed. Mater. Res. Part A* **79A**, 318–328 (2006).
258. Joseph D. Bronzino. *The Biomedical Engineering Handbook, Second Edition. 2 Volume Set : Joseph D. Bronzino : 9780849385940.*
259. Habraken, W. J. E. M. *et al.* Introduction of gelatin microspheres into an injectable calcium phosphate cement. *J. Biomed. Mater. Res. Part A* **87A**, 643–655 (2008).
260. Li, M., Liu, X., Liu, X., Ge, B. & Chen, K. Creation of macroporous calcium phosphate cements as bone substitutes by using genipin-crosslinked gelatin microspheres. *J. Mater. Sci. Mater. Med.* **20**, 925–934 (2009).
261. Habraken, W. J. E. M. *et al.* Introduction of enzymatically degradable poly(trimethylene carbonate) microspheres into an injectable calcium phosphate cement. *Biomaterials* **29**, 2464–2476 (2008).
262. Liao, H. *et al.* Injectable calcium phosphate cement with PLGA, gelatin and PTMC microspheres in a rabbit femoral defect. *Acta Biomater.* **7**, 1752–1759 (2011).
263. Simon, C. G., Khatri, C. A., Wight, S. A. & Wang, F. W. Preliminary report on the biocompatibility of a moldable, resorbable, composite bone graft consisting of calcium phosphate cement and poly(lactide-co-glycolide) microspheres. *J. Orthop. Res.* **20**, 473–482 (2002).
264. Qi, X. & Ye, J. Mechanical and rheological properties and injectability of calcium phosphate cement containing poly (lactic-co-glycolic acid) microspheres. *Mater. Sci. Eng. C* **29**, 1901–1906 (2009).

265. Qi, X., Ye, J. & Wang, Y. Improved injectability and in vitro degradation of a calcium phosphate cement containing poly(lactide-co-glycolide) microspheres. *Acta Biomater.* **4**, 1837–45 (2008).
266. Fei, Z. *et al.* Preparation and property of a novel bone graft composite consisting of rhBMP-2 loaded PLGA microspheres and calcium phosphate cement. *J. Mater. Sci. Mater. Med.* **19**, 1109–1116 (2008).
267. Schnieders, J., Gbureck, U., Thull, R. & Kissel, T. Controlled release of gentamicin from calcium phosphate—poly(lactic acid-co-glycolic acid) composite bone cement. *Biomaterials* **27**, 4239–4249 (2006).
268. Ruhé, P. Q. *et al.* Porous Poly(DL-lactic- co -glycolic acid)/Calcium Phosphate Cement Composite for Reconstruction of Bone Defects. *Tissue Eng.* **12**, 789–800 (2006).
269. Khan, W. *et al.* Antibiotics Delivery for Treating Bone Infections. in 459–472 (Springer, Boston, MA, 2014). doi:10.1007/978-1-4614-9434-8_21
270. Li, Y.-H. *et al.* The biocompatibility of calcium phosphate cements containing alendronate-loaded PLGA microparticles *in vitro*. *Exp. Biol. Med.* **240**, 1465–1471 (2015).
271. Zhou, Z., Kennell, C., Lee, J.-Y., Leung, Y.-K. & Tarapore, P. Calcium phosphate-polymer hybrid nanoparticles for enhanced triple negative breast cancer treatment via co-delivery of paclitaxel and miR-221/222 inhibitors. *Nanomedicine Nanotechnology, Biol. Med.* **13**, 403–410 (2017).
272. Shi, J., Votruba, A. R., Farokhzad, O. C. & Langer, R. Nanotechnology in drug delivery and tissue engineering: from discovery to applications. *Nano Lett.* **10**, 3223–30 (2010).
273. Wagner, V., Dullaart, A., Bock, A.-K. & Zweck, A. The emerging nanomedicine landscape. *Nat. Biotechnol.* **24**, 1211–1217 (2006).
274. Zhang, L. *et al.* Nanoparticles in Medicine: Therapeutic Applications and Developments. *Clin. Pharmacol. Ther.* **83**, 761–769 (2008).
275. Davis, M. E., Chen, Z. & Shin, D. M. Nanoparticle therapeutics: an emerging treatment modality for cancer. *Nat. Rev. Drug Discov.* **7**, 771–782 (2008).
276. Riehemann, K. *et al.* Nanomedicine-Challenge and Perspectives. *Angew. Chemie Int. Ed.* **48**, 872–897 (2009).
277. Zhang, S. & Uludağ, H. Nanoparticulate Systems for Growth Factor Delivery. *Pharm. Res.* **26**, 1561–1580 (2009).
278. Park, J., Ye, M. & Park, K. Biodegradable Polymers for Microencapsulation of Drugs. *Molecules* **10**, 146–161 (2005).
279. Sinha, V. R. & Trehan, A. Biodegradable microspheres for protein delivery. *J. Control. Release* **90**, 261–80 (2003).
280. Edgar, K. J. Cellulose esters in drug delivery. *Cellulose* **14**, 49–64 (2006).
281. Agnihotri, S. A., Mallikarjuna, N. N. & Aminabhavi, T. M. Recent advances on chitosan-based micro- and nanoparticles in drug delivery. *J. Control. Release* **100**, 5–28 (2004).
282. Kipper, M. J., Shen, E., Determan, A. & Narasimhan, B. Design of an injectable system based on bioerodible polyanhydride microspheres for sustained drug delivery. *Biomaterials* **23**, 4405–12 (2002).
283. Wang, C. *et al.* Molecularly engineered poly(ortho ester) microspheres for enhanced delivery of DNA vaccines. *Nat. Mater.* **3**, 190–196 (2004).
284. Lakshmi, S., Katti, D. S. & Laurencin, C. T. Biodegradable polyphosphazenes for drug delivery applications. *Adv. Drug Deliv. Rev.* **55**, 467–82 (2003).
285. Jain, R. A. The manufacturing techniques of various drug loaded biodegradable poly(lactide-co-glycolide) (PLGA) devices. *Biomaterials* **21**, 2475–90 (2000).
286. Mi, F.-L., Lin, Y.-M., Wu, Y.-B., Shyu, S.-S. & Tsai, Y.-H. Chitin/PLGA blend microspheres as a biodegradable drug-delivery system: phase-separation, degradation and release behavior. *Biomaterials* **23**, 3257–67 (2002).
287. Calandrelli, L. *et al.* Novel graft PLLA-based copolymers: Potential of their application to particle technology. *J. Biomed. Mater. Res.* **62**, 244–253 (2002).
288. Liu, J., Xiao, Y. & Allen, C. Polymer–drug compatibility: A guide to the development of delivery systems for the anticancer agent, ellipticine. *J. Pharm. Sci.* **93**, 132–143 (2004).
289. Kumari, A., Yadav, S. K. & Yadav, S. C. Biodegradable polymeric nanoparticles based drug delivery systems. *Colloids Surf. B. Biointerfaces* **75**, 1–18 (2010).
290. Varde, N. K. & Pack, D. W. Microspheres for controlled release drug delivery. *Expert Opin. Biol. Ther.*

- 4**, 35–51 (2004).
291. Freiberg, S. & Zhu, X. X. Polymer microspheres for controlled drug release. *Int. J. Pharm.* **282**, 1–18 (2004).
 292. Soppimath, K. S., Aminabhavi, T. M., Kulkarni, A. R. & Rudzinski, W. E. Biodegradable polymeric nanoparticles as drug delivery devices. *J. Control. Release* **70**, 1–20 (2001).
 293. McGinity & O'Donnell. Preparation of microspheres by the solvent evaporation technique. *Adv. Drug Deliv. Rev.* **28**, 25–42 (1997).
 294. Mano, J. F., Sousa, R. A., Boesel, L. F., Neves, N. M. & Reis, R. L. Bioinert, biodegradable and injectable polymeric matrix composites for hard tissue replacement: state of the art and recent developments. *Compos. Sci. Technol.* **64**, 789–817 (2004).
 295. Lin, H.-R., Kuo, C.-J., Yang, C. Y., Shaw, S.-Y. & Wu, Y.-J. Preparation of macroporous biodegradable PLGA scaffolds for cell attachment with the use of mixed salts as porogen additives. *J. Biomed. Mater. Res.* **63**, 271–279 (2002).
 296. Allison, S. D. Effect Of Structural Relaxation On The Preparation And Drug Release Behavior Of Poly(lactic-co-glycolic)acid Microparticle Drug Delivery Systems. *J. Pharm. Sci.* **97**, 2022–2035 (2008).
 297. Dawes, G. J. S. *et al.* Size effect of PLGA spheres on drug loading efficiency and release profiles. *J. Mater. Sci. Mater. Med.* **20**, 1089–1094 (2009).
 298. Kim, K. K. & Pack, D. W. Microspheres for Drug Delivery. in *BioMEMS and Biomedical Nanotechnology* 19–50 (Springer US). doi:10.1007/978-0-387-25842-3_2
 299. Edlund, U. & Albertsson, A.-C. Degradable Polymer Microspheres for Controlled Drug Delivery. in *Degradable Aliphatic Polyesters* 67–112 (Springer Berlin Heidelberg, 2002). doi:10.1007/3-540-45734-8_3
 300. Mu, L. & Feng, S. . Fabrication, characterization and in vitro release of paclitaxel (Taxol®) loaded poly (lactic-co-glycolic acid) microspheres prepared by spray drying technique with lipid/cholesterol emulsifiers. *J. Control. Release* **76**, 239–254 (2001).
 301. Ghalanbor, Z., Körber, M. & Bodmeier, R. Improved Lysozyme Stability and Release Properties of Poly(lactide-co-glycolide) Implants Prepared by Hot-Melt Extrusion. *Pharm. Res.* **27**, 371–379 (2010).
 302. Yang, Y.-Y., Chung, T.-S. & Ping Ng, N. Morphology, drug distribution, and in vitro release profiles of biodegradable polymeric microspheres containing protein fabricated by double-emulsion solvent extraction/evaporation method. *Biomaterials* **22**, 231–241 (2001).
 303. Hickey, T., Kreutzer, D., Burgess, D. J. & Moussy, F. In vivo evaluation of a dexamethasone/PLGA microsphere system designed to suppress the inflammatory tissue response to implantable medical devices. *J. Biomed. Mater. Res.* **61**, 180–187 (2002).
 304. Bilati, U., Allémann, E. & Doelker, E. Strategic approaches for overcoming peptide and protein instability within biodegradable nano- and microparticles. *Eur. J. Pharm. Biopharm.* **59**, 375–388 (2005).
 305. Poudyal, A. P. & Soundrapandian, C. Microspheres for local drug delivery in bone joints. *J. Drug Deliv. Ther.* **9**, 719–725 (2019).
 306. Ramazani, F. *et al.* Strategies for encapsulation of small hydrophilic and amphiphilic drugs in PLGA microspheres: State-of-the-art and challenges. *Int. J. Pharm.* **499**, 358–367 (2016).
 307. Sansdrap, P. & Moës, A. J. Influence of manufacturing parameters on the size characteristics and the release profiles of nifedipine from poly(DL-lactide-co-glycolide) microspheres. *Int. J. Pharm.* **98**, 157–164 (1993).
 308. Anderson, J. M. & Shive, M. S. Biodegradation and biocompatibility of PLA and PLGA microspheres. *Adv. Drug Deliv. Rev.* **64**, 72–82 (2012).
 309. Ramchandani, M. & Robinson, D. In vitro and in vivo release of ciprofloxacin from PLGA 50:50 implants. *J. Control. Release* **54**, 167–75 (1998).
 310. Hirenkumar, M. & Steven, S. Poly Lactic-co-Glycolic Acid (PLGA) as Biodegradable Controlled Drug Delivery Carrier. *Polymers (Basel)*. **3**, 1–19 (2012).
 311. Wei, G., Pettway, G. J., McCauley, L. K. & Ma, P. X. The release profiles and bioactivity of parathyroid hormone from poly(lactic-co-glycolic acid) microspheres. *Biomaterials* **25**, 345–352 (2004).
 312. Schliecker, G., Schmidt, C., Fuchs, S., Wombacher, R. & Kissel, T. Hydrolytic degradation of

- poly(lactide-co-glycolide) films: effect of oligomers on degradation rate and crystallinity. *Int. J. Pharm.* **266**, 39–49 (2003).
313. Witt, C. & Kissel, T. Morphological characterization of microspheres, films and implants prepared from poly(lactide-co-glycolide) and ABA triblock copolymers: is the erosion controlled by degradation, swelling or diffusion? *Eur. J. Pharm. Biopharm.* **51**, 171–81 (2001).
314. Grizzi, I., Garreau, H., Li, S. & Vert, M. Hydrolytic degradation of devices based on poly(DL-lactic acid) size-dependence. *Biomaterials* **16**, 305–11 (1995).
315. Jaraswekin, S., Prakongpan, S. & Bodmeier, R. Effect of poly(lactide-co-glycolide) molecular weight on the release of dexamethasone sodium phosphate from microparticles. *J. Microencapsul.* **24**, 117–128 (2007).
316. Frank, A., Rath, S. K. & Venkatraman, S. S. Controlled release from bioerodible polymers: effect of drug type and polymer composition. *J. Control. Release* **102**, 333–344 (2005).
317. SIEGEL, S. *et al.* Effect of drug type on the degradation rate of PLGA matrices. *Eur. J. Pharm. Biopharm.* **64**, 287–293 (2006).
318. Holy, C. E., Dang, S. M., Davies, J. E. & Shoichet, M. S. In vitro degradation of a novel poly(lactide-co-glycolide) 75/25 foam. *Biomaterials* **20**, 1177–85 (1999).
319. Alexis, F. Factors affecting the degradation and drug-release mechanism of poly(lactic acid) and poly[(lactic acid)-co-(glycolic acid)]. *Polym. Int.* **54**, 36–46 (2005).

Part 2

Results and discussion

3D Printed Graphene Oxide-based Scaffolds for Bone Tissue Engineering

Habib Belaid^{1, 2}, Sakthivel Nagarajan¹, Catherine Teyssier², Jonathan Barés³, Sebastien Balme¹, Hélène Garay⁴, Vincent Huon³, David Cornu¹, Vincent Cavaillès^{2£} and Mikhael Bechelany^{1£}*

¹Institut Européen des Membranes, IEM-UMR 5635, Université Montpellier, CNRS, ENSCM, Montpellier, France

²IRCM, Institut de Recherche en Cancérologie de Montpellier, INSERM U1194, Université Montpellier, Montpellier F-34298, France

³LMGC, Laboratoire de Mécanique et Génie Civil, Univ Montpellier, CNRS, Montpellier, France

⁴C2MA, IMT mines d'Alès, France

* Corresponding author:

mikhael.bechelany@umontpellier.fr, Phone: +33467149167, Fax: +33467149119

£ Co-last authors

Keywords: polylactic acid, graphene oxide, bionanocomposite, 3D printing, tissue engineering

Abstract

The aim of this work was to develop a bioresorbable, biodegradable and biocompatible synthetic polymer with good mechanical properties for bone tissue engineering applications. Polylactic acid (PLA) scaffolds were generated by 3D printing using the fused deposition modelling method, and reinforced by incorporation of graphene oxide (GO). Morphological analysis by scanning electron microscopy indicated that the scaffold average pore size was between 400 and 500 μm . Topography imaging revealed a rougher surface upon GO incorporation ($S_a = 5.8 \mu\text{m}$ for PLA scaffolds, and of $9.9 \mu\text{m}$ for PLA scaffolds with 0.2% GO), and contact angle measurements showed a transition from a hydrophobic surface (pure PLA scaffolds) to a hydrophilic surface after GO incorporation. PLA thermomechanical properties were enhanced by GO incorporation, as shown by the 70°C increase of the degradation peak (thermal gravimetric analysis). However, GO incorporation did not change significantly the melting point assessed by differential scanning calorimetry. Physicochemical analyses by X-ray diffraction and Raman spectroscopy confirmed the filler presence. Tensile testing demonstrated that the mechanical properties were improved upon GO incorporation (30% increase of the Young's modulus with 0.3% GO). Cell viability, attachment, proliferation and differentiation assays using MG-63 osteosarcoma cells showed that PLA/GO scaffolds were biocompatible and that they promoted cell proliferation and mineralization more efficiently than pure PLA scaffolds. In conclusion, this new 3D printed nanocomposite is a promising scaffold with adequate mechanical properties and composition to support bone formation.

1. Introduction

For decades, bone disease management, for instance in osteoporosis, has been challenging due to the reduced bone self-repair capacity¹. Therefore, in patients with critical bone loss, fractures are treated by surgical implantation of a passive artificial junction called "scaffold", used to promote bone growth². In this approach, the scaffold morphology, chemical composition and physico-chemical properties play key roles because they must mimic the multi-scale structure of the bone extracellular matrix to allow cell adhesion, proliferation and differentiation^{3,4}. The scaffold mechanical properties, degradation and biocompatibility are directly influenced by the composition of the used material⁵.

To fabricate biomaterials suitable for bone regeneration, formulations based on biodegradable polylactic acid (PLA) polymers⁶ have been developed. PLA is made of dextrose extracted from bio-based materials, such as corn or cellulose⁷. It is routinely used for medical applications, for instance in sutures⁸ or orthopaedic fixation devices⁹. Unfortunately, biodegradable synthetic materials, such as PLA, are rather brittle and usually display relatively small deformation at break, high rigidity, and low plasticity for small deformations. These mechanical characteristics (e.g., Young's modulus of about 2-3 GPa and ultimate strength of 53 MPa¹⁰ for bulk material) are often incompatible with biological applications. Specifically, cortical bone has a modulus of elasticity between 7 and 17 GPa and an ultimate strength up to 133 MPa, depending on the age. In trabecular bone, the elastic modulus is about 0.44 GPa and the ultimate strength is 6.8 MPa¹¹. Moreover, PLA hydrophobicity renders bone cell attachment and proliferation difficult.

To overcome these problems, PLA scaffold properties could be improved by incorporating nanofillers, such as graphene oxide (GO)¹³. Graphene (the elementary structure of graphite) is a single layer sheet composed of sp²-bonded carbon atoms arranged in a flat honeycomb structure. It possesses remarkable properties, such as high mechanical strength and extremely

large surface area^{14,15}. GO structure is similar with the addition of polar functional groups (such as epoxides, hydroxyl, carboxylic groups) that are crucial for promoting interaction with the polymer matrix^{16,17}. Different studies have investigated PLA reinforcement with GO^{18,20}. For example, Pinto *et al.* showed that GO addition increases the Young's modulus by 115% and the yield strength by 95%¹⁹. Other studies demonstrated that GO reinforcement of biopolymers is biocompatible, promotes cell adhesion and proliferation, and improves composite wetting^{21,22,23}.

To design scaffolds for bone tissue engineering, different synthesis techniques can be used: solvent casting and particulate leaching²⁴, emulsion freeze-drying²⁵, phase separation²⁶, or electrospinning²⁷. However, these techniques do not allow controlling efficiently the morphology and structure of the interconnected pores. On the other hand, various studies demonstrated that the 3D controlled scaffold architecture significantly affects its mechanical properties^{28,29} as well as bone cell adhesion and proliferation^{30,31}. Therefore, recent works focused on the development of 3D printed scaffolds³² using different techniques, such as stereolithography^{33,34}, 3D plotting³⁵, selective laser sintering³⁶, bioprinting³⁷, and fused deposition modelling (FDM)³⁸. FDM is the most widely used additive manufacturing method and presents several advantages compared with other techniques³⁹. Indeed, FDM is cheap, does not require solvents, and gives great possibilities in polymer handling and processing⁴⁰. Amorphous thermoplastic polymers, such as PLA, are among the most common materials used in this type of process⁴¹⁻⁴³.

The objective of this work was to create a 3D porous scaffold with controlled architecture, good mechanical properties and adequate composition to support bone formation. To this aim, we developed a PLA/GO nanocomposite material and created by FDM 3D printing a multifunctional scaffold with a customized structure. We then analysed many parameters of

these scaffolds (morphology, chemical, structural and mechanical properties, and biocompatibility) to demonstrate their usefulness for biological applications.

2. Experimental section

2.1. Materials. PLA pellets were purchased from NatureWorks LLC. Graphite powder (20 μ m synthetic, CAS 7782-42-5), dichloromethane (CH_2Cl_2 , <99.9%, CAS 75-09-2), sulfuric acid (H_2SO_4 , 95.0-98.0%, CAS 7664-93-9), phosphoric acid (H_3PO_4 , 85wt.% in H_2O , CAS 7664-38-2), hydrogen peroxide (H_2O_2 , 30% (w/w), CAS 7722-84-1), potassium permanganate (KMnO_4 , >99.0%, CAS 7722-64-7), ethanol (96% vol, CAS 64-17-5), cetylpyridinium chloride (CAS 6004-24-6), glutaraldehyde (25% in H_2O , CAS 111-30-8), 37% formaldehyde (37 wt. % in H_2O , CAS 50-00-0), phosphate buffered saline (PBS) (P4417) tablets, Triton X 100 (CAS 9002-93-11), Bovine Serum Albumin (BSA) (\geq 98%, CAS 9048-46-8), Mowiol 40-88 (CAS 9002-89-5), L-ascorbic acid (CAS 50-81-7), β -glycerophosphate (\geq 99%, CAS 154804-51-0), Alizarin Red S (CAS 130-22-3), anti-actin antibody (clone CA15, A5441), dexamethasone (\geq 80%, CAS 50-02-2), Hoechst 33342 (\geq 98%, CAS 23491-52-3) and 3-(4,5-dimethylthiazol-2-yl)-2,5-diphenyl tetrazolium bromide (MTT, 98%, CAS 298-93-1) were purchased from Sigma-Aldrich. Acetone (\geq 99% (GC), CAS 67-64-1) was purchased from Honeywell. Tween 20 (CAS 9005-64-5) was purchased from VWR International. Alexa-conjugated anti mouse IgG (Alexa fluor 488, A11001) was purchased from ThermoFisher Scientific. MEM alpha medium (Gibco 12571-063), dimethyl sulfoxide (DMSO) (BDH Prolabo 23486.297), foetal bovine serum (FBS) (Eurobio CVFSVF00-01), penicillin/streptomycin (Gibco 15140-122) and 0.05% trypsin-EDTA (Gibco 25300-054) were used for cell cultures.

2.2. Preparation of the PLA/GO scaffolds. GO was prepared according to the modified Hummers method⁴⁴. Briefly, 3 g of graphite powder was added to a 9:1 mixture of concentrated $\text{H}_2\text{SO}_4/\text{H}_3\text{PO}_4$ under stirring for 5min. Then, 18 g of KMnO_4 was added to the solution containing the graphite and the acid mixture, and stirred for 12h. Then, 3mL of H_2O_2 was added to the solution with magnetic stirring for 1 h, followed by centrifugation at 6000 rpm for 10min. The precipitates were first washed with 30% HCl , then with distilled water, and finally with ethanol. The purified GO precipitate was dried at 50°C for 24h.

The PLA solution (10 mL of 10% (w/v)) was prepared using dichloromethane as solvent. Different percentages of filler (0.1 to 0.3 wt %) were used. GO was dispersed in acetone (1mg per mL) and placed in an ultrasonic bath for 15min. The GO-containing solution was added to the polymer solution under constant magnetic stirring until the solution was homogeneous. The composite polymer solution was poured into a Teflon dish and allowed to dry at room temperature overnight. The obtained dried polymer was a film and was cut into pieces and introduced into a single screw extruder (Noztek pro) at an extrusion temperature of 200°C . A filament with a diameter of 1.75 mm was obtained and used for 3D printing. The scaffold was modelled using computer-aided design (CAD) software (Design Spark Mechanical). After deciding the scaffold shape, a STL file was created to be analysed with the Prusa3Dslicer software. Scaffolds were 3D printed using a Prusa Research MK2S printer. All printing parameters are given in Table S1.

2.3. Morphological properties. The scaffold size, morphology, and microstructure were analysed by scanning electron microscopy (SEM) (HITACHI S4800 system). For SEM observation, scaffolds were coated with platinum using a Polaron SC7620 Mini Sputter Coater. The diameters of the struts and of the obtained pores were calculated with the Image J software.

A chromatic confocal rugosimeter (STIL SA) equipped with a CHR1000 sensor was used for the 3D characterization of the topography of cylinder surface areas of 10 mm of 3D printed PLA and PLA/GO scaffolds (two different locations of 2*2 mm for each scaffold with 5 lateral μm step). Data post-treatment was done with MountainsMap7 (DigitalSurf). The determined roughness parameter was the arithmetical mean height of the surface (S_a).

The contact angles of ultrapure water on 3D printed PLA and PLA/GO scaffolds was measured using the sessile drop method with a B-CAM-21-BW (CCCIR) monochrome camera and a Led R60 lamp (Conrad). Equilibrium contact angles (considered at 60s) were measured for 5 μL droplet volumes in three different locations for each condition. One Touch Grabber and Image J were used to calculate the contact angles.

2.4. Chemical and structural properties. Raman spectra of scaffolds and films were obtained in ambient conditions using a 659.55 nm laser and a Horiba Jobin Yvon Raman spectrometer (model M.F.O). The X-ray diffraction (XRD) patterns of PLA and PLA/GO scaffolds were recorded using $\text{CuK}\alpha$ radiation, 2θ range of $10\text{--}70^\circ$ with a scan speed of $2^\circ.\text{min}^{-1}$, and the PANalytica Xpert powder XRD system. The Fourier Transform Infrared (FTIR) spectrum of PLA and PLA/GO nanocomposites was recorded with the NEXUS instrument, equipped with an attenuated total reflection accessory in the frequency range of $600\text{--}4000\text{ cm}^{-1}$. The FTIR spectrum was scanned at 1 cm^{-1} resolution, and signals were averaged from 32 scans.

2.5. Thermal properties. The different scaffolds were analysed using a differential scanning calorimeter 2920 (maker), equipped with a RCS90 cooling system (maker). Samples were accurately weighed ($\approx 4\text{ mg}$) in an aluminium TA pan (maker) and sealed. An empty sealed

pan was used as reference. Samples were first cooled to 25°C and then heated to 210°C with a heating rate of 10°C min⁻¹. Then, they were cooled again to 25°C with nitrogen as purge gas. The degree of polymer crystallinity was calculated with the following formula $\chi = \frac{\Delta H_f - \Delta H_{cf}}{\Delta H_{\infty}}$ where ΔH_f is the enthalpy of fusion, ΔH_{cf} is the enthalpy of cold crystallization, and ΔH_{∞} is the reference melting enthalpy for the 100% crystalline polymer ($\Delta H_{\infty} = 93 \text{ J.g}^{-1}$)⁴⁵. The resulting differential scanning calorimetry (DSC) curves were analysed to determine the polymer glass transition temperature (T_g), the melting temperature (T_m), the cold temperature crystallization (T_{cc}) and the crystallinity (X_c). The thermogravimetric analysis (TGA) was performed using a TGA G500 device (TA Instruments). About 10 mg of each sample was heated in air atmosphere from room temperature to 900°C, at a heating rate of 10°C.min⁻¹.

2.6. Mechanical properties. The mechanical properties of the 3D printed PLA/GO scaffolds were characterized using a modular traction system (1/ME) coupled with a 5 kN force sensor (maker). Samples were printed in the shape of a dog bone (40 mm length, 4 mm width, and 1.5 mm thick). The exact geometry is given in Figure S2. Samples were then clamped between dedicated jaws and pulled at a constant speed of 0.01 mm.s⁻¹ until they broke. Samples were imaged with a 16 Mb camera (SVS-VISTEK) at 1 Hz. Samples were initially randomly patterned with thin black paint to perform digital image correlation (DIC). Using an already described DIC algorithm dedicated to large deformations^{46,47}, sample strain changes could be computed without inaccuracy coming from the machine and jaw plays. Linear elastic regions from the stress–strain graphs were then used to calculate the Young’s modulus from at least three assays. The stress at which the sample begins to break was also measured.

2.7. Cell viability and adhesion assays. Scaffolds were sterilized with ethanol for 30min and under UV light (405 nm) for 1h. MG-63 osteosarcoma cells were cultured on the sterilized

scaffolds for 7 days. Cell viability was analysed using the MTT assay. Cells were incubated with 100 μL of culture medium containing 0.05 mg.mL^{-1} of MTT solution for 3h. The obtained purple-coloured formazan crystals, due to MTT reduction by living cells, were solubilized by addition of 100 μL of DMSO and absorbance recorded at 560 nm using a Multiskan microplate spectrophotometer (Thermofisher, USA). For the cell adhesion assay, MG-63 cells were fixed with 4% formaldehyde (500 μL per well) at room temperature for 20min. After washing with PBS and permeabilization with PBS/0.1% Triton X 100 for 15min, cells were incubated with PBS/1% BSA for 3h. Then, they were incubated with an anti-actin antibody (to stain the cytoskeleton) at 4°C overnight, and washed twice with PBS/0.05% Tween 20. After incubation with the Alexa-conjugated anti mouse IgG secondary antibody, nuclei were stained with Hoechst 33342 at room temperature for 1h. Samples were mounted with Mowiol and images acquired with a fluorescent microscope (DM6000 Leica).

2.8. Mineralization assay. MG-63 cells were plated in Petri dishes on the PLA/GO nanocomposites and grown until confluence (day 0). Then, they were switched to differentiation medium, supplemented with ascorbic acid (50 mg.ml^{-1}), β -glycerophosphate (5 mM) and dexamethasone (10^{-8} M) that was refreshed every 48h. Mineralized nodule formation was monitored at day 0, 14 and 21 by staining with Alizarin Red-S. Briefly, cells were rinsed twice with PBS and fixed with 4% formaldehyde at room temperature for 20min. Then, cells were rinsed twice with PBS (pH 4.2), and stained with 40 mM Alizarin Red-S (pH 4.2) at room temperature for 20min, followed by extensive rinsing with water. For quantification, the supernatant absorbance was measured at 540 nm using a microplate reader (Bio-Rad) after extraction with 10% (wt/vol) cetylpyridinium chloride. Differences between groups were determined with the Student's *t*-test and were considered significant for * $p < 0.05$ and ** $p < 0.005$.

3. Results and discussion

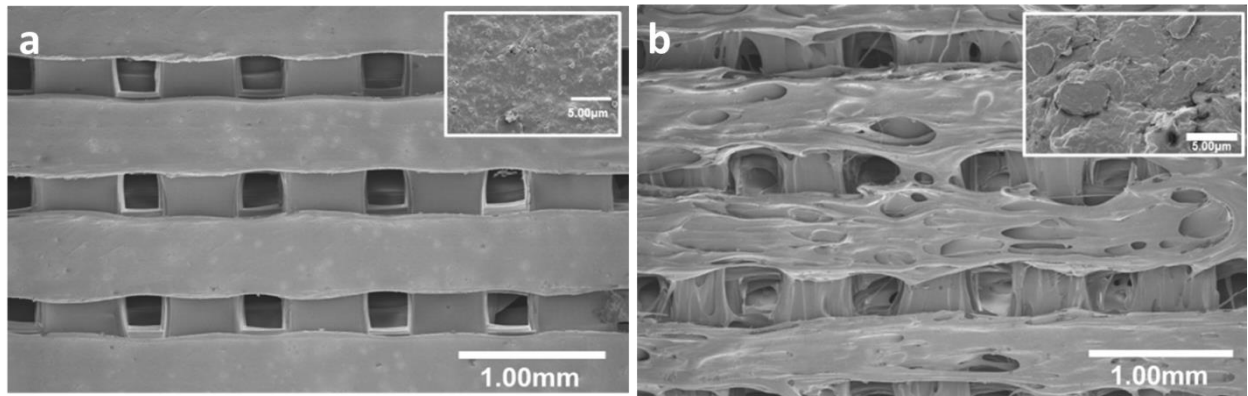
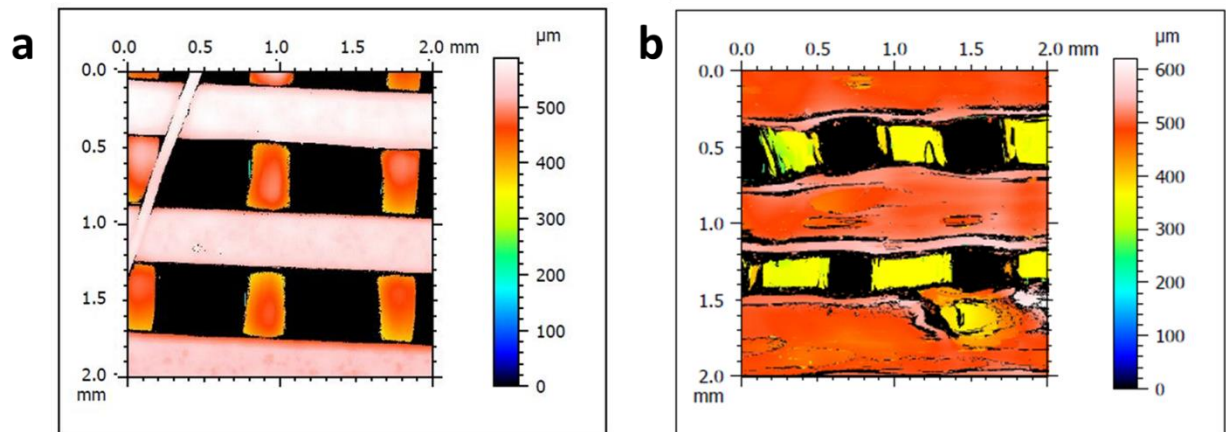
3.1. Generation and morphological analysis of PLA/GO scaffolds. To reinforce PLA, GO fillers were added to the polymer matrix at different percentages (0.1, 0.2, and 0.3%) and named PLA/GO-films. The composites were then extruded *via* a single screw extruder and put in shape with a FDM system. To facilitate bone regeneration, it was decided to generate scaffolds with a porous interconnected network and a pore size around 300 μm , corresponding to an infill of 70% (see Table S1 for the used printing parameters).

The SEM micrographs shown in Figure 1 illustrate the porous morphology of scaffolds obtained with PLA alone (Figure 1a) or with 0.2% GO (Figure 1b). The pore size ($405\pm 20\ \mu\text{m}$ and $485\pm 30\ \mu\text{m}$, respectively) and the wall width ($380\pm 65\ \mu\text{m}$ and $360\pm 130\ \mu\text{m}$, respectively) were comparable in the PLA scaffolds and in the PLA scaffolds with 0.2% of GO. Similar results were obtained with 0.1% and 0.3% GO (Table 1), showing that GO addition in the PLA matrix had a very moderate effect on pore morphology during the 3D printing step.

Analysis of the 3D topography images (Figure 2) indicated that the surface of PLA scaffolds with 0.2% GO (Figure 2b) was rougher compared with the smooth surface of PLA scaffolds (Figure 2a). In agreement, PLA scaffolds with 0.2% GO displayed higher S_a values (Table 1). This could be attributed to the presence of fillers at the surface and their good dispersions in the polymer matrix⁴⁸. Only in PLA scaffolds with 0.3% GO, roughness was slightly decreased compared with PLA scaffolds (Table 1), and this could be due GO agglomeration.

Table 1. Pore size, wall width, roughness (i.e., Sa, the arithmetic average height of the surface), and contact angles of ultrapure water for PLA and PLA/GO scaffolds.

Samples	Pore size (μm)	Wall width (μm)	Sa (μm)	Contact angles ($^{\circ}$)
PLA	405 ± 20	380 ± 65	5.8 ± 1.5	118 ± 2
PLA/GO (0.1%)	450 ± 25	350 ± 100	7.5 ± 0.6	70 ± 2
PLA/GO (0.2%)	485 ± 30	360 ± 130	9.9 ± 4.0	69 ± 1
PLA/GO (0.3%)	455 ± 24	400 ± 130	5.5 ± 0.9	54 ± 2

**Figure 1.** Scanning electron micrographs showing the architecture of FDM 3D printed (a) PLA and (b) PLA/GO (0.2%) scaffolds. Insets show a magnification of the surface.**Figure 2.** Scaffold topography. Representative 3D images of the surface roughness of (a) PLA and (b) PLA/GO (0.2%) scaffolds.

In bone tissue engineering, the surface properties of biomedical devices are very important. For instance, the material must display sufficient hydrophilicity to allow the attachment of cells on the scaffold surface, and their proliferation and differentiation for bone

regeneration^{49–51}. Water contact angles (Figure S1) were smaller for PLA/GO scaffolds compared with PLA scaffolds (Table 1). Pinto *et al.*¹⁸ reported similar results for PLA/GO films with a decrease of the contact angle of about 9° after GO addition. Conversely, Zhang *et al.* found that GO addition had no effect on the contact angle for PLA/GO electrospun fibers⁵². This suggests that GO presence at the scaffold surface increases its hydrophilicity, and that the method used to obtain the final material directly influences the surface properties. In our study, pristine PLA had a contact angle of 118°, while PLA with 0.3% of GO had a contact angle of 54°. This reduction might be caused by direct interactions of the liquids with partially exposed fillers at the PLA surface. Hydrogen bond interactions between oxygen-containing groups in GO and water can explain this behaviour. In conclusion, the presence of GO in the 3D PLA matrix decreased the surface hydrophobic properties and, as a consequence, should improve cell attachment and proliferation at the surface of the material.

3.2. Structural characterization of PLA/GO scaffolds. To confirm GO formation from graphite, XRD analysis of the obtained powder showed the characteristic GO peak at 11° that corresponded to the (002) plane (Figure 3a). This evidenced graphite exfoliation through the oxidation process. The PLA-film (red in Figure 3a) showed four characteristics peaks at $2\theta = 15, 17, 19$ and 23° that described the alpha form of PLA⁵³. PLA crystalline peaks disappeared after filament extrusion (green). This might be due to the quenching (air atmosphere) of PLA melting during 3D printing and the high speed of cooling that inhibited the crystalline structure rearrangement. Moreover, it has been shown that natural PLA has the lowest percentage of crystallinity among PLA filaments (coloured or not)⁵⁴. Hence, the XRD results suggest that PLA crystalline phase was lost during extrusion.

The PLA/GO biocomposites before extrusion (PLA/GO-film; blue in Figure 3a) displayed two characteristic PLA peaks at $2\theta = 17$ and 23° . However, these peaks were broader than in

the PLA-film, possibly due to micro-stresses induced by GO addition in the polymer matrix. Indeed, the peak corresponding to GO was not detected. This could be related to the low percentage of fillers or the good GO dispersion in the matrix⁵⁵. After extrusion, the same behaviour was observed for the PLA/GO scaffold (pink, Figure 3a), with a broad peak between 10° and 25° that corresponded to the polymer amorphous nature.

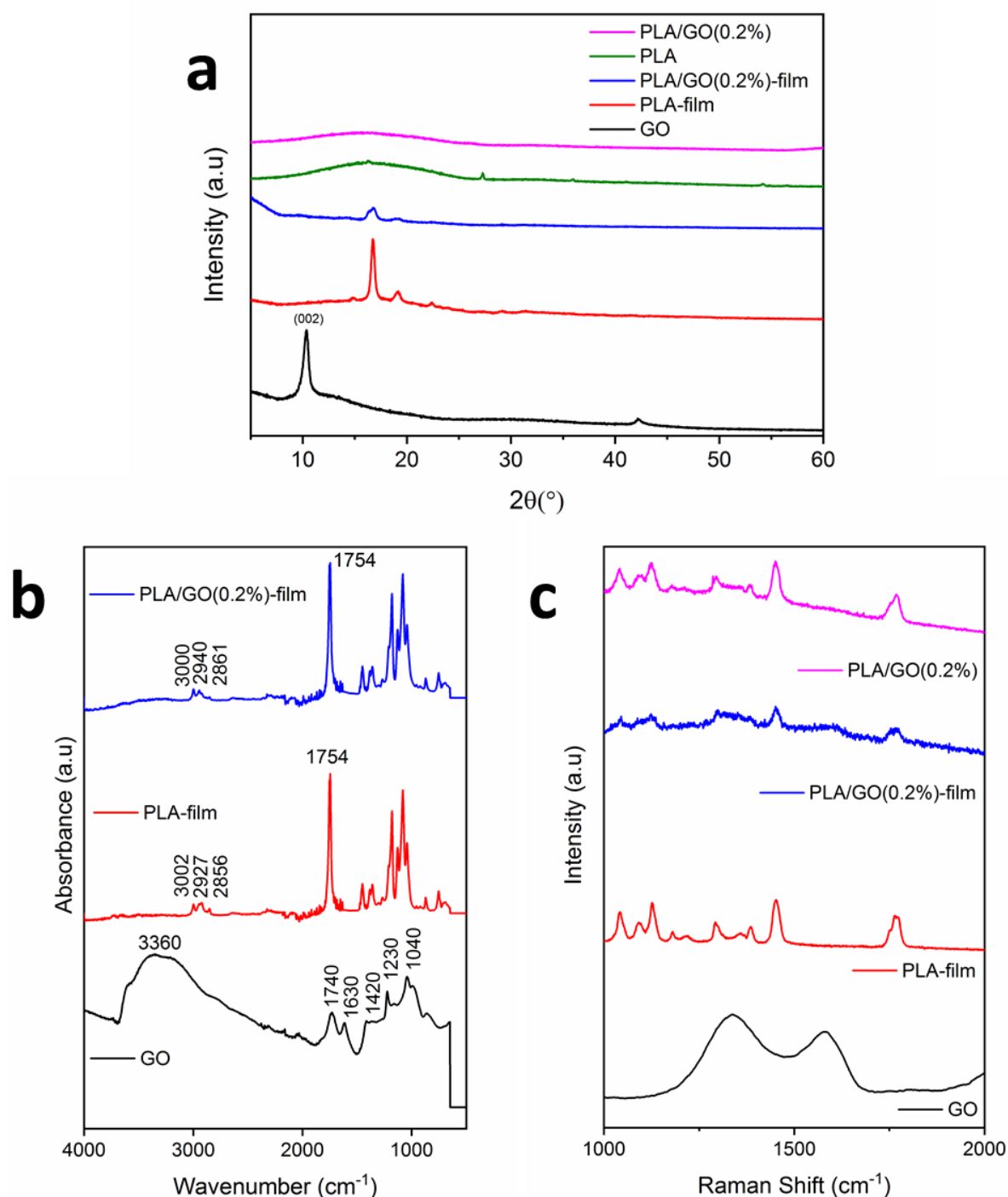


Figure 3. Chemical and structural properties of the nanocomposites. (a) XRD diffractograms, (b) FTIR spectra, and (c) Raman spectroscopy data of the synthesized GO and PLA/GO nanocomposites (films or 3D printed scaffolds, as indicated).

3.3. Chemical characterization of the scaffolds. To understand PLA organization and GO interactions with the polymer matrix during the nanocomposite fabrication, FTIR spectra were recorded (Figure 3b). The characteristic GO functions were the bands at 1040 cm^{-1} (C-O

elongation vibrations) and 1740cm^{-1} (C = O elongation vibrations of the carbonyl and carboxylic groups). The band at 1630 cm^{-1} was probably due to skeletal vibration of the graphite domains. The broad band around $3000\text{-}3500\text{ cm}^{-1}$ was attributed to hydroxyl groups. No difference was observed between the bands of pure PLA and PLA/GO scaffolds. Indeed, the greater PLA band absorbance and in the same range than that of GO did not allow detecting the GO bands in the PLA/GO biocomposites.

Similarly, the D and G-band signature of pure GO powder was detected at 1345 and 1590 cm^{-1} respectively, using Raman spectroscopy (Figure 3c). The vibration of sp^2 -bonded carbon atoms in a 2D hexagonal lattice gave the G-band, whereas the vibration of carbon atoms with pendent bonds in the plane of the disordered graphite was associated with the D band. The D band is generally correlated with defects from vacancies, grain boundaries, and amorphous carbon species that lead to sp^3 -hybridized carbon, hence a differentiated band of sp^2 -hybridized carbon. For the PLA/GO film, two bands were observed at 1345 and 1590 cm^{-1} that appeared as widened bands of weak intensities and corresponded to the presence of GO in the PLA. The Raman spectra of PLA/GO scaffolds were not significantly different from those of PLA scaffolds.

3.4. Thermal analysis of the PLA/GO scaffolds. The influence of GO on PLA thermal stability was monitored by TGA (Figure 4a). The 1% weight loss for PLA observed below 200°C was due to the adsorbed water. The second major weight loss observed between 300 and 400°C was caused by the degradation of the PLA polymer. As shown in the derivative weight curves (Figure 4b), the maximum degradation temperature peak shifted from 298°C to 366°C for the nanocomposites with 0.3% GO. This shift could be explained by the interfacial interactions between GO and PLA through hydrogen bonds and/or van der Waals forces, as previously reported^{56,57}. The strong interactions with GO led to the improvement of the

biocomposite thermal stability, possibly due to a diminution of the chain mobility at the interface with GO⁵⁸. The last weight loss from 400°C was due to the thermochemical decomposition of the remaining organic content from PLA and from GO due to pyrolysis of labile oxygenated groups when PLA is reinforced with GO⁵⁹.

The effects of GO addition on PLA crystallinity and on Tg, Tcc and Tm were evaluated by DSC analyses (Figure 4c). Enthalpy of fusion, glass transition and melting point were measured and are summarized in Table 2, together with the calculated crystallinity. For PLA, Tg were 59°C and 61°C and Tm were 168°C and 169°C before and after extrusion, respectively. This indicated that the extrusion process did not affect PLA thermal properties.

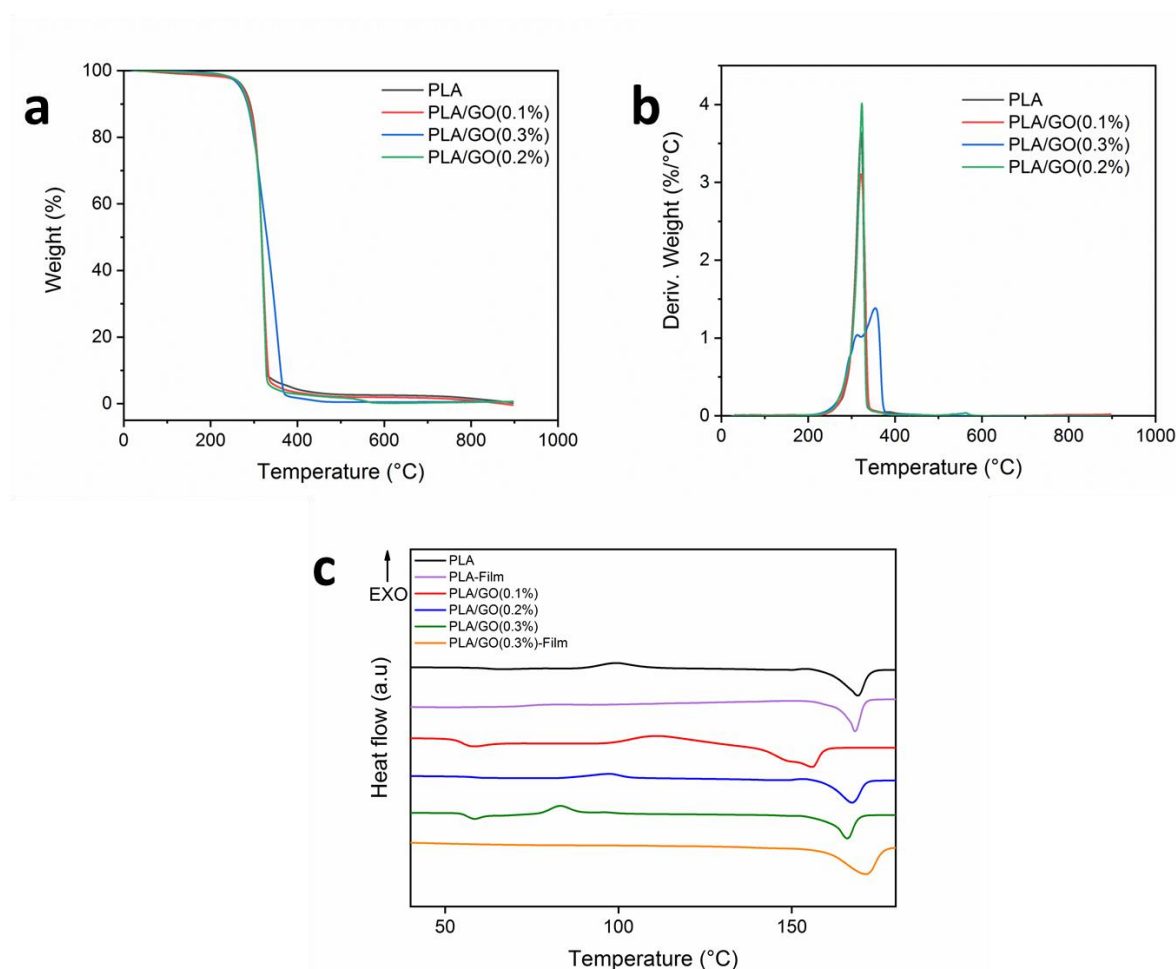


Figure 4. Thermal properties of nanocomposite materials. (a) TGA and (b) derivative TGA curves of 3D printed PLA nanocomposites with different GO percentages. (c) Representative DSC graphs showing Tg (glass transition temperature), Tm (melting temperature) and Tcc (cold temperature crystallization) of PLA and PLA/GO nanocomposites before and after 3D printing.

Table 2. Temperatures, enthalpies of different thermal transitions, and crystallinity of PLA and PLA/GO materials.

Samples	T _g (°C)	T _m (°C)	ΔH _f (J/g)	ΔH _{cf} (J/g)	χ (%)
PLA	61	169	30	10	21
PLA-film	59	168	30	-	32
PLA/GO (0.1%)	55	156	27	27	0
PLA/GO (0.2%)	57	171	43	19	26
PLA/GO (0.3%)	56	166	40	24	16
PLA/GO (0.3%)-film	55	169	42	-	45

T_g, glass transition temperature; T_m, melting temperature ; ΔH_f, enthalpy of fusion; ΔH_{cf}, enthalpy of cold crystallization; χ, crystallinity.

After extrusion, PLA showed a cold crystallization peak at 100°C. Conversely, the cold crystallization peak was suppressed before extrusion, as reported in a previous study on a PLA film⁶⁰. In line with these observations, PLA crystallinity level was lower after than before extrusion, and this change could have been caused by the extrusion process⁶¹. These results confirmed the XRD observations on the polymer crystallinity changes during extrusion.

For PLA reinforced with 0.1% GO, the glass transition at 55°C was followed by an exothermic cold crystallization peak at 112°C. When the GO content was increased to 0.3%, the T_g at 56°C was followed by a double peak of cold crystallization at 83°C. These results are surprising because a previous study reported that the T_g of graphene and GO/polymer nanocomposites is significantly increased (4°C or more) when using functionalized nanofillers, due to more interactions with the matrix⁶². Moreover, GO addition should increase the cold crystallization temperature because in the presence of enough GO content in the polymer matrix, the motion of PLA chains is confined, the cold crystallization process of PLA is restricted, and consequently the crystallization temperature increases⁶³.

The melting peak was not changed by GO addition to the PLA matrix, but a double melting peak appeared at 166 °C when GO loading level was increased to 0.3 wt%. The second melting peak was higher, indicating that more crystalline forms were generated with higher GO loading levels⁶⁴. Finally, thermal analysis by TGA and DSC showed that GO presence in the polymer matrix did not affect the filament extrusion. The 3D printing conditions also were not influenced by GO addition. However, GO enhanced the thermal stability of the nanocomposite scaffolds.

3.5. Mechanical properties of the 3D printed nanocomposites. Composites used for biomedical implants should withstand high tensile loads. The characterization of the mechanical properties of PLA and PLA/GO nanocomposites (Figure 5) focused on the region where samples responded elastically to traction. In this region, the elastic modulus was measured as a function of the GO percentage. The Young's modulus for PLA was in good agreement with the literature⁶⁵ (*i.e.*, about 2 GPa for a sample with 30% porosity). This value significantly increased to 2.6 GPa after addition of 0.3% GO (improvement of about 30% of the elastic modulus) for a scaffold with 30% porosity (Figure 5a).

Then, samples were loaded until breaking. When GO density was high enough, GO incorporation increased the tensile strength from 34 MPa for pure PLA to 39 MPa for samples with 0.3% GO. Conversely, in samples with lower GO density, tensile strength at break was lower (Figure 5b). This is due to the fact the GO induced flaws at the very local scale that made the material weaker. With higher GO densities, this phenomenon is counterbalanced by the fact that GO is intrinsically stronger than PLA, which makes the material stronger. The Poisson's ratio was 0.3 for PLA, which is characteristic for this polymer, and was not changed by GO addition (Figure 5c). The improved stiffness of the PLA/GO scaffold compared with the PLA scaffold highlighted the reinforcement of the scaffold by GO addition.

Here, only the influence of GO addition on the polymer mechanical properties was investigated. However, the architecture and percentage of filling inside the scaffold also have an effect on the mechanical properties of the material, particularly on the tensile strength, but these features were beyond the goal of this study.

Several studies have shown the improvement of mechanical properties and biological activity of PLA scaffolds generated by FDM^{66,67}. Different fillers were used in compression⁶⁸ and flexural studies⁶⁹, but to the best of our knowledge, the mechanical properties of PLA-based nanocomposites were never investigated by tensile strength analysis. Overall, our findings indicate that GO is a promising filler for improving the mechanical properties of biopolymers made by FDM.

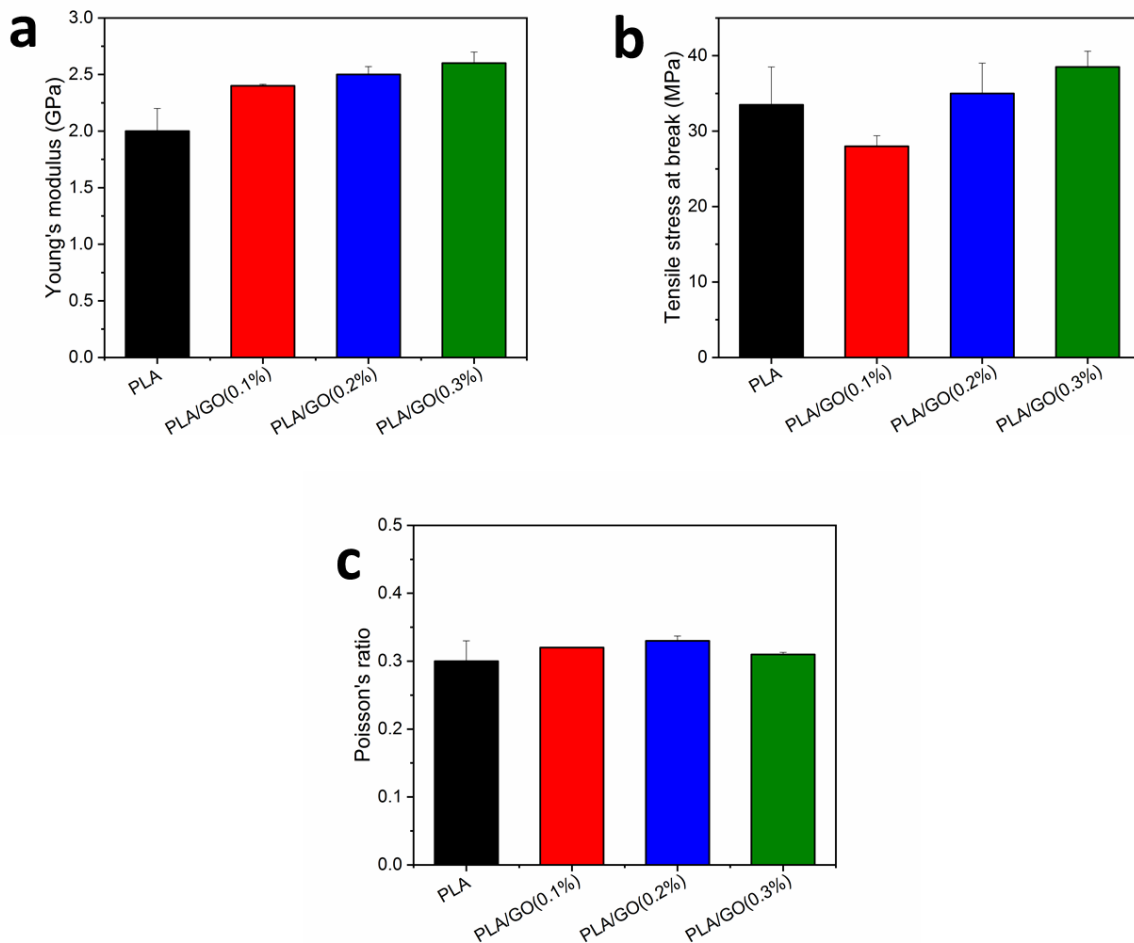


Figure 5. Mechanical properties of the scaffolds. (a) Young's modulus, (b) Tensile stress at break, and (c) Poisson's ratio values of the different PLA/GO scaffolds compared with PLA scaffolds.

3.6. Biological studies. The scaffold biocompatibility was then investigated using MG-63 cells that were derived from a human bone osteosarcoma and exhibit osteogenic potential. Compared with cells grown without scaffolds (control), PLA and PLA/GO (all tested GO concentrations) scaffolds did not have any significant effect on cell viability at day 4 and day 7 (Figure 6). These results suggest that GO incorporation as nanofiller for PLA is biocompatible.

Similarly, analysis of cell attachment to the scaffolds by staining cell nuclei with Hoechst 33342 and the cytoskeleton with an anti-actin antibody showed that cells readily attached to the scaffolds at 24h, and reached confluency after 7 days of culture in the presence of PLA and PLA/GO scaffolds (Figure 7a). Cell proliferation quantification with the MTT assay at day 4 and 7 (Figure 7b) showed that GO incorporation promoted cell attachment and proliferation compared with scaffolds made only of PLA.

Finally, MG-63 cell mineralization was monitored by Alizarin Red-S staining at day 1, 14 and 21 after induction of differentiation. Colorimetric quantification of calcium deposition on the scaffolds by MG-63 cells (Figure 8) showed that at day 21, it was increased by two-fold in samples with PLA/GO scaffolds compared with PLA scaffolds. This indicates that GO incorporation in the scaffold promotes mineralization. Altogether, these results demonstrate that PLA reinforced with 0.2% GO is biocompatible and may improve MG-63 cell mineralization activity.

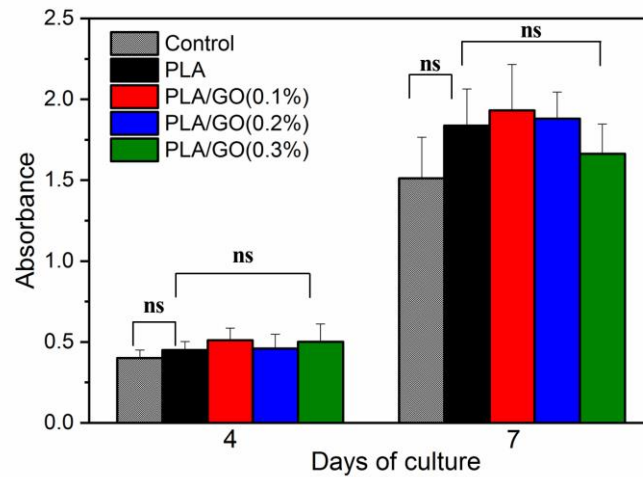


Figure 6. MG-63 cell viability when cultured in the presence of PLA and PLA/GO nanocomposite scaffolds was assessed with the MTT assay at day 4 and 7 after seeding (ns = not significant).

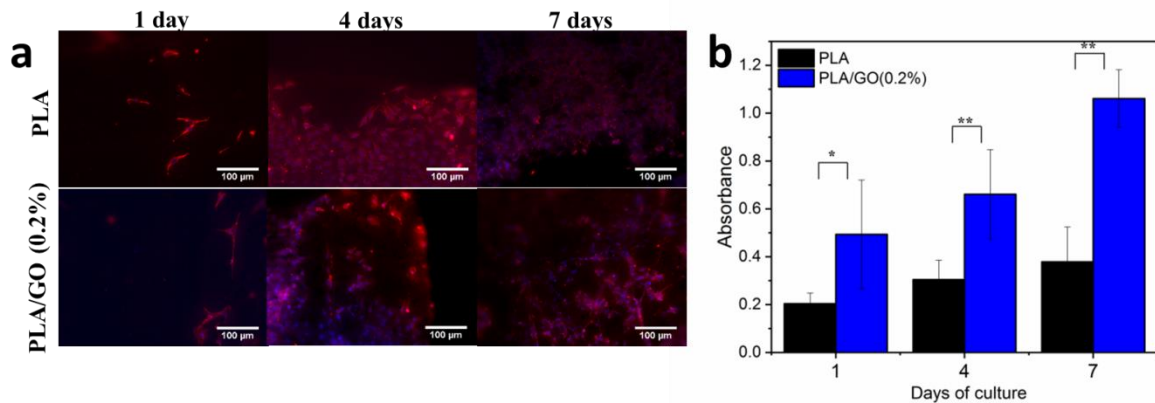


Figure 7. MG-63 cell attachment and proliferation on PLA and PLA/GO nanocomposite scaffolds. (a) Actin immunodetection (red) and DAPI staining of DNA (blue) in MG-63 cells attached on the scaffolds. (b) Cell proliferation was monitored with the MTT assay at different time points after seeding (ns = not significant, * $p < 0.05$, ** $p < 0.005$).

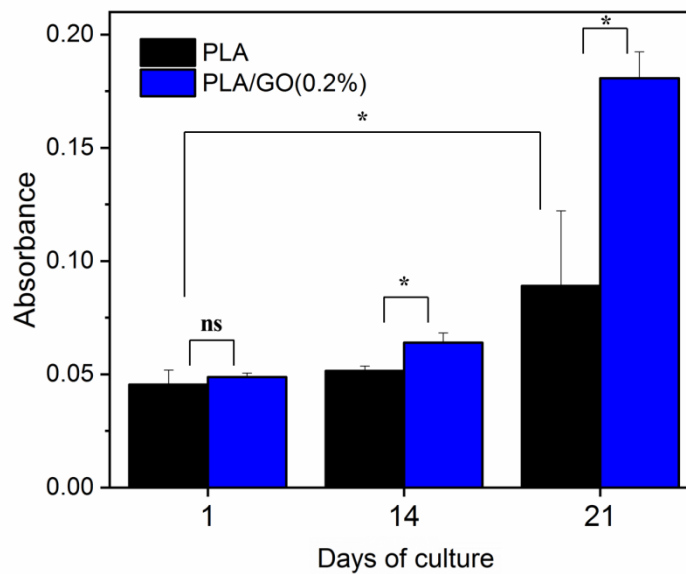


Figure 8. MG-63 cell differentiation on PLA and PLA/GO scaffolds was evaluated using the Alizarin Red-S mineralization assay at different time points after switching to differentiation medium (ns = not significant, * $p < 0.05$).

4. Conclusions

In conclusion, GO-reinforced PLA scaffolds were synthesized and thoroughly characterized, particularly their structural and mechanical properties and their biocompatibility. We successfully 3D printed PLA/GO nanocomposites with controlled morphology and a network of interconnected pores around 300 μm . Altogether, our results demonstrated that GO incorporation 1) increased the surface roughness and hydrophilicity, 2) did not modify the transition temperature, 3) decreased polymer crystallinity, 4) improved the mechanical properties of the scaffold, and 5) promoted bone cell attachment, proliferation and differentiation. Our data clearly indicate that PLA reinforcement with 0.2% GO might represent a good strategy to obtain 3D printed scaffolds with very attractive mechanical properties and bioactivity, thus providing a promising material for bone tissue engineering.

Acknowledgments:

We acknowledge the financial support from Indo-French Centre for the promotion of advanced research-Cefipra (Project 5608-1), from CNRS (Project “Osez l’Interdisciplinarité: TraitCancer”) and from University of Montpellier (MUSE “3DTraitCancer”).

REFERENCES

1. Tang, D. *et al.* Biofabrication of bone tissue: approaches, challenges and translation for bone regeneration. *Biomaterials* **83**, 363–382 (2016).
2. Aro, H. T. & Aho, A. J. Clinical use of bone allografts. *Ann. Med.* **25**, 403–412 (1993).
3. Rezwan, K., Chen, Q. Z., Blaker, J. J. & Boccaccini, A. R. Biodegradable and bioactive porous polymer/inorganic composite scaffolds for bone tissue engineering. *Biomaterials* **27**, 3413–3431 (2006).
4. Bose, S., Roy, M. & Bandyopadhyay, A. Recent advances in bone tissue engineering scaffolds. *Trends Biotechnol.* **30**, 546–554 (2012).
5. O’Brien, F. J. Biomaterials & scaffolds for tissue engineering. *Mater. Today* **14**, 88–95 (2011).
6. Lasprilla, A. J. R., Martinez, G. A. R., Lunelli, B. H., Jardini, A. L. & Maciel Filho, R. Poly-lactic acid synthesis for application in biomedical devices—A review. *Biotechnol. Adv.* **30**, 321–328 (2012).
7. Muller, J., González-Martínez, C. & Chiralt, A. Combination Of Poly(lactic) acid and starch for biodegradable food packaging. *Materials (Basel)*. **10**, 1–22 (2017).
8. Cutright, D. E. & Hunsuck, E. E. Tissue reaction to the biodegradable polylactic acid suture. *Oral Surgery, Oral Med. Oral Pathol.* **31**, 134–139 (1971).
9. Bos, R. R. M. *et al.* Degradation of and tissue reaction to biodegradable poly (L-lactide) for use as internal fixation of fractures: a study in rats. *Biomaterials* **12**, 32–36 (1991).
10. Madhavan Nampoothiri, K., Nair, N. R. & John, R. P. An overview of the recent developments in polylactide (PLA) research. *Bioresour. Technol.* **101**, 8493–501 (2010).
11. Karageorgiou, V. & Kaplan, D. Porosity of 3D biomaterial scaffolds and osteogenesis. *Biomaterials* **26**, 5474–5491 (2005).
12. Hollister, S. J. Porous scaffold design for tissue engineering. *Nat. Mater.* **4**, 518 (2005).
13. Kim, H., Abdala, A. A. & Macosko, C. W. Polymer Nanocomposites with Graphene. *Young* 1–13 (2010). doi:10.1021/ma100572e
14. Geim, A. K. Graphene : Status and Prospects. **1530**, 1530–1535 (2010).
15. Stankovich, S. *et al.* Graphene-based composite materials. *Nature* **442**, 282–286 (2006).
16. Zhu, Y. *et al.* Graphene and graphene oxide: Synthesis, properties, and applications. *Adv. Mater.* **22**, 3906–3924 (2010).
17. Gao, W. The chemistry of graphene oxide. *Graphene Oxide Reduct. Recipes, Spectrosc. Appl.* 61–95 (2015). doi:10.1007/978-3-319-15500-5_3
18. Pinto, A. M. *et al.* Biocompatibility of poly (lactic acid) with incorporated graphene-based materials. *Colloids Surfaces B Biointerfaces* **104**, 229–238 (2013).
19. Pinto, A. M., Cabral, J., Tanaka, D. A. P., Mendes, A. M. & Magalhães, F. D. Effect of incorporation of

- graphene oxide and graphene nanoplatelets on mechanical and gas permeability properties of poly (lactic acid) films. *Polym. Int.* **62**, 33–40 (2013).
20. Chen, Q. *et al.* 3D printing biocompatible polyurethane/poly(lactic acid)/graphene oxide nanocomposites: Anisotropic properties. *ACS Appl. Mater. Interfaces* **9**, 4015–4023 (2017).
 21. Papageorgiou, D. G., Kinloch, I. A. & Young, R. J. Mechanical properties of graphene and graphene-based nanocomposites. *Prog. Mater. Sci.* **90**, 75–127 (2017).
 22. Ryoo, S.-R. *et al.* Biomedical Applications of Graphene and Graphene Oxide. *Acc. Chem. Res.* **46**, 2211–2224 (2013).
 23. Nanda, S. S., Papaefthymiou, G. C. & Yi, D. K. Functionalization of Graphene Oxide and its Biomedical Applications. *Crit. Rev. Solid State Mater. Sci.* **40**, 291–315 (2015).
 24. Liao, C. *et al.* Fabrication of porous biodegradable polymer scaffolds using a solvent merging/particulate leaching method. *J. Biomed. Mater. Res. An Off. J. Soc. Biomater. Japanese Soc. Biomater. Aust. Soc. Biomater. Korean Soc. Biomater.* **59**, 676–681 (2002).
 25. Sultana, N. & Wang, M. PHBV/PLLA-based composite scaffolds fabricated using an emulsion freezing/freeze-drying technique for bone tissue engineering: surface modification and in vitro biological evaluation. *Biofabrication* **4**, 15003 (2012).
 26. Huang, Y. X., Ren, J., Chen, C., Ren, T. B. & Zhou, X. Y. Preparation and properties of poly (lactide-co-glycolide)(PLGA)/nano-hydroxyapatite (NHA) scaffolds by thermally induced phase separation and rabbit MSCs culture on scaffolds. *J. Biomater. Appl.* **22**, 409–432 (2008).
 27. Nagarajan, S. *et al.* Design of Boron Nitride/Gelatin Electrospun Nanofibers for Bone Tissue Engineering. *ACS Appl. Mater. Interfaces* **9**, 33695–33706 (2017).
 28. Senatov, F. S. *et al.* Mechanical properties and shape memory effect of 3D-printed PLA-based porous scaffolds. *J. Mech. Behav. Biomed. Mater.* **57**, 139–148 (2016).
 29. Gómez, S., Vlad, M. D., López, J. & Fernández, E. Design and properties of 3D scaffolds for bone tissue engineering. *Acta Biomater.* **42**, 341–350 (2016).
 30. Rogina, A. *et al.* Macroporous poly(lactic acid) construct supporting the osteoinductive porous chitosan-based hydrogel for bone tissue engineering. *Polymer* **98**, 172–181 (2016).
 31. Rosenzweig, D. H., Carelli, E., Steffen, T., Jarzem, P. & Haglund, L. 3D-printed ABS and PLA scaffolds for cartilage and nucleus pulposustissue regeneration. *Int. J. Mol. Sci.* **16**, 15118–15135 (2015).
 32. Bose, S., Vahabzadeh, S. & Bandyopadhyay, A. Bone tissue engineering using 3D printing. *Mater. today* **16**, 496–504 (2013).
 33. Melchels, F. P. W., Feijen, J. & Grijpma, D. W. A review on stereolithography and its applications in biomedical engineering. *Biomaterials* **31**, 6121–6130 (2010).
 34. Gauvin, R. *et al.* Microfabrication of complex porous tissue engineering scaffolds using 3D projection stereolithography. *Biomaterials* **33**, 3824–3834 (2012).
 35. Luo, Y., Lode, A., Akkineni, A. R. & Gelinsky, M. Concentrated gelatin/alginate composites for fabrication of predesigned scaffolds with a favorable cell response by 3D plotting. *RSC Adv.* **5**, 43480–43488 (2015).
 36. Williams, J. M. *et al.* Bone tissue engineering using polycaprolactone scaffolds fabricated via selective laser sintering. *Biomaterials* **26**, 4817–4827 (2005).

37. Murphy, S. V & Atala, A. 3D bioprinting of tissues and organs. *Nat. Biotechnol.* **32**, 773 (2014).
38. Zein, I., Hutmacher, D. W., Tan, K. C. & Teoh, S. H. Fused deposition modeling of novel scaffold architectures for tissue engineering applications. *Biomaterials* **23**, 1169–1185 (2002).
39. Turner, B. N., Strong, R. & Gold, S. A. A review of melt extrusion additive manufacturing processes: I. Process design and modeling. *Rapid Prototyp. J.* **20**, 192–204 (2014).
40. Ning, F., Cong, W., Qiu, J., Wei, J. & Wang, S. Additive manufacturing of carbon fiber reinforced thermoplastic composites using fused deposition modeling. *Compos. Part B Eng.* **80**, 369–378 (2015).
41. Poh, P. S. P. *et al.* Polylactides in additive biomanufacturing. *Adv. Drug Deliv. Rev.* **107**, 228–246 (2016).
42. Serra, T., Planell, J. A. & Navarro, M. High-resolution PLA-based composite scaffolds via 3-D printing technology. *Acta Biomater.* **9**, 5521–5530 (2013).
43. Serra, T., Mateos-Timoneda, M. A., Planell, J. A. & Navarro, M. 3D printed PLA-based scaffolds: A versatile tool in regenerative medicine. *Organogenesis* **9**, 239–244 (2013).
44. Marcano, D. C. *et al.* Improved synthesis of graphene oxide. *ACS Nano* **4**, 4806–4814 (2010).
45. Fischer, E. W., Sterzel, H. J. & Wegner, G. Investigation of the structure of solution grown crystals of lactide copolymers by means of chemical reactions. *Kolloid-Zeitschrift Zeitschrift für Polym.* **251**, 980–990 (1973).
46. Vu, T.-L. & Barés, J. Soft grain compression: beyond the jamming point. (2019).
47. Vu, T. L., Barés, J., Mora, S. & Nezamabadi, S. Deformation Field in Diametrically Loaded Soft Cylinders. *Exp. Mech.* (2019). doi:10.1007/s11340-019-00477-4
48. Deshmukh, K., Khatake, S. M. & Joshi, G. M. Surface properties of graphene oxide reinforced polyvinyl chloride nanocomposites. *J. Polym. Res.* **20**, (2013).
49. Arima, Y. & Iwata, H. Effect of wettability and surface functional groups on protein adsorption and cell adhesion using well-defined mixed self-assembled monolayers. *Biomaterials* **28**, 3074–3082 (2007).
50. Dowling, D. P., Miller, I. S., Ardhaoui, M. & Gallagher, W. M. Effect of surface wettability and topography on the adhesion of osteosarcoma cells on plasma-modified polystyrene. *J. Biomater. Appl.* **26**, 327–347 (2011).
51. Webb, K., Hlady, V. & Tresco, P. A. Relative importance of surface wettability and charged functional groups on NIH 3T3 fibroblast attachment, spreading, and cytoskeletal organization. *J. Biomed. Mater. Res.* **41**, 422–430 (1998).
52. Zhang, C. *et al.* The surface grafting of graphene oxide with poly (ethylene glycol) as a reinforcement for poly (lactic acid) nanocomposite scaffolds for potential tissue engineering applications. *J. Mech. Behav. Biomed. Mater.* **53**, 403–413 (2016).
53. Campos, J. M., Ferraria, A. M., Botelho Do Rego, A. M., Ribeiro, M. R. & Barros-Timmons, A. Studies on PLA grafting onto graphene oxide and its effect on the ensuing composite films. *Materials Chemistry and Physics* **166**, 122–132 (2015).
54. Wittbrodt, B. & Pearce, J. M. The effects of PLA color on material properties of 3-D printed components. *Addit. Manuf.* **8**, 110–116 (2015).
55. Gong, M., Zhao, Q., Dai, L., Li, Y. & Jiang, T. Fabrication of polylactic acid/hydroxyapatite/graphene oxide composite and their thermal stability, hydrophobic and mechanical properties. *Journal of Asian*

- Ceramic Societies* **5**, 160–168 (2017).
56. Villar-Rodil, S., Paredes, J. I., Martínez-Alonso, A. & Tascón, J. M. D. Preparation of graphene dispersions and graphene-polymer composites in organic media. *J. Mater. Chem.* **19**, 3591–3593 (2009).
 57. Ramanathan, T. *et al.* Functionalized graphene sheets for polymer nanocomposites. *Nat. Nanotechnol.* **3**, 327–331 (2008).
 58. Xu, Y., Hong, W., Bai, H., Li, C. & Shi, G. Strong and ductile poly(vinyl alcohol)/graphene oxide composite films with a layered structure. *Carbon N. Y.* **47**, 3538–3543 (2009).
 59. Shen, Y. *et al.* Chemical and thermal reduction of graphene oxide and its electrically conductive polylactic acid nanocomposites. *Compos. Sci. Technol.* **72**, 1430–1435 (2012).
 60. Huda, M. S., Yasui, M., Mohri, N., Fujimura, T. & Kimura, Y. Dynamic mechanical properties of solution-cast poly(L-lactide) films. *Mater. Sci. Eng. A* **333**, 98–105 (2002).
 61. Ravi, P., Shiakolas, P. S. & Welch, T. R. Poly-L-lactic acid: Pellets to fiber to fused filament fabricated scaffolds, and scaffold weight loss study. *Addit. Manuf.* **16**, 167–176 (2017).
 62. Liao, K. H., Aoyama, S., Abdala, A. A. & Macosko, C. Does graphene change T_g of nanocomposites? *Macromolecules* **47**, 8311–8319 (2014).
 63. Huang, H.-D. *et al.* Improved barrier properties of poly (lactic acid) with randomly dispersed graphene oxide nanosheets. *J. Memb. Sci.* **464**, 110–118 (2014).
 64. Xu, Z. *et al.* Morphology, rheology and crystallization behavior of polylactide composites prepared through addition of five-armed star polylactide grafted multiwalled carbon nanotubes. *Polymer (Guildf)*. **51**, 730–737 (2010).
 65. Song, Y. *et al.* Measurements of the mechanical response of unidirectional 3D-printed PLA. *Mater. Des.* **123**, 154–164 (2017).
 66. Grémare, A. *et al.* Characterization of printed PLA scaffolds for bone tissue engineering. *J. Biomed. Mater. Res. - Part A* **106**, 887–894 (2018).
 67. Gregor, A. *et al.* Designing of PLA scaffolds for bone tissue replacement fabricated by ordinary commercial 3D printer. *J. Biol. Eng.* **11**, 1–21 (2017).
 68. Esposito Corcione, C. *et al.* Highly loaded hydroxyapatite microsphere/ PLA porous scaffolds obtained by fused deposition modelling. *Ceram. Int.* **45**, 2803–2810 (2019).
 69. Corcione, C. E. *et al.* 3D printing of hydroxyapatite polymer-based composites for bone tissue engineering. *J. Polym. Eng.* **37**, 741–746 (2017).

Supporting Information

3D printed graphene oxide-based scaffolds for bone tissue engineering

Habib Belaid^{1, 2}, Sakthivel Nagarajan¹, Catherine Teyssier², Jonathan Barés³, Sebastien Balme¹, Hélène Garay⁴, Vincent Huon³, David Cornu¹, Vincent Cavaillès^{2£} and Mikhael Bechelany^{1£}*

¹Institut Européen des Membranes, IEM-UMR 5635, Université Montpellier, CNRS, ENSCM, Montpellier, France

²IRCM, Institut de Recherche en Cancérologie de Montpellier, INSERM U1194, Université Montpellier, Montpellier F-34298, France

³LMGC, Laboratoire de Mécanique et Génie Civil, Univ Montpellier, CNRS, Montpellier, France

⁴C2MA, IMT mines d'Alès, France

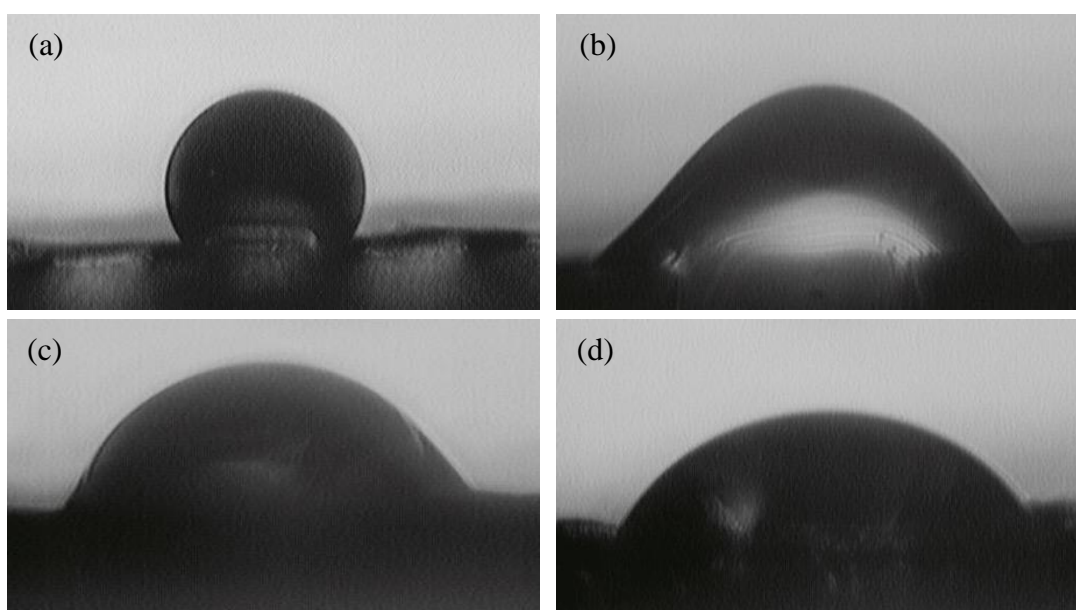
* Corresponding author:

mikhael.bechelany@umontpellier.fr, Phone: +33467149167, Fax: +33467149119

£ Co-last authors

Table S1. Printing parameters

	General features	Mechanical properties
First layer height	0.1mm	0.1mm
Other layers' height	0.2mm	0.2mm
Perimeters	1	1
Number of top & bottom layers	0	5
Infill percentage	70%	70%
Infill architecture	Rectilinear	Rectilinear
Combine infill layers	1	1
Infill angle	45°	0°
Bed temperature	60°C	60°C
Nozzle temperature (1 st layer)	215°C	215°C
Nozzle temperature (other layers)	210°C	210°C

**Figure S1.** Contact images of ultrapure water on: (a) PLA, (b) PLA/GO (0.1%), (c) PLA/GO (0.2%) and (d) – PLA/GO (0.3%) scaffolds.

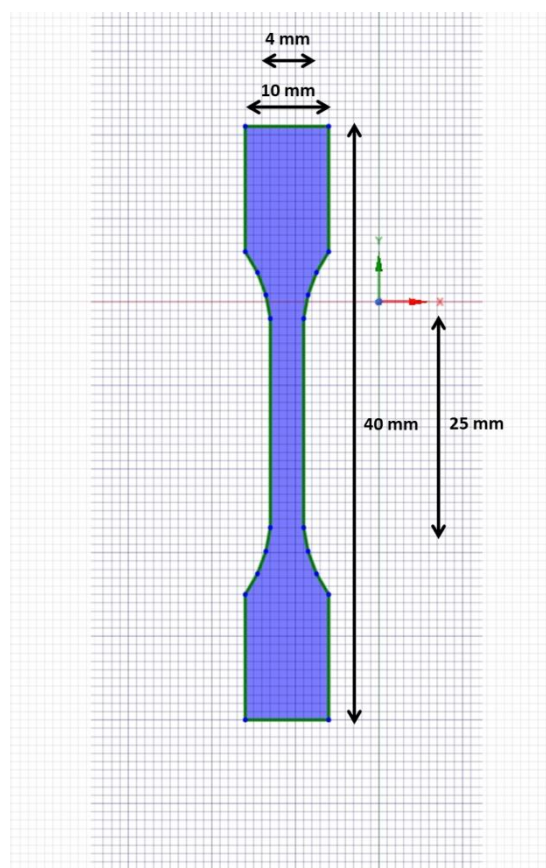


Figure S2. Schematic representation of PLA and PLA/GO scaffolds in dog bone shape for tensile strength testing.

Boron nitride-based nano-biocomposites: Design by 3D printing for bone tissue engineering

Habib Belaid^{1,2}, Sakthivel Nagarajan¹, Vincent Huon³, Jonathan Bares³, Sébastien Balme¹, Philippe Miele¹, David Cornu¹, Vincent Cavaillès,² Catherine Teyssier² and Mikhael Bechelany^{1}*

¹Institut Européen des Membranes, IEM-UMR 5635, Université Montpellier, CNRS, ENSCM, Montpellier, France

²IRCM, Institut de Recherche en Cancérologie de Montpellier, INSERM U1194, Université Montpellier, Montpellier F-34298, France

³LMGC, Laboratoire de Mécanique et Génie Civil, Université Montpellier, CNRS, Montpellier, France

* Corresponding author:

mikhael.bechelany@umontpellier.fr, Phone: +33467149167, Fax: +33467149119

Keywords: polylactic acid, boron nitride, bionanocomposite, 3D printing, tissue engineering

Abstract

The aim of this work was to develop a bioresorbable, biodegradable and biocompatible synthetic polymer with adequate mechanical properties for bone tissue engineering applications. Polylactic acid (PLA) biomimetic biodegradable scaffolds, generated by 3D printing using the fused deposition modeling method, were reinforced by incorporation of exfoliated boron nitride (EBN). The physicochemical analysis by X-ray diffraction and Raman spectroscopy confirmed the filler presence. Thermogravimetric analysis and differential scanning calorimetry showed that EBN incorporation did not modify the transition temperature, but decreased the polymer crystallinity. Morphology analysis by scanning electron microscopy indicated that the scaffolds had an average pore size of 500 μm . A tensile test demonstrated that the mechanical properties were not affected following EBN incorporation. Conversely, the surface roughness was modified upon EBN addition. Moreover, contact angle measurements showed a transition from a hydrophobic surface for the pure PLA to a hydrophilic surface for the PLA/EBN scaffold. Finally, the results of cytotoxicity, cell attachment and proliferation assays using MG-63 osteosarcoma cells indicated that PLA/EBN scaffolds are non-toxic, biocompatible and suitable for bone tissue engineering. Furthermore, EBN addition promoted MG-63 cell mineralization on the PLA scaffold. In conclusion, this new 3D printed nanocomposite is a promising scaffold for tissue engineering.

1. Introduction

For decades, bone disorder management has been a challenge due to the limited self-repair after critical damage¹. Therefore, passive artificial junctions are often implanted surgically². However, their removal after recovery is recommended, and this requires additional surgery. Regenerative tissue engineering allows overcoming the lack of bioactivity of passive implants. Scaffold-assisted regeneration methods are one of the most advantageous regenerative tissue engineering techniques. To facilitate cell adhesion and proliferation, it is crucial that the scaffold morphology, chemical composition and physico-chemical properties mimic the multi-scale structure of the bone extracellular matrix^{3,4}.

Biomimetic bone scaffolds are fabricated using biodegradable polymers, such as gelatin⁵, polycaprolactone⁶ and polylactic acid (PLA)⁷. PLA is a well-known and popular polymer synthesized from bio-sourced materials, such as corn and cellulose⁸, and currently the only one produced worldwide.⁹ It is widely used for biomedical applications, such as sutures¹⁰ and orthopedic fixation¹¹.

Unfortunately, such biodegradable synthetic materials usually have surface state properties that are incompatible with biological tissues¹². These properties could be improved by integrating boron nitride (BN), in its graphene form, in the scaffold formulation¹³. BN is an isoelectric analogue of graphite, non-toxic to cells, and BN-functionalized polymers are highly dispersed in aqueous and organic solvents¹⁴. Among the different nanofillers to reinforce polymer matrices, BN is electrically insulated and has major chemical, mechanical and thermal stability¹⁵. Moreover, BN nanosheet synthesis does not involve the use of acids or organic solvents¹⁶. BN use in biomedical fields has been much studied¹⁷. For example, our laboratory successfully exfoliated BN using gelatin and fabricated electrospun gelatin fibers reinforced with BN to improve their mechanical properties without affecting cell viability and proliferation¹⁸. Other studies have shown that BN nanotubes have a good potential for

biomedical applications^{14,19}. Moreover, boron-containing compounds are interesting for anticancer therapy²⁰, particularly in material composites for drug loading and release²¹. Moreover, BN nanotubes improve cell differentiation *in vitro*²² and *in vivo*²³.

In tissue engineering, many different methods have been used for scaffold fabrication, such as solvent casting/particulate leaching²⁴, emulsion freeze drying²⁵, phase separation²⁶ and electrospinning²⁷. However, these techniques are limited by the poor control of pore size and 3D architecture, and by the difficulty to process into different shapes. On the other hand, 3D printing allows printing customized structures (size, geometry, porosity) for tissue repair and regeneration^{28,29}. 3D printing techniques, such as stereolithography³⁰, 3D plotting³¹, selective laser sintering³², bioprinting³³ and fused deposition modeling (FDM)³⁴, are employed to print various polymers and polymer composites. Different studies have demonstrated that the 3D controlled architecture of the scaffold significantly affects its mechanical properties^{35,36} as well as cell adhesion and proliferation^{37,38}. Therefore, 3D printing can be used to put in shape BN-based nanocomposites in order to obtain a final material with improved mechanical properties. For example, FDM has been used to print different BN-based polymers, such as thermoplastic polyurethane or acrylonitrile-butadiene-styrene, with better thermal conductivity^{40,41}, while a photosensitive BN nanoplatelet-based polymer printed using stereolithography showed enhanced damping behavior⁴². A bio-ink containing poly-lactic-co-glycolic acid (PLGA)-based hexagonal BN was used to print a nanomaterial for bioelectronic applications. This study showed that the mechanical and thermal properties could be controlled using the right amount of filler without inducing any cytotoxicity⁴³. However, to the best of our knowledge, no study tried to improve BN capacity to enhance the bioactivity properties of 3D printed polymer materials for bone tissue engineering.

Therefore, the objective of this work was to create a 3D porous scaffold with controlled architecture and adequate composition to support cell adhesion and to promote bone tissue

formation. Using FDM, a 3D multifunctional PLA composite scaffold was fabricated with an interconnected porous structure and reinforced with exfoliated BN (PLA/EBN). Different parameters were analyzed to assess the influence of BN addition to PLA on the adhesion, proliferation and differentiation of osteosarcoma cells..

2. Experimental section

2.1. Materials. PLA pellets were purchased from Natureworks LLC. Type A gelatin (48722-500G-F) obtained from porcine skin (gel strength 170–195 g Bloom, CAS 9000-70-8), dichloromethane (CH_2Cl_2 , <99.9%, CAS 75-09-2), ethanol (96% vol, CAS 64-17-5), 37% formaldehyde (FA, 37 wt. % in H_2O , CAS 50-00-0), 25% glutaraldehyde (GTA, 25% in H_2O , CAS 111-30-8), cetylpyridinium chloride (CAS 6004-24-6), phosphate-buffered saline (PBS) (P44717) tablets, Triton X 100 (CAS 9002-93-11), bovine serum albumin (BSA) ($\geq 98\%$, CAS 9048-46-8), Mowiol 40-88 (CAS 9002-89-5), L-ascorbic acid (CAS 50-81-7), β -glycerophosphate ($\geq 99\%$, CAS 154804-51-0), Alizarin Red S (CAS 130-22-3), anti-actin antibody (clone CA15, A5441), dexamethasone ($\geq 80\%$, CAS 50-02-2), Hoechst 33342 ($\geq 98\%$, CAS 23491-52-3), and 3-(4,5-dimethylthiazol-2-yl)-2,5-diphenyl tetrazolium bromide (MTT, 98%, CAS 298-93-1) were purchased from Sigma-Aldrich. Combat Industrial Boron Nitride powder PHPP325B was purchased from Saint Gobain. Acetone ($\geq 99\%$ (GC), CAS 67-64-1) was purchased from Honeywell. Tween 20 (CAS 9005-64-5) was purchased from VWR International. Alexa-conjugated anti-mouse IgG (Alexa fluor 488, A11001) was purchased from ThermoFisher Scientific. MEM alpha medium (Gibco 12571-063), dimethyl sulfoxide (DMSO) (BDH Prolabo 23486.297), fetal bovine serum (FBS) (Eurobio CVFSVF00-01), penicillin/streptomycin (Gibco 15140-122) and 0.05% trypsin-EDTA (Gibco 25300-054) were used for cell cultures. MG-63 osteosarcoma cells were from ATCC.

2.2. Preparation of PLA/EBN scaffolds. BN sheets were exfoliated from BN powder as previously described²⁴. Briefly, 1 g of BN powder was added to 20% gelatin solution (100 mL) prepared by dissolving gelatin in water at 75°C. To facilitate exfoliation, the solution was sonicated using an ultrasonic probe system (SONOPULS HD 3100) (pulse on/off for 1 second) with 60% amplitude at 50°C overnight. EBN was separated by centrifugation at 6000 rpm for 30 minutes. The resulting precipitates were dried at 80°C for 48 hours and then calcined at 600°C in air for 2 hours to obtain EBN.²⁵

The PLA (10 mL of 10% (w/v)) solution was prepared using dichloromethane as solvent. EBN (0.1 wt %) was dispersed in acetone (1 mg per mL) and placed in an ultrasonic bath for 15 minutes. The solution containing EBN was introduced in the polymer solution under constant magnetic stirring until homogeneous. The PLA/EBN dispersion was poured into a Teflon dish and dried at room temperature overnight. The obtained dried polymer was a film that was cut into pieces and introduced into a single screw extruder (Noztek pro) at an extrusion temperature of about 200°C. The nozzle diameter of the extruder (1.75 mm) was suitable for the 3D printer. A filament with a diameter of 1.75 mm was obtained and used for 3D printing with a Prusa Research MK2S 3D printer.

The scaffold was modeled using the computer-aided design (CAD) software (Design Spark Mechanical). Once the scaffold shape was determined, a STL file was created to be analyzed by the Prusa 3D Slicer software. All printing parameters are given in Table S1.

2.3. Chemical and structural properties. Raman spectra of scaffolds and films were obtained in ambient conditions using a HORIBA Jobin Yvon microscope equipped with a 659.55 nm laser. The X-ray diffraction (XRD) patterns of PLA and PLA/EBN scaffolds were recorded using CuK α radiation, 2 θ range of 10-70° with a scan speed of 2° min⁻¹, using the PANalytica Xpert powder XRD system. The Fourier transform infrared (FTIR) spectrum of

PLA and PLA/EBN nanocomposites was recorded with a NEXUS instrument, equipped with an attenuated total reflection accessory in the frequency range of 600–4000 cm^{-1} . For FTIR spectrometry, resolution was 4 cm^{-1} , and the signals were averaged from 32 scans.

2.4. Thermal properties. The different scaffolds were analyzed using a DSC 2920 differential scanning calorimeter, equipped with the RCS90 cooling system. Samples were accurately weighed ($\approx 4\text{mg}$) in an aluminum TA pan and sealed. An empty sealed pan was used as a reference. Samples were first cooled to 25°C and then heated up to 210°C with a heating rate of 10°C.min⁻¹ using nitrogen as purge gas. The degree of polymer crystallinity was calculated with the following formula: $\chi = \frac{\Delta H_f - \Delta H_{cf}}{\Delta H_{\infty}}$ where ΔH_f is the enthalpy of fusion, ΔH_{cf} is the enthalpy of cold crystallization, and ΔH_{∞} is the reference melting enthalpy for 100% crystalline polymer ($\Delta H_{\infty} = 93 \text{ J.g}^{-1}$).

The resulting differential scanning calorimetry (DSC) curves were analyzed to determine the polymer glass transition (T_g) temperature, melting temperature (T_m), cold crystallization temperature (T_{cc}), and crystallinity (X_c). The thermogravimetric analysis (TGA) was performed with a TGA G500 apparatus (TA Instruments). About 10mg of each sample was heated from room temperature to 900°C in air atmosphere at a heating rate of 10°C min⁻¹.

2.5. Mechanical properties. The mechanical properties of the 3D printed PLA/EBN scaffold were characterized with standard centimeter samples loaded using a MTS (1/ME) traction machine coupled with a 5 kN force sensor. Samples were printed in the shape of a dog bone (40 mm length, 4 mm width, and 1.5 mm thick) (Figure S1), clamped between jaws, and pulled at a constant speed of 0.01 mm s⁻¹ until they broke. During loading, samples were imaged with a 16 Mb camera (SVS-VISTEK) at 1 Hz. Initially, samples were randomly patterned with thin black paint to perform digital image correlation (DIC). Using a DIC

algorithm dedicated to large deformations and already presented^{44,45}, the sample strain changes were reliably computed without inaccuracy coming from the machine and the jaws. Linear elastic regions from the stress–strain graphs were used to calculate the Young's modulus from at least three trials. The stress at which samples began to break was also measured.

2.6. Morphological properties. The size, morphology, and microstructure of the scaffolds were analyzed using a HITACHI S4800 scanning electron microscopy (SEM) system. For this, scaffolds were coated with platinum using a Polaron SC7620 Mini Sputter Coater. The Image J software was used to calculate the diameter of the struts and of the obtained pores. A stylus profilometer STIL equipped with a CHR1000 captor was used to characterize the 3D topography of 10mm cylinder surface areas of 3D printed PLA and PLA/EBN scaffolds. Determinations were made on two different locations of 2*2 mm for each scaffold with 5 μm step. The SurfaceMap software was used for data post-treatment. The chosen area roughness parameter was Sa (i.e., the surface arithmetical mean height).

A B-CAM-21-BW (CCCIR) monochrome camera and a Led R60 lamp (Conrad) were used to measure the contact angles of ultrapure water on 3D printed PLA and PLA/EBN scaffolds by the sessile drop method. Equilibrium contact angles (considered at 60 seconds) were measured for 5 μL droplet volumes in three different locations for each condition. One Touch Grabber and Image J were used to calculate the obtained contact angles.

2.7. Cell viability and adhesion assays. Scaffolds were sterilized with ethanol for 30 minutes and under UV light (405 nm) for 1 hour. MG-63 osteosarcoma cells were cultured on the sterilized scaffolds in MEM alpha, 10% FBS and 1% penicillin/streptomycin for up to 7 days before cell viability and adhesion assays. Cell viability and proliferation were analyzed with

the MTT assay. At different time points during culture, 100 μL of culture medium containing 0.05 $\text{mg}\cdot\text{mL}^{-1}$ of MTT solution was added to the cultures for 3h. MTT reduction by living cells leads to the production of purple-colored formazan crystals that were solubilized by addition of 100 μL of DMSO (BDH Prolab 23486.297). The absorbance of the formazan solution was recorded at 560 nm using a Multiskan plate reader (Thermos, USA). For the adhesion assay, MG-63 cells were fixed in 4% formaldehyde (500 $\mu\text{L}/\text{well}$) at room temperature for 20 minutes. Fixed cells were washed with PBS, permeabilized with PBS/0.1% Triton X 100 (Sigma) for 15 minutes, and incubated with PBS/1% BSA solution for 3 hours. Then, the cell cytoskeleton was stained with an anti-actin antibody at 4°C overnight. After two washes with PBS/0.05% Tween 20, an Alexa-conjugated anti-mouse IgG secondary antibody was added with Hoechst 33342, to stain the nuclei, at room temperature for 1 hour. Samples were mounted in Mowiol and fluorescent images were recorded using a fluorescent microscope (DM6000 Leica).

2.8. Mineralization assay. MG-63 cells were plated in Petri dishes on the scaffolds and grown until confluence (day 0). Then, medium was switched to differentiation medium supplemented with ascorbic acid (50 $\text{mg}\cdot\text{mL}^{-1}$), β -glycerophosphate (5 mM) and dexamethasone (10^{-8} M), and refreshed every 48 hours. Formation of mineralized nodules was monitored at day 0, 14 and 21 by Alizarin Red-S staining. Briefly, cells were rinsed twice with PBS followed by fixation in 4% formaldehyde at room temperature for 20 minutes. Then, cells were rinsed twice with PBS (pH 4.2) and stained with 40 mM Alizarin Red-S (pH 4.2) at room temperature for 20 minutes, and extensively rinsed with water. For quantification, the staining was eluted with 10% (wt/vol) cetylpyridinium chloride, and the supernatant absorbance was measured at 540 nm using a microplate reader (Bio-Rad). Differences between groups were assessed with the Student's *t*-test and were considered

significant at $*p<0.05$ and $**p<0.005$.

3. Results and discussion

3.1. Structural and chemical characterization of the scaffolds. To reinforce PLA, EBN fillers were added to the polymer matrix at 0.1% wt. The composite was extruded *via* a single screw extruder and put in shape using a FDM system. PLA before extrusion is denoted as PLA-film.

BN Raman spectrum showed a characteristic band at 1390 cm^{-1} that corresponded to the E2g mode (Figure 1a). PLA-film spectrum showed the characteristic bands at 1127, 1294, 1447 and 1764 cm^{-1} (asterisks in Figure 1a). In the PLA/EBN spectrum, the morphology and intensity of the characteristic Raman band at 1390 cm^{-1} changed compared with the PLA spectrum (arrows in Figure 1a). This change confirmed EBN incorporation in the polymer matrix.

To understand PLA organization and BN interactions with the polymer matrix during the nanocomposite fabrication, FTIR spectra were recorded (Figure 1b). The two major EBN bands observed at 1271 and 763 cm^{-1} were assigned to B–N stretching and out-of-plane B–N bending in the hexagonal rings, respectively. A slight difference between the bands at 1231 cm^{-1} of pure PLA and PLA/EBN was observed (arrows). This could be due to EBN incorporation, but cannot be confirmed because the absorbance of the PLA bands was greater than that of EBN. In addition, the EBN bands were in the same range as those of PLA and thus were covered by them.

The XRD patterns of the scaffolds are shown in Figure 1c. PLA-film showed four characteristics peaks at $2\theta = 15, 17, 19$ and 23° that described the alpha form of PLA⁴⁶. Concerning the PLA/EBN composites before extrusion, the characteristic PLA peaks were maintained, although they were broader, possibly due to micro-stresses induced by BN in the polymer matrix. The peaks at $2\theta = 26^\circ, 41.5^\circ$ and 43.7° corresponding to the (002), (100), and

(101) planes of BN³ did no longer appear, showing the good BN exfoliation in the PLA matrix.

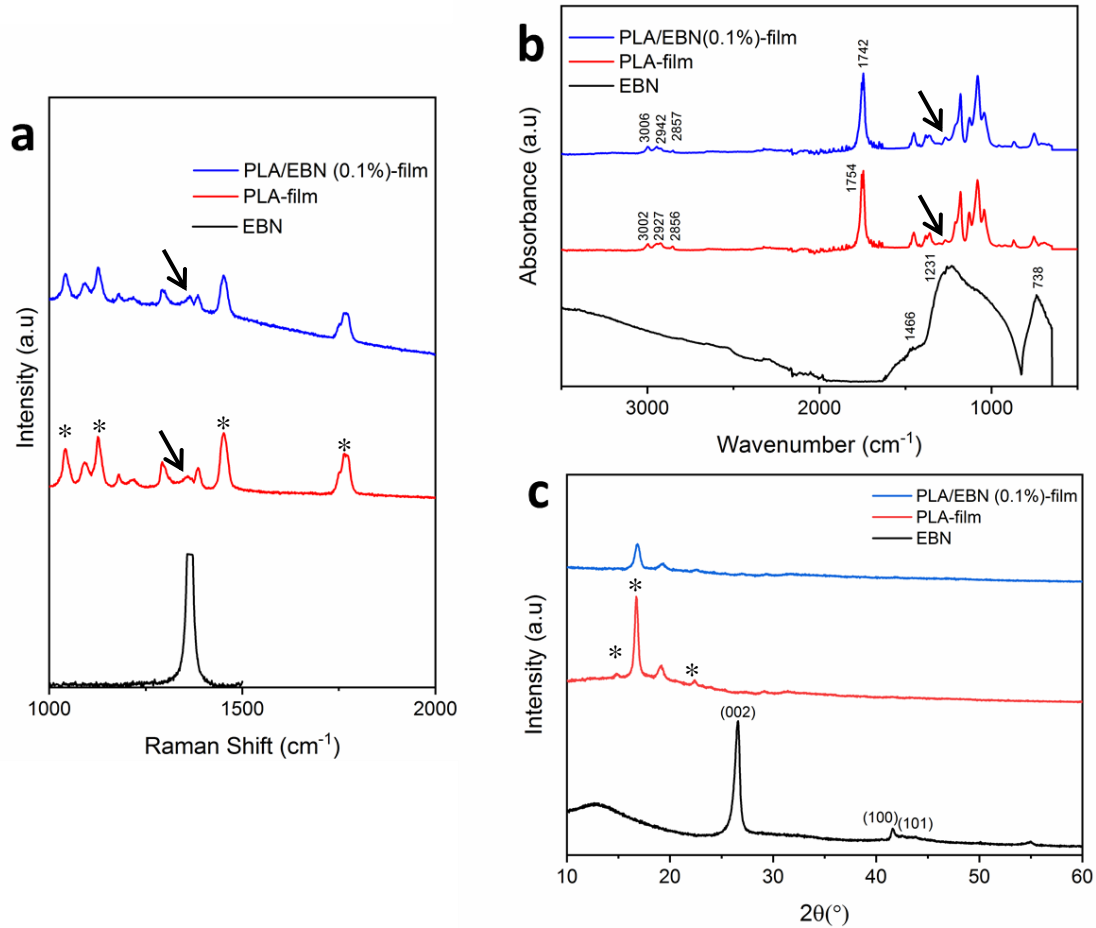


Figure 1. Chemical and structural properties of the nanocomposites: (a) Raman spectroscopy, (b) FTIR spectra, and (c) XRD diffractograms of exfoliated boron nitride (EBN), PLA-film, and PLA/EBN nanocomposites.

3.2. Thermal analysis of the PLA/EBN scaffolds. BN influence on PLA thermal stability was monitored by TGA analysis (Figure 2a). For PLA, the 1% weight loss observed below 200°C was due to the adsorbed water. The second major weight loss, observed between 300 and 400°C, showed the degradation of the PLA polymer with a maximum loss at 298°C. The third major weight loss, observed from ~410°C, was due to the thermochemical decomposition of the remaining organic content.

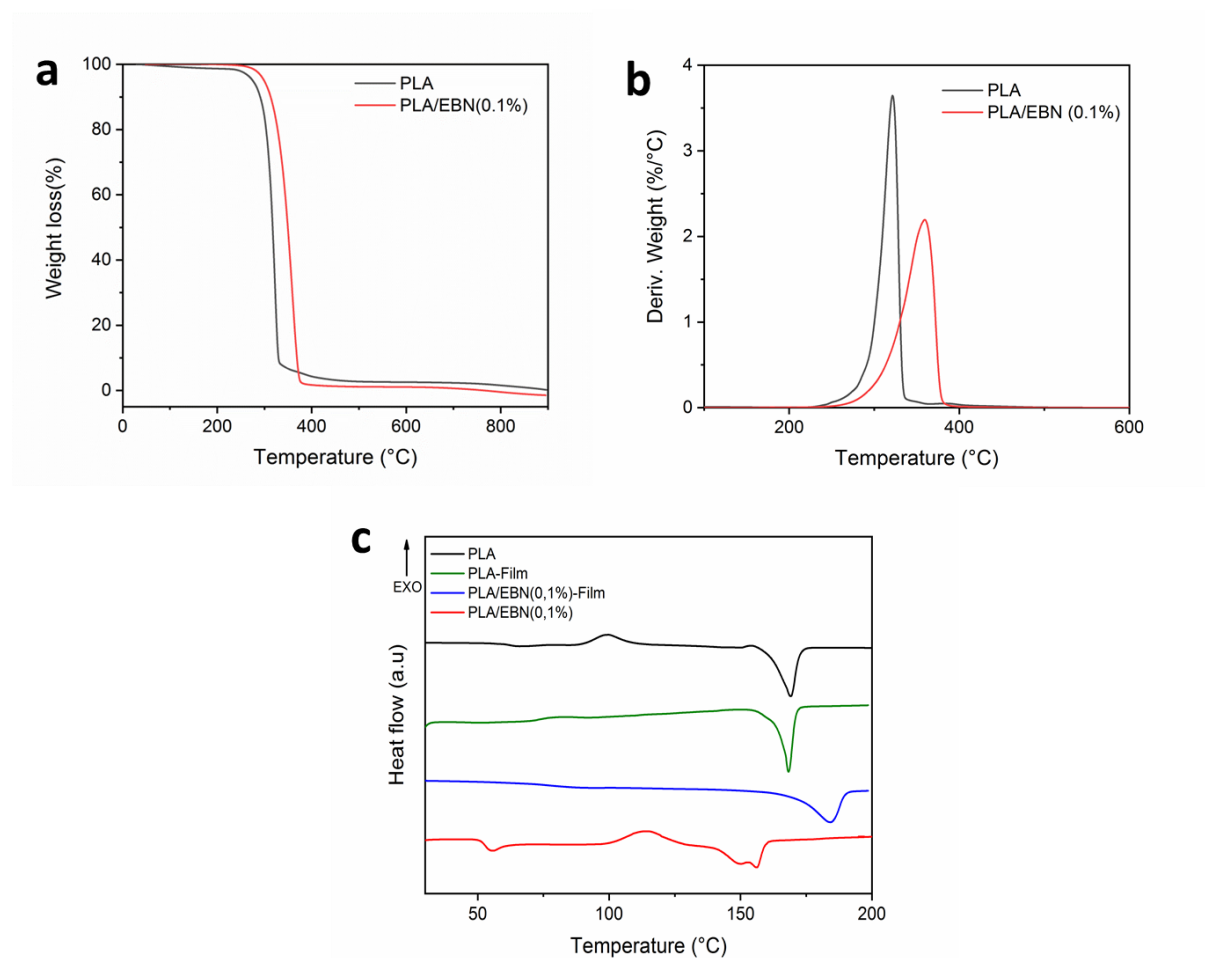


Figure 2. Thermal properties of nanocomposite materials: (a) TGA, and (b) derivative TGA curves of 3D printed PLA/EBN nanocomposites; (c) representative DSC graphs showing Tg, Tcc and Tm of PLA and PLA/EBN nanocomposites.

Concerning PLA/EBN, the first weight loss was observed at 225°C. The major decrease that corresponded to the degradation of the polymer composite was observed at 359°C, and the last degradation step was observed from 400°C with a weight loss of 3%.

Moreover the peak of maximum degradation temperature shifted from 298°C for PLA to 359°C for the nanocomposites with 0.1% of BN, as shown in the derivative weight curves (Figure 2b). The two curves showed little difference; however, this mass loss corresponding to the cleavage of the polymer chains started with an offset of 62°C for PLA/BN compared with pure PLA. This may be due to the relatively small amount of BN particles present in the sample, and to a low thermal barrier effect caused by BN. BN particles are expected to retard degradation, and randomly protect a few inner layers of polymer. BN trapped the degradation

products inside the polymer by dissipating the heat in the planar direction. When the heat energy is absorbed, the thermal equilibrium is reached⁴⁷. Samples exhibited strong interaction with BN, which resulted in the high thermal stability of the composites.

EBN influence on PLA crystallinity and on T_g , T_{cc} and T_m were evaluated by DSC analysis (Figure 2c). Enthalpy of fusion, glass transition and melting point were measured and are summarized in Table 1, together with the calculated crystallinity. The T_g and T_m of PLA were 59°C and 168°C before (PLA-film) and 61°C and 169°C after extrusion, respectively. This indicated that the extrusion process did not affect PLA thermal properties. After extrusion, PLA showed a cold crystallization peak at 100°C that was not present in the PLA-film before extrusion (Figure 2c), as reported in a previous study⁴⁸.

Table 1. Temperatures, enthalpies of different thermal transitions and crystallinity of PLA and PLA/EBN

Samples	T_g (°C)	T_m (°C)	ΔH_f (J/g)	ΔH_{cf} (J/g)	χ (%)
PLA-film	59	168	30	-	32
PLA	61	169	30	10	21
PLA/EBN-film	59	155	18	-	19
PLA/EBN	53	156	22	17	5

In line with these observations, PLA crystallinity was lower after (21%) than before (32%) extrusion, and this change could have been caused by the extrusion process⁴⁹. For PLA reinforced with 0.1% BN before extrusion, the T_g was 59°C, and decreased to 53°C after extrusion. This was followed by an exothermic cold crystallization peak at 110°C (Figure 2c). Addition of EBN significantly decreased the PLA T_m from 169°C to 156°C after extrusion, and this was associated with the appearance of a double melting peak at 156 °C (Figure 2c). This suggests the presence of two sizes of crystallites that could have been induced by BN charges in the polymer matrix.

After extrusion, EBN addition decreased PLA crystallinity from 21% to 5%. This lower crystallinity of the PLA/EBN scaffold could be due to the number of interacting sites between the polymer matrix and the filler that might reduce the PLA chain mobility. Additionally, EBN aggregates may have physically disturbed the polymer crystallization. Finally, thermal analysis by TGA and DSC showed that EBN presence in the polymer matrix did not affect filament extrusion. The 3D printing conditions also were not influenced by EBN addition. However, EBN increased the thermal stability of the nanocomposite scaffolds.

3.3. Mechanical properties of the 3D printed nanocomposites. Composites used for bone tissue engineering applications must withstand high loads. Therefore, the mechanical properties of PLA and PLA/EBN nanocomposites were analyzed using dog bone shaped samples (Figure S1). For bone engineering, the elastic region is a very important parameter and therefore, it was important to determine the influence of EBN addition on PLA elastic modulus. The Young's modulus of PLA increased with EBN from 2 to 2.2 GPa (not statistically significant) (Figure 3). Similarly, tensile stress at break and Poisson's ratio were not significantly different in PLA and PLA/EBN samples. This demonstrates that EBN addition did not affect the mechanical properties of the PLA scaffold, and that EBN can be used as a filler to improve the bioactivity of PLA scaffolds without effects on their mechanical properties.

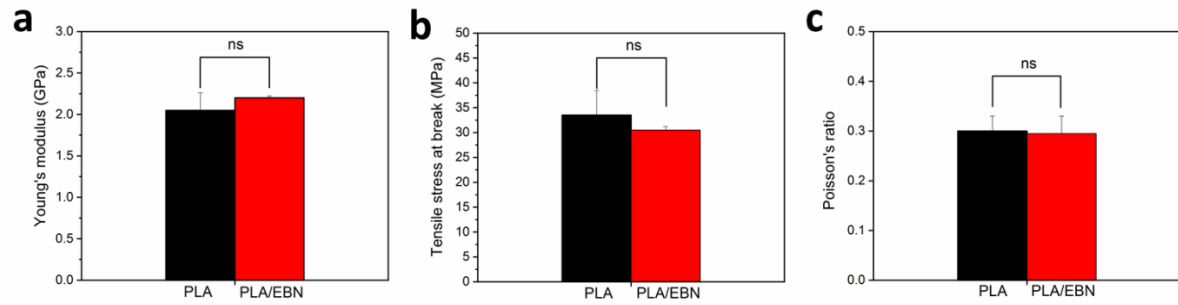


Figure 3. Mechanical properties of the scaffolds: (a) Young's modulus, (b) Tensile stress at break, and (c) Poisson's ratio of PLA and PLA/EBN nanocomposites (ns= not significant).

3.4. Morphological analysis of PLA/EBN scaffolds. To facilitate bone regeneration, scaffolds with a porous interconnected network and pore size between 300 μm and 500 μm were generated. SEM was used to analyze EBN effect on the morphology and pore size of the 3D printed PLA/EBN scaffolds. SEM micrographs revealed the scaffold porous morphology (Figures 4a and b). The pores size of PLA scaffolds was 405 μm (± 20) with a wall width of 380 μm (± 65), which is crucial for osteoblast cell infiltration and good mineralization^{50–52}. EBN addition to the PLA resulted in a modification of the composite filament. This change led to an increase in pore size during printing. The reduction of the walls separating the pores led to pore enlargement in the scaffold.

The 3D topography images allowed comparing the surfaces of the PLA and PLA/EBN composite scaffolds (Figures 4c and 4d). The scaffold surface was modified upon EBN incorporation in the polymer matrix. Scaffolds with EBN incorporation presented higher positive values of Sa than PLA scaffolds, due to the filler presence at the surface and fine dispersions in the polymer matrix (Table 2).

For bone tissue engineering application, the surface chemistry of 3D scaffold is very important. It influences the material hydrophilicity and is required for cell attachment to the scaffold surface to proliferate and differentiate for bone regeneration⁵³. The measurements of water contact angles (Figures 4e and f) showed reduced values for PLA/EBN scaffolds

compared with PLA (Table 2). In summary, EBN addition significantly improved the PLA scaffold hydrophilic character.

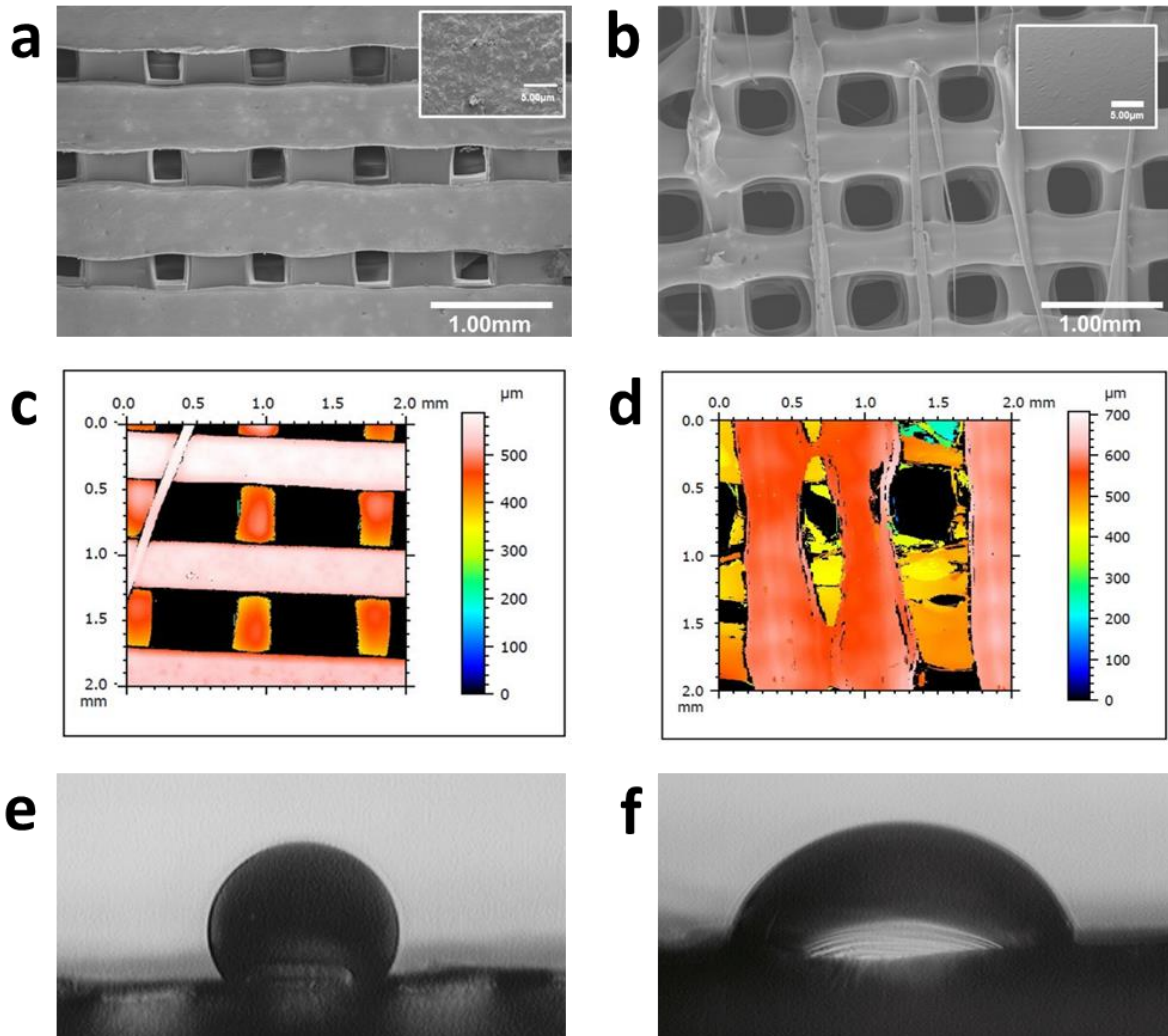


Figure 4. Scanning electron micrographs of FDM-based 3D printed PLA and PLA/EBN scaffolds: Top view of the architecture of 3D printed (a) PLA and (b) PLA/EBN scaffolds; inset, zoom showing the surface. Topography of the scaffolds: Representative 3D images of the surface roughness of PLA (c) and PLA/EBN (d) scaffolds. Images showing the contact angle of water on: (e) PLA and (f) PLA/EBN scaffolds.

Table 2. Roughness parameters and contact angles of PLA and PLA/EBN scaffolds with H₂O: Sa – arithmetical mean height of the surface.

Samples	Pore size (µm)	Wall width (µm)	Sa (µm)	Contact angles (°)
PLA	405 ± 20	380 ± 65	5.8 ± 1.5	118 ± 2
PLA/EBN	500 ± 80	350 ± 25	9.3 ± 2.7	81 ± 13

3.5. Biological studies. The biocompatibility of 3D printed PLA/EBN scaffolds was investigated using MG-63 osteosarcoma cells that display osteogenic potential⁵⁴. EBN effect

on cell viability, attachment and proliferation was analyzed and compared with the results obtained for cell grown on PLA scaffolds and without scaffolds (control). EBN presence (0.1%) in the scaffold did not affect viability (MTT assay) at day 4 and day 7 of culture (Figure 5a). This suggests that 3D printed PLA/EBN scaffolds do not release any toxic fragment and that direct contact of cells with EBN is possible without damage.

Cell attachment and proliferation on the scaffolds were monitored by staining the cytoskeleton with an anti-actin antibody and nuclei with Hoechst 333342 at day 1, 4 and 7 until maximum confluence. EBN incorporation did not affect cell attachment (Figure 5b). Similarly, quantification of cell proliferation using the MTT assays at day 1, 4 and 7 showed that the PLA/EBN scaffolds promoted cell proliferation compared with PLA (Figure 5c), indicating that the PLA/BN scaffolds are biocompatible.

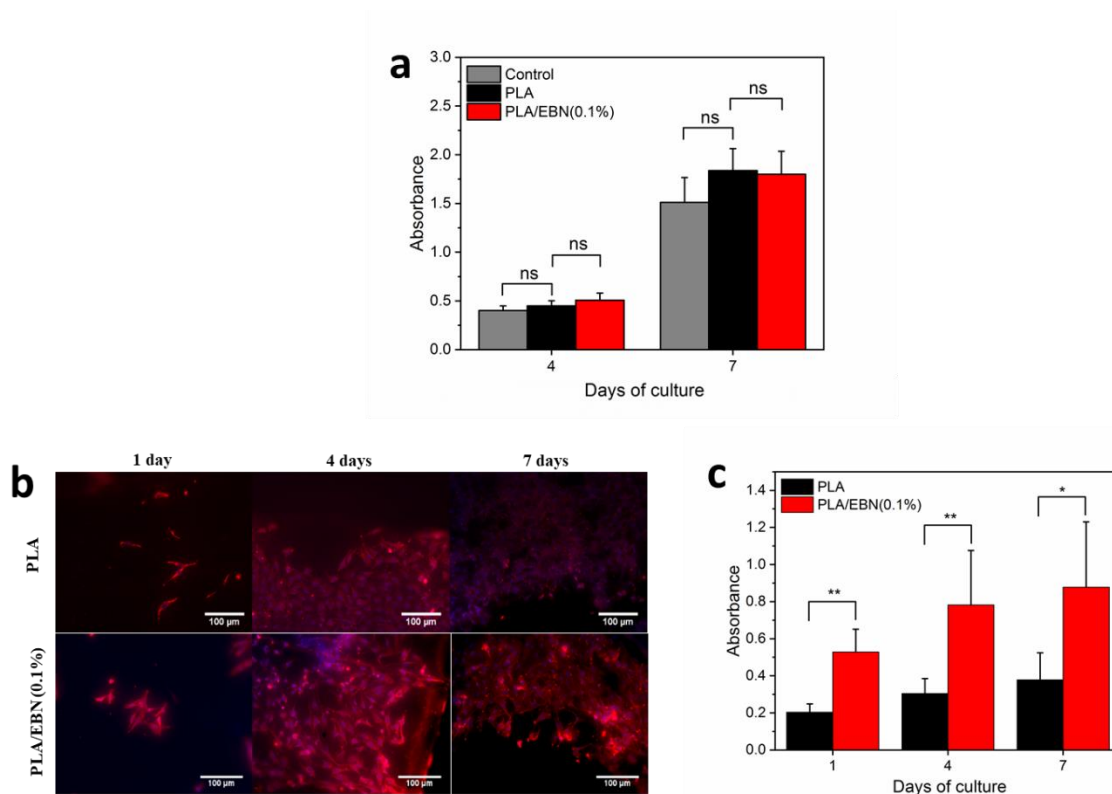


Figure 5. (a) Cell viability of MG-63 cells grown on PLA and PLA/EBN scaffolds assessed with the MTT at day 4 and 7 (ns = not significant). (b) MG-63 cell attachment on PLA nanocomposites was analyzed by immunofluorescence staining of actin (red), and DNA staining (blue) at the indicated time points, and (c) cell proliferation (MTT assay) (ns = not significant, * $p < 0.05$, ** $p < 0.005$).

Finally, mineralization (i.e., calcium deposition on scaffolds by MG-63 cells) was determined by colorimetric quantification after Alizarin Red-S staining at day 1, 14 and 21 of culture (Figure 6). A significantly higher calcium deposition was observed at day 21 in cultures with PLA/EBN scaffolds compared with PLA scaffolds, demonstrating the good mineralization on scaffolds. This effect could be linked to EBN interaction with the matrix and the modification of surface states or pore size upon EBN incorporation. These results demonstrate that EBN is biocompatible and shows good bioactivity by enhancing MG-63 cell mineralization activity.

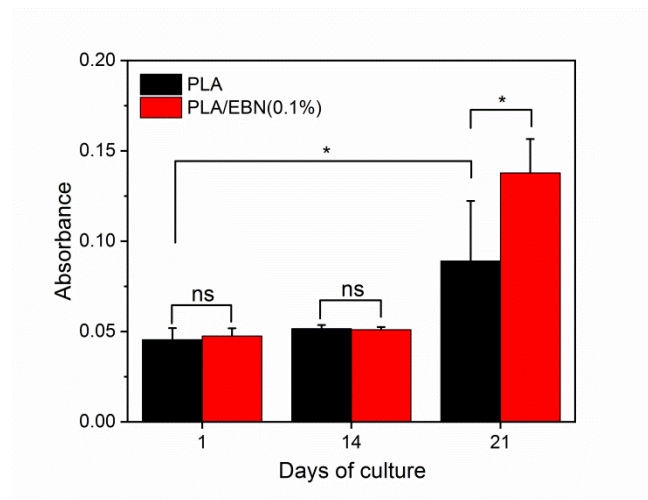


Figure 6. Mineralization evaluated by Alizarin Red-S staining of MG-63 cells cultured on PLA and PLA/EBN nanocomposite scaffolds at the indicated time points after switching to differentiation medium (ns = not significant, * $p < 0.05$).

4. Conclusions

This study shows that it is possible to fabricate PLA/EBN nanocomposites with controlled morphology and a network of interconnected pores around 500 μm using FDM-assisted 3D printing. Altogether, our results demonstrated that EBN incorporation 1) increased the polymer surface roughness and decreased its hydrophobicity, 2) enhanced the polymer thermal stability, 3) decreased the polymer crystallinity, 4) did not affect the scaffold mechanical properties, and 5) promoted MG-63 cell attachment, proliferation, and differentiation. Our data clearly indicate that PLA reinforcement with 0.1% EBN could

16. Biscarat, J., Bechelany, M., Pochat-Bohatier, C. & Miele, P. Graphene-like BN/gelatin nanobiocomposites for gas barrier applications. *Nanoscale* **7**, 613–618 (2015).
17. Lahiri, D. *et al.* Boron nitride nanotube reinforced polylactide–polycaprolactone copolymer composite: mechanical properties and cytocompatibility with osteoblasts and macrophages in vitro. *Acta Biomater.* **6**, 3524–3533 (2010).
18. Nagarajan, S. *et al.* Design of graphene-like boron nitride/gelatin electro spun nanofibers as new bio nanocomposite material for tissue engineering.
19. Ciofani, G., Raffa, V., Mencias, A. & Cuschieri, A. Cytocompatibility, interactions, and uptake of polyethyleneimine-coated boron nitride nanotubes by living cells: Confirmation of their potential for biomedical applications. *Biotechnol. Bioeng.* **101**, 850–858 (2008).
20. I. Scorei, R. & Popa, R. Boron-Containing Compounds as Preventive and Chemotherapeutic Agents for Cancer. *Anticancer. Agents Med. Chem.* **10**, 346–351 (2012).
21. Weng, Q. *et al.* Highly water-soluble, porous, and biocompatible boron nitrides for anticancer drug delivery. *ACS Nano* **8**, 6123–6130 (2014).
22. Li, X. *et al.* Boron nitride nanotube-enhanced osteogenic differentiation of mesenchymal stem cells. *J. Biomed. Mater. Res. - Part B Appl. Biomater.* (2016). doi:10.1002/jbm.b.33391
23. Salvetti, A. *et al.* In vivo biocompatibility of boron nitride nanotubes: Effects on stem cell biology and tissue regeneration in planarians. *Nanomedicine* (2015). doi:10.2217/nnm.15.46
24. Liao, C. *et al.* Fabrication of porous biodegradable polymer scaffolds using a solvent merging/particulate leaching method. *J. Biomed. Mater. Res. An Off. J. Soc. Biomater. Japanese Soc. Biomater. Aust. Soc. Biomater. Korean Soc. Biomater.* **59**, 676–681 (2002).
25. Sultana, N. & Wang, M. PHBV/PLLA-based composite scaffolds fabricated using an emulsion freezing/freeze-drying technique for bone tissue engineering: surface modification and in vitro biological evaluation. *Biofabrication* **4**, 15003 (2012).
26. Huang, Y. X., Ren, J., Chen, C., Ren, T. B. & Zhou, X. Y. Preparation and properties of poly (lactide-co-glycolide)(PLGA)/nano-hydroxyapatite (NHA) scaffolds by thermally induced phase separation and rabbit MSCs culture on scaffolds. *J. Biomater. Appl.* **22**, 409–432 (2008).
27. Nagarajan, S. *et al.* Design of graphene oxide/gelatin electrospun nanocomposite fibers for tissue engineering applications. *RSC Adv.* **6**, 109150–109156 (2016).
28. Murphy, S. V & Atala, A. 3D bioprinting of tissues and organs. *Nat. Biotechnol.* **32**, 773 (2014).
29. Chia, H. N. & Wu, B. M. Recent advances in 3D printing of biomaterials. *J. Biol. Eng.* **9**, 4 (2015).
30. Gauvin, R. *et al.* Microfabrication of complex porous tissue engineering scaffolds using 3D projection stereolithography. *Biomaterials* **33**, 3824–3834 (2012).
31. Luo, Y., Lode, A., Akkineni, A. R. & Gelinsky, M. Concentrated gelatin/alginate composites for fabrication of predesigned scaffolds with a favorable cell response by 3D plotting. *RSC Adv.* **5**, 43480–43488 (2015).
32. Williams, J. M. *et al.* Bone tissue engineering using polycaprolactone scaffolds fabricated via selective laser sintering. *Biomaterials* **26**, 4817–4827 (2005).
33. Murphy, S. V. & Atala, A. 3D bioprinting of tissues and organs. *Nat. Biotechnol.* **32**, 773–785 (2014).
34. Serra, T., Planell, J. A. & Navarro, M. High-resolution PLA-based composite scaffolds via 3-D printing technology. *Acta Biomater.* **9**, 5521–5530 (2013).
35. Senatov, F. S. *et al.* Mechanical properties and shape memory effect of 3D-printed PLA-based porous scaffolds. *J. Mech. Behav. Biomed. Mater.* **57**, 139–148 (2016).
36. Gómez, S., Vlad, M. D., López, J. & Fernández, E. Design and properties of 3D scaffolds for bone tissue engineering. *Acta Biomater.* **42**, 341–350 (2016).
37. Rogina, A. *et al.* Macroporous poly(lactic acid) construct supporting the osteoinductive porous chitosan-based hydrogel for bone tissue engineering. *Polymer* **98**, 172–181 (2016).
38. Rosenzweig, D. H., Carelli, E., Steffen, T., Jarzem, P. & Haglund, L. 3D-printed ABS and PLA scaffolds for cartilage and nucleus pulposus tissue regeneration. *Int. J. Mol. Sci.* **16**, 15118–15135 (2015).
39. Bose, S., Vahabzadeh, S. & Bandyopadhyay, A. Bone tissue engineering using 3D printing. *Mater. today* **16**, 496–504 (2013).
40. Liu, J., Li, W., Guo, Y., Zhang, H. & Zhang, Z. Improved thermal conductivity of thermoplastic polyurethane via aligned boron nitride platelets assisted by 3D printing. *Compos. Part A Appl. Sci.*

- Manuf.* **120**, 140–146 (2019).
41. Quill, T. J. *et al.* Thermal and mechanical properties of 3D printed boron nitride – ABS composites. *Appl. Compos. Mater.* **25**, 1205–1217 (2018).
42. Bustillos, J., Montero-Zambrano, D., Loganathan, A., Boesl, B. & Agarwal, A. Stereolithography-based 3D printed photosensitive polymer/boron nitride nanoplatelets composites. *Polym. Compos.* **40**, 379–388 (2019).
43. Guiney, L. M. *et al.* Three-Dimensional Printing of Cytocompatible, Thermally Conductive Hexagonal Boron Nitride Nanocomposites. *Nano Lett.* **18**, 3488–3493 (2018).
44. Vu, T.-L. & Barés, J. Soft grain compression: beyond the jamming point. (2019).
45. Vu, T. L., Barés, J., Mora, S. & Nezamabadi, S. Deformation Field in Diametrically Loaded Soft Cylinders. *Exp. Mech.* (2019). doi:10.1007/s11340-019-00477-4
46. Campos, J. M., Ferraria, A. M., Botelho Do Rego, A. M., Ribeiro, M. R. & Barros-Timmons, A. Studies on PLA grafting onto graphene oxide and its effect on the ensuing composite films. *Materials Chemistry and Physics* **166**, 122–132 (2015).
47. Barkoula, N.-M., Alcock, B., Cabrera, N. O. & Peijs, T. Fatigue properties of highly oriented polypropylene tapes and all-polypropylene composites. *Polym. Polym. Compos.* **16**, 101–113 (2008).
48. Huda, M. S., Yasui, M., Mohri, N., Fujimura, T. & Kimura, Y. Dynamic mechanical properties of solution-cast poly(L-lactide) films. *Mater. Sci. Eng. A* **333**, 98–105 (2002).
49. Ravi, P., Shiakolas, P. S. & Welch, T. R. Poly-L-lactic acid: Pellets to fiber to fused filament fabricated scaffolds, and scaffold weight loss study. *Addit. Manuf.* **16**, 167–176 (2017).
50. Di Luca, A. *et al.* Gradients in pore size enhance the osteogenic differentiation of human mesenchymal stromal cells in three-dimensional scaffolds. *Sci. Rep.* **6**, 1–13 (2016).
51. Matsiko, A., Gleeson, J. P. & O'Brien, F. J. Scaffold Mean Pore Size Influences Mesenchymal Stem Cell Chondrogenic Differentiation and Matrix Deposition. *Tissue Eng. Part A* **21**, 486–497 (2014).
52. Bružauskaitė, I., Bironaitė, D., Bagdonas, E. & Bernotienė, E. Scaffolds and cells for tissue regeneration: different scaffold pore sizes—different cell effects. *Cytotechnology* **68**, 355–369 (2016).
53. Mitra, J., Tripathi, G., Sharma, A. & Basu, B. Scaffolds for bone tissue engineering: Role of surface patterning on osteoblast response. *RSC Advances* (2013). doi:10.1039/c3ra23315d
54. Czekanska, E. M., Stoddart, M. J., Ralphs, J. R., Richards, R. G. & Hayes, J. S. A phenotypic comparison of osteoblast cell lines versus human primary osteoblasts for biomaterials testing. *J. Biomed. Mater. Res. Part A* **102**, 2636–2643 (2014).

Supporting Information

Boron nitride-based nano-biocomposites: Design by 3D printing for bone tissue engineering

*Habib Belaid^{1,2}, Sakthivel Nagarajan¹, Vincent Huon³, Jonathan Bares³, Sébastien Balme¹,
Philippe Miele¹, David Cornu¹, Vincent Cavaillès,² Catherine Teyssier² and Mikhael
Bechelany^{1*}*

¹Institut Européen des Membranes, IEM-UMR 5635, Université Montpellier, CNRS, ENSCM, Montpellier, France

²IRCM, Institut de Recherche en Cancérologie de Montpellier, INSERM U1194, Université Montpellier, Montpellier F-34298, France

³LMGC, Laboratoire de Mécanique et Génie Civil, Université Montpellier, CNRS, Montpellier, France

* Corresponding author:

mikhael.bechelany@umontpellier.fr, Phone: +33467149167, Fax: +33467149119

Table S1. Printing parameters

	General characterizations	Mechanical properties
1 st layer height	0.1mm	0.1mm
Layers height	0.2mm	0.2mm
Perimeters	1	1
Number of top & bottom layers	0	5
Infill percentage	70%	70%
Infill architecture	Rectilinear	Rectilinear
Combine infill layers	1	1
Infill angle	45°	0°
Bed temperature	60°C	60°C
Nozzle temperature 1 st layer	215°C	215°C
Nozzle temperature other layers	210°C	210°C

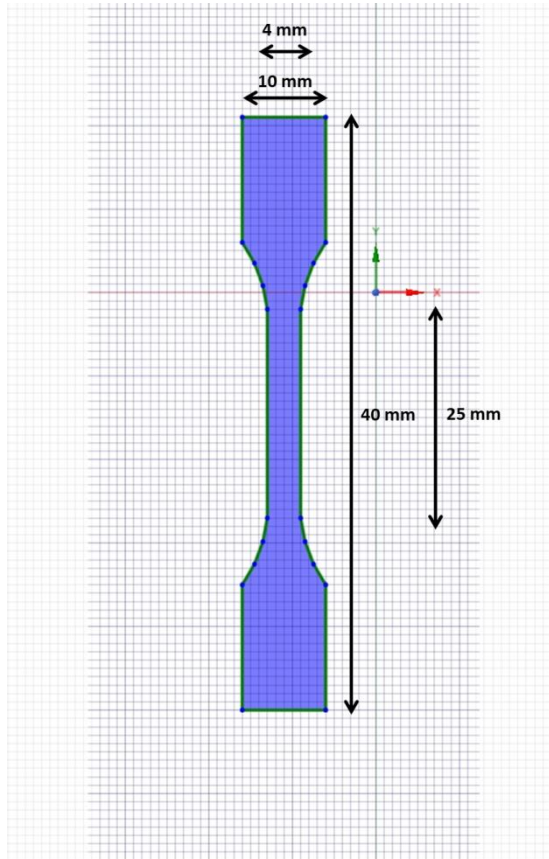


Figure S1. Schematic representation of PLA and PLA/EBN samples with a dog bone shape for tensile strength analysis.

Stereolithographic 3D printing of a PPF scaffold containing drug-loaded PLGA microspheres

Habib Belaid^{1,2}, Sébastien Blanquer³, Sébastien Balme¹, Catherine Teyssier², David Cornu¹, Vincent Cavailles^{2*£} and Mikhael Bechelany^{1*£}

¹Institut Européen des Membranes, IEM-UMR 5635, Université Montpellier, CNRS, ENSCM, Montpellier, France

²IRCM, Institut de Recherche en Cancérologie de Montpellier, INSERM U1194, Université Montpellier, Montpellier F-34298, France

³Institut Charles Gerhardt, ICGM-UMR 5253, Montpellier, France

* Corresponding authors:

mikhael.bechelany@umontpellier.fr, Phone: +33467149167, Fax: +33467149119

vincent.cavaillès@inserm.fr, Phone: +33467612405, Fax: +33467613787

£ Co-last authors

Keywords: polypropylene fumarate, PLGA microspheres, anticancer drugs, stereolithography, bone engineering, metastatic cancer treatment.

Abstract

The aim of this work was the development and characterization of biodegradable 3D printed scaffold designed for the treatment of breast cancer bone metastasis, *i.e.* allowing bone regeneration and inhibition of breast cancer cell proliferation. Synthesis of the scaffold was achieved using a poly(propylene fumarate) (PPF) photopolymer and a stereolithography 3D printer. The mechanical properties of the scaffold with a formulation containing 30% diethyl fumarate (DEF) and 5% Bis-acylphosphine oxide (BAPO) exhibited a Young's modulus of 350 ± 50 MPa and a tensile strength of 5 ± 3 MPa similar to trabecular bone. Differential scanning calorimetry showed a glass transition at 5°C for PPF before crosslinking which disappeared after printing. Moreover, thermal gravimetric analysis showed a shift of degradation peak around 40°C demonstrating that thermal properties of PPF were enhanced after printing. In parallel, in order to drug-arm the scaffold, PLGA microspheres were prepared and loaded with the bisphosphonate Alendronate (AL) and with raloxifene (RH), a selective-modulator of the estrogen receptor, both drugs having osteogenic and anticancer activities. Morphological analysis by scanning electron microscopy and digital light scattering showed the spherical shape of the microspheres and an average pore size around $1\text{ }\mu\text{m}$. UV-spectroscopy revealed an encapsulation efficiency of $60 \pm 20\%$ for AL and $15 \pm 5\%$ for RH. Drug release in saline buffers showed that AL and RH was released for up to one month. A cell viability test using MG63 osteosarcoma cells was conducted to validate microsphere biocompatibility. Moreover, the bioefficacy of the microspheres was validated on MCF7 breast cancer cell proliferation. Finally, the microspheres were successfully and homogeneously incorporated into the 3D PPF scaffold as demonstrated by scanning electron microscopy. In conclusion, although further characterizations are required, this new 3D printed AL and RH loaded PPF/PLGA scaffold, appears to be a suitable material for the treatment of bone metastasis in breast cancer.

1. Introduction

For decades, the treatment of bone has remained a big challenge. Fractures are usually caused by trauma (falls or shocks for example), but some can be the result of disease. For instance, breast cancer, the most common invasive cancer and the second main cause of cancer death in women, have a high metastatic tropism for bone. Indeed, tumor cells have the ability to escape from the primary tumor site, enter the systemic circulation and eventually find a distant site in which cell survival and growth are facilitated¹. Bone is the third most common site of breast metastases after the lung and the liver. The clinical course of metastatic breast cancer is relatively long, with patients likely to experience sequential skeletal-related events (SREs)² including bone pain, spinal cord compression, and fractures, all of which may profoundly impair a patient quality-of-life³. Furthermore, the median survival after a diagnosis of skeletal metastases is approximately 2–3 years. These facts illustrate the clinical importance of curing bone metastasis.

In the case of a pathologic fracture, bone cannot repair by itself and the use of bone grafts is necessary. Traditionally, bone grafts have been used to restore damaged bone. Due to a lack of availability and issues of bone grafts, the use of synthetic biomaterials have a great interest to repair bones and are now being used as bone graft substitutes. Indeed, biomaterials were initially selected for structural restoration based on their biomechanical properties. Now, these biomaterials (also called scaffold in the field) are engineered to be bioresorbable and bioactive in order to induce new bone formation and vascularization. Different types of scaffold have been used, made of biodegradable materials that support different growth factors, drugs, genes, or stem cells.

Tissue engineering methods can be used to fabricate artificial 3D scaffolds to replace damaged tissue in regenerative medicine⁴. 3D printing is a recent technology that can be used alternatively to produce scaffolds, in order to overcome some of the limitations of

conventional methods such as solvent-casting and particle leaching⁵, freeze drying⁶, phase separation⁷, gas foaming⁸ or electrospinning⁹. Indeed, this technique has a great potential to produce final scaffolds with complex shape and microarchitecture with desired pore geometries and size. This technology enables also the production of patient-specific scaffold shapes using medical images made by computed tomography.

Stereolithography (SLA) is regarded as the first rapid prototyping process and was created by Charles Hull in 1986¹⁰. He defined a method and apparatus for making solid objects by successively printing thin layers of ultraviolet curable material one on top of the other¹¹. The advantages of SLA are the ability to create complex shapes with internal architecture and extremely high feature resolution¹². The biodegradable macromers that have been applied in stereolithography are based on functionalized oligomers with hydrolyzable ester or carbonate bonds in the main chain. Poly(propylene fumarate) (PPF) is a linear unsaturated copolyester based upon fumaric acid, a component of the Krebs cycle¹³. Due to its tailorable mechanical performance¹⁴, biocompatibility¹⁵ and biodegradability¹⁶, PPF-based polymers have been widely investigated for a number of biomedical applications, such as the fabrication of orthopedic implants¹⁷, scaffolds for tissue engineering¹⁸, controlled bioactive factor delivery systems¹⁹, and cell transplantation vehicles^{20,21}.

A method to increase the bioactivity of PPF scaffolds in the case of the treatment of pathologic fractures from bone metastasis of breast cancer is to integrate drugs in order to promote bone formation and to limit the proliferation of cancer cells. There are numerous conventional routes of drug administration such as intravenous, intramuscular or oral ways. Free drug administration may cause various side effects. Hence, there is a need for alternative systems. Ideally, the drug should be delivered at a required concentration within the therapeutic dose at the right time to a specific target in a safe way.

Bisphosphonates (BP) such as Alendronate (AL) are the most prescribed medications for osteoporosis therapy^{22, 23} and possess a high affinity for bone. Their benefits are restricted to the skeleton where they decrease the risk of fractures²⁴. But, when administrated orally, only 1% of BPs can be absorbed *via* oral administration and only 20% of the absorbed drug can be eventually incorporated in bones²⁵. Moreover, AL may have negative effects on the bone biomechanical properties at the structural level by increasing bone volume²⁶. To overcome these drawbacks, different studies using PLGA microspheres showed a controlled release of AL, *in vitro* and *in vivo*, suggesting that the local delivery of AL with PLGA microspheres has good potential for the treatment of bone^{27–30}.

Raloxifene Hydrochloride (RH), a nonsteroidal benzothiophene derivative, is a second-generation selective-modulator of the estrogen receptor (SERM). RH was found to decrease breast cancer incidence in high-risk postmenopausal women³¹ and was approved in 1998, by the Food and Drug Administration (FDA) for the treatment and prevention of osteoporosis, and in 2007 to reduce breast cancer risk³². Although about 60% of RH administrated orally is absorbed, the absolute bioavailability of the drug is just 2%. Systemic administration of higher doses of RH would increase the risk of side effects such as venous thromboembolism, pulmonary embolism, hot flushes, and leg cramps^{32,33}. Besides, RH has been reported to be equally efficient with AL in preventing osteoporosis-related fractures and it has been found to have lower side effects than AL³⁴.

Different studies have found that greater skeletal benefits are obtained when two anti-resorptive therapies are administered in combination, compared with single agent delivery^{35,36}. The rationale for combining two anti-resorptive agents with different mechanisms of action such as AL and RH could be an interesting option for the treatment of pathologic fractures resulting from breast cancer bone metastases.

In order to treat patients suffering from such pathologic fracture, an interesting approach might be to deliver appropriate drugs at the time of prosthetic implantation. This local drug delivery could avoid systemic side effects by using lower and safer quantities of drug and exhibit a more localized efficacy. On another hand, an appropriate carrier is required.

The most commonly used biodegradable synthetic polymers in biomedical applications are saturated poly(α -hydroxy esters), including poly(lactic acid) (PLA) and poly(glycolic acid) (PGA), as well as poly(lactic-co-glycolide) (PLGA) copolymers^{37,38}. PLGA has been among the most attractive polymeric candidates as base material devices for drug delivery and tissue engineering applications. In particular, PLGA has been extensively studied for the development of devices with controlled delivery of small molecule drugs, proteins, and other macromolecules³⁹.

The objective of this work was to create a 3D scaffold with controlled architecture able to support bone formation and to inhibit tumor cell proliferation. To this aim, we first developed and characterized a 3D printed PPF scaffold by stereolithography. In parallel, we generated Alendronate and Raloxifene loaded PLGA microspheres that were analyzed for several parameters including morphology, biocompatibility and bioactivity. Finally, these drug-loaded microspheres were homogenously embedded in the PPF structure to produce a scaffold that could be used for biomedical applications.

2. Experimental section

2.1. Materials. Methanol (>99.8% (GC), CAS 67-56-1), 2- propanol (CAS 67-63-0) , fumaric acid (>99.0%, CAS 110-17-8), propylene glycol (CAS 57-55-6), diethyl fumarate (DEF, 98%, CAS 623-91-6)), bis-acylphosphine oxide (BAPO, CAS 162881-26-7), monoacylphosphine oxide (Lucirin[®] TPO, 97%, CAS 75980-60-8), Poly(D,L-lactide-co-glycolide) (Resomer RG503H), Raloxifene Hydrochloride (CAS 82640-04-8), Alendronate sodium (CAS 121268-17-5), HEPES (>99.5%, CAS 7365-45-9), perchloric acid (70%, CAS 7601-90-3), iron(III) chloride hexahydrate (97%, CAS 10025-77-1), dichloromethane (>99.9% (GC), CAS 75-09-2), ethanol (96% vol, CAS 64-17-5), phosphate buffered saline (PBS) (P4417) tablets, 3-(4,5-dimethylthiazol-2-yl)-2,5-diphenyl tetrazolium bromide (MTT, 98%, CAS 298-93-1) were purchased from Sigma-Aldrich. Acetone (\geq 99% (GC), CAS 67-64-1) and poly(vinyl alcohol) (PVA, CAS 9002-83-5) was purchased from Honeywell. Foetal bovine serum (FBS, CVFSVF00-01) was purchased from Eurobio. Dimethyl sulfoxide (DMSO) (BDH Prolabo 23486.297) was purchased from VWR. MEM alpha medium (Gibco 12571-063), DMEM/F-12 (1:1) + GlutaMAX (Gibco 31331-028), DMEM/F-12 (Gibco 21041-025), penicillin/streptomycin (Gibco 15140-122) and 0.05% trypsin-EDTA (Gibco 25300-054) were used for cell cultures and purchased from Thermo Fisher Scientific.

2.2. Synthesis of the poly(propylene fumarate) polymer. PPF was synthesized *via* a condensation reaction according to method of Gerhart⁴⁰. 2.4 mol of fumaric acid and 3.0 mol of propylene glycol were placed in a triple-necked 1 L flask with an overhead electrical stirrer. During synthesis, the mixture was stirred continuously at 150 rpm and the temperature of the solution was maintained at 140°C during 17 h. Then, the temperature was increased to 190°C during 5 h. The reaction was ended after that, and the final product was a clear, light-yellow, very viscous liquid. The molecular weight of the synthesized PPF was measured using gel

permeation chromatography (GPC) system with an infrared detector. Samples were eluted with THF through a column at a flow rate of 1 ml/min. Molecular weight was determined relative to a polystyrene standard by the data plotting. The weight-average molecular weight (M_w) was 5330 Da, the number average molecular weight (M_n) was 1534 Da and PDI of 4.37 as it shown in Figure S1. The PPF polymer has high viscosity at room temperature. To be able to use PPF as a liquid polymer for Stereolithography, DEF, a low viscosity cross-linking agent, was added to reduce the viscosity. The PPF was heated to approximately 60°C to reduce its viscosity, and DEF was added in different ratio. After mixing for about 1 h, the PPF/DEF mixture was filtered to remove impurities. The photoinitiator BAPO or Lucirin-TPO were added at different percentages and the mixture was stirred continuously for 3 h. The viscosity of the PPF and PPF/DEF mixed were measured using an advanced rheometric expansion system (Anton Paar, MCR 302) at 37°C, data are shown in Table S1.

2.3. Scaffold printing by stereolithography. PPF/DEF scaffold was fabricated using a Formlabs Form 2 printer equipped with a Class 1, 405 nm violet laser with a power of 250 mW and laser spot size of 140 μ m. Axis resolution (i.e., layer thickness) used for printing was 50 μ m. After printing, the printed samples were then washed for several hours in an isopropyl alcohol (IPA) bath (Form Wash, Formlabs). Then the scaffolds were post-cured for 1 hour using formlabs Form Cure equipped with 405 nm UV-light at room temperature.

2.4. Morphological and size distributions of scaffolds. The scaffold size, morphology, and microstructure were analysed by scanning electron microscopy (SEM) (HITACHI S4800 system). For SEM observation, scaffolds were coated with platinum using a Polaron SC7620 Mini Sputter Coater. Microspheres size was measured by dynamic light scattering (Litesizer 500, Anton Paar).

2.5. Mechanical properties. The mechanical properties of the 3D printed PPF scaffolds were characterized using a dynamic mechanical analysis (DMA) system (Metravib 50N) at controlled force mode. Samples were printed in rectangular shape (50 mm length, 5 mm width, and 1 mm thick). The samples were then clamped between dedicated jaws and pulled at a 0.5 N.s^{-1} until breaking. Linear elastic regions from the stress–strain graphs were then used to calculate the Young’s modulus from at least three assays. The stress at which the sample begins to break was also measured.

2.6. Thermal properties. The different scaffolds were analysed using a differential scanning calorimeter 2920 (maker), equipped with a RCS90 cooling system (maker). Samples were accurately weighed ($\approx 5 \text{ mg}$) in an aluminium TA pan (maker) and sealed. An empty sealed pan was used as reference. Samples were first cooled to -20°C and then heated to 50°C with a heating rate of $10^{\circ}\text{C min}^{-1}$. Then, they were cooled again to -20°C with nitrogen as purge gas. The resulting differential scanning calorimetry (DSC) curves were analysed to determine the polymer glass transition temperature (T_g). The thermogravimetric analysis (TGA) was performed using a TGA G500 device (TA Instruments). About 5 mg of each sample was heated in air atmosphere from room temperature to 900°C , at a heating rate of $10^{\circ}\text{C.min}^{-1}$.

2.7. Preparation of AL-loaded PLGA microspheres. To prepare AL-loaded PLGA-microspheres of around $1 \mu\text{m}$ in diameter, a double-emulsion-solvent-evaporation method (water-in-oil-in-water or $W_1/O/W_2$) was used. Microspheres were produced by first dissolving 25mg of Alendronate in 1 ml of distilled water. This is the first aqueous phase (W_1). Then 500 mg of PLGA were dissolved in 5 mL dichloromethane (DCM), forming oil phase (O). The mixture was emulsified using an Ultra-Turrax emulsifier (T25 digital, IKA) for 90 s at 22000

rpm. Then, 10 mL 2% aqueous poly(vinyl alcohol) (PVA) solution (W_2) was added and emulsified for another 90 s at 22000 rpm to produce the second emulsion. After which another 10 mL of 2% PVA solution were added to the mixture. The resultant $W_1/O/W_2$ emulsion was stirred overnight at room temperature to evaporate the solvent and solidify PLGA/AL microspheres. Then, the microspheres were finally washed in distilled water and collected through centrifugation at 3000 rpm for 10 min, lyophilized and stored at 4°C until use.

2.8. Preparation of RH-loaded PLGA microspheres. To prepare RH-loaded PLGA-microspheres of around 1 μm in diameter, a single-emulsion (W/O) technique was used. Microspheres were produced by dissolving 25 mg of Raloxifene and 500 mg of PLGA in 5 mL DCM. The mixture was emulsified using an Ultra-Turrax emulsifier (T25 digital, IKA) for 90 s at 22000 rpm. Then, 10 mL 2% aqueous PVA solution was added to the mixture. The resultant W/O emulsion was stirred overnight at room temperature to evaporate the solvent and solidify PLGA/RH microspheres. Then, the microspheres were finally washed as described for AL-loaded microspheres. As a control, PLGA microspheres were similarly fabricated without the addition of any drug into PLGA solution before emulsification.

2.9. Determination of drugs encapsulation efficiency. Microspheres were produced by dissolving 500 mg of PLGA in 5 mL DCM. The portion of encapsulated AL in PLGA was measured as described as follows⁴¹. The collected supernatant, which is an AL suspension in PLGA/DCM solution, was rinsed in an iron (III) chloride/perchloric acid solution so that the suspended AL was entirely extracted into the aqueous phase. The AL in the iron (III) chloride/perchloric acid solution extraction, which represents the portion of encapsulated AL in PLGA, was quantified using an UV spectrophotometer (V-570, Jasco) at 300 nm.

Therefore, the total AL encapsulation efficiency in PLGA/AL microspheres could be obtained from calibrations curves obtained beforehand.

To determine RH encapsulation in PLGA microspheres, a spectrophotometric method was followed with some modifications⁴². Briefly, microspheres were dissolved in DCM and then equal volume of MeOH was added to solubilize RH. The portion of RH in the solution was quantified using an UV spectrophotometer at 287 nm. It was validated that PLGA in the extraction samples did not give interference with RH optical measurements at this wavelength. Calibration curve was constructed using different concentrations of RH in the solvent mixture of DCM:MeOH (1:1) in order to determine RH encapsulation efficiency. Encapsulation efficiency (EE) (%) of PLGA/AL and PLGA/RH microspheres was calculated as follows: $EE = \frac{C(drug)}{C(Ti)} \times 100$ with C(drug) the concentration of AL or RH obtained by UV-spectrophotometer and C(Ti) the total initial concentrations of drugs.

2.10. Determination of drug release. In-vitro AL release trials were performed in a shaking incubator (Incu-Saker mini, Benchmark) at 70 rpm under 37°C. Fifty milligram AL-loaded microspheres were soaked in 10 ml HEPES (pH=7.4). The sample media were collected at regular time intervals with equal amount of HEPES makeup. The determination of AL concentration was obtained following the method described above. PLGA/RH microspheres (50 mg) were incubated in 10 ml of PBS, maintained at 37°C in a shaking incubator. At specific time intervals total release media were collected and the supernatant was used to determine the amount of RH release with respect to time. After taking the supernatant, total release media was refreshed with the same amount of fresh PBS. The determination of RH concentration was obtained following the method described above. Release data for both drugs were expressed as cumulative percent release with respect to time.

2.11. Biocompatibility and bioefficacy of microspheres. Microspheres were sterilized under UV light (405 nm) for 1h. MG-63 osteosarcoma cells were cultured on the sterilized microspheres for up to 7 days. Cell viability was analysed using the MTT assay. Cells were incubated with 100 μL of culture medium containing 0.05 mg.mL^{-1} of MTT solution for 3h. The obtained purple-coloured formazan crystals, due to MTT reduction by living cells, were solubilized by the addition of 100 μL of DMSO and absorbance recorded at 560 nm using a Multiskan microplate spectrophotometer (Thermofisher, USA). The effects of the two drugs on MCF7 breast cancer cell proliferation was analysed using the MTT assay. Typically, 100 mg of PLGA/AL and 1 mg of PLGA/RH were added to 10^3 MCF7 cells seeded in a 96-well plate in 200 μL of medium containing steroid-stripped foetal bovine serum for 10 days. At defined end point, MTT assay was conducted as described above.

3. Results and discussion

3.1. Generation and characterization of a 3D printed PPF scaffold.

A 3D scaffold was fabricated using PPF/DEF photopolymer and a stereolithographic system. The scaffold was modelled with a square shape using computer-aided design (CAD) software (Design Spark Mechanical). A STL file was created to be analysed with the PreForm software. Scaffolds were 3D printed without supports. The UV laser of the stereolithography system irradiated the surface of the liquid polymer, and the scaffold was obtained using a layer-by-layer process with each layer of 50 μm .

Scaffolds used for biomedical implants should possess mechanical properties similar to that of bones. The characterization of the mechanical properties of PPF scaffolds using different PPF to DEF ratio and two different photoinitiators was focused on the region where samples responded elastically to traction. Several parameters can play a role on the mechanical properties of a PPF scaffold. As shown in Figure 1, when modifying the PPF to DEF ratio

with the same content of the photoinitiator BAPO, Young's modulus increased from 15 to 100 MPa. Furthermore, a higher content of photoinitiator also increased the tensile modulus. Indeed, Young's modulus reached 350 MPa with the formulation containing 5% of BAPO. Finally, for the same PPF to DEF ratio, the use of a different photoinitiator also impacted tensile modulus, since when Lucirin[®] TPO was used instead of BAPO, Young's modulus decreased about 50% (Figure 1). To further characterize the mechanical properties of the scaffold, samples were also loaded until breaking. When BAPO content was high enough, it increased the tensile strength from 1 MPa for 1% BAPO to 5 MPa for samples with 5% BAPO.

Several studies have generated PPF scaffolds by different methods leading to variable mechanical properties. Indeed, the Young's modulus of PPF reported in such studies varied from 0.2 to 1.4 GPa^{43,44,45}. The values of the Young's modulus obtained in the present work (350 MPa) is in the same range and highly comparable to that of trabecular bone (440 MPa)⁴⁶. Similarly, the tensile strength that we measured for samples with 5% BAPO is very comparable to that of trabecular bone (6.8 MPa)⁴⁶. Hence, our PPF scaffold appeared highly suitable for the replacement of this type of bone tissue. It should be mentioned that the architecture and the porosity inside the scaffold also had an effect on the mechanical properties of the material, particularly on the tensile strength, but manipulating these features was beyond the goal of this first study.

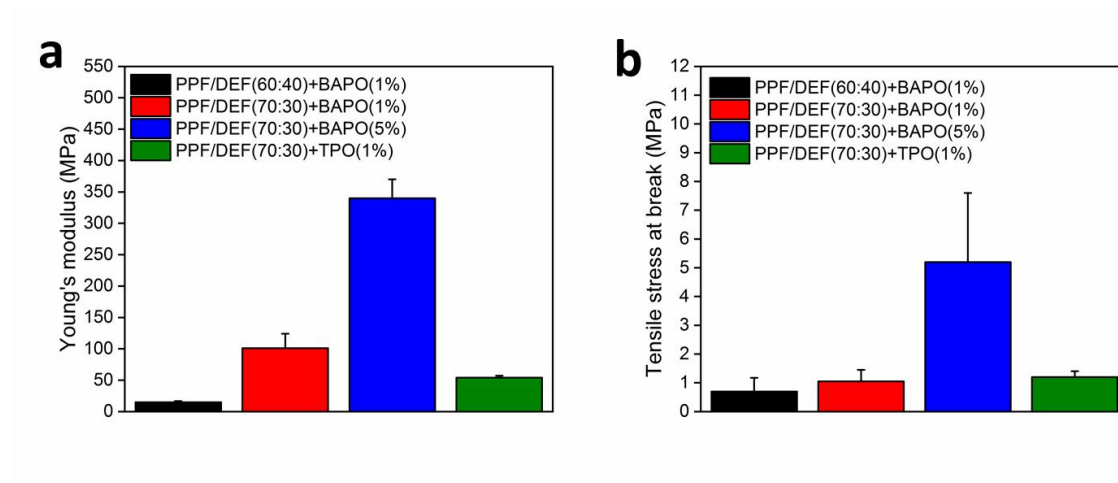


Figure 1. Mechanical properties of the scaffolds.

(a) Young's modulus and (b) tensile stress at break values of the different PPF scaffolds.

3.2. Thermal analysis of the PPF scaffolds.

The influence of crosslinking agent and 3D printing on PPF thermal stability was monitored by TGA (Figure 2a and b) using the scaffold containing 5% of BAPO. PPF exhibited four major steps of degradation with the maximum loss of weight at 360°C. PPF scaffold had two major steps of degradation with a maximum loss of weight at 400°C. Despite a degradation profile relatively comparable, the data showed that the thermal stability of the PPF scaffold was slightly better than that of uncrosslinked PPF.

Furthermore, 3D printed PPF scaffold appeared rigid, whereas uncrosslinked PPF was highly viscous at room temperature. These observations were confirmed by DSC analyses (Figure 2c). Indeed, glass transition of PPF was around 4°C which is in adequacy with values found in the literature⁴⁷ for PPF of similar molecular weight. By contrast, no glass transition was observed with the 3D printed PPF scaffold (Figure 2c).

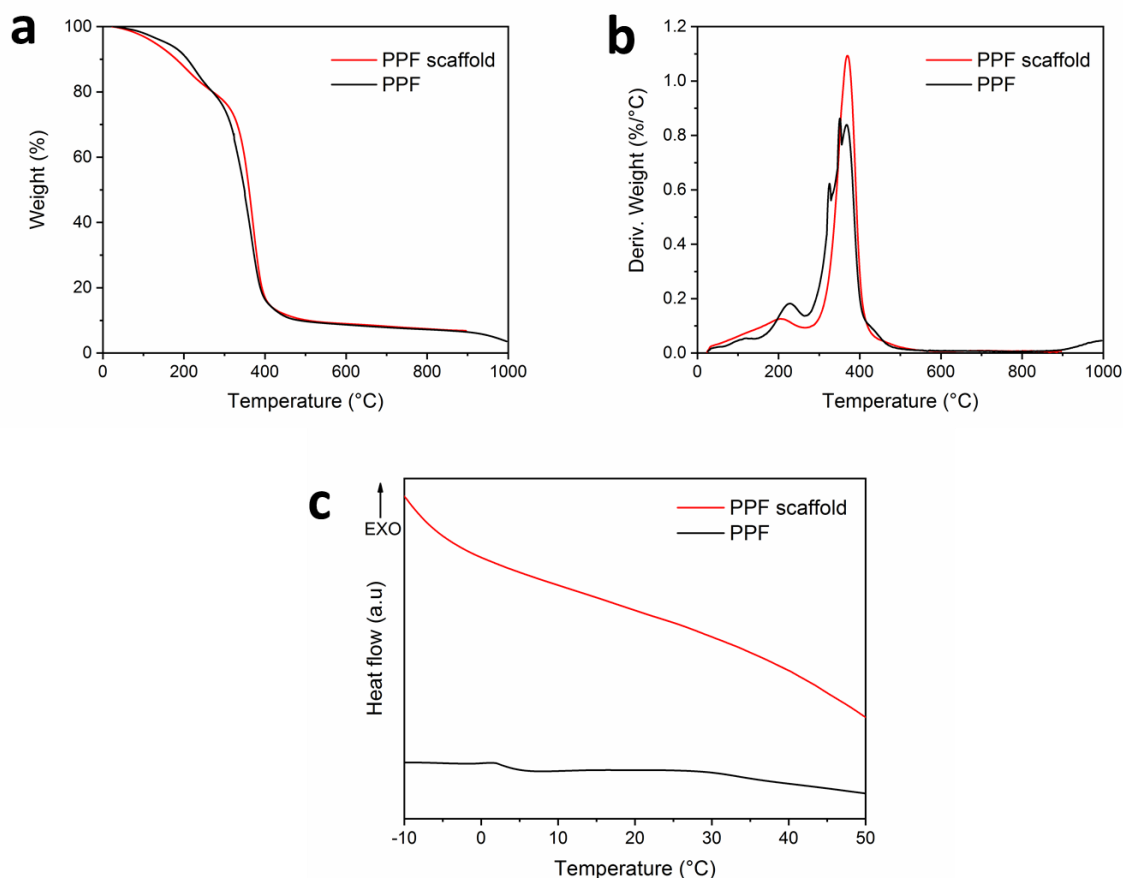


Figure 2. Thermal properties of uncrosslinked and 3D printed PPF.

(a) TGA and (b) derivative TGA curves of uncrosslinked and 3D printed (scaffold) PPF. (c) Representative DSC graphs showing Tg (glass transition temperature) of PPF before and after (scaffold) 3D printing.

3.3. Generation and morphological analysis of PLGA microspheres.

The use of microspheres with PLGA as a polymer matrix and their incorporation in the PPF 3D printed scaffold appeared as a good approach for the local delivery of a combination of both AL and RH. Therefore, AL and RH-loaded PLGA microspheres were obtained, as described in the Experimental section, by double or single emulsion solvent evaporation techniques, respectively.

SEM analysis was performed to observe the morphology and particle size distribution of the different microspheres (Figure 3). All microspheres preserved their spherical shape and smooth surface. The incorporations of AL or RH did not influence the microspheres

morphology. It can be observed a homogeneous distribution of size in the range of 1 to 5 μm for each group of microspheres.

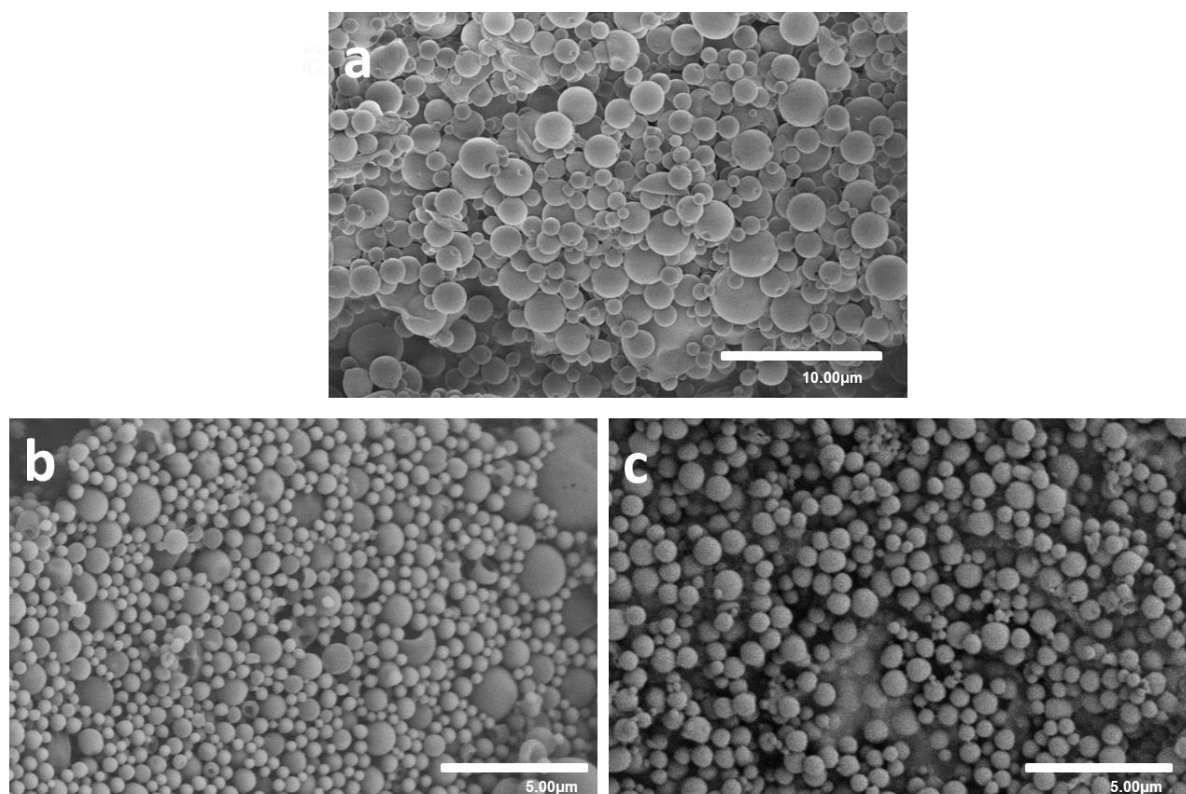


Figure 3. Scanning electron micrographs showing microspheres morphology.

(a) PLGA, (b) PLGA/AL and c) PLGA/RH.

These data were confirmed by DLS analyses which showed that double emulsion PLGA/RH microspheres were bigger than PLGA/AL microspheres obtained by single emulsion (Data of particle size for all types of microspheres are given in Table 1). This can be due to the external layer of PVA present in PLGA microspheres formed by double emulsion. Moreover, PLGA/AL microspheres presented a polydispersity index (PDI) of 4.2 (7-fold higher than that of PLGA/RH microspheres), indicating that these microspheres had the broadest size distribution.

Table 1. Characteristics of the different PLGA microspheres.

	PLGA	PLGA/AL	PLGA/RH
Dx (50) (μm)	1.2 \pm 0.2	2.1 \pm 0.4	0.5 \pm 0.1
PDI	1.2	4.2	0.6
Encapsulation efficiency (%)	-	63 \pm 20	15 \pm 5
Loading (%)	-	3.2	0.8
Loading ($\mu\text{moles/g}$ of spheres)	-	100	15

3.4. Drug release studies.

The value of the encapsulation efficiency of the two drugs (AL and RH) in PLGA microspheres are given in Table 1. The PLGA/AL microspheres had the highest encapsulation efficiency (63 \pm 20%). RH encapsulation efficiency was found significantly lower than AL encapsulation (15 \pm 5%). This result was expected since RH is a highly hydrophobic drug⁴⁸.

A release study of the fabricated drug-loaded microspheres was then carried out in buffered solutions. The released solution was extracted at various time points until 30 days. The profiles of AL and RH release from both PLGA/AL and PLGA/RH are shown in Figure 4. The curves indicate different shapes but with a common initial burst. However, this burst is much higher for Alendronate release from PLGA/AL microspheres. Indeed, for PLGA/AL, 15% of the drug release had been accomplished during the first day. While after the curve inflexion at day 3, the subsequent release rate lowered down to reach 30% of release at 25 days.

Concerning the PLGA/RH curve, a moderate burst release of RH was observed during the first day with 1.6% of drug released. The burst effect may be due to the release of RH adsorbed on the microspheres or near their surface. Then, for the next days, the release was stable until day 10 where the drug release increased to reach 15% of released drug until day

30. It is known that controlled-release mechanism for biodegradable polymeric drug delivery systems has 4 major steps; 1) drug diffusion through water-filled pores, 2) diffusion through the polymer matrix, c) osmotic pumping and 4) erosion of the polymer matrix⁴⁹. During hydrolytic degradation of PLGA polymer, a high increase in rate of drug release took place. Thus, it can be concluded that, for AL and RH-loaded PLGA microspheres, the corresponding critical molecular weight might have been reached during degradation of PLGA around day 3 for PLGA/AL and day 10 for PLGA/RH. Degradation of PLGA microspheres occurred sooner for PLGA/AL than PLGA/RH, probably due to the hydrophilic nature of Alendronate compared to the hydrophobic nature of Raloxifene. The influence of the method to obtain microspheres, double emulsion for AL against single emulsion for RH could also explain the observed difference. Moreover, AL-loaded PLGA microspheres might exhibit a higher rate of drug release due to a higher efficiency of drug encapsulation than RH-loaded PLGA microspheres.

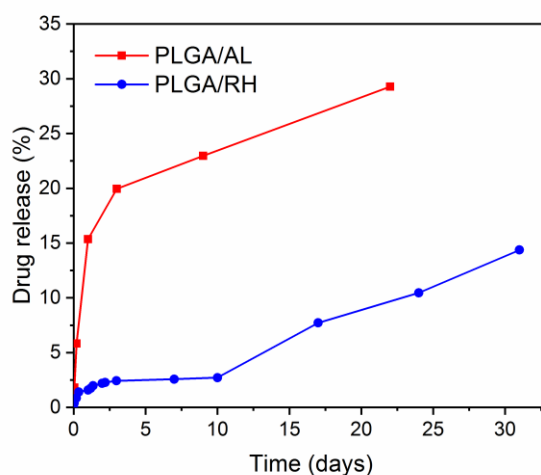


Figure 4. Cumulative release of Alendronate and Raloxifene from PLGA microspheres.

3.5. Biocompatibility and bioefficacy of drug-loaded microspheres.

The biocompatibility of the different microspheres was investigated using MG-63 human bone osteosarcoma cells which exhibit an osteogenic potential. Compared with cells grown without microspheres (control), PLGA microspheres exhibit only a slight inhibitory effect on cell viability at day 4 and day 7 (Figure 5a) confirming that PLGA microspheres are biocompatible.

In order to determine whether the concentration of AL and RH encapsulated within the PLGA microspheres was sufficient to have an effect on breast cancer cell proliferation (Figure 5b), MCF7 cells were cultured in the presence of microspheres loaded or not with the drugs. After 10 days, the microspheres loaded with drugs showed a very significant impact on breast cancer cell proliferation as compared to microspheres alone. It can also be noted that, as expected, microspheres loaded with Raloxifene had a better effect than those loaded with Alendronate since a 100-fold lower amount of PLGA/RH microspheres was required to achieve an inhibition of MCF-7 cell proliferation comparable to that obtained with each drug alone (Figure 5c). These data thus validated the biocompatibility and bioefficiency of the drug-loaded PLGA microspheres.

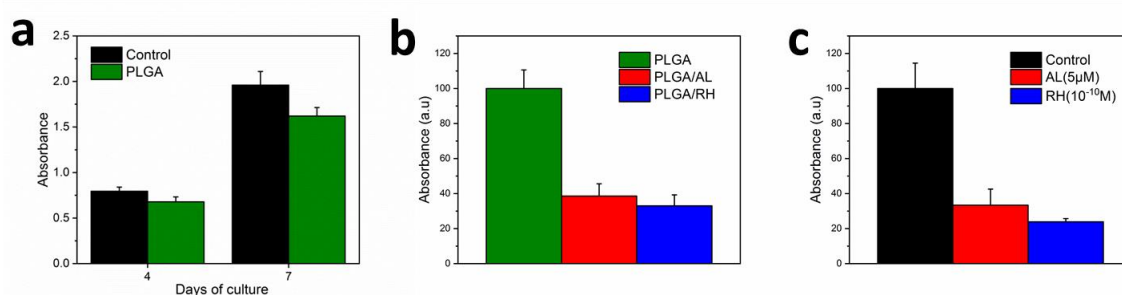


Figure 5. Biocompatibility and bioefficacy of drug-loaded microspheres.

(a) MG63 cell proliferation measured for 8 days in the presence or not of PLGA microspheres. (b) MCF7 cell proliferation in presence of PLGA microspheres loaded or not with AL (100mg of PLGA/AL microspheres in 200μl of medium) and RH (1mg of PLGA/RH microspheres) at day 10. (c) MCF7 cell proliferation measured at day 10 in the presence of the indicated concentration of AL or RH.

3.6. Generation and morphological analysis of the PPF/PLGA scaffold.

To generate a PPF/PLGA scaffold, microspheres at 10% (w/w) to the content of PPF/DEF, were added to the PPF/DEF photopolymer and the suspension was stirred to homogeneity. The SEM micrographs shown in Figure 6 illustrate the incorporation of the PLGA microspheres. The microspheres were spread into the PPF matrix. It can be noticed the agglomeration of microspheres between them.

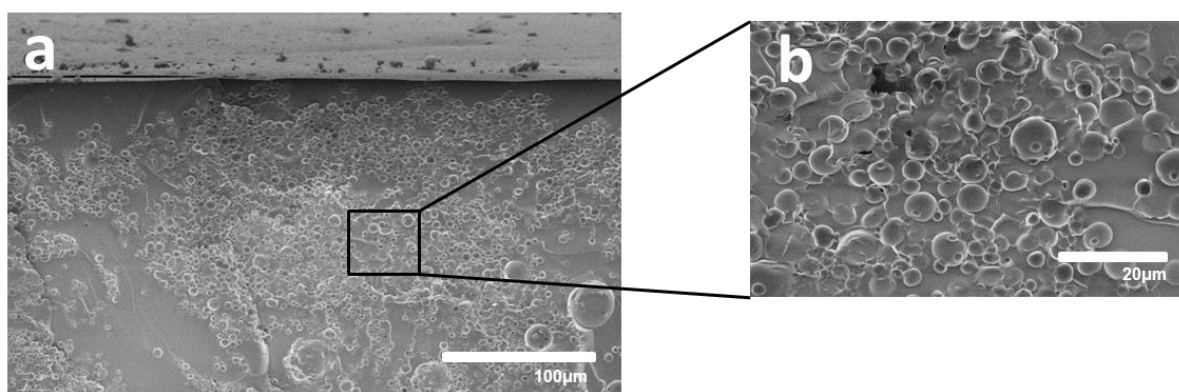


Figure 6. Scanning electron micrographs showing microspheres incorporation in PPF scaffold.

(b) Inset shows a magnification of the surface.

4. Conclusions

In this study, we used stereolithography to print a 3D PPF/DEF scaffold with mechanical properties comparable to trabecular bone. In parallel, AL and RH-loaded PLGA microspheres were respectively obtained by double or single emulsion solvent evaporation techniques. The AL-loaded microspheres showed much higher encapsulation efficiency and release than the PLGA/RH microspheres. Both PLGA microspheres were biocompatible, bioactive on breast cancer cells and successfully embedded into a 3D printed scaffold. Therefore, this drug-loaded PPF/PLGA scaffold appears as a promising multifunctional scaffold for the treatment of breast cancer bone metastasis, allowing concomitantly an improvement of bone regeneration as well as an inhibition of breast cancer cell proliferation.

REFERENCES

1. Hanahan, D. & Weinberg, R. A. Hallmarks of cancer: the next generation. *Cell* **144**, 646–74 (2011).
2. Oster, G. *et al.* Natural history of skeletal-related events in patients with breast, lung, or prostate cancer and metastases to bone: A 15-year study in two large US health systems. *Support. Care Cancer* **21**, 3279–3286 (2013).
3. Weilbaecher, Katherine N. Guise, T. A. & McCauley, L. K. Cancer To Bone: a Fatal Attraction. *Nat. Rev.* **11**, 411–425 (2013).
4. Do, A.-V., Khorsand, B., Geary, S. M. & Salem, A. K. 3D Printing of Scaffolds for Tissue Regeneration Applications. *Adv. Healthc. Mater.* **4**, 1742–62 (2015).
5. Agrawal, C. M. & Ray, R. B. Biodegradable polymeric scaffolds for musculoskeletal tissue engineering. *J. Biomed. Mater. Res.* **55**, 141–150 (2001).
6. Zhu, N. & Che, X. Biofabrication of Tissue Scaffolds. in *Advances in Biomaterials Science and Biomedical Applications* (InTech, 2013). doi:10.5772/54125
7. Nam, Y. S. & Park, T. G. Porous biodegradable polymeric scaffolds prepared by thermally induced phase separation. *J. Biomed. Mater. Res.* **47**, 8–17 (1999).
8. Harris, L. D., Kim, B.-S. & Mooney, D. J. Open pore biodegradable matrices formed with gas foaming. *J. Biomed. Mater. Res.* **42**, 396–402 (1998).
9. Sill, T. J. & von Recum, H. A. Electrospinning: Applications in drug delivery and tissue engineering. *Biomaterials* (2008). doi:10.1016/j.biomaterials.2008.01.011
10. Apparatus for production of three-dimensional objects by stereolithography. (1984).
11. Cordonnier, T., Sohier, J., Rosset, P. & Layrolle, P. Biomimetic Materials for Bone Tissue Engineering - State of the Art and Future Trends. *Adv. Eng. Mater.* **13**, B135–B150 (2011).
12. Zhang, X., Jiang, X. N. & Sun, C. *Micro-stereolithography of polymeric and ceramic microstructures. Sensors and Actuators* **77**,
13. Kasper, F. K., Tanahashi, K., Fisher, J. P. & Mikos, A. G. Synthesis of poly(propylene fumarate). *Nat. Protoc.* **4**, 518–525 (2009).
14. Kharas, G. B. *et al.* Synthesis and characterization of fumarate-based polyesters for use in bioresorbable bone cement composites. *J. Appl. Polym. Sci.* **66**, 1123–1137 (1997).
15. Gunatillake, P. A. & Adhikari, R. Biodegradable synthetic polymers for tissue engineering. *Eur. Cell. Mater.* **5**, 1–16; discussion 16 (2003).
16. Shanfeng Wang, Lichun Lu, and & Yaszemski*, M. J. Bone-Tissue-Engineering Material Poly(propylene fumarate): Correlation between Molecular Weight, Chain Dimensions, and Physical Properties. (2006). doi:10.1021/BM060096A
17. Timmer, M. D., Carter, C., Ambrose, C. G. & Mikos, A. G. Fabrication of poly(propylene fumarate)-based orthopaedic implants by photo-crosslinking through transparent silicone molds. *Biomaterials* **24**, 4707–14 (2003).
18. Cooke, M. N., Fisher, J. P., Dean, D., Rimnac, C. & Mikos, A. G. Use of stereolithography to manufacture critical-sized 3D biodegradable scaffolds for bone ingrowth. *J. Biomed. Mater. Res.* **64B**, 65–69 (2003).
19. Hacker, M. C. *et al.* Biodegradable fumarate-based drug-delivery systems for ophthalmic applications. *J. Biomed. Mater. Res. Part A* **88A**, 976–989 (2009).
20. Payne, R. G., McGonigle, J. S., Yaszemski, M. J., Yasko, A. W. & Mikos, A. G. Development of an injectable, in situ crosslinkable, degradable polymeric carrier for osteogenic cell populations. Part 3. Proliferation and differentiation of encapsulated marrow stromal osteoblasts cultured on crosslinking poly(propylene fumarate). *Biomaterials* **23**, 4381–7 (2002).
21. Payne, R. G., McGonigle, J. S., Yaszemski, M. J., Yasko, A. W. & Mikos, A. G. Development of an injectable, in situ crosslinkable, degradable polymeric carrier for osteogenic cell populations. Part 2. Viability of encapsulated marrow stromal osteoblasts cultured on crosslinking poly(propylene fumarate). *Biomaterials* **23**, 4373–80 (2002).

22. Shaw, N. J. & Bishop, N. J. Bisphosphonate treatment of bone disease. *Arch. Dis. Child.* **90**, 494–499 (2005).
23. Bhuvanewari Ramaswamy, M. C. L. S. M. Bisphosphonates in the Prevention and Treatment of Bone Metastases. (2003).
24. Manley, G. Bisphosphonates: Mechanism of Action and Role in Clinical Practice. **71**, 233–236 (2013).
25. Ezra, A. & Golomb, G. Administration routes and delivery systems of bisphosphonates for the treatment of bone resorption. *Adv. Drug Deliv. Rev.* **42**, 175–195 (2000).
26. Diab, T., Wang, J., Reinwald, S., Guldberg, R. E. & Burr, D. B. Effects of the combination treatment of raloxifene and Alendronate on the biomechanical properties of vertebral bone. *J. Bone Miner. Res.* **26**, 270–276 (2011).
27. Bae, J. & Park, J. W. Preparation of an injectable depot system for long-term delivery of Alendronate and evaluation of its anti-osteoporotic effect in an ovariectomized rat model. *Int. J. Pharm.* **480**, 37–47 (2015).
28. Cruz, L. *et al.* Gastroresistant microparticles containing sodium Alendronate prevent the bone loss in ovariectomized rats. *Eur. J. Pharm. Sci.* **40**, 441–447 (2010).
29. Miladi, K., Sfar, S., Fessi, H. & Elaissari, A. Encapsulation of Alendronate sodium by nanoprecipitation and double emulsion: From preparation to in vitro studies. *Ind. Crops Prod.* **72**, 24–33 (2015).
30. Nafea, E. H., El-Massik, M. A., El-Khordagui, L. K., Marei, M. K. & Khalafallah, N. M. Alendronate PLGA microspheres with high loading efficiency for dental applications. *J. Microencapsul.* **24**, 525–538 (2007).
31. Vogel, V. G. *et al.* Effects of Tamoxifen vs Raloxifene on the Risk of Developing Invasive Breast Cancer and Other Disease Outcomes<SUBTITLE>The NSABP Study of Tamoxifen and Raloxifene (STAR) P-2 Trial</SUBTITLE> JAMA **295**, 2727 (2006).
32. Maximov, P. Y., Lee, T. M. & Jordan, V. C. The discovery and development of selective estrogen receptor modulators (SERMs) for clinical practice. *Curr. Clin. Pharmacol.* **8**, 135–55 (2013).
33. Ellison, N. Goodman & Gilman's The Pharmacological Basis of Therapeutics, 10th Edition. *Anesth. Analg.* **94**, 1377 (2002).
34. Lee, W.-L., Chao, H.-T., Cheng, M.-H. & Wang, P.-H. Rationale for using raloxifene to prevent both osteoporosis and breast cancer in postmenopausal women. *Maturitas* **60**, 92–107 (2008).
35. Bone, H. G. *et al.* Alendronate and Estrogen Effects in Postmenopausal Women with Low Bone Mineral Density. *J. Clin. Endocrinol. Metab.* **85**, 720–726 (2000).
36. Lindsay, R. *et al.* Addition of Alendronate to Ongoing Hormone Replacement Therapy in the Treatment of Osteoporosis: A Randomized, Controlled Clinical Trial. *J. Clin. Endocrinol. Metab.* **84**, 3076–3081 (1999).
37. Mano, J. F., Sousa, R. A., Boesel, L. F., Neves, N. M. & Reis, R. L. Bioinert, biodegradable and injectable polymeric matrix composites for hard tissue replacement: state of the art and recent developments. *Compos. Sci. Technol.* **64**, 789–817 (2004).
38. Lin, H.-R., Kuo, C.-J., Yang, C. Y., Shaw, S.-Y. & Wu, Y.-J. Preparation of macroporous biodegradable PLGA scaffolds for cell attachment with the use of mixed salts as porogen additives. *J. Biomed. Mater. Res.* **63**, 271–279 (2002).
39. Jain, R. A. The manufacturing techniques of various drug loaded biodegradable poly(lactide-co-glycolide) (PLGA) devices. *Biomaterials* **21**, 2475–90 (2000).
40. Gerhart, T. N. *et al.* Antibiotic release from an experimental biodegradable bone cement. *J. Orthop. Res.* (1988). doi:10.1002/jor.1100060417
41. Kuljanin, J., Jankovi, I., Nedeljkovi, J., Prstojevi, D. & Marinkovi, V. Spectrophotometric determination of Alendronate in pharmaceutical formulations via complex formation with Fe(III) ions. *J. Pharm. Biomed. Anal.* **28**, 1215–1220 (2002).
42. Ocal, Y. *et al.* Characterization and evaluation of triamcinolone, raloxifene, and their dual-loaded microspheres as prospective local treatment system in rheumatic rat joints. *J. Pharm. Sci.* **103**, 2396–2405 (2014).
43. Diez-Pascual, A. M. Tissue engineering bionanocomposites based on poly(propylene fumarate). *Polymers (Basel)*. **9**, 1–19 (2017).
44. Salarian, M., Xu, W. Z., Biesinger, M. C. & Charpentier, P. A. Synthesis and characterization of novel

- TiO₂-poly(propylene fumarate) nanocomposites for bone cementation. *J. Mater. Chem. B* **2**, 5145–5156 (2014).
45. Cai, L., Wang, K. & Wang, S. Poly(ethylene glycol)-grafted poly(propylene fumarate) networks and parabolic dependence of MC3T3 cell behavior on the network composition. *Biomaterials* **31**, 4457–4466 (2010).
 46. Karageorgiou, V. & Kaplan, D. Porosity of 3D biomaterial scaffolds and osteogenesis. *Biomaterials* **26**, 5474–5491 (2005).
 47. Wang, S., Lu, L. & Yaszemski, M. J. Bone-tissue-engineering material poly(propylene fumarate): Correlation between molecular weight, chain dimension, and physical properties. *Biomacromolecules* (2006). doi:10.1021/bm060096a
 48. Teeter, J. S. & Meyerhoff, R. D. Environmental fate and chemistry of raloxifene hydrochloride. *Environ. Toxicol. Chem.* **21**, 729–736 (2002).
 49. Kamaly, N., Yameen, B., Wu, J. & Farokhzad, O. C. Degradable Controlled-Release Polymers and Polymeric Nanoparticles: Mechanisms of Controlling Drug Release. (2016). doi:10.1021/acs.chemrev.5b00346

Supporting information

Stereolithographic 3D printing of a PPF scaffold containing drug-loaded PLGA microspheres

Habib Belaid^{1,2}, Sébastien Blanquer³, Sébastien Balme¹, Catherine Teyssier², David Cornu¹, Vincent Cavailles^{2*£} and Mikhael Bechelany^{1*£}

¹Institut Européen des Membranes, IEM-UMR 5635, Université Montpellier, CNRS, ENSCM, Montpellier, France

²IRCM, Institut de Recherche en Cancérologie de Montpellier, INSERM U1194, Université Montpellier, Montpellier F-34298, France

³Institut Charles Gerhardt, ICGM-UMR 5253, Montpellier, France

* Corresponding authors:

mikhael.bechelany@umontpellier.fr, Phone: +33467149167, Fax: +33467149119

vincent.cavaillès@inserm.fr, Phone: +33467612405, Fax: +33467613787

£ Co-last authors

Keywords: polypropylene fumarate, PLGA microspheres, anticancer drugs, stereolithography, bone engineering, metastatic cancer treatment.

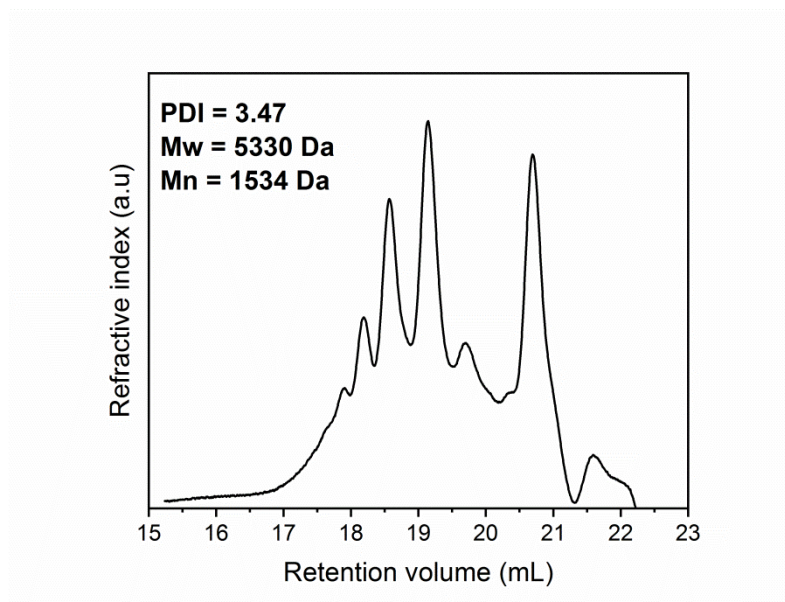


Figure 1. Representation of GPC characterization. Polydispersity index (PDI), mass average molar mass (Mw) and number average molar mass (Mn) are given.

Table 1. Viscosity of PPF resins.

Samples	Viscosity (Pa.s)
PPF	21±0.5
PPF/DEF (70:30)	0.7±0.03
PPF/DEF (60:40)	0.2±0.02
PPF/DEF (70:30)-PLGA (10%)	0.1±0.01

Fabrication of injectable calcium phosphate cement containing PLGA microspheres

Habib Belaid^{1,2}, Pierre-Yves Collart-Dutilleul³, Alban Desoutter³, Frédéric Cuisinier³, Jonathan Barés⁴, Vincent Huon⁴, Catherine Teyssier², David Cornu¹, Vincent Cavaillès^{2*£} and Mikhael Bechelany^{1*£}

¹Institut Européen des Membranes, IEM-UMR 5635, Université Montpellier, CNRS, ENSCM, Montpellier, France

²IRCM, Institut de Recherche en Cancérologie de Montpellier, INSERM U1194, Université Montpellier, Montpellier F-34298, France

³Laboratoire de bioingénierie et nanosciences, EA4203, Université de Montpellier, Montpellier, France

⁴Laboratoire de Mécanique et Génie Civil, Univ Montpellier, CNRS, Montpellier, France

* Corresponding authors:

mikhael.bechelany@umontpellier.fr, Phone: +33467149167, Fax: +33467149119

vincent.cavaillès@inserm.fr, Phone: +33467612405, Fax: +33467613787

£ Co-last authors

Keywords: Calcium phosphate cement, PLGA microspheres, vertebroplasty, bone metastasis

Abstract

The aim of this work was the development and the characterization of an injectable calcium phosphate cement (CPC) to be used as a bone substitute for the treatment of pathologic vertebrae fractures. A radiopaque CPC containing zirconium dioxide (ZrO_2) has been developed with a compressive strength of 23 MPa and a Young's modulus of 3.5 GPa. In parallel, the synthesis of Poly Lactic-co-Glycolic Acid (PLGA) microspheres around 100 μm was achieved using a double emulsion technique. CPC containing PLGA microspheres (CPC/PLGA cement) was then obtained and characterized by scanning electron microscopy (SEM) to show the incorporation of microspheres. Physicochemical analyses by X-ray diffraction and Fourier-transform infrared spectroscopy confirmed the brushite phase of the cement. The mechanical properties of the CPC/PLGA cement containing 30% PLGA were significantly decreased as compared to CPC with a compressive strength of 2 MPa and a Young's modulus of 1 GPa. The CPC/PLGA exhibited initial and final setting times of 7 and 12 min, respectively. Although the incorporation of PLGA microspheres increased the force necessary to inject the cement and decreased the percentage of injected mass as function of time, the CPC/PLGA appeared fully injectable at 4 min. Moreover, in comparison with CPC, CPC/PLGA showed a full degradation in 6 weeks (with 100% mass loss) and this was associated with an acidification of the medium containing the CPC/PLGA sample (pH of 3.5 after 6 weeks). A cell viability test using MG63 osteosarcoma cells was conducted to validate CPC/PLGA biocompatibility. Finally, *in vivo* analyses using a bone defect assay in caudal vertebrae of Wistar rat showed the good opacity of the CPC through the tail and a significant degradation the CPC/PLGA cement over a month with the beginning of new bone formation. In conclusion, although further characterizations are required, this injectable calcium phosphate cement scaffold appears to be an interesting material for bone substitution.

1. Introduction

For decades, the treatment of bones is a big challenge. There is a risk of suffering from a fracture during one lifetime. Fractures are usually caused by trauma (falls or shocks for example), but some fractures can be the result of disease. Pathologic fractures are increasing these recent years due to a raise in the median age of the population. The repair of bone defects caused by diseases, such as breast cancer bone metastases, has become a major health issue over the years. In numerous cases, when a person undergoes a pathologic fracture, bone cannot repair by itself and the use of bone grafts is necessary. Traditionally, bone grafts have been used to restore damaged bone. However, due to the lack of availability and issues of bone grafts, the use of synthetic biomaterials have a great interest to repair bones and are now being used as bone graft substitutes. This problem makes bone tissue engineering a rapidly expanding field.

The concept of tissue engineering was defined by Langer and Vacanti¹. The role of a scaffold for bone repair is to provide a suitable 3D architecture and mechanical properties to support bone formation. Depending on the size and morphology of the damaged bone, different scaffolds can be used, but they must meet a certain number of properties. For example, for the filling of small bone defects such as vertebral fractures, minimally invasive surgery with injection of biomaterials seems the most appropriate. Percutaneous vertebroplasty consists in stabilizing the fracture using a minimally invasive injection (controlled by radiography or computerized tomography) of bone cement in the damaged vertebra². Vertebroplasty is an effective short-term treatment for fracture pain and in most cases, a cement based on a methyl methacrylate (PMMA) resin is used with specific injection systems³.

The use of PMMA in orthopedics was initiated by Charnley in 1960⁴. This material is the gold standard of injectable cement because it is easy to use, inexpensive, bio-inert, biocompatible and has excellent mechanical properties. However, the polymerization, which

is highly exothermic, can causes necrosis and possible residual monomers are associated with risks of cytotoxicity and emboli⁵. Moreover, its hydrophobic nature and bio-inertia do not allow good integration into the surrounding bone tissue. Its hardness causes fractures of adjacent vertebrae due to poor load distribution. In addition, the injectable material must permit secondary bone reconstruction, which is not the case with PMMA, which remains a foreign body in the recipient bone. Therefore, there is a need for injectable cements able to support new bone tissue formation.

the bone mineral phase is made of a polysubstituted non-stoichiometric apatite. Phosphocalcic biomaterials, with a composition similar to calcified tissues, have been developed in recent years. Ceramics are an interesting alternative due to the richness of their compositions and formulations. Phosphocalcic ceramics and cements are perfectly biocompatible materials but above all they are bioactive and can be bioresorbable, *i.e.* they facilitate bone reconstruction and a complete recolonization of lesions linked to their progressive resorption^{6,7}. Calcium phosphate ceramics are very interesting for their applications in bone filling and can be found in various forms (granules, dense or porous solid parts, etc.). The main advantage of biomedical cements over bioceramics is their ability to perfectly fill the defect due to their implantation as malleable or injectable pastes.

The first calcium phosphate cement (CPC) was discovered in 1982 by Brown and Chow⁸. Since this discovery, many formulations have been published and some of them patented. CPC are hydraulic cements that can be obtained by an acid-base reaction in an aqueous phase (water, acid solution or different buffers) between acidic calcium phosphates and more basic calcium phosphates⁹. This setting reaction is generally isothermic, thus eliminating the risk of bone necrosis encountered with PMMA cements¹⁰. CPCs have osteogenic properties and are absorbable more or less quickly with satisfactory mechanical properties. The advantage of CPCs is due in particular to their biological properties (biocompatibility and bioactivity), their

ability to adapt to the shape of the bone defect to be filled, and their ease of implementation and implantation.

Despite a large number of formulations, CPCs can be classified according to the nature of the product resulting from the setting reaction. This can be either apatite or brushite which is the most thermodynamically stable calcium phosphate at low pH and which will then turn into apatite after *in vivo* implantation^{11–13}. Brushite (slightly acidic) can be obtained for instance by a reaction between β -TCP (almost neutral) and monocalcium phosphate monohydrate, MCPM (acidic)¹⁴. Injectable CPC must satisfy a number of standards in order to be used in vertebroplasty¹⁵. In addition to good injectability, biocompatibility, compressive strength, setting time, *in situ* settability, which allows excellent adaptation to the most complex cavity shapes, CPCs must have good radio-opacity. Furthermore, CPCs have to be osteoconductive with a macroporous structure. Indeed, to avoid leakage during injection into the vertebra, it is mandatory to follow the cement with X-ray imaging and, as a consequence, the cement must be radio-opaque. A number of additives such as bismuth and strontium have been proposed to increase radio-opacity of CPCs. More recently, different studies have shown that the use of ZrO_2 is a promising alternative to synthesize radiopaque injectable CPC^{16,17}.

The resorbability of cement generally remains slow, with *in vivo* biodegradation slower than the growth of neoformed bone¹⁸. To allow vascular and cellular penetration into the bulk of the biomaterial before its resorption, an interconnected macroporous structure is an essential condition. CPCs are naturally microporous due to the presence of water from the liquid phase and the acid-base setting reaction. These pores have generally a diameter lower than 5 μm and represent 35 to 50% of the cement volume depending on the liquid/powder ratio used to prepare the cement¹⁹. This pore size allows only the penetration of biological fluids but do not allow the penetration of cellular or vascular elements. In addition, the sought structure often tends to resemble that of the trabecular bone. The size of the macropores must be at least 50

μm^{18} (or better $100 \mu\text{m}^{20}$) and up to $300 \mu\text{m}^{21}$. The absence of natural macroporosities of a given material explains its low osteoconductivity and limits clinical applications.

Several strategies have been implemented to improve the resorbability, including playing on the architecture²², adding a porous agent, or using a phase with a better resorbability, such as calcium sulfate or a metastable calcium carbonate²³. In recent years, better results have been obtained by introducing composite material as a solution into the liquid phase or into the solid phase (mainly as powder, fibers or microspheres). Different polymers have been used such as gelatin^{24,25}, poly(trimethylene carbonate) (PTMC)^{26,27} or most commonly poly(lactic-co-glycolide) (PLGA)^{28–33}.

The objective of this work was to develop an injectable CPC with good opacity and porosity able to support bone formation. To this aim, we first fabricated brushitic cement with the incorporation of ZrO_2 as radio-opacifier. The composite nature of CPCs has been developed with the aim of improving porosity and by consequence the osteoconductivity as well the resorption rate, by introducing PLGA microspheres in the cement. CPC/PLGA was analyzed for several parameters including opacity, handling, and mechanical properties. In vitro degradation and biocompatibility were studied. Finally, this CPC/PLGA was studied in vivo with a model of caudal rat vertebrae.

2. Experimental section

2.1. Materials. Poly(D,L-lactide-co-glycolide) (Resomer RG503H), sodium pyrophosphate dibasic ($\text{H}_2\text{Na}_2\text{O}_7\text{P}_2$, CAS 7758-16-9), β -tri-calcium phosphate (β -TCP, >98% β -phase basis, CAS 7758-87-4), zirconium(IV) oxide (ZrO_2 , 99% trace metals basis, CAS 1314-23-4), citric acid (>99.5%, CAS 77-92-9), 2- propanol (CAS 67-63-0), ethanol (96% vol, CAS 64-17-5), dichloromethane (>99.9% (GC), CAS 75-09-2), phosphate buffered saline (PBS) (P4417) tablets, and 3-(4,5-dimethylthiazol-2-yl)-2,5-diphenyl tetrazolium bromide (MTT, 98%, CAS

298-93-1) were purchased from Sigma-Aldrich. Acetone ($\geq 99\%$ (GC), CAS 67-64-1) and poly(vinyl alcohol)(PVA, CAS 9002-83-5) was purchased from Honeywell. Calcium phosphate monobasic monohydrate, (MPCM, 99%, CAS 10031-30-8) was purchased from STREM chemicals, Inc. MEM alpha medium (Gibco 12571-063), dimethyl sulfoxide (DMSO) (BDH Prolabo 23486.297), foetal bovine serum (FBS) (Eurobio CVFSVF00-01), penicillin/streptomycin (Gibco 15140-122) and 0.05% trypsin-EDTA (Gibco 25300-054) were used for cell cultures.

2.2. Preparation of PLGA microspheres. To prepare PLGA-microspheres of around 100 μm in diameter, a double-emulsion-solvent-evaporation method (water-in-oil-in-water or $W_1/O/W_2$) was used. Microspheres were produced by first dissolving 500 mg of PLGA in 5 ml dichloromethane (DCM), forming oil phase (O). Then 1 mL of distilled water which is the first aqueous phase (W_1) was added to the oil phase. The mixture was emulsified using an Ultra-Turrax emulsifier (T25 digital, IKA) for 90 s at 22000 rpm. Then, 6 mL 0.3% aqueous poly(vinyl alcohol) (PVA) solution (W_2) was added and emulsified for another 90 s at 22000 rpm to produce the second emulsion. After which 394 mL 0.3% PVA solution and 400 mL 2% 2-propanol solution were added to the mixture. The resultant $W_1/O/W_2$ emulsion was stirred overnight at room temperature to evaporate the solvent and solidify PLGA microspheres. Then, the microspheres were finally washed in distilled water and collected through centrifugation at 3000 rpm for 10 min, lyophilized and stored at 4°C until use. The size distribution of PLGA microspheres was characterized using a laser diffraction particle size analyzer (Mastersizer 3000).

2.3. Fabrication of CPC/PLGA samples. The cement powder was composed of MPCM and β -TCP at a 55 to 45 molar ratio. The MPCM and β -TCP powder were sieved to obtain only

150 and 50 μm particles, respectively. Zirconia (20% wt) as opacifier and disodium dihydrogen pyrophosphate (1% wt) as supplement to slow down the reaction time were added directly to the powder. The cement (CPC) was fabricated by addition of citric acid (0.5M) solution, to powder at liquid ratio of 0.4 mL per gram of cement (irrespective of ZrO_2 content). Macroporous cement was fabricated by addition of 30% of PLGA microsphere to the powder mixture and denoted as CPC/PLGA30. The addition of liquid was adjusted to keep a powder/liquid ratio of 0.4. CPC and CPC/PLGA30 formulations were mixed using a spatula for 1 min in a glass plate and immediately transferred to a 5 mL syringe. After which, the paste was injected in silicon rubber molds of 5 mm diameter and 2 mm height. Within 15 min samples were transferred to calcium free Dulbecco's phosphate buffered saline (DPBS, Sigma) to allow for complete setting at 37°C for 24 h.

2.4. Opacity measurements. For X-ray opacity measurements, 2 mm thick samples were produced. The X-ray opacity was measured at 0.65 mAs, 80 kV using an OBI (On-Board Imager®) (TrueBeam-Stx, Varian). A 2 mm sample of a PMMA-based cement (Vertebroplastic, Biomet, France), which has zirconia as radiopacifier, was used as control along with an aluminum wedge (2–8 mm) in 1 mm steps. The photos were treated with the software Image J to determine the grey level between the samples.

2.5. Morphology analysis. The PLGA microspheres, CPC and CPC/PLGA scaffold morphology, and microstructure were analyzed by scanning electron microscopy (SEM) (HITACHI S4800 system). For SEM observation, scaffolds were coated with platinum using a Polaron SC7620 Mini Sputter Coater.

2.6. Mechanical properties. The mechanical properties of the CPC and CPC/PLGA30 scaffolds were characterized using a modular traction system (1/ME) in compression mode coupled with a 5 kN force sensor (maker). Samples were moulded in cylindrical shape (10 mm diameter and 20 mm height). Samples were then placed between dedicated jaws and compressed at a constant speed of 0.01 mm.s^{-1} until they broke. Samples were imaged with a 16 Mb camera (SVS-VISTEK) at 1 Hz. Samples were initially randomly patterned with thin black paint to perform digital image correlation (DIC). Using an already described DIC algorithm dedicated to large deformations^{34,35}, sample strain changes could be computed without inaccuracy coming from the machine and jaw plays. Linear elastic regions from the stress–strain graphs were then used to calculate the Young’s modulus from at least three assays. The stress at which the sample begins to break was also measured.

2.7. Structural and chemical properties. The X-ray diffraction (XRD) patterns of CPC and CPC/PLGA30 scaffolds were recorded using $\text{CuK}\alpha$ radiation, 2θ range of $10\text{--}70^\circ$ with a scan speed of $2^\circ.\text{min}^{-1}$, and the PANalytica Xpert powder XRD system. The Fourier Transform Infrared (FTIR) spectrum of CPC and CPC/PLGA30 nanocomposites was recorded with the NEXUS instrument, equipped with an attenuated total reflection accessory in the frequency range of $600\text{--}4000 \text{ cm}^{-1}$. The FTIR spectrum was scanned at 1 cm^{-1} resolution, and signals were averaged from 32 scans. Energy-dispersive X-ray spectroscopy analysis (EDX) was taken with Zeiss EVO ED15 microscope coupled with an Oxford X-MaxN EDX detector.

2.8. Degradation study. For the degradation study, CPC and CPC/PLGA30 samples were placed in 3 ml PBS (pH 7.4) and incubated using an Incu-Shaker (Benchmark) in at 37°C and 70 rpm for 10 weeks. 3 samples were analyzed at each week 1, 2, 4, 6 and 10 of incubation. Immediately after removal of the samples from the incubator, the pH of the PBS medium was

measured. The samples were then washed with distilled water and vacuum dried overnight before measuring the mass. Mass change of the samples was calculated using the following equation:

Mass loss (%) = $\frac{m_0 - m_n}{m_0} \times 100$, where mass loss = mass change of sample at $t = n$ (%), m_0 = mass of sample at $t = 0$ (g), m_n = mass of sample at $t = n$ (g).

2.9. Setting time and injectability. Initial and final setting time was assessed using custom available Gillmore needles (ASTM C266). For this, a plastic mould 10 mm in diameter and 15 mm in height was used as a mould. Samples were mixed and injected into the mould, after which the initial and final setting time was determined. Tests were performed in at least 3 samples. Injectability tests were done on the CPC and CPC/PLGA30 samples in two different methods. Briefly, the first method consist to evaluate by extrusion (i.e., quantification of residual-cement mass retained in the syringe after applying a standard force), during a predetermined injection time period the injectability. Syringes of 10 mL (Omnifix® luer lock solo) were filled with ~ 8 g fresh-cement paste. After predetermined times from the mixing, the cement was extruded manually. The injectability was calculated as: $I = [(m_i - m_f)/m_i] \times 100\%$ where I is the injectability, m_i is the initial mass and m_f is the final mass of the extrusion. The second method consists to after mixing the powder with liquid, to place the syringe, vertically in a fixture and put under the plates of a handmade injection machine. At a predetermined time of 4 min after mixing the cement, the cement was extruded with a compression rate of $0.2 \text{ mm} \cdot \text{min}^{-1}$ up to a maximum force of 100 N. Compressive force was applied to the syringe and recorded as a function of the plunger travel length. All tests were performed in threefold.

2.10. Cell viability assays. Scaffolds were sterilized with ethanol for 30 min and under UV light (405 nm) for 1h. MG-63 osteosarcoma cells were cultured on the sterilized scaffolds for 7 days. Cell viability was analyzed using the MTT assay. Cells were incubated with 100 μ L of culture medium containing 0.05 mg.mL⁻¹ of MTT solution for 3h. The obtained purple-colored formazan crystals, due to MTT reduction by living cells, were solubilized by addition of 100 μ L of DMSO and absorbance recorded at 560 nm using a Multiskan microplate spectrophotometer (Thermofisher, USA).

2.11. Implantation in rat vertebrae. One male Wistar rat ((CrI:(Wi)Br), Charles River, France) with weight around 400 g was used for an adequate vertebrae size. The rat was kept in light controlled, air-conditioned rooms and fed ad libitum. One vertebra was used as a control (defect which remained empty of materials) and two other vertebrae were used for CPC and CPC/PLGA30 implantation. The rat was anesthetized with an intraperitoneal injection of ketamine and xylazine (Alcyon, Pau, France) (40 and 9mg/kg, respectively). The tail was disinfected and a dorsal incision was made approximately from Cd31 to Cd35 vertebrae. The skin and the muscles were retracted with buffered saline solution irrigation, the vertebrae were exposed and an intra-osseous defect of 3x3 mm was performed in the exposed surface of the vertebrae. CPC and CPC/PLGA30 were prepared freshly and injected directly after the required setting time to allow the incorporation of the material in each vertebra. After treating the hard tissue, the skin was tightly sutured with resorbable sutures (Vicryl 3/0, Ethicon, Issy les Moulineaux, France). Following surgery, Buprenorphine SR-LAB (Wildlife Pharmaceuticals, Windsor, CO, USA) was used at a dose of 1.2 mg/kg to provide 72 h analgesia.

2.12. X-ray micro-CT analysis. The wound healing was controlled daily during the healing period and, after a period of one month, the rat was sacrificed by intraperitoneal injection of Pentothal (Alcyon, Pau, France) (133 mg/kg). The tail between Cd31 and Cd32 was harvested and 3D radiographic evaluation was performed using an X-ray micro-CT instrument (SKYSCAN 1172 X-ray Microtomograph, Microphotronics Inc, Allentown, USA) with 3D reconstruction software (Aviso, FEI company, Hillsboro, USA). Implanted samples were planned to be scanned at 360° rotation at 0.7 degree intervals. Measurements were made on the Region of Interest (ROI) \times 1.5 mm Tissue Volume (TV) on the computer-reconstructed 3D samples.

3. Results and discussion

A CPC doped with ZrO₂ was first obtained by mixing a powder phase (MCPM, β -TCP and ZrO₂) with a solution of 0.5M citric acid. Then PLGA microspheres were added to formulation to obtain macroporous injectable cement.

3.1. Obtention of a radio-opaque CPC.

A major concern with vertebroplasties is the risk of cement leakage. The use of an injectable cement requires an imaging monitoring of its injection into vertebrae and therefore to use of a radio-opaque material is essential. To achieve this requirement, different percentages of zirconia have been introduced in the CPC formulation. CPC cement have been produced using MCPM and β -TCP at a 55 to 45 molar ratio³⁶. Figure 1 shows the comparison of the opacity of our ZrO₂-containing CPCs with commercial PMMA cement (Biomet Bone Cement V) and with aluminum sheets used as references.

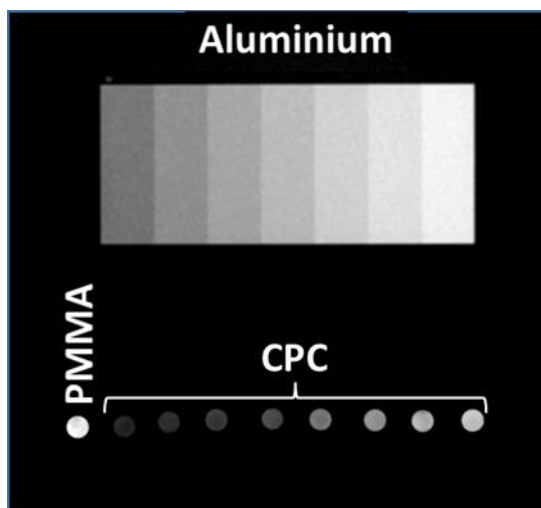


Figure 1. Illustrations of the opacity of aluminium sheets (from 2 to 8 mm), commercial PMMA and CPC with different ZrO_2 percentages (0, 1, 5, 10, 20, 30, 40 and 50%).

Below 20% of ZrO_2 , CPC are not visible by radiography meaning that such CPC cannot be used in vertebroplasty. CPC containing 20% ZrO_2 are equivalent to 2 mm of aluminium and clearly visible by X-ray imaging. Intensities of grey level are given in Table 1.

Table 1. Opacity intensities of aluminum sheets, commercial PMMA and different CPCs.

Samples	Aluminium (2mm)	PMMA	CPC (0% ZrO_2)	CPC (10% ZrO_2)	CPC (20% ZrO_2)	CPC (30% ZrO_2)	CPC (40% ZrO_2)	CPC (50% ZrO_2)
Intensity (a.u.)	48051	54306	44153	46513	48323	50039	51219	52136

In Figure 2, the compression strength and Young's modulus of the samples are given as a function of the ZrO_2 percentage. The influence of zirconia on the mechanical properties was evaluated on CPC with 20 to 40% of ZrO_2 . CPC without zirconia had compression strength of 3MPa; in comparison CPC with 20% ZrO_2 had 23MPa which represent a significant increase. This compressive strength improvement by the incorporation of ZrO_2 had never been observed in the literature as far as we know. Above 30% of ZrO_2 , compression strength

decreased by half. The same behavior was observed for Young's modulus, CPC with 20% ZrO_2 had a Young's modulus 7 fold-higher than CPC alone but after 30% the value decreased. The decrease of mechanical properties after a certain content of ZrO_2 was probably due to a change in L/P ratio which was not optimal anymore or by the aggregation of ZrO_2 in the calcium phosphate. In conclusion, the incorporation of 20% ZrO_2 in the CPC formulation was enough to obtain good radio opacity and, in the same time, a strong increase of the mechanical properties of the cement. From this point and for the rest of the study, the CPC formulation with 20% of ZrO_2 was chosen and will be denoted as CPC.

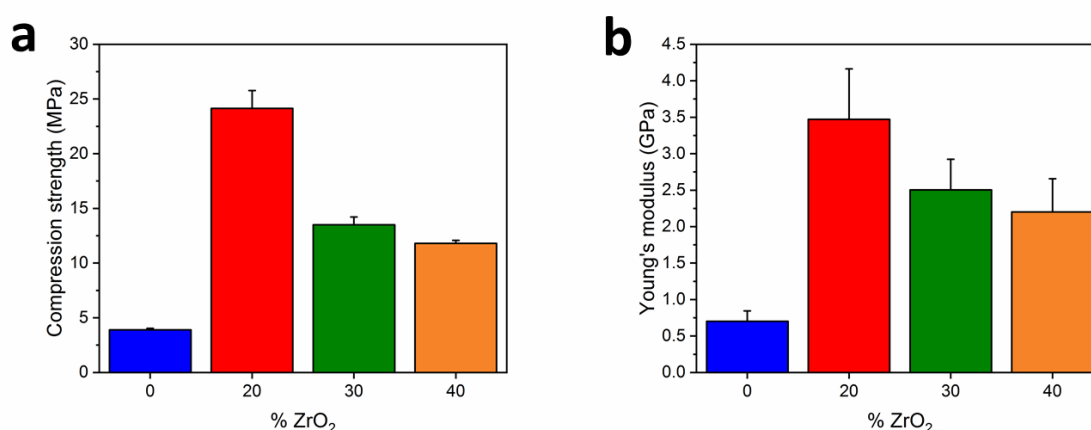


Figure 2. Mechanical properties of the different CPC containing different concentrations of ZrO_2 . (a) Compression strength and (b) Young's modulus values.

3.2. Introduction of PLGA microspheres in the CPC.

PLGA microspheres were synthesized as described in the Experimental section and observed by SEM as shown in Figure S1. Microspheres had a spherical shape, a smooth surface and homogeneous sizes. This was confirmed by granulometry which gave an average size of 133 μm and a polydispersity index of 1.1 (Table S1).

To generate CPC/PLGA scaffold, microspheres at 30% (w/w) were added to the CPC and cylindrical blocks were generated. The SEM micrographs showing the inside surface after sectioning cylindrical block of CPC and CPC/PLGA30 are presented in Figure 3a-d. All pictures illustrated the incorporation of the PLGA microspheres. The microspheres were

dispersed and homogeneously spread in the CPC as shown in Figure S2. According to previous studies, interconnected porosity was observed when PLGA microspheres with size above 50 μm were introduced in CPC with a loading of 20%. In Figure 3e and 3f, SEM micrographs showed CPC/PLGA30 after calcination at 600°C for 2 hours which destroyed the PLGA microspheres and generated a CPC with a high porosity.

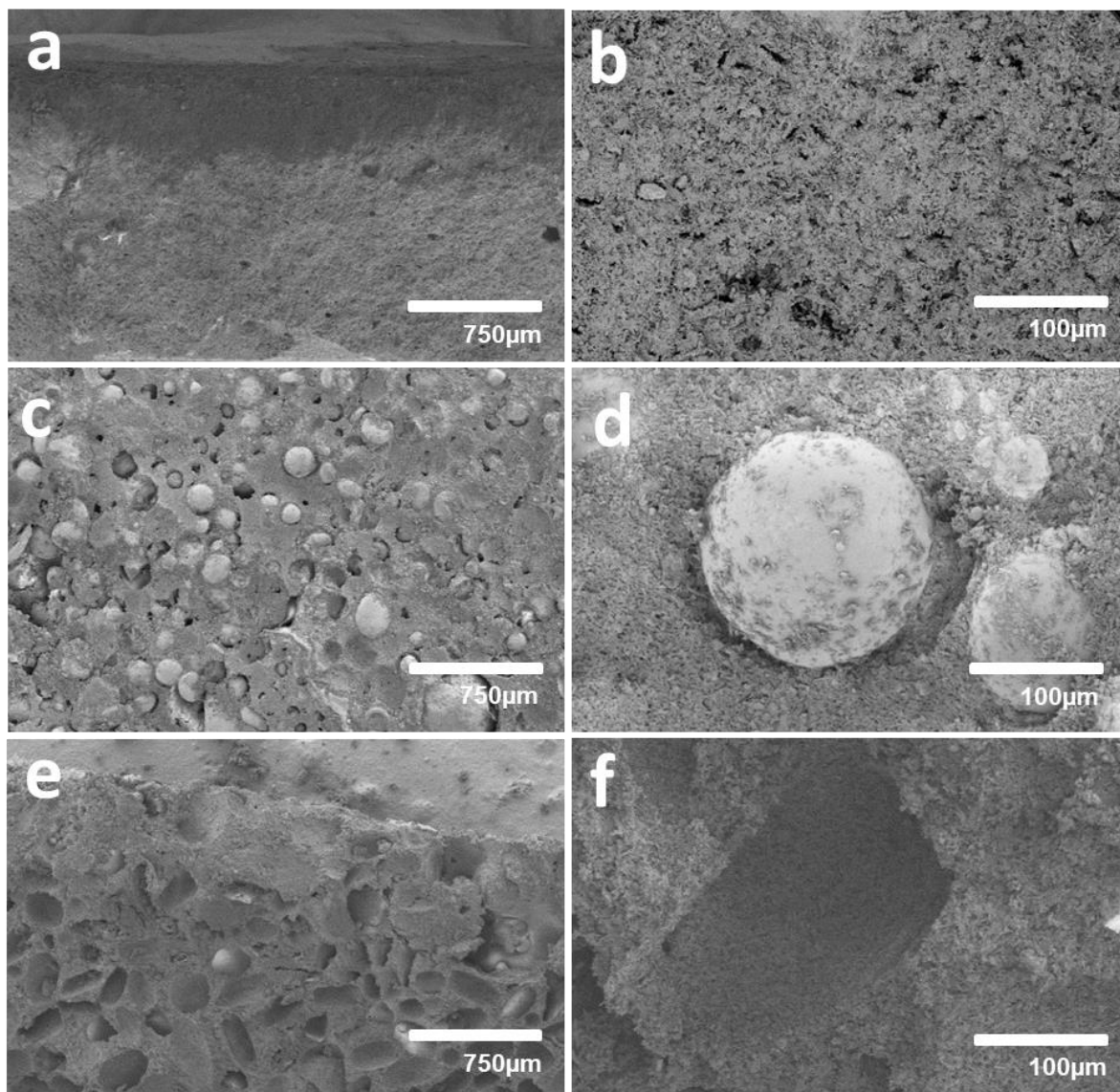


Figure 3. SEM images showing sections of CPC (a and b) or CPC/PLGA30 (c and d). SEM images showing surface of CPC/PLGA30 after calcination (e and f).

To confirm brushite formation during the cement preparation, as well ZrO_2 and PLGA incorporation, XRD analysis was performed on the CPC and CPC/PLGA30 cements and data

are shown in Figure 4a. The CPC (shown blue) showed five characteristics peaks of brushite phase at $2\theta = 11.6, 21, 30.5, 31.3$ and 30.4° as mentioned by the symbol \square , that described the formation of a unique phase during the cement preparation. The addition of ZrO_2 was demonstrated by the presence of four peaks at $2\theta = 31, 35, 50$ and 60° corresponding to the plan (111), (200), (220) and (311), respectively (mentioned by \blacksquare in the red diffractogramm). The last diffractogram (black line) showed the presence of one peak at $2\theta = 24^\circ$ mentioned by “*” corresponding to PLGA.

To understand cement organization and the interactions with ZrO_2 and PLGA microspheres during the cement fabrication, FTIR spectra were recorded (Figure 4b). The powder mixture used to prepare the cement showed characteristics peaks of β -TCP at 600 and 1000 cm^{-1} . The addition of ZrO_2 was validated by the peak at 750 cm^{-1} (■ in the graph). After initiation of the cement by the addition of the liquid phase, the spectra corresponding to brushite cement appeared with characteristics peaks at 1000 cm^{-1} .

These peaks (mentioned by ●) are attributed to the stretching mode of P-O and bending mode of O-H. O-H bending mode was also found at 1650 cm^{-1} . The last characteristic peak corresponding to the stretching mode of O-H was found at 3500 cm^{-1} . The addition of PLGA microspheres to the cement composition was confirmed by the apparition of a peak at 1750 cm^{-1} mentioned by * corresponding to C=O stretching mode.

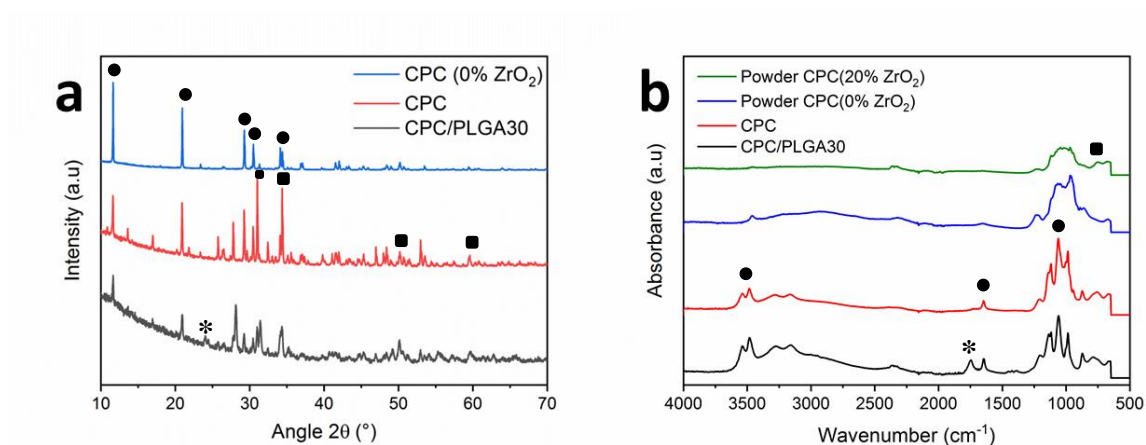


Figure 4. Structural and chemical properties of the CPC and CPC/PLGA cements. (a) X-ray-diffractograms of CPC and CPC/PLGA cements and (b) FTIR spectra of CPC powders, CPC and CPC/PLGA cements.

The incorporation of PLGA microspheres modifies the cement structure and has an influence on some of its intrinsic properties such as opacity (Fig 5.). CPC/PLGA30 showed a slight decrease of the opacity but the sample remains still opaque. In comparison to CPC without sphere, CPC/PLGA30 corresponds to a CPC with 10% of ZrO_2 which is acceptable.

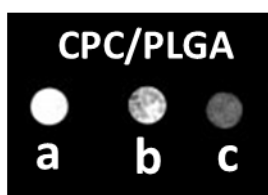


Figure 5. Illustrations of the opacity. (a) CPC with different PLGA percentages (b) CPC/PLGA5 and (c) CPC/PLGA30

As anticipated, PLGA microspheres addition had an impact on the mechanical properties of CPC as shown in Figure 6. Indeed, the incorporation of 30% PLGA microspheres decreased the compression strength by ten times and the same trend was observed for Young's modulus (from 3.5 to 1 GPa). This decrease of the mechanical properties is probably due to the change of the L/P ratio which is not optimal with the incorporation of microspheres. Similar results have been already observed in another study³⁷.

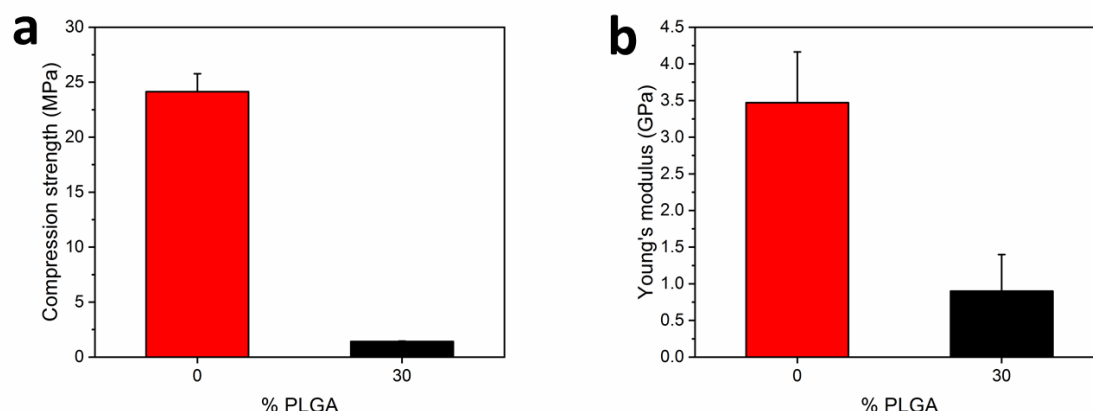


Figure 6. Effect of PLGA microspheres on the mechanical properties of CPC. (a) Compression strength and (b) Young's modulus values of CPC and CPC/PLGA30.

Important parameters to quantify are the setting time and the injectability of the cement. Indeed the CPC must be handling easily by the operator. Figure 7a showed the initial and final setting time of CPC and CPC/PLGA30 pastes. The incorporation of PLGA microspheres decreased the initial setting time from 12 to 7min. The same effect was observed for final setting time, CPC/PLGA30 showed a final setting time at 12 min while CPC had a final setting time at 22 min. The PLGA microspheres induced a global diminution of setting of CPC paste. The injectability graphs are presented in Figure 7b and 7c. When both pastes were injected at 4 min, almost 100% of the mass was injected. A slight difference between CPC and CPC/PLGA30 was noticed when the pastes were injected at 6 min. By contrast, a significant difference appeared between the samples at 10 min since at that time, CPC was injected at 50% while CPC/PLGA30 was not enough viscous to be injected. The incorporation of PLGA microspheres decreased the injectability after 8 min which is correlated with the setting time. Figure 7c showed the force to inject the paste in function of time (start at 4 min). The graphs showed that the force necessary to inject CPC/PLGA30 is higher until 80 seconds, after which the force reach 100N which is the limit of the machine at 100 s.

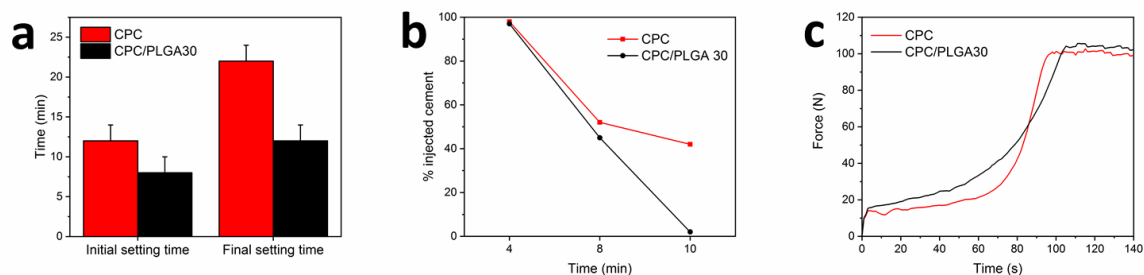


Figure 7. Initial and final setting time of CPC and CPC/PLGA30. Injectability graphs of CPCs. b) Comparison of percentage injected at different time point and c) comparison of injectability under pressure between CPC and CPC/PLGA microspheres.

The influence of PLGA microsphere on the degradation rate of the CPC is an important parameter to quantify. The mass loss of CPC and CPC/PLGA30 as a function of time is given in Figure 8a. The CPC did not show any significant mass loss even at week 10. In comparison, mass loss of CPC/PLGA30 after 2 weeks is about 5%. At week 4, CPC/PLGA30 samples showed a high decrease in mass of 70%, indicating PLGA erosion. After 6 weeks, almost all the sample was degraded. The incorporation of 30% of PLGA microspheres in the CPC formulation leads to an almost complete *in vitro* degradation of the sample after 6 weeks, meaning that the porosity induced by PLGA erosion accelerated the CPC degradation.

The pH of the PBS solution containing CPC and CPC/PLGA30 is given in Figure 7b. The medium of CPC showed a stability of the pH around 7 even after 10 weeks. However, the pH of CPC/PLGA30 showed a high decreased after 2 weeks (pH5 .5), and stabilized from 6 weeks to reach an ultimate pH of 3.5 which is much lower than the pH of CPC. This diminution is due to the hydrolysis of PLGA microspheres that lead to an acidification of the medium.

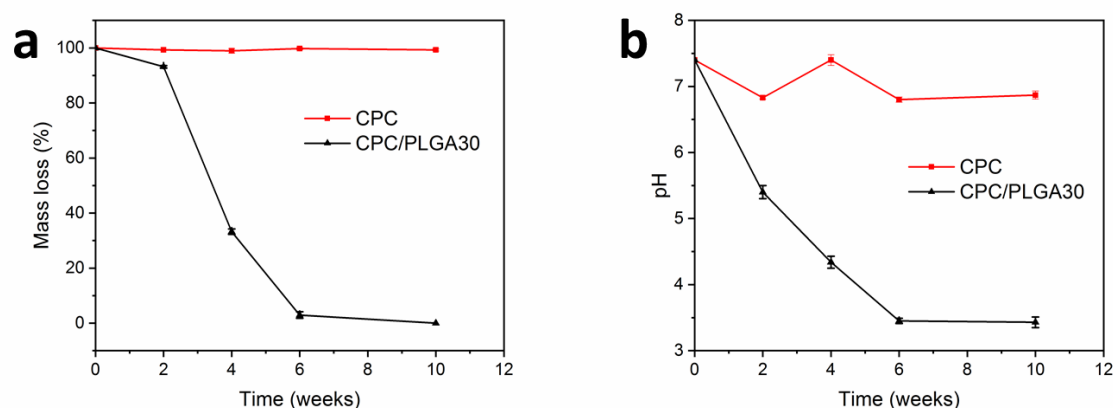


Figure 8. Degradation analysis of the different CPC/PLGA compositions. (a) Percentage of mass loss and (b) pH in PBS medium of CPC and CPC/microspheres, as a function of time.

3.3. Biological studies.

3.3.1. *In vitro* analyses.

The biocompatibility of CPC and CPC/PLGA30 was investigated using MG-63 human bone osteosarcoma cells which are cells with an osteogenic potential. CPC and CPC/PLGA30 did not induced any significant effect on cell proliferation measured at day 4 and 7 as compared to cells grown without scaffolds (Figure 9). This cell viability test confirmed that CPC and CPC/PLGA30 are biocompatible.

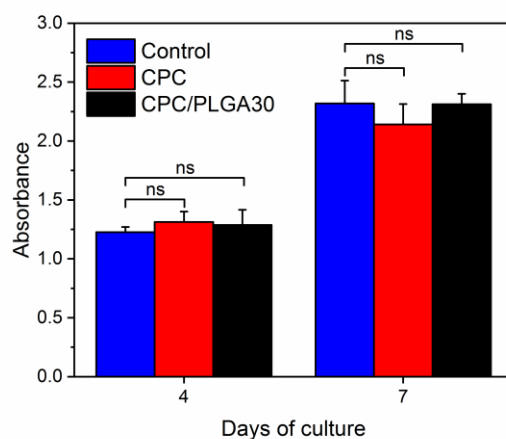


Figure 9. MG-63 cell viability in the presence of CPC and CPC/PLGA30 assessed with the MTT assay at day 4 and 7 after seeding (ns = not significant).

3.3.2. *In vivo* experiments.

Figure 10 shows micro-CT reconstruction of rat caudal vertebrae with or without implantation of material after one month. During the experimentations, no infection of the operative site was observed. Micro-CT analyses did not show a significant bone formation without the addition of the biomaterial. The opacity of the CPC after one month is clearly efficient after one month while CPC/PLGA showed a diminution of the opacity which is probably due to the degradation of the cement (Fig.S3). Concerning the vertebra containing the CPC, the micro-CT imaging showed a good visualization of the material which was still present in the defect. For the last vertebrae with CPC/PLGA30, we observed a good degradation of the cement after 1 month. New bone formation through the cement could be validated by histological analyses.

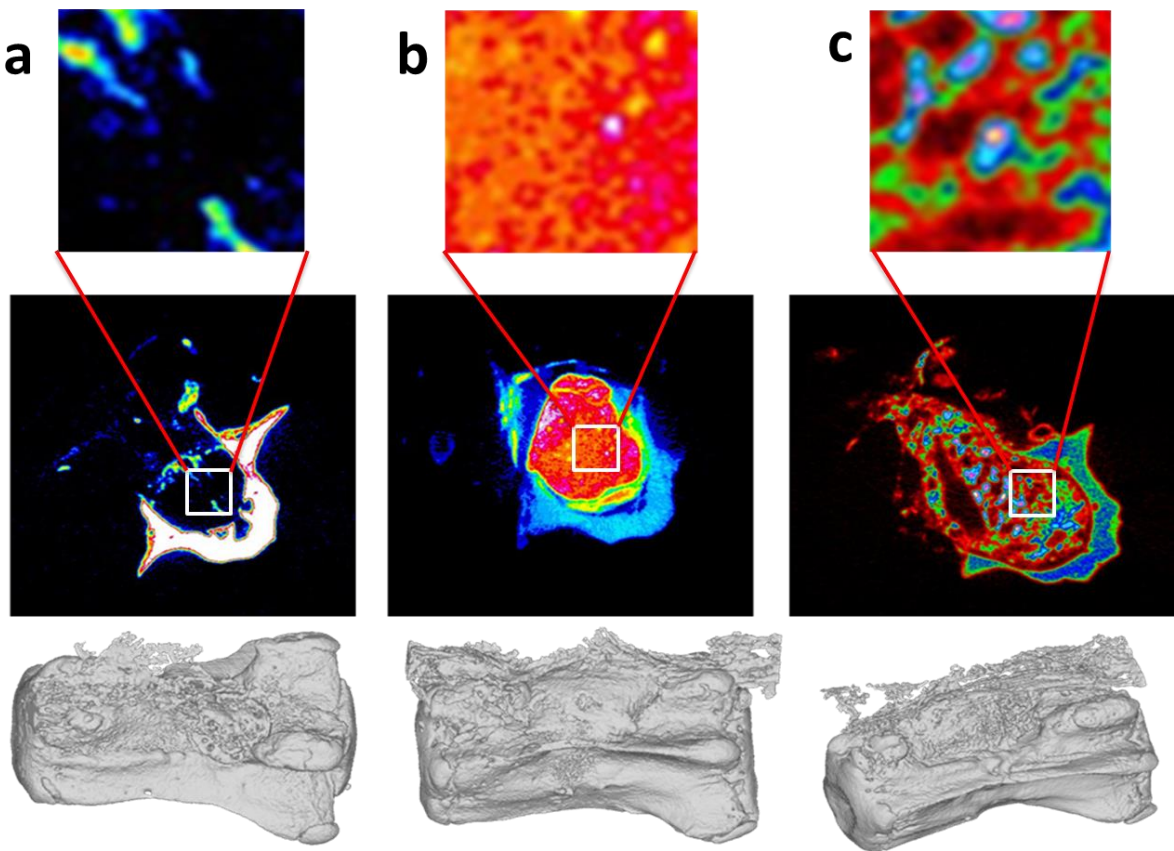


Figure 10. *In vivo* imaging. Micro-CT reconstruction of rat caudal vertebrae after 1month. a) Empty defect, b) CPC and c) CPC/PLGA30.

4. Conclusions

In this study, we fabricated a new CPC containing ZrO₂ and PLGA microspheres. The CPC/PLGA cement was found to have good handling (injectability, initial and final setting time, cohesive properties) but also sufficient radio-opacity. The mechanical strength of CPC was acceptable due to the reinforcement by ZrO₂. This composite has also a good macroporosity and an increased degradability. Indeed, *in vitro* analysis of CPC/PLGA showed full degradation over 10 weeks, which has for consequences to decrease the pH due to PLGA hydrolysis. The *in vitro* assay with MG63 cells showed the biocompatibility of the material and the *in vivo* study in rat caudal vertebrae showed that it was partially resorbed after one month.

REFERENCES

1. Langer, R. & Vacanti, J. Advances in tissue engineering. *J. Pediatr. Surg.* **51**, 8–12 (2016).
2. Nakano, M. *et al.* Vertebroplasty Using Calcium Phosphate Cement for Osteoporotic Vertebral Fractures: Study of Outcomes at a Minimum Follow-up of Two Years. *Asian Spine J.* **6**, 34 (2012).
3. McGraw, J. K. *et al.* Society of Interventional Radiology quality improvement guidelines for percutaneous vertebroplasty. *J. Vasc. Interv. Radiol.* **14**, 827–31 (2003).
4. A. Hardinger, S. & Wijaya, N. A mild method for rapid tert-butyl-diphenylsilylation of primary and secondary alcohols. *Tetrahedron Lett.* **34**, 3821–3824 (1993).
5. Lieberman, I. H., Togawa, D. & Kayanja, M. M. Vertebroplasty and kyphoplasty: filler materials. *Spine J.* **5**, S305–S316 (2005).
6. Nguyen, L. H. *et al.* Vascularized bone tissue engineering: approaches for potential improvement. *Tissue Eng. Part B. Rev.* **18**, 363–82 (2012).
7. Saijo, H. *et al.* Maxillofacial reconstruction using custom-made artificial bones fabricated by inkjet printing technology. *J. Artif. Organs* **12**, 200–205 (2009).
8. Brown, W. E. & Chow, L. C. Dental restorative cement pastes. (1985).
9. Ginebra, M., Canal, C., Pastorino, D. & Montufar, E. B. Calcium phosphate cements as drug delivery materials ☆. *Adv. Drug Deliv. Rev.* **64**, 1090–1110 (2012).
10. Passuti, N. & Gouin, F. Antibiotic-loaded bone cement in orthopedic surgery. *Joint. Bone. Spine* **70**, 169–74 (2003).
11. Brown, P. W. & Fulmer, M. Kinetics of Hydroxyapatite Formation at Low Temperature. *J. Am. Ceram. Soc.* **74**, 934–940 (1991).
12. Apelt, D. *et al.* In vivo behavior of three different injectable hydraulic calcium phosphate cements. *Biomaterials* **25**, 1439–51
13. Constantz, B. R. *et al.* Histological, chemical, and crystallographic analysis of four calcium phosphate cements in different rabbit osseous sites. *J. Biomed. Mater. Res.* **43**, 451–61 (1998).
14. Dorozhkin, S. V. Self-setting calcium orthophosphate formulations. *J. Funct. Biomater.* **4**, 209–311 (2013).
15. Lewis, G. Injectable bone cements for use in vertebroplasty and kyphoplasty: State-of-the-art review. *J. Biomed. Mater. Res. Part B Appl. Biomater.* **76B**, 456–468 (2006).
16. Åberg, J. *et al.* In vivo evaluation of an injectable premixed radiopaque calcium phosphate cement. *Int. J. Biomater.* **2011**, (2011).

17. Åberg, J. *et al.* Biocompatibility and resorption of a radiopaque premixed calcium phosphate cement. *J. Biomed. Mater. Res. - Part A* **100 A**, 1269–1278 (2012).
18. Bohner, M. Design of ceramic-based cements and putties for bone graft substitution. *Eur. Cell. Mater.* **20**, 1–12 (2010).
19. Espanol, M. *et al.* Intrinsic porosity of calcium phosphate cements and its significance for drug delivery and tissue engineering applications. *Acta Biomater.* **5**, 2752–2762 (2009).
20. Takagi, S. & Chow, L. C. Formation of macropores in calcium phosphate cement implants. *J. Mater. Sci. Mater. Med.* **12**, 135–9 (2001).
21. Karageorgiou, V. & Kaplan, D. Porosity of 3D biomaterial scaffolds and osteogenesis. *Biomaterials* **26**, 5474–5491 (2005).
22. Ginebra, M. P., Espanol, M., Montufar, E. B., Perez, R. A. & Mestres, G. New processing approaches in calcium phosphate cements and their applications in regenerative medicine. *Acta Biomater.* **6**, 2863–2873 (2010).
23. Combes, C., Bareille, R. & Rey, C. Calcium carbonate–calcium phosphate mixed cement compositions for bone reconstruction. *J. Biomed. Mater. Res. Part A* **79A**, 318–328 (2006).
24. Habraken, W. J. E. M. *et al.* Introduction of gelatin microspheres into an injectable calcium phosphate cement. *J. Biomed. Mater. Res. Part A* **87A**, 643–655 (2008).
25. Li, M., Liu, X., Liu, X., Ge, B. & Chen, K. Creation of macroporous calcium phosphate cements as bone substitutes by using genipin-crosslinked gelatin microspheres. *J. Mater. Sci. Mater. Med.* **20**, 925–934 (2009).
26. Habraken, W. J. E. M. *et al.* Introduction of enzymatically degradable poly(trimethylene carbonate) microspheres into an injectable calcium phosphate cement. *Biomaterials* **29**, 2464–2476 (2008).
27. Liao, H. *et al.* Injectable calcium phosphate cement with PLGA, gelatin and PTMC microspheres in a rabbit femoral defect. *Acta Biomater.* **7**, 1752–1759 (2011).
28. Simon, C. G., Khatri, C. A., Wight, S. A. & Wang, F. W. Preliminary report on the biocompatibility of a moldable, resorbable, composite bone graft consisting of calcium phosphate cement and poly(lactide-co-glycolide) microspheres. *J. Orthop. Res.* **20**, 473–482 (2002).
29. Qi, X. & Ye, J. Mechanical and rheological properties and injectability of calcium phosphate cement containing poly (lactic-co-glycolic acid) microspheres. *Mater. Sci. Eng. C* **29**, 1901–1906 (2009).
30. Qi, X., Ye, J. & Wang, Y. Improved injectability and in vitro degradation of a calcium phosphate cement containing poly(lactide-co-glycolide) microspheres. *Acta Biomater.* **4**, 1837–45 (2008).
31. Fei, Z. *et al.* Preparation and property of a novel bone graft composite consisting of rhBMP-2 loaded PLGA microspheres and calcium phosphate cement. *J. Mater. Sci. Mater. Med.* **19**, 1109–1116 (2008).
32. Schnieders, J., Gbureck, U., Thull, R. & Kissel, T. Controlled release of gentamicin from calcium phosphate–poly(lactic acid-co-glycolic acid) composite bone cement. *Biomaterials* **27**, 4239–4249 (2006).
33. Ruhé, P. Q. *et al.* Porous Poly(DL-lactic- co -glycolic acid)/Calcium Phosphate Cement Composite for Reconstruction of Bone Defects. *Tissue Eng.* **12**, 789–800 (2006).
34. Vu, T.-L. & Barés, J. Soft grain compression: beyond the jamming point. (2019).
35. Vu, T. L., Barés, J., Mora, S. & Nezamabadi, S. Deformation Field in Diametrically Loaded Soft Cylinders. *Exp. Mech.* (2019). doi:10.1007/s11340-019-00477-4
36. Sladkova, M. *et al.* Fabrication of macroporous cement scaffolds using PEG particles: In vitro evaluation with induced pluripotent stem cell-derived mesenchymal progenitors. *Mater. Sci. Eng. C* **69**, 640–652 (2016).
37. Habraken, W. J. E. M., Wolke, J. G. C., Mikos, A. G. & Jansen, J. A. PLGA microsphere/calcium phosphate cement composites for tissue engineering: In vitro release and degradation characteristics. *J. Biomater. Sci. Polym. Ed.* **19**, 1171–1188 (2008).

Supporting information

Fabrication of injectable calcium phosphate cement containing PLGA microspheres

Habib Belaid^{1,2}, Pierre-Yves Collart-Dutilleul³, Alban Desoutter³, Frédéric Cuisinier³, Jonathan Barés⁴, Vincent Huon⁴, Catherine Teyssier², David Cornu¹, Vincent Cavaillès^{2*£} and Mikhael Bechelany^{1*£}

¹Institut Européen des Membranes, IEM-UMR 5635, Université Montpellier, CNRS, ENSCM, Montpellier, France

²IRCM, Institut de Recherche en Cancérologie de Montpellier, INSERM U1194, Université Montpellier, Montpellier F-34298, France

³Laboratoire de bioingénierie et nanosciences, EA4203, Université de Montpellier, Montpellier, France

⁴Laboratoire de Mécanique et Génie Civil, Univ Montpellier, CNRS, Montpellier, France

* Corresponding authors:

mikhael.bechelany@umontpellier.fr, Phone: +33467149167, Fax: +33467149119

vincent.cavaillès@inserm.fr, Phone: +33467612405, Fax: +33467613787

£ Co-last authors

Keywords: Calcium phosphate cement, PLGA microspheres, vertebroplasty, bone metastasis

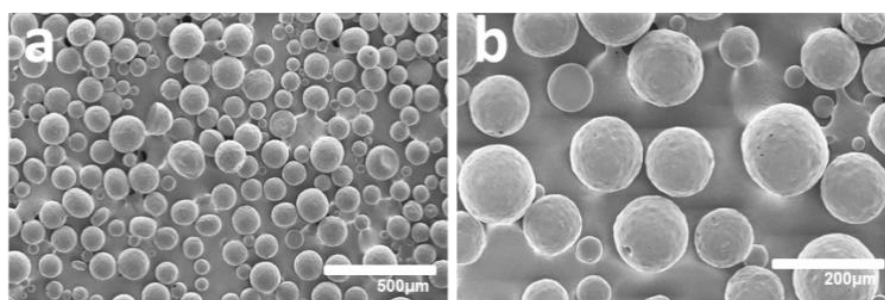


Figure S1. Scanning electron micrographs showing microspheres morphology. (a) and (b) PLGA microspheres.

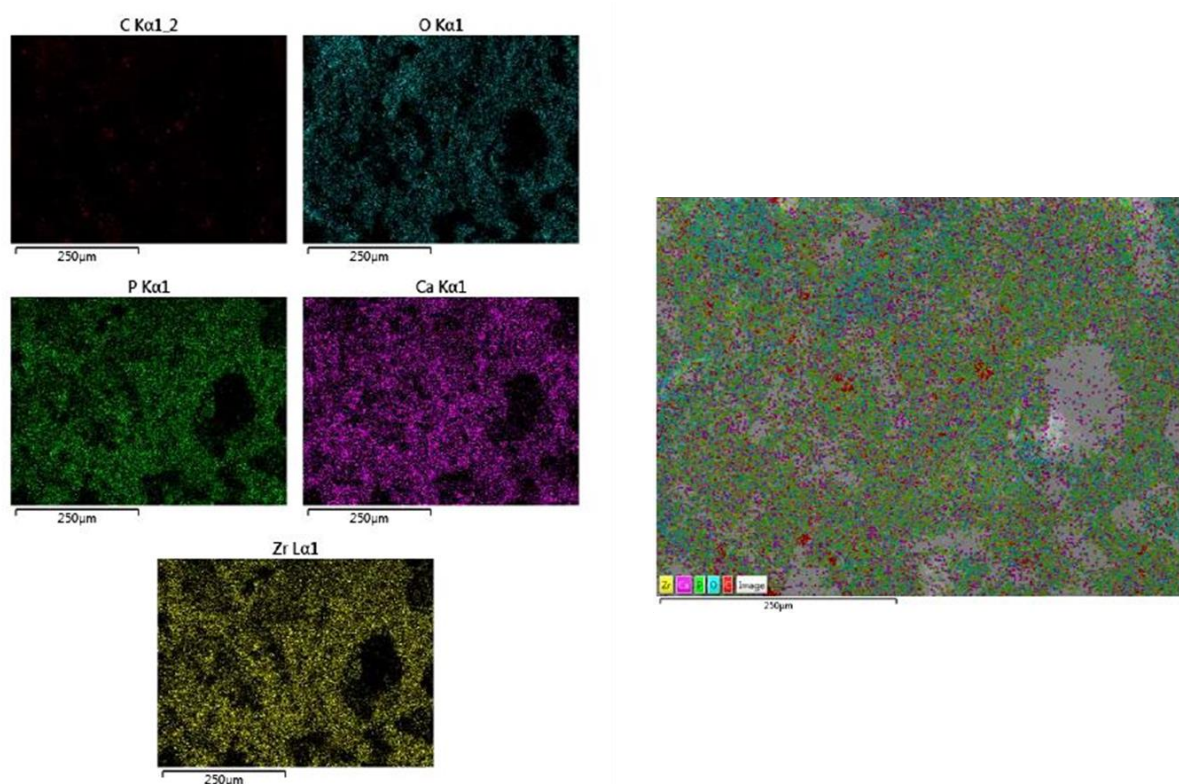


Figure S2. EDX mapping images of atoms elements present in CPC/PLGA30.

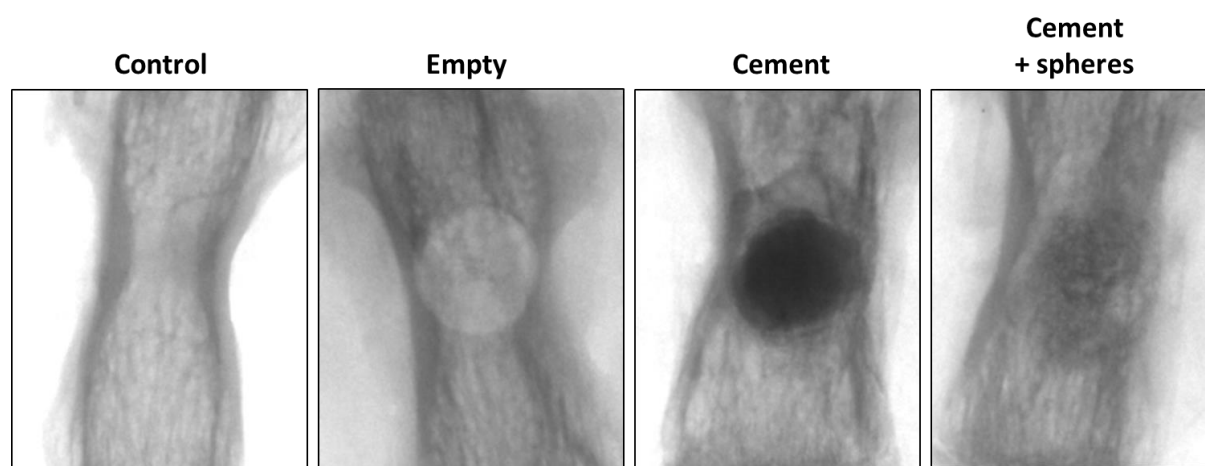


Figure S3. X-ray images of rat vertebrae showing the opacity of the material after one month.

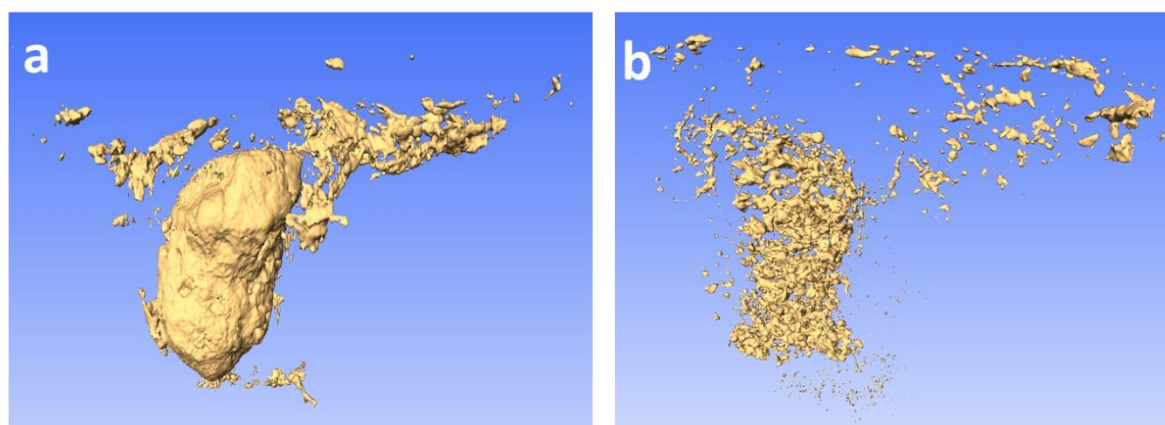


Figure S4. 3D reconstruction of (a) CPC and (b) CPC/PLGA30 in rat vertebrae after one month.

Table 2. Size distribution of PLGA microspheres (Dx50, D[3;2] and PDI).

	PLGA
Dx (50) (μm)	133 ± 2
D [3;2] (μm)	101 ± 3
PDI	1.1 ± 0.1

Part 3

General discussion and perspectives

During this thesis, different scaffolds were synthesized for bone tissue engineering applications. Many key parameters have been studied to characterize these scaffolds as bone substitutes for pathological fractures which occur after breast cancer bone metastases. First of all, the results dealing with the scaffolds obtained by 3D printing will be discussed. Then, the parameters concerning phosphocalcic cements will be reviewed. Finally, the *in vivo* model used to study these scaffolds will be argued.

A- 3D printed scaffold

Additive manufacturing is of growing interest in the field of bone tissue scaffold fabrication since it enables fast 3D model fabrication with high resolution. In the last few decades, many different techniques of 3D printing have been developed and a lot of 3D printers are available on the market¹. FDM is the most widely used additive manufacturing method and presents several advantages compared with other techniques². Indeed, FDM is cheap, it does not require solvents and gives great possibilities in polymer handling and processing³. Amorphous thermoplastic polymers, such as PLA, are among the most common materials used in this type of process^{4,5}. PLA is routinely used for medical applications, for instance in sutures⁶ or orthopaedic fixation devices⁷. PLA has a Young's modulus of about 2-3 GPa and ultimate strength of 53 MPa⁸ for bulk material. Unfortunately, these mechanical characteristics are incompatible with biological applications, especially in bone tissue engineering (BTE). Indeed, cortical bone has a modulus of elasticity between 7 and 17 GPa and an ultimate strength up to 133 MPa, depending on the age. In trabecular bone, the elastic modulus is about 0.44 GPa and the ultimate strength is 6.8 MPa⁹. Moreover, PLA hydrophobicity renders bone cell attachment and proliferation difficult.

1. Mechanical properties

To overcome mechanical properties issues, different methods have been used such as the incorporation of glass particles¹⁰ or carbon fibers¹¹. PLA scaffold properties could also be improved by incorporating nanofillers, such as graphene oxide (GO)¹². In our study, GO-reinforced PLA scaffolds were successfully 3D printed with a controlled morphology and a network of interconnected pores around 500 μm . We demonstrated that GO incorporation improved the mechanical properties of the scaffold. In our study, Young's modulus of PLA was in good agreement with the literature¹³ (*i.e.*, about 2 GPa for a sample with 30% porosity). This value significantly increased to 2.6 GPa after addition of GO (improvement of about 30% of the elastic modulus). When GO density was high enough, GO incorporation increased the tensile strength from 34 MPa for pure PLA to 39 MPa. Our data clearly indicated that PLA reinforcement with GO might represent a promising material for bone tissue engineering. The mechanical properties of 3D scaffolds can also be influenced by the internal architecture. With the FDM technique, it is possible to obtain an interconnected porosity with a pore size of 300 to 500 μm with different choices of infill (rectilinear or honeycomb for example)¹⁴. This has not been studied during the thesis work, but it might be interesting to investigate the reinforcement of PLA with a right content of GO depending on the pore architecture.

2. Biocompatibility

As it was mentioned above, biodegradable synthetic materials such as PLA usually have surface states properties incompatible with biological tissues¹⁵. In our study we have chosen to integrate boron nitride (BN) in its graphene form in the scaffold formulation¹⁶. We had successfully 3D printed PLA/EBN nanocomposites which promoted bone cell attachment, proliferation and differentiation.

Another possibility to improve those properties is to modify the PLA with another polymer such as PEG. It has been shown that the incorporation of PEG increased surface roughness and wettability, accelerated the degradation rate of the scaffold but decreased mechanical properties of the 3D structures¹⁷. In another study, murine osteocyte-like MLO-A5 cell attachment was not affected by the addition of PEG but observed excellent cell migration in the scaffolds containing PEG which supported greater metabolic activity enhanced over time. Moreover, ALP activity and mineralized matrix production was significantly increased in the composite scaffolds containing the highest ratio of PEG¹⁸. Particles ceramics such as TCP or HA were also studied in order to improve PLA bioactivity properties¹⁹. For example, PLA/HA composite scaffolds fabricated by TIPS method in a previous study possessed higher osteoblast survival rate, more uniform cell distribution and growth, enhanced new tissue formation, and improved bone specific gene expression in addition to superior mechanical properties compared with PLA scaffolds²⁰.

Finally, it has been also demonstrated that the pore size of the scaffold plays a role in cell penetration^{9,21}. It could be interesting to play with porosity gradient to improve cell attachment proliferation.

3. Bioefficacy

The treatment of certain fractures caused by a disease such as breast cancer requires, in addition to bone filling, local drug delivery for effective bone reconstruction and for limitation of cancer cell proliferation. To do this, the addition of drugs in the scaffolds is necessary to treat this type of fracture. One major disadvantage with FDM is the inability to incorporate temperature sensitive biological agents during extrusion due to the high processing temperature. One alternative to create drugs-loaded 3D scaffold would be to use another 3D printing technique. The advantages of SLA is to allow incorporation of biological

agents and to create complex shapes with internal architecture and extremely high feature resolution²². The main disadvantage of SLA is that few biodegradable and biocompatible biomaterials are dimensionally stable during photopolymerization for tissue engineering applications²³. Poly(propylene fumarate) (PPF) is a linear unsaturated copolyester which can be crosslinked with the use of photoinitiators²⁴. Due to its tailorable mechanical performance²⁵, biocompatibility²⁶, and biodegradability²⁷, PPF-based polymers have been widely investigated for a number of biomedical applications^{28,29,30}.

In our study, we used stereolithography to print a 3D PPF/DEF scaffold with mechanical properties comparable to trabecular bone (Young's modulus around 350 MPa and tensile strength around 5 MPa). One interesting possibility with this PPF and SLA technology will be to incorporate polyethylene glycol functionalized graphene oxide (PEG-GO). Indeed, one previous study³¹ has shown a gradual rise in the level of hydrophilicity, biodegradation rate and surface roughness upon increasing GO concentration in the composites. Tensile tests revealed improved mechanical properties for the composites compared to unfilled PPF. Further, the nanocomposites retained enough stiffness and strength under a biological state to provide effective support for bone tissue formation. Moreover, it was demonstrated that PPF/PEG-GO composites do not induce toxicity over human dermal fibroblasts. More than to tune PPF to improve its mechanical properties and its bioactivity, the incorporation of drugs in the scaffold to treat some pathologic fractures is necessary.

In addition to the investigations did on polymer reinforced with 2D nanosheets, it could be interesting to study their biodegradation. Indeed, some studies have shown a beneficial potential of GO³² and BN³³ on cancer and in our case the obtained products from the biodegradation could give us a supplementary option to treat bone pathology from cancer.

4. Drug delivery

In order to develop effective therapeutic treatment³⁴, a variety of organic/inorganic nanomaterials and devices have been used as delivery vehicles. Polymeric microspheres composed of a biodegradable polymer matrix such as poly(α -hydroxy esters), in which the drug is encapsulated, are the most commonly used system and are advantageous for their biocompatibility and biodegradability^{35,36,37,38}. Due to its degradation rate, PLGA50, is the most used poly(α -hydroxy esters) as delivery material³⁹.

In our study, we initially decided to use two specific drugs to treat pathologic fractures of bone metastasis of breast cancer. The first one is Alendronate (AL) which is a bisphosphonate and acts as a bone resorption inhibitor but has also an anti-tumor effect⁴⁰. The second drug is Raloxifene (RH) which is a selective estrogen receptor modulator (SERM) and has an antagonist effect on breast cancer cells and an agonist effect on bone. The rationale for combining two anti-resorptive agents with different mechanisms of action such as Alendronate (osteoclast metabolism suppression) and Raloxifene (RANKL access to osteoclasts decrease) could be an interesting option for the treatment of pathologic fractures generated by bone metastases of breast cancer.

In one study⁴¹, the combination of RH and AL was shown to have greater beneficial effects on bone volume and biomechanical properties of vertebral bone compared with single agent. As mentioned in the Chapter 1, AL has poor metabolic absorption. Several studies used PLGA microspheres to overcome this drawback and use AL in local delivery treatment. Indeed, different systems using PLGA microspheres showed a controlled release of AL both *in vitro* and *in vivo*. For instance, AL loaded PLGA/HA microspheres enhanced the proliferation of osteoblasts *in vitro*⁴². AL loaded PLGA showed a better effect of microsphere-released AL *in vivo* on bone regeneration as compared to daily oral administration⁴³. In addition, using AL loaded porous PLGA microspheres in rats with

critical-sized calvarial defect, Lee *et al.* showed an increased mineralization and bone matrix formation⁴⁴. This suggests that the local delivery of AL with PLGA microspheres has good potential for bone treatment. On the other hand, RH is hydrophobic and possesses very low bioavailability as mentioned before. Controlled delivery systems such as PLGA microspheres could increase the efficacy of RH released locally.

Different studies have been published on the encapsulation of RH in PLGA microspheres. For example Park *et al.*, showed that RH release could be effectively controlled by varying the preparation parameters of the preparation route⁴⁵. Another study using conjugated RH-PEG with PCL/PLGA as a polymer carrier showed interesting rate of release⁴⁶.

The use of microspheres with PLGA as a polymer matrix for the release of a combination of AL and RH might be a good alternative to the actual systemic treatments. The incorporation of PLGA/AL and PLGA/RH at the same time in our PPF scaffold could avoid systemic side effects by using lower and safer quantities of drug, with more localized efficacy and efficiency. During this thesis work, the efficacy of Alendronate and Raloxifene were tested on MCF7 breast cancer cells as shown in Fig.1. As predicted, RH had a better efficacy than AL in inhibiting proliferation of MCF7 cells after 8 days (Fig.1a). The effect of both drugs was still significant in the presence of estradiol (E2) (Fig.2b).

Then, AL and RH-loaded PLGA microspheres were respectively obtained by double or single emulsion solvent evaporation techniques. The AL-loaded microspheres showed much higher encapsulation efficiency and release than the PLGA/RH microspheres. The biocompatibility of the different microspheres was demonstrated using MG-63 human bone osteosarcoma cells. Moreover, the microspheres loaded with drugs showed a very significant impact on MCF7 breast cancer cell proliferation as compared to microspheres alone (Ref part 2-A chapter 3 Fig.5).

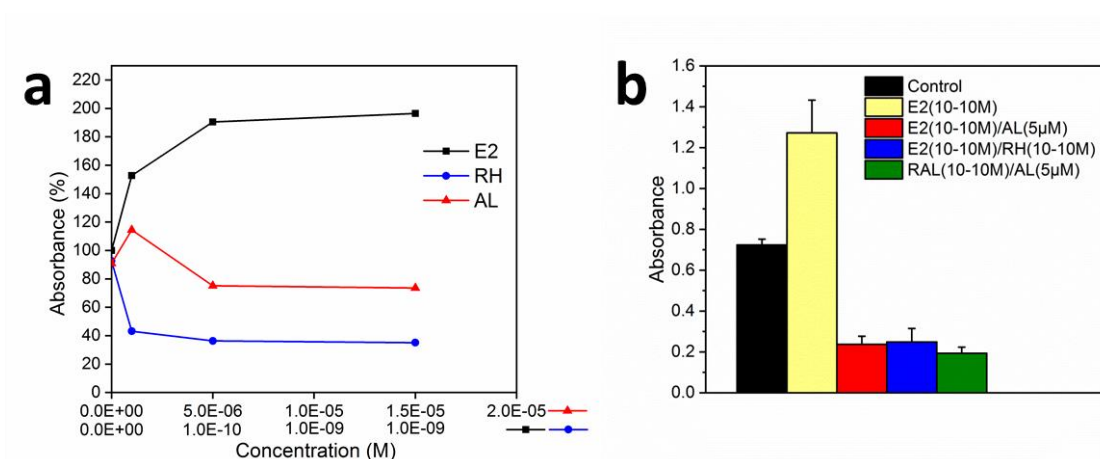


Figure 1. Bioefficacy of drugs on MCF7 breast cancer cell proliferation.

(a) MCF7 cell proliferation in presence of AL and RH at different concentrations with estradiol as positive control for 8 days. (b) MCF7 cell proliferation measured after 8 days in the presence of different combinations of AL, RH and E2.

To overcome the poor encapsulation efficiency and releasing of hydrophobic drugs such as RH, porous microsphere can be used (Fig. 2). Different studied showed a better cell attachment and proliferation using porous microspheres⁴⁷⁻⁴⁹. Indeed, one study demonstrated that the loading and release profile of drug could be manipulated in a controlled manner⁵⁰.

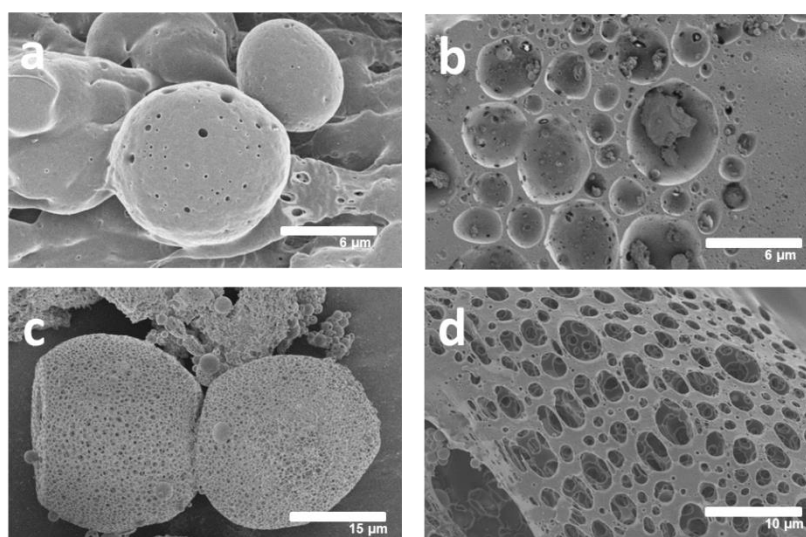


Figure 2. Scanning electron micrographs showing porous microspheres morphology.

(a) and (b) internal pores, (c) and (d) interconnected pores.

4.1. Alternatives drug options

Different alternatives to bisphosphonates and SERMS as anti-resorptive agents exist. For example denosumab (Fig. 3a), a human monoclonal antibody that targets RANKL, inhibits osteoclast formation, function and survival and thus decreases bone resorption in the cortical and trabecular bone⁵¹. Bone morphogenetic protein (BMP2) (Fig. 3b), can also be used to stimulate bone formation⁵². New molecules such as C21 (Fig. 3c), inhibitor of Rac activation by Dock5 could be used to block bone resorption without affecting bone formation⁵³. To deliver those molecules, some modifications in our encapsulation method could be necessary to obtain a good efficacy.

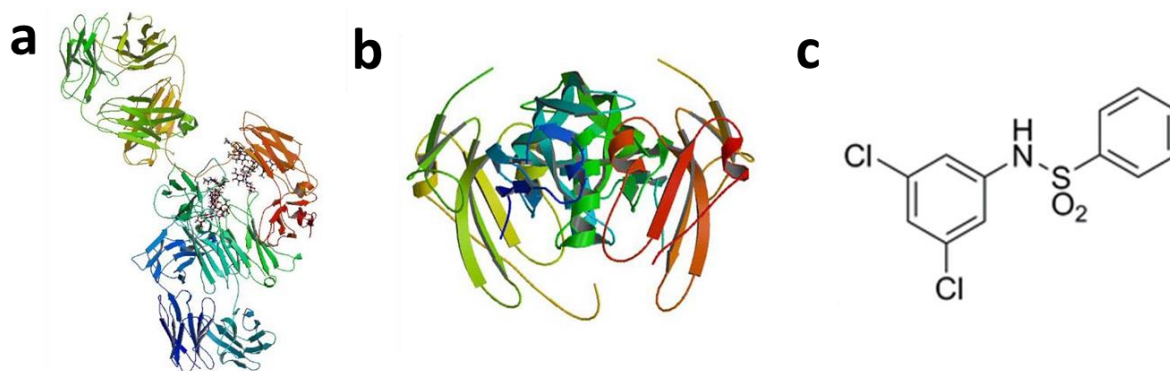


Figure 3. Structure representation of (a) denosumab (adapted from ref 54), (b) BMP-2 (adapted from ref 55) and (c) C21 (adapted from ref 53).

4.2. Stem cell incorporation

The use of porous microspheres could be a promising material to deliver living cells in tissue engineering⁵⁶. In addition to deliver drugs, 3D scaffold could, for instance, allow the integration of stem cells during their manufacturing in order to enhance the regeneration of new tissue. Bioprinting technology has gained much attention due to its ability to meet some of the challenges encountered in the traditional BTE approaches⁵⁷. This technique allows combining cells, growth factors, and biomaterials to create tissue-like structures able to imitate natural tissues^{58,59}. For example Narayanan *et al.* succeeded to develop a bio ink of

PLA nanofiber-alginate containing human adipose-derived stem cells able to be used in 3D bioprinting⁶⁰ (Fig. 4).

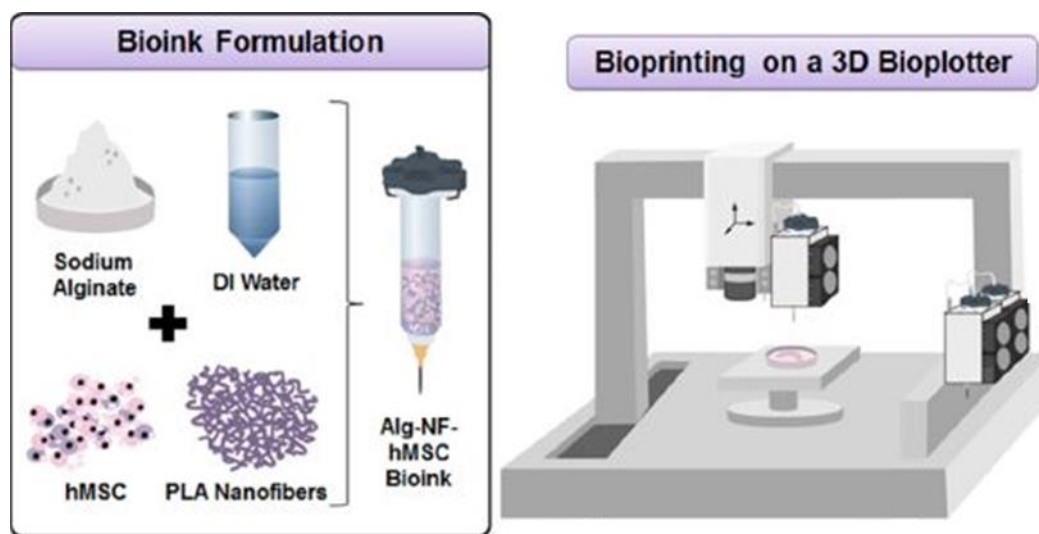


Figure 4. Bioink formulation of polymer and stem cells used to create scaffolds by Bioprinting. Adapted from REF 60.

B- Injectable Calcium Phosphate Cement

Vertebroplasty was developed to mechanically reinforce weakened vertebral bodies. Polymethylmethacrylate (PMMA) bone cement is the most commonly used cement but it causes many complications. Calcium phosphate cements (CPC) offer the potential for biological resorption and regeneration of new bone, restoring vertebral body structure. Brushite cements were discovered by Mirtchi and Lemaître in 1989. These materials were prepared by mixing liquid phase with a powder consisting of an acidic calcium phosphate (monocalcium phosphate monohydrate) and a basic calcium phosphate (β tricalcium phosphate). The result of this mixture was a paste that can solidify in a hard material mainly composed of dicalcium phosphate dihydrate also known as brushite. Subsequent studies showed that brushite has a unique advantage over the other CPCs such as hydroxyapatite cement, which is its ability to be resorbed under physiological conditions. Injectable CPC must satisfy a number of standards in order to be used in vertebroplasty⁶¹. Some of the key parameters will be discussed more precisely in the next sections.

1. Opacity

To avoid leakage during injection into the vertebra, it is mandatory to follow the cement with X-ray imaging and, as a consequence, the cement must be radio-opaque. A number of additives such as bismuth and strontium have been proposed to increase radio-opacity of CPCs. For example, it has been demonstrated that strontium carbonate (8% wt or more) provided a good radio-opacity⁶². In addition to opacity, strontium carbonate has been used to promote drug delivery from CPC^{63,64}. Despite these advantages, strontium has also an effect on bone⁶⁵ and, since recently, strontium ranelate is available as a drug to treat osteoporosis.

In order to avoid a modification of the efficacy of the drugs chosen in our study (Alendronate and Raloxifene), we made the choice to use a radio-opacifier without any effect on bone. Recently, different studies have shown that the use of Zirconium Oxide (ZrO_2) is a promising alternative to synthesize radiopaque injectable CPC^{66,67}. In our study, we have demonstrated that 20%wt of ZrO_2 was high enough to obtain a good radio-opacity and to improve the compression strength at the same time.

2. Mechanical properties and porosity

Ideally scaffolds such as CPC should have mechanical properties similar to those of bone. It has been reported that the original formulation of brushite cements had a compressive strength of 1 MPa⁶⁸. Different compositions of cements have been studied and the highest compressive strength reported in the literature was 52 MPa⁶⁹. One way to reinforce CPC mechanical properties is to incorporate fiber polymers⁷⁰ or GO nanosheets⁷¹ as we did previously for 3D printed scaffolds. In our study, we obtained CPC with compressive strength around 25 MPa but after the introduction of 30% of PLGA microspheres, it decreased to 1 MPa. It is important to have a balance between the mechanical properties and the porosity, knowing the correlation between these parameters.

The macroporosity of CPC is important in allowing cellular infiltration and proliferation inside the biomaterial. We have decided to use PLGA microspheres around 100 μm to create this porosity as shown in Fig.5.

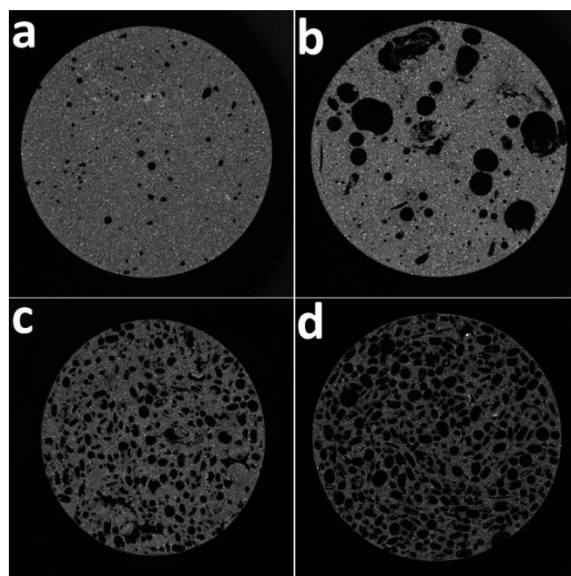


Figure 5. Micro-tomography images.
Slice Y of a) CPC, b) CPC/PLGA5, c) CPC/PLGA15 and d) CPC/PLGA30.

Different percentages of microspheres have been introduced in the CPC to increase the macroporosity from 3.8% to 44.2% with 30% microspheres (Table 1). The introduction of macroporosity can accelerate the degradation of the cement as shown in our study (ref article IV Figure 7a). The cement macroporosity can be modulated to obtain enough porosity to allow cellular infiltration and proliferation with good mechanical properties, degradation and opacity.

Table 1. Porosity and pores size of CPC and CPC/PLGA samples.

Samples	Porosity (%)	Pores size (μm)
CPC	3.8 ± 0.4	37 ± 5
CPC/PLGA5	23.4 ± 0.4	222 ± 10
CPC/PLGA15	31.5 ± 1.8	250 ± 5
CPC/PLGA30	44.2 ± 0.6	60-211

3. Bioefficacy

PLGA microspheres can play a second role in addition to the creation of macroporosity. Indeed, as stated above for the PPF 3D scaffold, PLGA microspheres can allow drug delivery. In the section, we will discuss the integration of drugs-loaded PLGA microspheres in our CPC.

As mentioned above, the combination of PLGA/AL and PLGA/RH to enhance the efficacy of scaffold in the treatment of pathologic fractures is very interesting, and therefore, we have synthesized as well these drugs-loaded microspheres around $100\mu\text{m}$ (Fig.6).

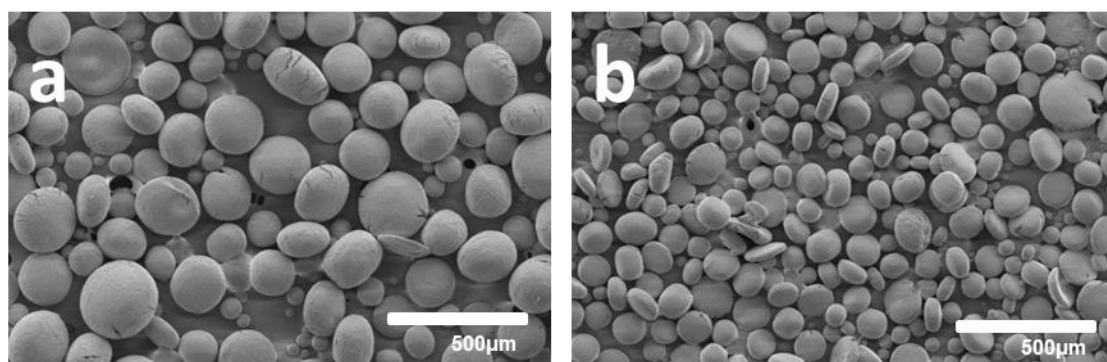


Figure 6. Scanning electron micrographs showing microspheres morphology.
(a) PLGA/AL and (b) PLGA/RH microspheres.

In that way, we could introduce those microspheres in the CPC and study the releasing through this one over 10 weeks. In Fig.7a, we showed the releasing of AL and RH directly

from the microspheres up to 1 month. We obtained a release of 40% and 30% for AL and RH, respectively. When added in the CPC, AL was released with superior efficacy at 10 weeks with 50% of releasing while RH released at 15% (Fig.7b).

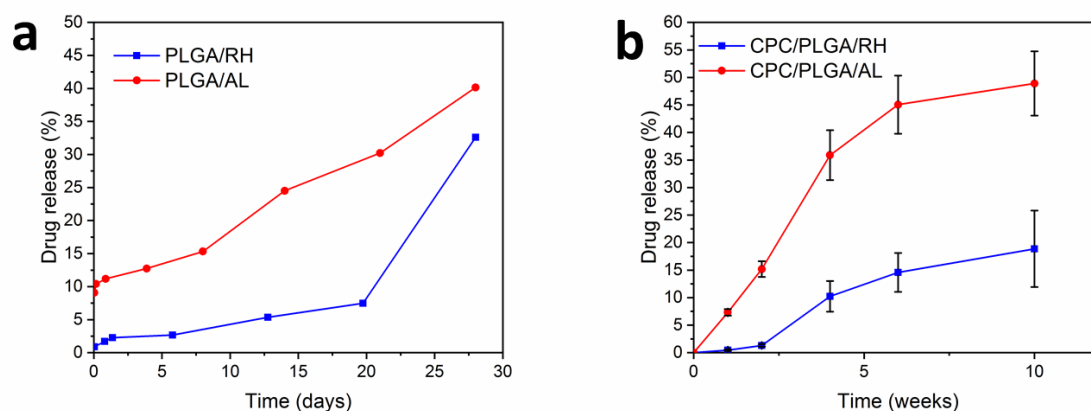


Figure 7. Releases profile of AL and RH.
Release profiles of AL and RH-loaded PLGA microspheres (a) and AL and RH-loaded CPC/PLGA scaffolds (b).

C- In vivo study

Different in vivo models have been developed for bone tissue engineering based on reproducible defects in different bone locations such as femoral⁷³ or cranial⁷⁴ critical size bone defects. Most of the time animal models used is mouse. Unfortunately, with these models it is difficult to have easy surgical access with a good number, type and localization of defect sites close to the pathology that we want to treat. To evaluate the efficacy of bone regeneration of our scaffold, we used a rat caudal vertebrae critical size defect model⁷². We showed the good incorporation and retention of the CPC in the vertebra after 1 month. Moreover, we demonstrated a better degradation with the CPC/PLGA scaffold. In addition to μ -CT characterization, histological analysis are ongoing and will allow us to determine if new bone formation appeared while the cement was degraded. We also used this model to initiate the study of the implantation of our PPF 3D printed scaffold (data not shown). In order to use our PPF/PLGA or CPC/PLA scaffolds for the treatment of bone metastasis in breast cancer,

we want to use this animal model to investigate the efficacy of Alendronate and Raloxifene. Firstly, we implanted CPC/PLGA/AL scaffold to show the enhancement of bone regeneration due to AL released (Fig.8). But our goal is to combine AL to improve bone regeneration and RH to limit the cancer cell proliferation. In this perspective, an interesting tumor metastatic immunocompetent animal model has been developed⁷⁵. Our next study will be to inject Walker Carcinoma 256 cells into the bone defect to provoke a localized increase in bone resorption. Walker 256 is a rat breast carcinoma cell line syngeneic to Wistar rats and commonly used to induce secondary brain tumors. *In vivo* bioluminescence imaging of luciferase-labeled W256 cells will allow us to follow the proliferation of the cells in bone defect of the rat vertebrae. Bioluminescence imaging is an indirect cell labeling technique for cell tracking in small animal models⁷⁶. Bioluminescence is generated by conversion of chemical energy into visible light by the action of luciferase enzymes and their substrates in living animals. At the same time, it will be possible to implant our scaffolds loaded or not with AL and/or RH for a period of 1 or 3 months and to study the effect on the growth of the luminescent W256 cells and on bone.

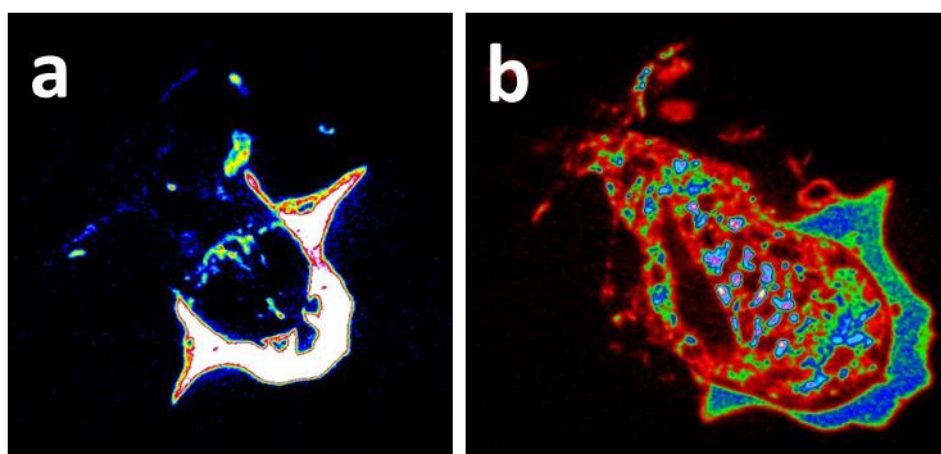


Figure 8. In vivo imaging. Micro-CT reconstruction of rat caudal vertebrae after 1 month.
(a) Empty defect and (b) CPC/PLGA/AL.

D- Conclusions and perspectives

In summary, two types of 3D printed scaffold have been developed to overcome some issues in bone tissue engineering. GO and BN nanosheets could be used to improve mechanical properties and biocompatibility of PLA scaffold created by fused deposition modeling. Other alternative such as the addition of PEG or ceramics exist to improve properties of 3D printed scaffold. Future research in scaffolds obtained by FDM should be devoted to the study of the influence of degradation products on cancer cells proliferation. Moreover, *in vivo* study is necessary to complete the biological study done with these scaffolds.

PPF scaffold has been developed to allow drugs incorporation and improve the bioefficacy of 3D printed scaffold. Bioprinting is a promising technique to create scaffold to incorporate stem cells and enhance the bone regeneration. To continue this project, some further investigations are necessary. The drugs release through the scaffold PPF/PLGA must to be study *in vitro* to know the efficacy of the drugs. The preliminary experiments done *in vivo* should be continued to see the effect of the scaffold on bone regeneration and cancer cells proliferation.

Injectable Calcium Phosphate Cement has been developed for its use in vertebroplasty. We showed that ZrO_2 could be a valid alternative to other radio-opacifiers. Alendronate and Raloxifene-loaded PLGA microspheres with different sizes were synthesized to enhance the bioefficacy of PPF 3D printed scaffold and CPC. Porous microspheres could be used to enhance the encapsulation and releasing of both drugs. Finally, a rat caudal vertebrae model was used to investigate the effect of the scaffold on bone regeneration. More investigations are still ongoing, in particular the histological analysis to determine if the macroporous cement is able to induce bone regeneration *in vivo*. Moreover, AL and RH-loaded PLGA microspheres were already introduced in the CPC. Some *in vitro* experiments are necessary to check the effect of the drugs on osteosarcoma and breast cancer cells. At last, *in vivo* study

using walker carcinoma cells has to be performing to conclude on the potential application of a CPC containing alendronate and raloxifene to treat pathologic fracture of bone metastasis of breast cancer.

REFERENCES

1. Jariwala, S. H., Lewis, G. S., Bushman, Z. J., Adair, J. H. & Donahue, H. J. 3D Printing of Personalized Artificial Bone Scaffolds. *3D Print. Addit. Manuf.* **2**, 56–64 (2015).
2. Turner, B. N., Strong, R. & Gold, S. A. A review of melt extrusion additive manufacturing processes: I. Process design and modeling. *Rapid Prototyp. J.* **20**, 192–204 (2014).
3. Ning, F., Cong, W., Qiu, J., Wei, J. & Wang, S. Additive manufacturing of carbon fiber reinforced thermoplastic composites using fused deposition modeling. *Compos. Part B Eng.* **80**, 369–378 (2015).
4. Serra, T., Mateos-Timoneda, M. A., Planell, J. A. & Navarro, M. 3D printed PLA-based scaffolds: A versatile tool in regenerative medicine. *Organogenesis* **9**, 239–244 (2013).
5. Poh, P. S. P. *et al.* Polylactides in additive biomanufacturing. *Adv. Drug Deliv. Rev.* **107**, 228–246 (2016).
6. Cutright, D. E. & Hunsuck, E. E. Tissue reaction to the biodegradable polylactic acid suture. *Oral Surgery, Oral Med. Oral Pathol.* **31**, 134–139 (1971).
7. Bos, R. R. M. *et al.* Degradation of and tissue reaction to biodegradable poly (L-lactide) for use as internal fixation of fractures: a study in rats. *Biomaterials* **12**, 32–36 (1991).
8. Madhavan Nampoothiri, K., Nair, N. R. & John, R. P. An overview of the recent developments in polylactide (PLA) research. *Bioresour. Technol.* **101**, 8493–501 (2010).
9. Karageorgiou, V. & Kaplan, D. Porosity of 3D biomaterial scaffolds and osteogenesis. *Biomaterials* **26**, 5474–5491 (2005).
10. Serra, T., Planell, J. A. & Navarro, M. High-resolution PLA-based composite scaffolds via 3-D printing technology. *Acta Biomater.* **9**, 5521–5530 (2013).
11. Li, N., Li, Y. & Liu, S. Rapid prototyping of continuous carbon fiber reinforced polylactic acid composites by 3D printing. *J. Mater. Process. Technol.* **238**, 218–225 (2016).
12. Kim, H., Abdala, A. A. & Macosko, C. W. Polymer Nanocomposites with Graphene. *Young* 1–13 (2010). doi:10.1021/ma100572e
13. Song, Y. *et al.* Measurements of the mechanical response of unidirectional 3D-printed PLA. *Mater. Des.* **123**, 154–164 (2017).
14. Farbman, D. & McCoy, C. Materials Testing of 3D Printed ABS and PLA Samples to Guide Mechanical Design. V002T01A015 (2016). doi:10.1115/msec2016-8668
15. Hamad, K., Kaseem, M., Yang, H. W., Deri, F. & Ko, Y. G. Properties and medical applications of polylactic acid: A review. *Express Polym. Lett.* **9**, (2015).
16. Kumar, A., Rao, T. V., Chowdhury, S. R. & Reddy, S. V. S. R. Compatibility confirmation and refinement of thermal and mechanical properties of poly (lactic acid)/poly (ethylene-co-glycidyl methacrylate) blend reinforced by hexagonal boron nitride. *React. Funct. Polym.* **117**, 1–9 (2017).
17. Serra, T., Ortiz-Hernandez, M., Engel, E., Planell, J. A. & Navarro, M. Relevance of PEG in PLA-based blends for tissue engineering 3D-printed scaffolds. *Mater. Sci. Eng. C* **38**, 55–62 (2014).
18. Bhaskar, B. *et al.* Composite porous scaffold of PEG/PLA support improved bone matrix deposition in vitro compared to PLA-only scaffolds. *J. Biomed. Mater. Res. - Part A* **106**, 1334–1340 (2018).
19. Tajbakhsh, S. & Hajiali, F. A comprehensive study on the fabrication and properties of biocomposites of poly(lactic acid)/ceramics for bone tissue engineering. *Materials Science and Engineering C* **70**, 897–912 (2017).
20. McMillan, R., Meeks, B., Bensebaa, F., Deslandes, Y. & Sheardown, H. Engineering new bone tissue in vitro on highly porous poly(α -hydroxyl acids)/hydroxyapatite composite scaffolds. *J. Biomed. Mater.*

- Res.* **54**, 284–293 (2001).
21. Sobral, J. M., Caridade, S. G., Sousa, R. A., Mano, J. F. & Reis, R. L. Three-dimensional plotted scaffolds with controlled pore size gradients: Effect of scaffold geometry on mechanical performance and cell seeding efficiency. *Acta Biomater.* **7**, 1009–1018 (2011).
 22. Zhang, X., Jiang, X. N. & Sun, C. *Micro-stereolithography of polymeric and ceramic microstructures. Sensors and Actuators* **77**,
 23. Chia, H. N. & Wu, B. M. Recent advances in 3D printing of biomaterials. *J. Biol. Eng.* **9**, 4 (2015).
 24. Kasper, F. K., Tanahashi, K., Fisher, J. P. & Mikos, A. G. Synthesis of poly(propylene fumarate). *Nat. Protoc.* **4**, 518–525 (2009).
 25. Kharas, G. B. *et al.* Synthesis and characterization of fumarate-based polyesters for use in bioresorbable bone cement composites. *J. Appl. Polym. Sci.* **66**, 1123–1137 (1997).
 26. Gunatillake, P. A. & Adhikari, R. Biodegradable synthetic polymers for tissue engineering. *Eur. Cell. Mater.* **5**, 1–16; discussion 16 (2003).
 27. Shanfeng Wang, Lichun Lu, and & Yaszemski*, M. J. Bone-Tissue-Engineering Material Poly(propylene fumarate): Correlation between Molecular Weight, Chain Dimensions, and Physical Properties. (2006). doi:10.1021/BM060096A
 28. Timmer, M. D., Carter, C., Ambrose, C. G. & Mikos, A. G. Fabrication of poly(propylene fumarate)-based orthopaedic implants by photo-crosslinking through transparent silicone molds. *Biomaterials* **24**, 4707–14 (2003).
 29. Cooke, M. N., Fisher, J. P., Dean, D., Rimnac, C. & Mikos, A. G. Use of stereolithography to manufacture critical-sized 3D biodegradable scaffolds for bone ingrowth. *J. Biomed. Mater. Res.* **64B**, 65–69 (2003).
 30. Hacker, M. C. *et al.* Biodegradable fumarate-based drug-delivery systems for ophthalmic applications. *J. Biomed. Mater. Res. Part A* **88A**, 976–989 (2009).
 31. Díez-Pascual, A. M. & Díez-Vicente, A. L. Poly(propylene fumarate)/Polyethylene Glycol-Modified Graphene Oxide Nanocomposites for Tissue Engineering. *ACS Appl. Mater. Interfaces* **8**, 17902–17914 (2016).
 32. Ghanbarzadeh, S. *et al.* Application of Graphene and its Derivatives in Cancer Diagnosis and Treatment Properties of Graphene and its Derivatives Applications of Different Modified Graphene-Based Materials PEGylated nano Graphene.
 33. I. Scorei, R. & Popa, R. Boron-Containing Compounds as Preventive and Chemotherapeutic Agents for Cancer. *Anticancer. Agents Med. Chem.* **10**, 346–351 (2012).
 34. Shi, J., Votrubá, A. R., Farokhzad, O. C. & Langer, R. Nanotechnology in drug delivery and tissue engineering: from discovery to applications. *Nano Lett.* **10**, 3223–30 (2010).
 35. Park, J., Ye, M. & Park, K. Biodegradable Polymers for Microencapsulation of Drugs. *Molecules* **10**, 146–161 (2005).
 36. Varde, N. K. & Pack, D. W. Microspheres for controlled release drug delivery. *Expert Opin. Biol. Ther.* **4**, 35–51 (2004).
 37. Mano, J. F., Sousa, R. A., Boesel, L. F., Neves, N. M. & Reis, R. L. Bioinert, biodegradable and injectable polymeric matrix composites for hard tissue replacement: state of the art and recent developments. *Compos. Sci. Technol.* **64**, 789–817 (2004).
 38. Lin, H.-R., Kuo, C.-J., Yang, C. Y., Shaw, S.-Y. & Wu, Y.-J. Preparation of macroporous biodegradable PLGA scaffolds for cell attachment with the use of mixed salts as porogen additives. *J. Biomed. Mater. Res.* **63**, 271–279 (2002).
 39. Hirenkumar, M. & Steven, S. Poly Lactic-co-Glycolic Acid (PLGA) as Biodegradable Controlled Drug Delivery Carrier. *Polymers (Basel)*. **3**, 1–19 (2012).
 40. Clézardin, P. Bisphosphonates' antitumor activity: An unravelled side of a multifaceted drug class. *Bone* **48**, 71–79 (2011).
 41. Diab, T., Wang, J., Reinwald, S., Guldborg, R. E. & Burr, D. B. Effects of the combination treatment of raloxifene and alendronate on the biomechanical properties of vertebral bone. *J. Bone Miner. Res.* **26**, 270–276 (2011).
 42. Shi, X., Wang, Y., Ren, L., Gong, Y. & Wang, D.-A. Enhancing Alendronate Release from a Novel PLGA/Hydroxyapatite Microspheric System for Bone Repairing Applications. *Pharm. Res.* **26**, 422–430

- (2009).
43. Bae, J. & Park, J. W. Preparation of an injectable depot system for long-term delivery of alendronate and evaluation of its anti-osteoporotic effect in an ovariectomized rat model. *Int. J. Pharm.* **480**, 37–47 (2015).
 44. Lee, J. Y. *et al.* Osteogenesis and new bone formation of alendronate-immobilized porous PLGA microspheres in a rat calvarial defect model. *J. Ind. Eng. Chem.* **52**, 277–286 (2017).
 45. Park, J. H., Eom, S., Kim, D. S., Kim, W. & Kim, Y. K. Double-Layered PLGA Microspheres for Effective Controlled Release of Raloxifene-HCl: Preparation and Characterization. *Tissue Eng. Regen. Med.* **6**, 1172–1178 (2009).
 46. Kavas, A., Keskin, D., Altunbaş, K. & Tezcaner, A. Raloxifene-/raloxifene-poly(ethylene glycol) conjugate-loaded microspheres: A novel strategy for drug delivery to bone forming cells. *Int. J. Pharm.* **510**, 168–183 (2016).
 47. Sahoo, S. K., Panda, A. K. & Labhasetwar, V. Characterization of Porous PLGA/PLA Microparticles as a Scaffold for Three Dimensional Growth of Breast Cancer Cells. 1132–1139 (2005).
 48. Qutachi, O. *et al.* Injectable and porous PLGA microspheres that form highly porous scaffolds at body temperature. *Acta Biomater.* **10**, 5090–5098 (2014).
 49. Wang, Y., Shi, X., Ren, L., Wang, C. & Wang, D. A. Porous poly (lactic-co-glycolide) microsphere sintered scaffolds for tissue repair applications. *Mater. Sci. Eng. C* **29**, 2502–2507 (2009).
 50. Bae, S. E., Son, J. S., Park, K. & Han, D. K. Fabrication of covered porous PLGA microspheres using hydrogen peroxide for controlled drug delivery and regenerative medicine. *J. Control. Release* **133**, 37–43 (2009).
 51. Lipton, A. *et al.* Randomized active-controlled phase II study of denosumab efficacy and safety in patients with breast cancer-related bone metastases. *J. Clin. Oncol.* **25**, 4431–4437 (2007).
 52. Kempen, D. H. R. *et al.* Retention of in vitro and in vivo BMP-2 bioactivities in sustained delivery vehicles for bone tissue engineering. *Biomaterials* **29**, 3245–3252 (2008).
 53. Ferrandez, Y. *et al.* Allosteric inhibition of the guanine nucleotide exchange factor DOCK5 by a small molecule. *Sci. Rep.* **7**, (2017).
 54. Drug bank. Available at: <https://www.drugbank.ca/drugs/DB06643>.
 55. Biologics international corp. Available at: <https://www.biologicscorp.com/rhbm-2/structure.html#.XWeUoygza70>.
 56. Young Sook Lee, Kwang Suk Lim, Jung-Eun Ohb, A-Rum Yoon, Wan Seok Joo, Hyun Soo Kim, Chae-Ok Yun, S. K. Development of porous PLGA/PEI1.8k biodegradable microspheres for the delivery of mesenchymal stem cells (MSCs). *J. Control. Release* (2015).
 57. Murphy, S. V. & Atala, A. 3D bioprinting of tissues and organs. *Nat. Biotechnol.* **32**, 773–785 (2014).
 58. Ong, C. S. *et al.* 3D bioprinting using stem cells. *Pediatr. Res.* **83**, 223–231 (2018).
 59. Eswaramoorthy, S. D., Ramakrishna, S. & Rath, S. N. Recent advances in three-dimensional bioprinting of stem cells. *J. Tissue Eng. Regen. Med.* **13**, 908–924 (2019).
 60. Narayanan, L. K. *et al.* 3D-Bioprinting of Polylactic Acid (PLA) Nanofiber-Alginate Hydrogel Bioink Containing Human Adipose-Derived Stem Cells. *ACS Biomater. Sci. Eng.* **2**, 1732–1742 (2016).
 61. Lewis, G. Injectable bone cements for use in vertebroplasty and kyphoplasty: State-of-the-art review. *J. Biomed. Mater. Res. Part B Appl. Biomater.* **76B**, 456–468 (2006).
 62. Wang, X., Ye, J. & Wang, Y. Influence of a novel radiopacifier on the properties of an injectable calcium phosphate cement. *Acta Biomater.* **3**, 757–763 (2007).
 63. Taha, A., Akram, M., Jawad, Z., Alshemary, A. Z. & Hussain, R. Strontium doped injectable bone cement for potential drug delivery applications. *Mater. Sci. Eng. C* **80**, 93–101 (2017).
 64. Masaeli, R. *et al.* Efficacy of the biomaterials 3 wt%-nanostrontium-hydroxyapatite-enhanced calcium phosphate cement (nanoSr-CPC) and nanoSr-CPC-incorporated simvastatin-loaded poly(lactic-co-glycolic-acid) microspheres in osteogenesis improvement: An explorative multi-phases. *Mater. Sci. Eng. C* **69**, 171–183 (2016).
 65. Reitmaier, S. *et al.* Strontium(II) and mechanical loading additively augment bone formation in calcium phosphate scaffolds. *J. Orthop. Res.* **36**, 106–117 (2018).
 66. Åberg, J. *et al.* In vivo evaluation of an injectable premixed radiopaque calcium phosphate cement. *Int. J. Biomater.* **2011**, (2011).

67. Åberg, J. *et al.* Biocompatibility and resorption of a radiopaque premixed calcium phosphate cement. *J. Biomed. Mater. Res. - Part A* **100 A**, 1269–1278 (2012).
68. Tamimi, F., Sheikh, Z. & Barralet, J. Dicalcium phosphate cements: Brushite and monetite. *Acta Biomater.* **8**, 474–487 (2012).
69. Hofmann, M. P., Mohammed, A. R., Perrie, Y., Gbureck, U. & Barralet, J. E. High-strength resorbable brushite bone cement with controlled drug-releasing capabilities. *Acta Biomater.* **5**, 43–49 (2009).
70. Canal, C. & Ginebra, M. P. Fibre-reinforced calcium phosphate cements: A review. *J. Mech. Behav. Biomed. Mater.* **4**, 1658–1671 (2011).
71. Wang, S., Zhang, S., Wang, Y., Sun, X. & Sun, K. Reduced graphene oxide/carbon nanotubes reinforced calcium phosphate cement. *Ceram. Int.* **43**, 13083–13088 (2017).
72. Renaud, M. *et al.* A New Rat Model for Translational Research in Bone Regeneration. *Tissue Eng. Part C. Methods* **22**, 125–131 (2016).
73. Livingston, T., Ducheyne, P. & Garino, J. In vivo evaluation of a bioactive scaffold for bone tissue engineering. *J. Biomed. Mater. Res.* **62**, 1–13 (2002).
74. Spicer, P. P. *et al.* Evaluation of bone regeneration using the rat critical size calvarial defect. *Nat. Protoc.* **7**, 1918–1929 (2012).
75. Chung, Y. S., Kang, H. C. & Lee, T. Comparative effects of ibandronate and paclitaxel on immunocompetent bone metastasis model. *Yonsei Med. J.* **56**, 1643–1650 (2015).
76. Kim, J. E., Kalimuthu, S. & Ahn, B.-C. In Vivo Cell Tracking with Bioluminescence Imaging. doi:10.1007/s13139-014-0309-x

Part 4

Materials and methods

A- Materials

PLA pellets were purchased from NatureWorks LLC. Type A gelatin (48722-500G-F) obtained from porcine skin (gel strength 170–195 g Bloom, CAS 9000-70-8), Graphite powder (20µm synthetic, CAS 7782-42-5), Methanol (>99.8% (GC), CAS 67-56-1), 2-propanol (CAS 67-63-0), fumaric acid (>99.0%, CAS 110-17-8), propylene glycol (CAS 57-55-6), diethyl fumarate (DEF, 98%, CAS 623-91-6), bis-acylphosphine oxide (BAPO, CAS 162881-26-7), monoacylphosphine oxide (Lucirin[®] TPO, 97%, CAS 75980-60-8), Poly(D,L-lactide-co-glycolide) (Resomer RG503H), Raloxifene Hydrochloride (CAS 82640-04-8), Alendronate sodium (CAS 121268-17-5), HEPES (>99.5%, CAS 7365-45-9), perchloric acid (70%, CAS 7601-90-3), iron(III) chloride hexahydrate (97%, CAS 10025-77-1), dichloromethane (CH₂Cl₂, <99.9%, CAS 75-09-2), sulfuric acid (H₂SO₄, 95.0-98.0%, CAS 7664-93-9), phosphoric acid (H₃PO₄, 85wt.% in H₂O, CAS 7664-38-2), hydrogen peroxide (H₂O₂, 30% (w/w), CAS 7722-84-1), potassium permanganate (KMnO₄, >99.0%, CAS 7722-64-7), ethanol (96% vol, CAS 64-17-5), cetylpyridinium chloride (CAS 6004-24-6), glutaraldehyde (25% in H₂O, CAS 111-30-8), 37% formaldehyde (37 wt. % in H₂O, CAS 50-00-0), phosphate buffered saline (PBS) (P4417) tablets, Triton X 100 (CAS 9002-93-11), Bovine Serum Albumin (BSA) (≥98%, CAS 9048-46-8), Mowiol 40-88 (CAS 9002-89-5), L-ascorbic acid (CAS 50-81-7), β-glycerophosphate (≥99%, CAS 154804-51-0), Alizarin Red S (CAS 130-22-3), anti-actin antibody (clone CA15, A5441), dexamethasone (≥80%, CAS 50-02-2), Hoechst 33342 (≥98%, CAS 23491-52-3) sodium pyrophosphate dibasic (H₂Na₂O₇P₂, CAS 7758-16-9), β-tri-calcium phosphate (β-TCP, >98% β-phase basis, CAS 7758-87-4), zirconium(IV) oxide (ZrO₂, 99% trace metals basis, CAS 1314-23-4), citric acid (>99.5%, CAS 77-92-9), and 3-(4,5-dimethylthiazol-2-yl)-2,5-diphenyl tetrazolium bromide (MTT, 98%, CAS 298-93-1) were purchased from Sigma-Aldrich. Acetone (≥99% (GC), CAS 67-64-1) and poly(vinyl alcohol) (PVA, CAS 9002-83-5) was purchased from Honeywell.

Calcium phosphate monobasic monohydrate, (MPCM, 99%, CAS 10031-30-8) was purchased from STREM chemicals, Inc. Combat Industrial Boron Nitride powder PHPP325B was purchased from Saint Gobain. Tween 20 (CAS 9005-64-5) was purchased from VWR International. Alexa-conjugated anti mouse IgG (Alexa fluor 488, A11001) was purchased from ThermoFisher Scientific. MEM alpha medium (Gibco 12571-063), DMEM/F-12 (1:1) + GlutaMAX (Gibco 31331-028), DMEM/F-12 (Gibco 21041-025), dimethyl sulfoxide (DMSO) (BDH Prolabo 23486.297), foetal bovine serum (FBS) (Eurobio CVFSVF00-01), penicillin/streptomycin (Gibco 15140-122) and 0.05% trypsin-EDTA (Gibco 25300-054) were and purchased from Thermo Fisher Scientific and used for cell cultures. MG-63 osteosarcoma cells were from ATCC.

B- Two-dimensional nanosheets

1. Graphene oxide

Graphene oxide (GO) is formed by heavily oxidizing graphite to chemically exfoliate the flakes of the graphitic stack into mono- and few-layer sheets, depending on the degree of oxidation and post-processing. The structure of GO is notoriously difficult to characterize and define broadly because of its inherently nonstoichiometric structure and dependence on production parameters. According to existing direct imaging evidence, GO is largely considered to have long-range order in sp^2 lattice. The graphene oxide used in all the experiments was synthesized by modified Hummers method from graphite flakes. 3g of graphite were dispersed in concentrated ($H_2SO_4:H_3PO_4$ 9:1, 400 mL) solution. Then, 18 g of $KMnO_4$ were added gradually to the mixture with stirring for 12 h. Later on, the mixture was cooled down to room temperature and then H_2O_2 (3 mL) was added. A brown precipitate was observed, showing the exfoliation of graphene oxide from graphite. After one hour of stirring, GO was separated by centrifugation at 6000 rpm for 10 minutes and the supernatant was

decanted away. The resultant precipitate was washed several times with 30% hydrochloric acid and absolute ethanol. Finally, the obtained powder was dried at 50°C for 24 hours to obtain the pure graphene oxide.

2. Boron nitride

Hexagonal Boron Nitride (h-BN) is a white block or powder. It has a layered structure similar to that of graphene and similar characteristics; it is therefore sometimes referred to as ‘white graphene’. h-BN is a lattice alternately arranged by B and N atoms in a two-dimensional plane by hexagonal lattice formation, displaying a honeycomb structure. The N and B atoms are combined by a sp² orbital to form a strong σ bond combined by weak interlayer Van der Waals forces. Hexagonal boron nitride (h-BN) is very attractive for many applications, particularly, as protective coating, dielectric substrates, transparent membranes, or deep ultraviolet emitters. The h-BN used in all the experiments was PHPP325B COMBAT® powder purchased from Saint Gobain. The material appearance is a white powder with particle size around 3 μm . It possesses a surface area of 60 $\text{m}^2.\text{g}^{-1}$ and an apparent density of 2.2. Ultrasonic acoustic cavitation has been extensively used for exfoliation and dispersion of nanomaterials because it can concentrate the acoustic energy in small volumes. In particular, acoustic cavitation has been used in the production of 2D nanosheets such as graphene, transition metal dichalcogenides or boron nitride from bulk layered materials in liquid solutions. The acoustic cavitation concerns physical effects of high energy including the formation, growth and implosive collapse of bubbles at high ultrasonic intensities in a liquid medium. However, the high speed jets and intense shock waves can diminish the size of the nanosheets or generates defects on the surfaces.

An ultrasonic homogenizer consists essentially of three components: the high-frequency (HF) generator, the ultrasonic converter (UW), and the functioning tip. The HF generator first

transforms the alternating supply voltage from 50-60 Hz into a HF voltage of 20 kHz. If this voltage is applied to a suitable oscillator inside the ultrasonic converter, it is possible to transform electric oscillations into mechanical oscillations of same frequency. The mechanical oscillation is transmitted by the ultrasonic converter through sonotrodes and is transmitted into the sample through the horns connected in between. The working intensity transmitted into the medium increases in inverse proportion with the diameter of the sonotrode area. The smallest tips transmit the largest power per measure of area in maximum oscillation amplitudes of several tenths of a millimeter. EBN were fabricated using liquid phase exfoliation with the assistance of an ultrasounds device (model SONOPLUS HD 3100, 100W, 20 kHz) with a microtip of diameter 3 mm (MS73). 1.0 g of pristine h-BN was added to 100 mL of water. The solution was heated up to 80 °C, then 20 g of gelatin from porcine skin (gel strength 300, Type A) were added, the mixture was kept under stirring at the same temperature until the complete dissolution of the gelatin. The dispersion was kept in a bath at 50 °C to avoid the gelatin solidification and it was sonicated overnight at 65 % amplitude with pulse off/on 0.5 – 1 s. After the sonication, the suspension was subjected to two centrifugation steps. In a first step, the solution was centrifuged at 3000 rpm for 30 min. Then, the supernatant was collected and subjected to a second centrifugation step at 6000 rpm for 30 min. The speed during the centrifugation also plays an important role in the obtained EBN lateral size, because the large nanosheets will be separated from the thinner ones during this centrifugation steps. The supernatant, where are the lightest nanosheets, was collected and dried at 60 °C overnight. The resultant material was heated up to 600 °C under air atmosphere to remove the gelatin.

C- PLGA microspheres

1. Single and double emulsion solvent evaporation method

1.1. Microspheres of 1 μm

1.1.1. Preparation of AL-loaded PLGA microspheres

To prepare AL-loaded PLGA-microspheres of around 1 μm in diameter, a double-emulsion-solvent-evaporation method (water-in-oil-in-water or $W_1/O/W_2$) was used. Microspheres were produced by first dissolving 25mg of alendronate in 1 ml of distilled water. This is the first aqueous phase (W_1). Then 500 mg of PLGA (Resomer RG503H) were dissolved in 5 mL dichloromethane (DCM), forming oil phase (O). The mixture was emulsified using an Ultra-Turrax emulsifier (T25 digital, IKA) for 90 s at 22000 rpm. Then, 10 mL 2% aqueous poly(vinyl alcohol) (PVA) solution (W_2) was added and emulsified for another 90 s at 22000 rpm to produce the second emulsion. After which another 10 mL 2% PVA solution were added to the mixture. The resultant $W_1/O/W_2$ emulsion was stirred overnight at room temperature to evaporate the solvent and solidify PLGA/AL microspheres. Then, the microspheres were finally washed in distilled water and collected through centrifugation at 3000 rpm for 10 min, lyophilized and stored at 4°C until use.

1.1.2. Preparation of RH-loaded PLGA microspheres

To prepare RH-loaded PLGA-microspheres of around 1 μm in diameter, a single-emulsion (W/O) technique was used. Microspheres were produced by dissolving 25 mg of raloxifene and 500 mg of PLGA in 5 mL DCM. The mixture was emulsified using an Ultra-Turrax emulsifier (T25 digital, IKA) for 90 s at 22000 rpm. Then, 10 mL 2% aqueous PVA solution was added to the mixture. The resultant W/O emulsion was stirred overnight at room temperature to evaporate the solvent and solidify PLGA/RH microspheres. Then, the microspheres were finally washed as described for AL-loaded microspheres. As a control,

PLGA microspheres were similarly fabricated without the addition of any drug into PLGA solution before emulsification.

1.2. Microspheres of 100 μm

1.2.1. Preparation of AL-loaded PLGA microspheres

To prepare AL-loaded PLGA-microspheres of around 100 μm in diameter, a double-emulsion-solvent-evaporation method (water-in-oil-in-water or $W_1/O/W_2$) was used. Microspheres were produced by first dissolving 500mg of PLGA in 5 ml dichloromethane (DCM), forming oil phase (O). Then 1 mL of distilled water containing 10mg of AL which is the first aqueous phase (W_1) was added to the oil phase. The mixture was emulsified using an Ultra-Turrax emulsifier (T25 digital, IKA) for 90 s at 22000 rpm. Then, 6 mL 0.3% aqueous poly(vinyl alcohol) (PVA) solution (W_2) was added and emulsified for another 90 s at 22000 rpm to produce the second emulsion. After which 394 mL 0.3% PVA solution and 400 mL 2% 2-propanol solution were added to the mixture. The resultant $W_1/O/W_2$ emulsion was stirred overnight at room temperature to evaporate the solvent and solidify PLGA microspheres. Then, the microspheres were finally washed in distilled water and collected through centrifugation at 3000 rpm for 10 min, lyophilized and stored at 4°C until use.

1.2.2. Preparation RH AL-loaded PLGA microspheres

To prepare RH-loaded PLGA-microspheres of around 100 μm in diameter, a single-emulsion-solvent-evaporation method (water-in-oil or W/O) was used. Microspheres were produced by first dissolving 500mg of PLGA in 5 ml dichloromethane (DCM) containing 10mg of RH, forming oil phase (O). Then 1 mL of 0.3% PVA which is the first aqueous phase (W) was added to the oil phase. The mixture was emulsified using an Ultra-Turrax emulsifier (T25 digital, IKA) for 90 s at 22000 rpm. After which 149 mL 0.3% PVA solution and 50 mL 2%

2-propanol solution were added to the mixture. The resultant W/O emulsion was stirred overnight at room temperature to evaporate the solvent and solidify PLGA microspheres. Then, the microspheres were finally washed in distilled water and collected through centrifugation at 3000 rpm for 10 min, lyophilized and stored at 4°C until use.

2. Characterization techniques

2.1. Dynamic light scattering

Dynamic light scattering is a technique used to determine the size distribution profile of small particles or polymers in suspension or polymers in solution. This method relies upon the measurement of scattering intensity of nanoparticles in Brownian motion when illuminated by a monochromatic beam of light. This scattering intensity fluctuates on a microsecond timescale, the fluctuations corresponding to the diffusion rate of the particles. It should also be noted that the scattering of light depends on the refractive index of macromolecules. Since intensity fluctuations of macromolecules are being collected and analyzed in a DLS experiment, the first-hand information on hydrodynamic radius (R_h) is based on the intensity distribution that provides z-average R_h . As light scattering depends on the refractive index of macromolecules and solvent viscosity, the z-averaged R_h requires input of these two properties.

2.2. Granulometry

Laser diffraction is a widely used particle sizing technique for materials ranging from hundreds of nanometers up to several millimeters in size. Laser diffraction measures particle size distributions by measuring the angular variation in intensity of light scattered as a laser beam passes through a dispersed particulate sample. Large particles scatter light at small angles relative to the laser beam and small particles scatter light at large angles, as illustrated

below. The angular scattering intensity data is then analyzed to calculate the size of the particles responsible for creating the scattering pattern, using the Mie theory of light scattering. The particle size is reported as a volume equivalent sphere diameter. Laser diffraction uses Mie theory of light scattering to calculate the particle size distribution, assuming a volume equivalent sphere model. Mie theory requires knowledge of the optical properties (refractive index and imaginary component) of both the sample being measured, along with the refractive index of the dispersant. Usually the optical properties of the dispersant are relatively easy to find from published data, and many modern instruments will have in-built databases that include common dispersants. For samples where the optical properties are not known, the user can either measure them or estimate them using an iterative approach based upon the goodness of fit between the modeled data and the actual data collected for the sample. The size distribution of PLGA microspheres was characterized using a laser diffraction particle size analyzer (Mastersizer 3000).

2.3. Scanning Electron Microscopy

Scanning electron microscopy (SEM) is a type of electron microscopy that produces images of a sample by scanning the surface with a focused beam of electrons and can provide information about the sample's surface topography and composition. SEM uses a focused beam of high-energy electrons, which scans the surface, and the secondary (inelastic emitted electrons) and backscattered electrons are detected in order to image the surface characteristics. It is desirable that the specimen be rendered electrically conducting; otherwise, a sharp picture will not be obtained. Conductivity is usually achieved by evaporating a film of metal, such as gold or other metals, 50–100 Å thick onto the specimen in vacuum (such a thickness does not materially affect the resolution of the surface details).

The morphology of the intern structure and surface of the obtained membranes was observed using a Hitachi S4800 SEM system. It was equipped with a secondary and backscattered

electron detector with an acceleration voltage from 0.1 kV to 30 kV. To carry out the analysis, samples were first coated with platinum using an ion sputter coater.

2.4. UV-Spectroscopy

2.4.1. Principle

This technique is based on the fact that transition metal complexes and highly conjugated organic compounds are capable of absorbing photons that have energy in this spectral range. The absorbent electrons come from the outer layers, in the case of organic compounds; they are the electrons π which passes on the level π anti-binder. During measurement, the absorbance can be measured as a function of time at a fixed wavelength, or as a function of wavelength. With Beer-Lambert's law and under appropriate concentration conditions, it is possible to determine the concentration of the analyzed solutions:

$A = \epsilon \times C \times l$ where A is the absorbance; ϵ is the molar extinction coefficient in $\text{mol}^{-1} \cdot \text{l} \cdot \text{cm}^{-1}$; C is the concentration in $\text{mol} \cdot \text{L}^{-1}$; l is the length of the optical path in the solution.

A light source that is generally a tungsten filament (for the 350-1700 nm range) and a deuterium lamp (190-400 nm) are used to cover the entire spectral range of interest. The beam from this light source passes through a monochromator (diffraction grating) and can be separated to obtain two monochrome beams that will pass through the sample. The beams can be collected by a single detector which is preceded by an optical separator that alternately blocks one of the beams. There can also be a detector for each beam. The detector can be a photodiode or a CCD sensor. The sample is in solution form (analyte + suitable solvent).

2.4.2. Determination of AL and RH encapsulation efficiency

Microspheres were produced by dissolving 500 mg of PLGA in 5 mL DCM. The portion of encapsulated AL in PLGA was measured as described as follows³⁷. The collected supernatant,

which is an AL suspension in PLGA/DCM solution, was rinsed in an iron (III) chloride/perchloric acid solution so that the suspended AL was entirely extracted into the aqueous phase. The AL in the iron (III) chloride/perchloric acid solution extraction, which represents the portion of encapsulated AL in PLGA, was quantified using an UV spectrophotometer (V-570, Jasco) at 300 nm. Therefore, the total AL encapsulation efficiency in PLGA/AL microspheres could be obtained from calibrations curves obtained beforehand.

To determine RH encapsulation in PLGA microsphere, a spectrophotometric method was followed with some modifications³⁸. Briefly, microspheres were dissolved in DCM and then equal volume of MeOH was added to solubilize RH. The portion of RH in the solution was quantified using an UV spectrophotometer at 287 nm. It was validated that PLGA in the extraction samples did not give interference with RH optical measurements at this wavelength. Calibration curve was constructed using different concentrations of RH in the solvent mixture of DCM:MeOH (1:1) in order to determine RH encapsulation efficiency. Encapsulation efficiency (EE) (%) of PLGA/AL and PLGA/RH microspheres was calculated as follows: $EE = \frac{C(drug)}{C(Ti)} \times 100$ with C(drug) the concentration of AL or RH obtained by UV-spectrophotometer and C(Ti) the concentration total initials of drugs.

2.4.3. Determination of drug release

In-vitro AL release trials were performed in a shaking incubator (Incu-Shaker, Benchmark) at 70 rpm under 37°C. Fifty milligram AL-loaded microspheres were soaked in 10 ml HEPES (pH=7.4). The sample media were collected at regular time intervals with equal amount of HEPES makeup. The determination of AL concentration was obtained following the method described above. PLGA/RH microspheres (50 mg) were incubated in 10 ml of PBS, maintained at 37°C in a shaking incubator. At specific time intervals total release media were collected and the supernatant was used to determine the amount of RH release with respect to

time. After taking the supernatant, total release media was refreshed with same amount of fresh PBS. The determination of RH concentration was obtained following the method described above. Release data for both drugs were expressed as cumulative percent release with respect to time.

D- 3D printing

1. Fused Deposition Modeling

Fused deposition modeling (FDM) is a common technique for scaffold fabrication. FDM is the deposition on the platform of molten thermoplastic materials through a heated extrusion head called nozzle. The structure is built in a layer-by-layer fashion where the layers are fused together. When each layer in the XY plane is finished, the platform (z-axis) is lowered and the procedure is repeated. This results in scaffolds with controlled pore size, morphology, and interconnectivity.



Figure 1. Image of single crew extruder noztek pro

The PLA solution (10 mL of 10% (w/v)) was prepared using dichloromethane as solvent. Different percentages of filler (0.1 to 0.3 wt %) were used. GO or BN was dispersed in acetone (1mg per mL) and placed in an ultrasonic bath for 15min. The GO or BN-containing solution was added to the polymer solution under constant magnetic stirring until the solution was homogeneous. The composite polymer solution was poured into a Teflon dish and allowed to dry at room temperature overnight. The obtained dried polymer was a film and was

cut into pieces and introduced into a single screw extruder (Noztek pro Fig. 1) at an extrusion temperature of 200°C.

A filament with a diameter of 1.75 mm was obtained and used for 3D printing. The scaffold was modelled using computer-aided design (CAD) software (Design Spark Mechanical). After deciding the scaffold shape, a STL file was created to be analyzed with the Prusa3Dslicer software. Scaffolds were 3D printed using a Prusa Research MK2S printer as show in Fig.2.



Figure 2. Prusa Research MK2S printer

2. Stereolithography

SLA is regarded as the first rapid prototyping process. It defined a method and apparatus for making solid objects by successively printing thin layers of ultraviolet (UV) curable material one on top of the other. Schematically, an SL system consists of a tank of photo-sensitive liquid resin, a moveable built platform, a UV laser to irradiate the resin and a dynamic mirror system. The process starts with the UV laser depositing a layer of a photo-sensitive liquid resin onto the platform. Once the layer is completely solidified, the platform is vertically lowered. Subsequently, another layer is deposited onto the first one. These steps are repeated until a complete 3D scaffold is formed. Finally, uncured resin is washed off and the scaffold is post-cured under UV light, yielding a fully cured part.



Figure 3. Formlabs Form 2 printer

PPF/DEF scaffold was fabricated using a Formlabs Form 2 printer (Fig.3) equipped with a Class 1, 405 nm violet laser with a power of 250 mW and laser spot size of 140 μm . Axis resolution (i.e., layer thickness) use for printing was 50 μm . After printing, the printed samples were then washed for several hours in an isopropyl alcohol (IPA) bath (Form Wash, Formlabs). Then the scaffolds were post-cured for 1 hour using formlabs Form Cure equipped with 405 nm UV-light at room temperature (Fig.4).



Figure 4. Formlabs Form Wash and Form Cure.

3. Synthesis of polypropylene fumarate

Poly (propylene fumarate) (PPF) was synthesized via a condensation reaction according to method of Gerhart⁴⁰. 2.4 mol of fumaric acid and 3.0 mol of propylene glycol were placed in a triple-necked 1 L flask with an overhead electrical stirrer. During synthesis, the mixture was stirred continuously at 150 rpm and the temperature of the solution was maintained at 140°C during 17 h. Then, the temperature was increased to 190°C during 5 h. The reaction was ended after that, and the final product was a clear, light-yellow, very viscous liquid. The

weight-average molecular weight (M_w) was 5330 Da, the number average molecular weight (M_n) was 1534 Da and PDI of 4.37. The PPF polymer has high viscosity at room temperature. To be able to use PPF as a liquid polymer for Stereolithography, DEF, a low viscosity cross-linking agent, was added to reduce the viscosity. The PPF was heated to approximately 60°C to reduce its viscosity, and DEF was added in different ratio. After mixing for about 1 h, the PPF/DEF mixture was filtered to remove impurities. The photoinitiator (BAPO or Lucirin-TPO) were added at different percentages and the mixture was stirred continuously for 3 h.

4. Characterization techniques

4.1. Optical interferometry

Profilometry is a technique used to extract topographical data from a surface. This can be a single point, a line scan or even a full three dimensional scan. The purpose of profilometry is to get surface morphology, step heights and surface roughness. This can be done using a physical probe or by using light. All profilometers consist of at least two parts – a detector and a sample stage. The detector is what determines where the points on the sample are and the sample stage is what holds the sample. In some systems, the sample stage moves to allow for measurement, in others the detector moves and in some both move. Optical profilometry uses light instead of a physical probe. This can be done a number of ways. The key component to this technique is directing the light in a way that it can detect the surface in 3D. Examples include optical interference, using a confocal aperture, focus and phase detection, and projecting a pattern onto the optical image.

A chromatic confocal rugosimeter (STIL SA) equipped with a CHR1000 sensor was used for the 3D characterization of the topography of cylinder surface areas of 10 mm of 3D printed PLA and PLA/GO scaffolds (two different locations of 2*2 mm for each scaffold with 5

lateral μm step). Data post-treatment was done with MountainsMap7 (DigitalSurf). The determined roughness parameter was the arithmetical mean height of the surface (S_a).

4.2. X-ray diffraction

X-ray diffraction (XRD) is a rapid analytical technique, which gives a robust image of the crystallographic structure and chemical composition. X-rays are generated by a cathode ray tube, filtered to produce monochromatic radiation, collimated to concentrate the beam and directed toward the sample. The measurement of the intensity of the scattered X-ray is plotted as a function of the angle 2θ between incident and scattered radiation. The distance between scattering planes d can be expressed according to Bragg's law: $n\lambda = 2d \sin \theta$ where n is an integer, λ is the wavelength and θ is the half-angle between the incident and scattered beam. X-rays of the incident beam can interact elastically with the electron cloud of the atoms of a material. These elastically diffracted waves from different atoms interfere either constructively or destructively resulting in a diffraction pattern, in which the intensities and position are directly related to atomic distribution and atom-atom distances. XRD was used to determine the interlayer spacing and the crystallite size of h-BNNS. The XRD patterns of used materials were recorded using a PANalytical Xpert powder XRD system with $\text{Cu K}\alpha$ radiation, a scan speed of 2° min^{-1} , a 2θ range between 10 and 70° , and a step rate of 0.02° per second.

4.3. Fourier transmission infrared

Fourier Transform Infrared Spectroscopy (FTIR) is a technique providing an infrared spectrum of absorption or emission of a specimen. The molecular vibrational spectrum can be divided into three regions: the far infrared (400 cm^{-1} to 0 cm^{-1}), the mid infrared (4000 cm^{-1} to 400 cm^{-1}), the most common used region due to the fact that most organic and inorganic

compounds absorb within it), and the near infrared ($> 4000\text{ cm}^{-1}$). When exposed to infrared radiation, molecules selectively absorb radiations of specific wavelengths, which causes a change in their dipolar momentum. Consequently, the vibrational energy levels of sample molecules transfer from their ground state to an excited state. The frequency of the absorption peak is determined by the vibrational energy gap. The number of absorption peaks is related to the number of vibrational degrees of freedom of the molecule. The intensity of the absorption peaks is related to the change of dipole moment and to the possibility of the transition of energy levels. The FTIR spectra were obtained using the attenuated total reflection (ATR) technique with a ThermoNicolet Nexus 710 FTIR spectrometer. The spectra were obtained from 4000 to 600 cm^{-1} with 32 scans and 4 cm^{-1} resolution.

4.4. Raman spectroscopy

Raman spectroscopy is a technique based on inelastic scattering of monochromatic light, usually from a laser in the visible, near infrared, or near ultraviolet range. This technique is used to observe vibrational, rotational, and other low-frequency modes in a system. In chemistry, it is commonly used to provide a structural fingerprint, according to which molecular units can be identified. Typically, the sample is illuminated by a laser, and then the incident light interacts with the molecule and distorts the cloud of electrons to form a “virtual state”. This state is not stable and the photon is immediately re-radiated as scattered light. A peak appearing in the Raman spectrum will be derived from a specific molecular vibration or lattice vibration. Peak position shows the specific vibrational mode of each molecular functional group included in the material. The shape of a Raman peak is important, not just its position. The width of the peak gives also information about size-effects. Any residual stress inside the crystal can also be evaluated from the direction and amount of any shift of the Raman peak. The spectra have been obtained from a Horiba xplora, using a wavelength $\lambda=$

659 nm. The samples were deposited onto a glass slide to perform the analysis. The data were treated with the Labspec software.

4.5. Wettability

The contact angle is defined as the angle formed by the intersection of the liquid-solid interface and the liquid-vapor interface. The interface where solid, liquid, and vapor co-exist is referred to as the “three-phase contact line. The contact angle depends on how the liquid behaves when deposited on a surface. When the fluid spreads over a large area on the surface, a contact angle less than 90° is observed; while contact angles greater than 90° generally means that wetting surface is unfavorable. Therefore, water contact angles (WCA) smaller than 90° usually refer to “hydrophilic” surfaces, while WCA larger than 90° characterize “hydrophobic” surfaces. WCA were measured using a B-CAM-21-BW (CCCIR) monochrome camera and a Led R60 lamp purchased from CONRAD. For each sample, 3.0 μL of ultrapure water was deposited on the membranes using a needle. The images were recorded by the One Touch Grabber software and treated using the ImageJ software.

4.6. Mechanical properties

4.6.1. Dynamic mechanical analysis

Dynamic mechanical analysis (DMA) is a technique where a small deformation is applied to a sample of a known geometry in a cyclic manner. The sample can be subjected by a controlled stress or a controlled strain. For a known stress, the sample will then deform a certain amount. How much it deforms is related to its stiffness. A force motor is used to generate the sinusoidal wave, which is transmitted to the sample via a drive shaft. The mechanical properties of the obtained membranes were characterized using the DMA system (Metravib 50N) at a tensile testing speed (crosshead speed) of 0.05 mm min^{-1} . The sample was clamped

at top and bottom; thereby the specimen is subjected to an underlying tensile stress to prevent it from buckling during loading. The Young's modulus of the membranes was calculated from the elastic region of the stress–strain curves.

4.6.2. Tensile and compressive strength

Stress is defined as the force per unit area. Thus, the formula for calculating stress is: $\sigma = F/A$. Where σ denotes stress, F is load and A is the cross sectional area. The most commonly used units for stress are the SI units, or Pascals (or N.m^{-2}), although other units like psi (pounds per square inch) are sometimes used. Forces may be applied in different directions such as: Tensile or stretching; Compressive or squashing/crushing; Shear or tearing/cutting; Torsional or twisting. This gives rise to numerous corresponding types of stresses and hence measure/quoted strengths. While data sheets often quote values for strength (e.g compressive strength), these values are purely uniaxial, and it should be noted that in real life several different stresses may be acting. The tensile strength is defined as the maximum tensile load a body can withstand before failure divided by its cross sectional area. This property is also sometimes referred to Ultimate Tensile Stress or UTS. Compressive strength is defined as the maximum compressive load a body can bear prior to failure, divided by its cross sectional area. The mechanical properties of the PLA 3D printed scaffolds and calcium phosphate were characterized using a modular traction system (1/ME) in tensile or compression mode coupled with a 5 kN force sensor (maker). Samples were printed in the shape of a dog bone (40 mm length, 4 mm width, and 1.5 mm thick) for tensile test and moulded in cylindrical shape (10 mm diameter and 20 mm height) for compressive test. Samples were then clamped between dedicated jaws and pulled or compressed at a constant speed of 0.01 mm.s^{-1} until they broke. Samples were imaged with a 16 Mb camera (SVS-VISTEK) at 1 Hz. Samples were initially randomly patterned with thin black paint to perform digital image correlation (DIC). Using an

already described DIC algorithm dedicated to large deformations^{46,47}, sample strain changes could be computed without inaccuracy coming from the machine and jaw plays. Linear elastic regions from the stress–strain graphs were then used to calculate the Young's modulus from at least three assays. The stress at which the sample begins to break was also measured.

4.7. Thermogravimetric Analysis

Thermogravimetric analysis (TGA) is one of the members of the family of thermoanalytical techniques used to characterize a wide variety of materials. TGA provides complimentary and supplementary characterization information to the most commonly used thermal technique, DSC. TGA measures the amount and rate (velocity) of sample mass changes as a function of temperature or time in a controlled atmosphere. The measurements are used primarily to determine the thermal and/or oxidative stability of materials as well as their compositional properties. TGA consists of a pan where the material is deposited; this pan is supported by a precision balance. That pan resides in a furnace and is heated or cooled during the experiment. The mass of the sample is monitored during the experiment. A sample purge gas controls the sample environment. Thermal behavior of the as prepared membranes was examined by Thermogravimetric Analyzer model TA instruments TGA G500 from 20°C to 900°C. A heating rate of 10°C.min⁻¹ was used under air atmosphere and at flow rate of 60 mL.min⁻¹. Dry samples weighing about 5 mg were used.

4.8. Differential Scanning Calorimetry

Differential scanning calorimetry (DSC) is a thermoanalytical technique in which the difference in the amount of heat required to increase the temperature of a sample and a reference is measured as a function of temperature. Thermal transitions comprise the changes in the polymer melting or in the glass transition temperatures. The thermal transition behavior

of the membranes was determined by a differential scanning calorimeter (model TA instruments DSC Q20) equipped with a RCS90 cooling system, from 20°C to 200°C. A heating rate of 10°C.min⁻¹ was used under nitrogen atmosphere and at flow rate of 50 mL.min⁻¹. The samples weight was about 5 mg and they were sealed into an aluminum capsule for the analysis.

4.9. Gel Permeation Chromatography

Gel permeation chromatography (GPC) is one of the most powerful and versatile analytical techniques available for understanding and predicting polymer performance. It is the most convenient technique for characterizing the complete molecular weight distribution of a polymer. GPC separates molecules in solution by their "effective size in solution." To prepare a sample for GPC analysis the resin is first dissolved in an appropriate solvent. Inside the gel permeation chromatograph, the dissolved resin is injected into a continually flowing stream of solvent (mobile phase). The mobile phase flows through millions of highly porous, rigid particles (stationary phase) tightly packed together in a column. The pore sizes of these particles are controlled and available in a range of sizes. The molecular weight of the synthesized PPF was measured using gel permeation chromatography (GPC) system with an infrared detector. Samples were eluted with THF through a column at a flow rate of 1 mL.min⁻¹. Molecular weight was determined relative to a polystyrene standard by the data plotting.

4.10. Rheology

Rheology is the science that describes, explains and quantifies the phenomena appearing while bodies or liquids are deformed or flowing under the effect of an applied force.

Viscosity (η) is an important parameter. The flow behavior of an ideal liquid is described by the dynamic viscosity law: $\eta = \tau / \dot{\gamma}$ (Pa·s) where η is the viscosity (Pa·s), τ shear stress (Pa) and

$\dot{\gamma}$ is the shear rate (s⁻¹). The viscosity could be also described as the measurement of resistance against the flow. The applied forces also can induce structural changes in the material and therefore in its viscosity. Depending on the material response, two different behaviors can be defined. In one hand, the shear thinning behavior, where the molecules or particles suffer an arrangement when the system starts to flow. On the other hand, the shear-thickening behavior, this is characterized by the disorder of the particles or molecules when the system starts flowing. To analyze our PPF and PPF/DEF mixed, 1 mL of sample was deposited on the module. The rheometer (Anton Paar MCR 302) temperature was fixed at 37°C for all the experiments. The experiment was carried out using cone-plate geometry; with 50 mm diameter and a gap set at the center of the cone of 101 μ m. The viscosity evolution is followed over the time varying the shear rate between 1 and 100 rad s⁻¹.

E- Calcium Phosphate Cement

1. Materials and synthesis

The cement powder was composed of Calcium phosphate monobasic monohydrate and β -tricalcium phosphate at a 55 to 45 molar ratio. The MCPM and β -TCP powder were sieved to obtain only 150 and 50 μ m particles, respectively. Zirconia (20% wt) and disodium dihydrogen pyrophosphate (1% wt) were added directly to the powder. The cement (CPC) was fabricated by addition citric acid (0.5M) solution, to powder at liquid ratio of 0.4 mL per gram of cement (irrespective of ZrO₂ content). Macroporous cement was fabricated by addition of different % of PLGA microsphere to the powder mixture and denoted as CPC/PLGA. The addition of liquid was adjusted to keep a powder/liquid ratio of 0.4. CPC and CPC/PLGA formulations were mixed using a spatula for 1 min in a glass plate and immediately transferred to a 5 mL syringe. After which, the paste was injected in silicon rubber molds of 5 mm diameter and 2 mm height. Within 15 min samples were transferred to

calcium free Dulbecco's phosphate buffered saline (DPBS, Sigma) to allow for complete setting at 37°C for 24 h.

2. Characterization techniques

2.1. Energy-dispersive X-ray

Scanning electron microscopy with energy dispersive X-ray spectroscopy (SEM/EDX) is the best known and most widely-used of the surface analytical techniques. High resolution images of surface topography, with excellent depth of field, are produced using a highly-focused, scanning (primary) electron beam. The primary electrons enter a surface with an energy of 0.5 – 30 kV and generate many low energy secondary electrons. The intensity of these secondary electrons is largely governed by the surface topography of the sample. An image of the sample surface can thus be constructed by measuring secondary electron intensity as a function of the position of the scanning primary electron beam. High spatial resolution is possible because the primary electron beam can be focused to a very small spot (<10 nm). High sensitivity to topographic features on the outermost surface (< 5 nm) is achieved when using a primary electron beam with an energy of < 1 kV. In addition to low energy secondary electrons, backscattered electrons and X-rays are generated by primary electron bombardment. The intensity of backscattered electrons can be correlated to the atomic number of the element within the sampling volume. Hence, some qualitative elemental information can be obtained. The analysis of characteristic X-rays (EDX or EDS analysis) emitted from the sample gives more quantitative elemental information. Such X-ray analysis can be confined to analytical volumes as small as 1 cubic micron. SEM, accompanied by X-ray analysis, is considered a relatively rapid, inexpensive, and basically non-destructive approach to surface analysis. It is often used to survey surface analytical problems before proceeding to techniques that are more surface-sensitive and specialized. Energy-dispersive X-ray

spectroscopy analysis (EDX) was taken with Zeiss EVO ED15 microscope coupled with an Oxford X-MaxN EDX detector.

2.2. Opacity

Radioopacity of injectable cement is necessary to avoid risk cement leakage. For X-ray opacity measurements 2 mm thick samples were produced. The X-ray opacity was measured at 0.65 mAs, 80 kV using an OBI (On-Board Imager®) (TrueBeam-Stx, Varian). A 2mm sample of a PMMA-based cement (Vertebroplastic, Biomet, France), which has zirconia as radiopacifier, was used as control along with an aluminium wedge 2–8 mm in 1 mm steps. The photos were treated with the software Image J to determine the grey level between the samples.

2.3. Injectability

Injectability is defined as the possibility to extrude cement with a syringe in the bone defect without modifying its integrity. Injectability is linked to the viscosity of the paste. Different methods allow determining the injectability. The method depends of the measurement parameters such as: syringe's geometry, diameter of the nozzle, strength and speed of injection, cement preparation and time setting. Injectability tests were done on the CPC and CPC/PLGA30 samples in two different methods. Briefly, the first method consist to evaluate by extrusion (i.e., quantification of residual-cement mass retained in the syringe after applying a standard force), during a predetermined injection time period the injectability. Syringes of 10 mL (Omnifix® luer lock solo) were filled with 8 g fresh-cement paste. After predetermined times from the mixing, the cement was extruded manually. The injectability was calculated as: $I = [(m_i - m_f)/m_i] \times 100\%$ where I is the injectability, m_i is the initial mass and m_f is the final mass of the extrusion. The second method consists to after mixing the

powder with liquid, to place the syringe, vertically in a fixture and put under the plates of a handmade injection machine. At a predetermined time of 4min after mixing the cement, the cement was extruded with a compression rate of 0.2 mm.min^{-1} up to a maximum force of 100 N. Compressive force was applied to the syringe and recorded as a function of the plunger travel length. All tests were performed in threefold.

2.4. Setting time

Cement setting time was evaluated using the Gillmore needle method (ISO 9917-1:2007 standard). The device consists of two needles: the first (113.4 g ; $\varnothing = 2.12 \text{ mm}$) measures the "initial setting time", the second (453.6 g ; $\varnothing = 1.06 \text{ mm}$) estimates the "final setting time". These needles are placed manually at different times on the surface of the cement, previously shaped to provide a flat surface. The "initial" take and "final" is effective when the first or second needle, respectively, no longer makes mark on the cement (visual estimation).

Initial and final setting time was assessed using custom available Gillmore needles (ASTM C266). For this, a plastic mould 10 mm in diameter and 15 mm in height was used as a mould. Samples were mixed and injected into the mould, after which the initial and final setting time was determined. Tests were performed in at least 3 samples.

2.5. X-ray microtomography

X-ray tomography uses the ability of X-ray radiation to penetrate objects. On the way through an object, part of the impinging radiation is absorbed. The longer the radiographic length of the object, the less radiation escapes from the opposite side. The absorption also depends on the material. An X-ray detector (sensor) captures the escaping X-ray radiation as a two-dimensional radiographic image. At detector sizes of approximately 50 mm to 400 mm, a large portion of the measured object can be captured in a single image. In order to use

tomography on an object, several hundred two-dimensional radiographic images are made in sequence, with the measured object in various rotated positions. The object is located on a rotating table for this purpose, which is gradually rotated step by step. The three-dimensional information about the measured object contained in this series of images is extracted using a suitable mathematical process and is made available as a “voxel image”. Each voxel (**v**olume **p**ixel) embodies the X-ray absorption by the measured object for a defined location in the measured volume. Similar to two-dimensional image processing, the actual measured points are calculated from the voxel data using a suitable threshold process. The sensors currently used capture up to 4 million image points. Typically, several hundred thousand to a few million measurement points are derived in the measured volume. These points are distributed evenly across the surface of the part being measured. Geometries in the interior of the measured object, such as hollow cavities or undercuts, are also captured. The measurement points can be evaluated using the familiar methods of coordinate measuring technology.

Similar to measurement using image processing, it is possible to change the magnification using tomography in order to capture small parts with higher magnification, or larger parts completely with lower magnification. To do this, either the measured object is positioned in the radiation path or the X-ray components (X-ray source and detector) are moved in an axial direction relative to the measured object. In some cases, the size of the sensor or the number of pixels available is still not enough to meet the requirements for the measuring task. In such cases, several images are stitched together by moving the rotary table with the measured object relative to the X-ray components. Reconstruction of the voxel volume image is then accomplished on the basis of the stitched 2-D radiographic images.

Cylindrical CCP of 10 mm diameter for 20 mm length were analyzed. 3D radiographic evaluation was performed using an X-ray micro-CT instrument (Easy Tom 150Kv

Microtomograph) with 3D reconstruction software (Xact). Implanted samples were planned to be scanned at 360° rotation.

F- Biological studies

1. In vitro

Two cell lines were mainly used for this thesis project: MG63 osteosarcoma cells and MCF7 breast cancer cells.

1.1. MTT assays

Scaffolds were sterilized with ethanol for 30 minutes and under UV light (405nm) for 1 hour.

MG-63 osteosarcoma cells were cultured on the sterilized scaffolds in MEM alpha, 10% FBS and 1% penicillin/streptomycin for up to 7 days before cell viability and adhesion assays.

MCF7 breast cancer cells were cultured in DMEM/F-12 (1:1) + GlutaMAX medium prior a switch of medium (DMEM/F-12). Cell viability and proliferation were analyzed with the MTT assay. The effects of the two drugs on MCF7 breast cancer cell proliferation was analyzed using the MTT assay as well. At different time points during culture, 100 µL of culture medium containing 0.05 mg.mL⁻¹ of MTT solution was added to the cultures for 3h. MTT reduction by living cells leads to the production of purple-colored formazan crystals that were solubilized by addition of 100 µL of DMSO. The absorbance of the formazan solution was recorded at 560 nm using a Multiskan plate reader (Thermos, USA).

1.2. Immunofluorescence

For the adhesion assay of cells on material, MG-63 cells were seeded with the cell concentration necessary. Then cells were fixed in 4% formaldehyde (500 µL/well) at room temperature for 20 minutes. Fixed cells were washed with PBS/0.05%, then permeabilized with PBS/0.1% Triton X 100 (Sigma) for 15 minutes, and incubated with PBS/1% BSA

solution for 3 hours. Then, the cell cytoskeleton was stained with an anti-actin antibody at 4°C overnight. After two washes with PBS/0.05% Tween 20, an Alexa-conjugated anti-mouse IgG secondary antibody was added with Hoechst 33342, to stain the nuclei, at room temperature for 1 hour. Samples were mounted in Mowiol and fluorescent images were recorded using a fluorescent microscope (DM6000 Leica).

1.3. Cell differentiation or mineralization

MG-63 cells were plated in Petri dishes on the scaffolds and grown until confluence (day 0). Then, medium was switched to differentiation medium supplemented with ascorbic acid (50 mg.ml⁻¹), β-glycerophosphate (5 mM) and dexamethasone (10⁻⁸ M), and refreshed every 48 hours. Formation of mineralized nodules was monitored at different time point by Alizarin Red-S staining. Briefly, cells were rinsed twice with PBS followed by fixation in 4% formaldehyde at room temperature for 20 minutes. Then, cells were rinsed twice with PBS (pH 4.2) and stained with 40 mM Alizarin Red-S (pH 4.2) at room temperature for 20 minutes, and extensively rinsed with water. For quantification, the staining was eluted with 10% (wt/vol) cetylpyridinium chloride, and the supernatant absorbance was measured at 540 nm using a microplate reader (Bio-Rad).

2. In vivo

Animal (male Wistar rats ((CrI:(Wi)Br), Charles River, France). with weight ranging from around 400 g was used for an adequate vertebrae size. Animal was kept in light controlled, air-conditioned rooms and fed ad libitum. One vertebra was used as a control (defect empty of materials) and two other vertebrae were used for CPC and CPC/PLGA30 implantation, for one month period. CPC and CPC/PLGA30 were prepared fresh and injected directly after the required setting time to allow the incorporation of the material in each vertebra. Animals were

anesthetized with an intraperitoneal injection of ketamine and xylazine (Alcyon, Pau, France) (40 and 9mg/kg, respectively). The tail was disinfected and a dorsal incision was made approximately from Cd31 to Cd35 vertebrae. The skin and the muscles were retracted with buffered saline solution irrigation and the vertebrae were exposed. For CPC, CPC/PLGA30 implantation and for the empty cavity control, an intraosseous defect preparation of 3x3mm was performed in the exposed surface of the vertebrae. After the hard tissue treating, the skin was tightly sutured with resorbable sutures (Vicryl 3/0, Ethicon, Issy les Moulineaux, France). Following surgery, Buprenorphine SR-LAB (1 mg/mL), (Wildlife Pharmaceuticals, Windsor, CO, USA) at dose of 1.2mg/kg was used for systemic relief and to provide 72 h analgesia. The Rat was kept in individual cage and the wound healing was controlled daily during the healing period. At the end of the experimental period, the rat was sacrificed by intraperitoneal injection of Pentothal (Alcyon, Pau, France) with a suitable dosage (200 mg/1.5kg). The tail was harvested between Cd31 and Cd32. 3D radiographic evaluation was performed using an X-ray micro-CT instrument (SKYSCAN 1172 X-ray Microtomograph, Microphotronics Inc, Allentown, USA) with 3D reconstruction software (Aviso, FEI company, Hillsboro, USA). Implanted samples were planned to be scanned at 360° rotation at 0.7 degree intervals. Measurements were made on the Region of Interest (ROI) \times 1.5 mm Tissue Volume (TV) on the computer-reconstructed 3D samples.

Scientific contributions

➤ Publications

1. Sakthivel Nagarajan, **Habib Belaid**, Céline Pochat-Bohatier, Catherine Teyssier, Igor Iatsunskyi, Emerson Coy, Sébastien Balme, David Cornu, Philippe Miele, Narayana S. Kalkura, Vincent Cavaillès and Mikhael Bechelany (2017). Design of Boron Nitride/Gelatin Electrospun Nanofibers for Bone Tissue Engineering. *ACS applied materials & interfaces*, 9(39), 33695-33706
2. **Habib Belaid**, Sakthivel Nagarajan, Catherine Teyssier, Jonathan Barés, Sébastien Balme, Hélène Garay, Vincent Huon, David Cornu, Vincent Cavaillès and Mikhael Bechelany. (2019) 3D Printed Graphene Oxide-based Scaffolds for Bone Tissue Engineering. *Materials Science & Engineering C*. **Accepted**
3. **Habib Belaid**, Sakthivel Nagarajan, Vincent Huon, Jonathan Barés, Sébastien Balme, Philippe Miele, David Cornu, Vincent Cavaillès, Catherine Teyssier and Mikhael Bechelany. (2019) Boron nitride-based nano-biocomposites: Design by 3D printing for bone tissue engineering. *ACS Applied Bio Materials*, **In revision**
4. **Habib Belaid**, Sébastien Blanquer, Sébastien Balme, Catherine Teyssier, David Cornu, Vincent Cavaillès and Mikhael Bechelany. (2019) Stereolithographic 3D printing of a PPF scaffold containing drug-loaded PLGA microspheres. **Ready for submission**
5. **Habib Belaid**^{1,2}, Pierre-Yves Collart-Dutilleul³, Alban Desoutter³, Frédéric Cuisinier³, Jonathan Barés⁴, Vincent Huon⁴, Catherine Teyssier², David Cornu¹, Vincent Cavaillès^{2*£} and Mikhael Bechelany^{1*£}. (2019) Fabrication of injectable calcium phosphate cement containing PLGA microspheres. **Ready for submission**

➤ **Conferences**

• **Oral communications**

1. **Habib Belaid**, Catherine Teyssier, David Cornu, Vincent Cavaillès and Mikhael Bechelany. *Development of an injectable cement allowing multiple drug delivery for the treatment of breast cancer bone metastasis*. Balard conference, June 18-21th 2018, Montpellier, France
2. **Habib Belaid**, Catherine Teyssier, David Cornu, Vincent Cavaillès and Mikhael Bechelany. *Development of an injectable cement allowing multiple drug delivery for the treatment of breast cancer bone metastasis*. 2ème workshop "BioFabrication & Cancer", June 27-28th 2018, Bordeaux, France
3. **Habib Belaid**, Catherine Teyssier, David Cornu, Vincent Cavaillès and Mikhael Bechelany. *Development of an injectable cement allowing multiple drug delivery for the treatment of breast cancer bone metastasis*. Congress SCF 18, July 2-4th 2018, Montpellier, France
4. **Habib Belaid**, Catherine Teyssier, David Cornu, Vincent Cavaillès and Mikhael Bechelany. *Development of an injectable cement allowing multiple drug delivery for the treatment of breast cancer bone metastasis*. 4th International Conference on Bioinspired and Biobased Chemistry and Materials, October 14-17th 2018, Nice, France
5. **Habib Belaid**, Catherine Teyssier, David Cornu, Vincent Cavaillès and Mikhael Bechelany. *3D printed scaffold allowing multiple drug delivery for the treatment of bone metastasis in breast cancers*. 4th International Conference on Bioinspired and Biobased Chemistry and Materials, October 14-17th 2018, Nice, France
6. **Habib Belaid**, Catherine Teyssier, David Cornu, Vincent Cavaillès and Mikhael Bechelany. *Development of an injectable cement allowing multiple drug delivery for the treatment of breast cancer bone metastasis*. 6th Mediterranean Young Researchers Days, October 18-19th 2018, Marseille, France
7. **Habib Belaid**, Catherine Teyssier, David Cornu, Vincent Cavaillès and Mikhael Bechelany. *3D printed PLA/BN scaffolds for bone tissue engineering application*. 8th European Conference on Boron Chemistry, June 24-27th 2019, Montpellier, France
8. **Habib Belaid**, Catherine Teyssier, David Cornu, Vincent Cavaillès and Mikhael Bechelany. *3D printed PLA/BN scaffolds for bone tissue engineering application*. 30th annual conference of the European Society for Biomaterials, September 9-13th 2019, Dresden, Germany

9. **Habib Belaid**, Catherine Teyssier, David Cornu, Vincent Cavaillès and Mikhael Bechelany. *3D printed PLA/BN scaffolds for bone tissue engineering application*. Materials Oceania, September 16-18th 2019, Melbourne, Australia
10. **Habib Belaid**, Catherine Teyssier, David Cornu, Vincent Cavaillès and Mikhael Bechelany. *3D printed scaffold allowing multiple drug delivery for the treatment of bone metastasis in breast cancers*. Materials Oceania, September 16-18th 2019, Melbourne, Australia

- **Posters**

1. **Habib Belaid**, Catherine Teyssier, David Cornu, Vincent Cavaillès and Mikhael Bechelany. *3D printed scaffold allowing multiple drug delivery for the treatment of bone metastasis in breast cancers*. Balard conference, June 18-21th 2018, Montpellier, France
2. **Habib Belaid**, Catherine Teyssier, David Cornu, Vincent Cavaillès and Mikhael Bechelany. *3D printed scaffold allowing multiple drug delivery for the treatment of bone metastasis in breast cancers*. 2ème workshop "BioFabrication & Cancer", June 27-28th 2018, Bordeaux, France
3. **Habib Belaid**, Catherine Teyssier, David Cornu, Vincent Cavaillès and Mikhael Bechelany. *3D printed scaffold allowing multiple drug delivery for the treatment of bone metastasis in breast cancers*. Congress SCF 18, July 2-4th 2018, Montpellier, France
4. **Habib Belaid**, Catherine Teyssier, David Cornu, Vincent Cavaillès and Mikhael Bechelany. *3D printed scaffold allowing multiple drug delivery for the treatment of bone metastasis in breast cancers*. 30th annual conference of the European Society for Biomaterials, September 9-13th 2019, Dresden, Germany